EFFECTS OF A PERIODIC DISTURBANCE ON STRUCTURE AND MIXING IN TURBULENT SHEAR LAYERS AND WAKES

by

Fredrick Allen Roberts

This report was also submitted as a thesis in partial fullfillment

of the requirements for the degree of Doctor of Philosophy

California Institute of Technology

Pasadena, California

1985

(submitted 12 September 1984)

Dedicated to the memory of my father ,

John D. (Bud) Roberts

ACKNOWLEDGEMENTS

I am grateful to my advisor, Professor Anatol Roshko, for years of advice, patience, and support. There were many times when others gave up but he never did. Professor Paul Dimotakis is acknowledged for his advice on various hardware matters and, most important, for his moral support during difficult times. I am deeply indebted to my friend and colleague Manooch Koochesfahani for his help with the experiments and data processing. He was both a patient teacher and critical listener. Dan Nosenchuck and Dan Lang are acknowledged for their electronics genius. They always had the answers to my questions. I am grateful to Kathy Eriksen for her expert help in preparing the manuscript and to Harry Hamaguchi for his photographic expertise. Betty Wood and Jim Cummings are acknowledged for their help with preparation of the figures. It has been my pleasure, over the many years I have been here, to interact with the members of the technical and secretarial staffs at GALCIT. They were always willing to appease a *do it myself* attitude, even when they knew faster methods existed. I would like to thank my family and loved ones for their support during a most difficult ordeal. Mom, Nana, Darnell, Darlene, Dave, Hoss, and Denise all encouraged me. I wish my father could have lived to read this document and share my pride. Finally, I want to thank my *57 Chevy* for reminding me of curiosity, ingenuity, dedication, and skinned knuckles.

ABSTRACT

Large scale structure and mixing processes are investigated in chemically reacting wakes and shear layers to which a periodic disturbance is applied. The experiments employ a diffusion-limited acid-base reaction to directly measure the extent of mixing. Optical diagnostics used include laser absorption and laser induced fluorescence. Absorption of laser light by reacted product provides a measure of cross-stream average product. Fluorescence was measured by a self-scanning linear photodiode array using high speed computer data acquisition to obtain the product distribution across the layer.

Previous results showing that forcing alters the structure and growth rate of shear layers are confirmed. Forcing artificially extends the lifetime of vortices whose size is consistent with the disturbance wavelength. Amalgamation of smaller vortices is enhanced over that in the natural layer until the frequency locked scale is achieved. At high Reynolds number product measurements show reduction of product with forcing. At moderate Reynolds numbers, on the other hand, there is an increase in product when forced. In one case a five fold increase in product was observed. The differences are related to the different effects of forcing on entrainment, composition ratio and secondary structure.

A dramatic, order of magnitude increase in mixing was discovered for certain forced wake flows. This effect is strongly associated with an interaction between the spanwise organized wake vortices and the test-section side walls.

TABLE OF CONTENTS

LIST OF FIGURES

LIST OF SYMBOLS

Symbol	Description
C_D	cylinder drag coefficient
$c_p(t)$	product concentration
$\overline{c_p}$	mean product concentration
C_{1_0}	high-speed freestream reference concentration
C_{2_0}	low-speed freestream reference concentration
d	cylinder diameter
D	mass diffusion coefficient
F	forcing frequency
F_0	initial most unstable frequency
LDV	laser doppler velocimeter
L.I.F.	laser induced fluorescence
P	time average product thickness
PDF	probability density function
Re	large structure Reynolds number; $\dfrac{\Delta U \, \delta_\omega}{\nu}$

Re'   unit Reynolds number; $\dfrac{\Delta U}{\nu}$

Re_d cylinder Reynolds number; $\dfrac{U_\infty d}{\nu}$

Re_{θ_1} initial Reynolds number; $\dfrac{U_1 \theta_1}{\nu}$

Re_{θ_w} wake Reynolds number; $\dfrac{U_\infty \theta_w}{\nu}$

r velocity ratio; $\dfrac{U_2}{U_1}$

Sc Schmidt number; $\dfrac{\nu}{D}$

U' disturbance amplitude

U_1 high speed velocity

U_2 low speed velocity

U_c convection velocity; $\dfrac{U_1 + U_2}{2}$

U_∞ free stream speed for wake flow

x streamwise coordinate

y transverse coordinate

z spanwise coordinate

ΔU velocity difference, $U_1 - U_2$

δ vorticity thickness

δ' root mean square product thickness

δ_{p_2} mean product thickness

δ_v visual thickness

δ_{vis} visual thickness

δ_ω vorticity thickness, equivalent to δ

ε growth rate parameter; $\dfrac{U_1 - U_2}{U_1 + U_2}$

λ forcing wavelength; $\dfrac{U_c}{F}$

λ_0 initial most unstable wavelength

ν kinematic viscosity

θ mean velocity profile integral thickness

θ_1 high speed boundary layer momentum thickness

θ_2 low speed boundary layer momentum thickness

θ_w wake flow initial momentum thickness

Appendix A Symbols

$L(z)$ product thickness as a function of z

$\bar{L}$ spanwise average product thickness

L_{max} maximum value of $L(z)$

L^* dimensionless product thickness

$P_{in}(z)$ laser sheet input power

$P_{out}(z)$ laser sheet power after absorption

V output voltage of detector circuit

V_{in} detector voltage when no product is present, $\beta \mu P_{in}$

W width of laser sheet

z^* dimensionless spanwise coordinate

α absorption coefficient

α^* dimensionless absorption coefficient

β current to voltage converter sensitivity

μ photodiode sensitivity

Appendix B Symbols

A vorticity concentration parameter in Stuart's solution; § B.3, eq B.11

a constant, $A e^{-\hat{\psi}}$, eq B.29

b constant, $e^{-\hat{\psi}}$, eq B.29

$c(t)$ see equation (B.71) in § B.5

cn	Jacobian elliptic function, § B.3
dn	Jacobian elliptic function, § B.3
$F(\varphi,k)$	incomplete elliptic integral of the first kind, eq B.64
$g(\xi)$	kernal function, $\left[(1-a\cos\xi)^2-b^2\right]^{-\frac{1}{2}}$, eq B.47
h	vortex spacing parameter, eq B.11
$INT(x)$	truncate x after decimal point, eq B.42
$K(k)$	complete elliptic integral, eq B.40
l	vortex spacing; § B.7.3, eq B.74
M	number of vortex centers traversed, eq B.57
M_0	see equation (B.59) in § B.5
N	number of complete revolutions about a vortex, eq B.42
nc	Jacobian elliptic function, § B.3
nd	Jacobian elliptic function, § B.3
ns	Jacobian elliptic function, § B.3
p	pressure
r	constant, $\dfrac{\sqrt{\alpha^2-\gamma^2}}{\alpha}$, eq B.56
s	constant, $\dfrac{\alpha}{\sqrt{\alpha^2+\beta^2}}$, eq B.41
sn	Jacobian elliptic function, § B.3
T	time for one revolution about vortex center, eq B.40
t	time
t_0	origin of time, § B.2
$\hat{t}$	dimensionless time, $\dfrac{\Delta U t}{2h}$, eq B.17
$\hat{t}_0$	non-dimensional t_0, eq B.17
$\hat{t}'$	$\hat{t}$ with effect of non-zero M removed, eq B.58
t^{*}	$\displaystyle\int_{x^{*}}^{\hat{x}_0} g(\xi)d\xi$, eq B.46

u	velocity in the x direction, § B.3
v	velocity in the y direction, § B.3
w	width of cat's eye at widest point, eq B.73
$w(z)$	complex potential; § B.7.3, eq B.74
$\hat{x}$	non-dimensional x, eq B.17
$\hat{x}_0$	non-dimensional x_0, eq B.17
$\hat{x}_{00}$	reference origin for outside flow, eq B.59
$\hat{x}_a'$	$\hat{x}$ in above flow with M effect removed, eq B.58
$\hat{x}_b'$	$\hat{x}$ in below flow with M effect removed, eq B.58
$x^\bullet$	lower bound on $\hat{x}$ for inside flow, eq B.44
y_0	initial y location of the interface, eq B.84
$\hat{y}$	non-dimensional y, eq B.17
$\hat{y}_0$	non-dimensional y_0, eq B.17
z_1	complex position of row 1, eq B.74
z_2	complex position of row 2, eq B.74
α	constant, $\sqrt{(1-a+b)/(1+a+b)}$, eq B.33
β	constant, $\sqrt{(a+b-1)/(a-b+1)}$, eq B.33
γ	constant, $\sqrt{(1-a-b)/(1+a-b)}$, eq B.56
γ	combined vortex strength, $\gamma_1+\gamma_2$, eq B.76
γ_1	strength of vortices in row 1, eq B.74
γ_2	strength of vortices in row 2, eq B.74
ζ	complex spacing, z_1-z_2 , eq B.77
ζ	new integration variable, $\tan(x/2)$, eq B.31
$\hat{\zeta}$	$\tan(\hat{x}/2)$, eq B.33
$\hat{\zeta}_0$	$\tan(\hat{x}_0/2)$, eq B.33
η	y coordinate of a point on the interface, § B.2
η	imaginary part of ζ , § B.7.3
η_0	η at $t=t_0$, § B.2

θ_a	constant, see equation (B.65b) in § B.5
ξ	x coordinate of a point on the interface, § B.2
ξ	real part of ζ, § B.7.3
ξ_0	ξ at $t = t_0$
ρ	fluid density
σ	constant, $(1 + a + b)(1 + a - b)$, § B.4
τ	$\int_0^{2\pi} g(\xi)d\xi$, eq B.54
τ_0	dimensionless time to travel from $\hat{x}_{00}$ to $\hat{x}_0$, eq B.63
φ_a	constant, see equation (B.65a) in § B.5
φ_a'	constant, see equation (B.69) in § B.5
ψ	streamfunction, § B.3
$\hat{\psi}$	dimensionless streamfunction, § B.3, eq B.24
ω	z component of vorticity, § B.2

Chapter 1

Introduction

1.1. Historical Background

The experiments reported in this thesis are the latest in a series of investigations of the mixing layer which began with the discovery by Brown and Roshko (1971, 1974) that organized vortical structures play a prominent role in those shear flows, even when they are turbulent at high Reynolds numbers. Another important step occurred when Oster and Wygnanski (1982) found that those large structures could be controlled by introducing relatively small periodic perturbations into the flow and that the development of the shear layer could thereby be drastically altered. In the meantime, Konrad (1976) and Breidenthal (1978), (1981) had been investigating the relation of those structures to mixing at the smallest scales, i.e., molecular mixing. It had become evident that the primary structures play a prominent role in bringing fluids from the two sides into the mixing layer, the so-called "entrainment" process, but it was not clear how the ultimate, "chemical" mixing is accomplished and how it depends on Reynolds number. Their principal finding was that, in flows which develop from laminar boundary layers, the initial Kelvin-Helmholtz instability and the large, primary vortices which result from it are followed, at some distance downstream, by a "mixing transition" where the amount of mixed (or chemically reacted) fluid in the shear layer dramatically increases although the interactions and mechanics of the primary vortices do not appear to be greatly or qualitatively altered. The enhanced mixing was attributed to increase of interface area between fluids from the two sides, created by secondary and smaller scale motions. Konrad found that after the mixing transition the rate of production

of mixed fluid reached what seemed to be a plateau, remaining independent of increasing downstream distance, and thus of increasing local Reynolds number, within the accuracy of the measurements.

The next obvious question following from the measurements of Konrad and of Breidenthal and the experiments of Oster and Wygnanski is the following: what is the effect of periodic forcing on the chemical mixing? Is it similar to the effect on growth rate, which is connected with momentum mixing? Certainly the development of negative Reynolds stress will not have a counterpart in species unmixing! The main aim of the present experiments was to study these effects.

1.2. Recent Developments

Experimental investigations more recent than the pioneering ones discussed above are also relevant to the present work.

Some insights into the structure of the secondary, streamwise vortices, which precede and contribute to the mixing transition, was obtained by Bernal (1981) who, in particular, obtained unexpected views of the cross-sections of those vortices, using laser induced fluorescence (L.I.F.) techniques developed in this laboratory by Dimotakis, et al. (1983).

Konrad's measurements through the mixing transition were made in gas flows while Breidenthal's were in water. The post-mixing-transition plateau in water was found to be lower by a factor of two than in air (Figure 1.1). Some of this could be attributed to a systematic experimental effect (see Breidenthal, 1978) but also to the effects of Schmidt number (Broadwell and Breidenthal, 1981) which is about 0.7 for air and 600 for water. More recent measurements by Mungal (1983) in gas flow, using a chemically reacting shear layer, defined a somewhat lower post-mixing-transition plateau level than Konrad's; Koocheshahani, working in water with a technique different from Breidenthal's,

measured a lower post-mixing-transition plateau level than Breidenthal's. The ratio between the gaseous and aqueous plateau valves is approximately 2 for the Konrad-Breidenthal set (Figure 1.1) and about the same for the Mungal-Koochesfahani set, but the latter are about 20% lower than the former. Thus there is some uncertainty about the correct values for mixing product. What is not controversial and relevant for our investigations is that there is a *mixing transition*.

Returning to the aspects of the problem concerning forcing effects, an important contribution was made by Ho and Huang (1982). They forced shear layers by superimposing periodic perturbations on the free stream; Oster and Wygnanski had utilized an oscillating flap at the trailing edge of the splitter plate. Whereas Oster and Wygnanski's experiments were at high Reynolds number, and they observed post-mixing-transition flow, Ho and Huang's were mainly in pre-mixing-transition flows.

1.3. Variables and Parameters of the Problem

In the unforced layer, the mixing effects are usually expressed in terms of the growth of a thickness $\delta(x)$; this may be any measure of the thickness based on velocity profile or on visual appearance or, especially in this investigation, the reaction or mixing product thickness δ_p (Konrad and Breidenthal called it P). The rate of growth, or of production, $\dfrac{d\delta}{dx}$, is then a measure of the mixing rates. For a self-similar shear layer, growing linearly with x, these rates are constant. Of interest is how they depend on parameters of the flow and under what circumstances are they not constant in x, an important point in question being the mixing transition.

For unforced layers in incompressible, homogeneous flows, the effect of different velocities in the two streams $\dfrac{U_2}{U_1} \equiv r$ can usually be normalized by the

ratio

$$\varepsilon = \frac{U_1 - U_2}{U_1 + U_2}$$

to which the post-mixing-transition growth rates are proportional. This leaves the possible effects of viscosity, which are sometimes expressed as a local Reynolds number $\dfrac{(U_1 - U_2)x}{\nu}$ to non-dimensionalize the development distance x; alternatively, the downstream distance can be made nondimensional, $\dfrac{x}{\theta_1}$, with an initial length such as the momentum thickness θ_1, of the splitter-plate boundary layers. With this the role of Reynolds number is expressed somewhat indirectly, through its role in establishing the value of θ_1; in a particular geometry, the direct effect of Reynolds number should then, in principle, require another parameter such as $\dfrac{U_1 \theta_1}{\nu}$. Of course, if the Reynolds number is "high enough" it is often assumed that there is no direct effect of Reynolds number.

When periodic perturbation or forcing is applied to the shear layer, additional parameters are introduced into the flow: the perturbation amplitude, say U', which could be normalized by U_1 or $U_1 - U_2$; and the forcing frequency F. This latter was established by Oster and Wygnanski as a very prominent parameter for forced layers. In presenting the effects of F on growth rates $\delta(x)$, they found that the effects of F on a given shear layer could be correlated by using the normalizing length $\dfrac{U_c}{F}$ where $U_c \equiv \frac{1}{2}(U_1 + U_2)$ is taken to be the convection velocity of the large organized vortices. Thus $\dfrac{\delta F}{U_c}$ is a function of $\dfrac{x F}{U_c}$. To correlate the effects of U_2/U_1, the growth parameter $\varepsilon \equiv \dfrac{(U_1 - U_2)}{(U_1 + U_2)}$ is incorporated so that,

$$\frac{\delta F}{U_c} = fn\left[\frac{\varepsilon x U_c}{F}\right] = fn(X_{wo}) \tag{1.1}$$

where we have introduced what we call the "Wygnanski-Oster parameter" X_{wo}.

Oster and Wygnanski did not actually show such plots; that was done by Browand and Ho (1983), who incorporated the Oster-Wygnanski and the Ho-Huang results into a plot which is reproduced in Figure 1.2. The dependent thickness here is

$$\theta \equiv \int\limits_{-\infty}^{\infty} \frac{(U_1 - U)(U - U_2)}{(U_1 - U_2)^2} \, dy$$

This figure displays the dramatic effects of forcing on the growth rate and exhibits the three different response regions of the shear layer, which had already been introduced by Oster and Wygnanski. The characteristics of these regions are, briefly, as follows:

I. $X_{wo} < 1$; the growth rate is enhanced by up to a factor of 2 (reached at a saturating value of forcing amplitude)

II. $1 \le X_{wo} \le 2$; in this "frequency locked" region growth rate is inhibited, even reduced to zero; Reynolds stresses are reversed.

III. $X_{wo} > 2$; relaxation to unforced growth rate.

The significance of Region II is that the passage frequency of the vortices (which are all equally spaced in that region) is equal to the forcing frequency. The spacing or scale of the vortices entering that region has been determined by whatever amalgamation processes are needed to accomplish this in region I. The forcing wave length is large compared to the scales of region I and this has

the effect of enhancing growth in that region.

The Browand-Ho plot in Figure 1.2 gives, ideally, a single correlation curve and it is rather impressive that both pre-mixing-transition and post-mixing-transition data fall quite well onto it. Nevertheless, one should expect to see, for a wide range of conditions, some dependence on other (dimensionless) parameters. Indeed, a later plot prepared by Ho and Huerre (1984) have on it other data which do not all fall onto the "universal" curve so well.

On the basis of our experiments to be described, we have chosen as an additional parameter F_0, the frequency of the *initial* Kelvin-Helmholtz structure in the shear layer. This is *in lieu* of the initial parameter θ_1 which we discussed above in connection with unforced layers; in fact, F_0 is proportional to U_c/θ_1. Finally, the parameter characterizing direct Reynolds number effects would be Re_{θ_1}, so that equation 1.1 generalizes to

$$\frac{\delta F}{U_c} = fn\left(X_{\pi 0} ; \frac{F}{F_0}, Re_{\theta_1}\right)$$

The plot of Browand and Ho, which is influenced heavily by the high Reynolds-number results of Oster and Wygnanski, should be appropriate for the asymptotic conditions $Re_{\theta_1} \gg 1$ and $\frac{F}{F_0} \ll 1$. The latter may also be expressed as $\frac{\lambda}{\lambda_0} \gg 1$, i.e., the forcing wave length is large compared to initial scales.

In the experiments to be described we attempted to define a corresponding plot for the distribution of reaction product, $\delta_p(x)$, along the layer at the asymptotic conditions above, but were somewhat limited by the range of conditions available in the flow facility we used; in fact, a rather large range of conditions extending to low Reynolds number and values of $\frac{F}{F_0} \sim 1$ were covered.

1.4. Outline

A brief description of the flow facility and the measurement techniques is given in Chapter 2.

The major part of the experiments was devoted to mixing layers, the results for which are presented in Chapter 3, the main body of this report. Here the effects of forcing on the large vortex structure, on growth rate, and on mixing product are described, together with their relation to the mixing transition. -

Chapter 4 is a briefer description of the effects of forcing on the wake of the splitter plate, i.e., the flow to which the mixing layer degenerates when $U_2 = U_1$, which had also been investigated by Breidenthal.

A short discussion in Chapter 5 summarizes the observations, measurements and some of their ramifications.

Appendix A is a short note on some aspects of the laser technique for measuring product thickness. Appendix B was motivated by the visual pictures which were obtained. It is a model computation of a mixing layer utilizing point vortices to represent the spanwise organized, large structures. The main purpose was to compute the patterns produced by the interface between the two sides of the layer as it is rolled up and distorted by the action of the vortices, for comparison with those obtained in the laboratory.

Chapter 2

Experimental Facilities and Instrumentation

2.1. Breidenthal's Mixing-Layer Apparatus

The flow facility constructed by Breidenthal (1978) was used for all the experiments. Some minor improvements were made in the honeycomb and screen configuration in an effort to reduce the freestream turbulence level. Breidenthal reported a turbulence intensity of 0.5% and our measurements confirmed this. Prof. Hassan M. Nagib, with his considerable experience in such matters, suggested some changes that reduced the turbulence intensity to 0.3% for the high Reynolds number flows we studied.

The screens were replaced with ones made from smaller diameter wire spaced on a coarser mesh yielding a 65% open area ratio thereby reducing the anomalous effects common to screens possessing 60% or less open area ratio. The six-inch-long honeycomb section was replaced with a pair of two-inch honeycombs spaced two inches apart. Each honeycomb had a chopper screen on the downstream end. The reader is refered to Loehrke and Nagib (1976) for the reasoning behind these changes.

A reference scale for the photographs throughout this work is provided by the test section dimensions; 7 cm high × 11 cm span × 45 cm length.

2.2. The Forcing Mechanism

A considerable part of the effort in the preliminary phase of the work was aimed at producing a controllable periodic disturbance. Wygnanski and Oster (1980) forced the flow with an oscillating flap that was hinged to the trailing edge of the splitter plate while Ho and Huang (1982) used rotating valves in the

supply lines to each stream to provide periodic disturbances to the free streams. For the present experiments, it was important that the forcing mechanism should not limit optical access or add complexity to test section maintenance. For this reason a flapping splitter plate tip was not considered viable. Instead, a periodic pressure drop device seemed a better choice. The forcing mechanism provided a periodic loss in head which produced a periodic component in the mass flow through the test section.

The periodic pressure drop was produced by a variable area orifice plate. The drop in pressure across an orifice plate depends on the ratio of area of the orifice to area of the pipe in which it is placed; the smaller the ratio the greater the pressure drop. The forcing mechanism emulated an orifice plate whose area ratio was a periodic function of time. This was accomplished by a fixed stator which was a thin plate with an off-center circular hole and a rotor which was a disc with a pie-shaped wedge cut out of it. As the rotor turned at constant speed, the flow saw an open area that was a periodic function of time. Figure 2.1 shows the rotor and stator viewed from the downstream side looking upstream. Figure 2.1a shows the largest open area and Figure 2.1b demonstrates the smallest area for the particular rotor and stator shown in the photographs. The rotor was powered by a DC electric motor and the speed of rotation was monitored with an optical pick-up.

Figure 2.2 shows the complete forcing mechanism with drive motor and optical pick-up as it appears before installation. The device was inserted from above into the drain pipe leading to the high speed settling chamber and supported with angle iron braces as shown in Figures 2.3 and 2.4. The motor was powered by a DC power supply and the pulse train from the optical pick-up was monitored with a counter from which frequency was inferred. The frequency was very easy to change as it was only necessary to literally turn a knob on the

power supply to change rotation speed and therefore frequency. The amplitude and shape of the waveform were changed by either changing stators (different circular cut-outs with different off-center dimensions) or rotors (different size pie-shaped cut-outs). Trial and error produced a reasonable disturbance with at least 90% of the total energy, as measured with a spectrum analyzer, in the primary purely sinusoidal component and amplitudes less than 2% of the freestream high speed velocity. The forcing was always applied to the high speed stream only.

2.3. Laser Doppler Velocimeter

A Laser Doppler Velocimeter (LDV) and phase-locked-loop processor was constructed, complete with three-dimensional traverse and processing electronics to allow accurate, non-intrusive, velocity measurements. The LDV and phase-locked loop were copies of successful designs perfected by Prof. Paul Dimotakis and his students in this laboratory.

A photograph of the LDV, traverse, and test section is included in Figure 2.5.

The short-duration, blow-down nature of the facility did not allow detailed mean velocity measurements on the high-speed flows. Measurements of this type were made only on the very low speed laminar shear layer. The LDV was used mainly for setting the speeds prior to a run and for measurement of the amplitude of the forcing disturbance.

2.4. Measurements of Structure and Growth Rates from Photographs

Flow visualization was used extensively in these experiments. As found by past investigators, it is an attractive technique, providing a relatively simple, almost unique method for seeing and recording detailed spatial structure in the flow. We used passive dye marking as well as reaction-product marking techniques to obtain either short exposure photographs to "freeze" instantaneous

spatial structure or long time exposures to give measures of mean growth rates. Two different visualization techniques were employed. The first was the phenol-phthalein method of Breidenthal (1978) and the second was the laser induced fluorescence method of Dimotakis, Miake-Lye and Papantoniou (1982). Both allow one to visualize the product of a chemical reaction (i.e., mixed fluid) or to visualize concentration of a particular reactant (i.e., as a passive contaminant).

Simple photographic methods were employed to record the photographs. Three different 35mm cameras were used; a Nikon Model F, a Pentax ME Super, and a Konica FS-1. All were essentially equivalent as regards performance. Ektachrome 160 and Kodachrome 40 color slide films were used to photograph the phenolphthalein experiments. The laser induced fluorescence experiments required "faster" film so Tri-X black-and-white film gave better results than color slide film. Time exposures with high contrast were difficult to obtain with the available lighting. A very dark green filter (Kodak Number 54) and Panatomic-X black-and-white film were used when taking time exposures of the red reacted phenolphthalein. The filter passed green and blue-green light while stopping red light almost entirely. Acceptable time exposures of as long as ten seconds were obtained by this method.

Because snap shots require only a fraction of a second, flows where measurements could be made only tediously or not at all could at least be photographed. The many photographs obtained during the course of this research were carefully cataloged for future reference. The phenomena documented ranged from truly laminar flows to turbulent post-mixing transition shear layers. Wake flows ($U_1 = U_2$) were also studied for a wide range of Reynolds numbers by photographic means.

Some quantitative information was obtained from time exposures. The edge of the mixed region in a time exposure was selected and digitized with a Hewlett-

Packard 9874A digitizer at several points along the top and bottom of the side view wedge of reacted fluid. The resulting data were curve fitted to an eight parameter function using a least squares method to produce a continuous curve on top and bottom that represented the long time average edges of the mixed region. The perpendicular distance between edges was measured and found to be nearly equal to the visual thickness, δ_{vis}.

2.5. Measurements of Reaction Product by Light Absorption

The absorption technique of Breidenthal (1978) was used to obtain quantitative information about the mixing. For this technique and the laser induced fluorescence technique to be described later, the product of a chemical reaction was measured. A pH sensitive dye was placed in one stream and mixed with an acid such that the dye was in the "off" state, i.e., was transparent. A base was added to the other stream. Hence, the pure fluids are transparent but when mixed at a molecular level, the base causes the pH indicator to turn "on" thus marking the product of the reaction.

For the absorption technique, the pH indicator was phenolphthalein which is transparent in the "off" state and red in the "on" state. Breidenthal used a mercury-argon discharge lamp as a light source and passed a beam through the test section perpendicular to the plane of the layer, thus measuring the integrated concentration of product along the line of sight of the beam as a function of time. The technique was modified for the present work in the following way: an argon-ion laser was used as a source and the beam was spread into a sheet so that a spanwise average was measured.

The exponential relationship between incident and transmitted light was the basis for calculating the product thickness. For a sheet, it was necessary to approximate the exponential function if the measurement was to be interpreted as spanwise average product. The details of how this was done and other

relevant information on the absorption method are discussed in Appendix A.

During the absorption runs, four channels of data were recorded; the output of the photodiode, the input laser power, the free stream velocity, and a reference pulse train, were all digitized at a 500 hertz rate and multiplexed. Thirty seconds of data were taken at sixteen downstream locations for eight different flows. The data acquisition computer was designed and built by D. Nosenchuck. The reader is referred to his thesis, Nosenchuck (1982), for details.

2.6. Measurements of Structure and Reaction Product by L.I.F.

Koochesfahani, Dimotakis and Broadwell (1983) have shown that fluorescence intensity can be used to observe product concentration in a turbulent shear layer. This technique uses a pH sensitive dye, fluorescein, which fluoresces efficiently in the presence of green laser light (the 5145 angstrom line of a Lexel Model 95 Argon-ion laser was used). The intensity of fluorescence is linearly proportional to concentration of dye in the measuring volume. The laser beam was passed through the shear layer perpendicular to its plane and imaged with a camera lens onto a self-scanning linear photodiode array called a "Reticon Array". The end result is that it was possible to measure product concentration as a function of time at 1024 points simultaneously in an entirely non-intrusive way. These points were equally spaced along the height of the test section.

The present experiments using this technique were conducted in collaboration with M. Koochesfahani who developed the hardware and data-aquisition software for this application. The reader is referred to his thesis, Koochesfahani (1984), for detailed discussion of the limitations of this technique.

One limitation worth mentioning is the resolution problem. Each photodiode in the array provided a measurement which was an average in two ways. First, it was an average over space. The optics collected light from a small volume of

fluid and focused it onto the detector which simply added up the total. For this experiment a length scale for the volume was about 0.1 millimeters. Second, it was an average in time. The current from the diode charged a capacitor which, in a sense, was a bucket that collected and added up the current flow for a short period of time and then dumped it out when the measurement was made. The time scale was the period of the sampling rate which in this case was 2 milliseconds. The smallest length scale in the flow, it turns out, was always smaller than the measuring volume for conditions in this experiment. For pre-mixing-transition flows the, smallest scale was the interface thickness (i.e., molecular diffusion length) which is small for a liquid (estimated to be $0.3\mu m$ in these flows). For post-mixing-transition flows the length associated with the fine scale turbulence, namely the Kolmogorov scale, is small and the interfacial diffusion scale in even smaller. Both were estimated to be smaller than the measuring volume for the Reynolds numbers studied in this work. This resolution difficulty must be kept in mind when interpreting the fluorescence data.

All of the laser induced fluorescence data were taken at a location 25 centimeters downstream of the splitter plate tip. This represented about 2/3 of the test section length. A total of 39 runs were made. Approximately 20 seconds of data were taken for each run, meaning that 10,000 data points were recorded for each diode (pixel) on the array. Only every fourth pixel was sampled, so output from 256 pixels was recorded, implying that over two million data points were recorded for each 20 second run. The data were stored, temporarily, on hard disc and later transfered to mag tape for permanent storage. Processing was conducted on our computer, a PDP 11/44 based system.

2.7. Measures of Shear Layer Thickness

Throughout this work, reference is made to many different measures of thickness. All of them have been introduced by previous investigators and we have used the conventional symbol for each whenever possible. The following is a list of the thicknesses along with a description of each.

Symbol	Description

δ, δ_ω *Vorticity thickness* of the mean velocity profile. It is computed from $\bar{u}(y)$ as follows:

$$\delta = \frac{U_1 - U_2}{\left[\dfrac{d\bar{u}}{dy}\right]_{max}} \qquad (2.1)$$

Within the assumption of the boundary layer approximation, δ is thus physically the same as the maximum slope thickness.

θ *Integral thickness* of the mean-velocity profile. It is computed from $\bar{u}(y)$ as follows:

$$\theta = \int_{-\infty}^{\infty} \left[\frac{\bar{u}(y) - U_2}{U_1 - U_2}\right]\left[\frac{U_1 - \bar{u}(y)}{U_1 - U_2}\right] dy \qquad (2.2)$$

θ is often incorrectly refered to as the momentum thickness because it appears to be a generalization of the formula for momentum thickness of a boundary layer appropriate for a shear layer. For $U_2 = 0$ it is true that θ is momentum thickness. However, for $U_2 \neq 0$ it can be shown that θ is unrelated to momentum.

θ_1 *Momentum thickness of the high speed boundary layer.* This is the

conventional thickness used to represent initial conditions. It can be computed from the measured boundary layer mean-velocity profile in the usual way. In the case of a laminar boundary layer, Thwaite's method can be applied to get an estimate of θ_1. Breidenthal computed θ_1 by this method. Throughout the present study, θ_1 was computed using

$$\theta_1 = \left[\frac{\nu x_{eff}}{U_1} \right]^{\frac{1}{2}} \qquad (2.3)$$

where x_{eff} is an effective development length equal to 5 centimeters for our facility.

δ_1 *1% thickness*. The 1% here refers to 1% of the maximum mean product concentration. δ_1 is the distance from the 1% level on the low speed side to the 1% level on the high speed side. Mungal (1983) and Koochesfahani (1984) have found it is very nearly equal to the visual thickness.

δ_{vis} *Visual thickness*. Brown and Roshko (1974) introduced this thickness as a means of extracting quantitative information from photographs. It is the thickness obtained by drawing straight lines tangent to the top and bottom edges of the structures in a short exposure photograph. In the present work, the edge in a long time exposure, taken with the method described earlier, was nearly equal to the visual thickness and is thus refered to as δ_{vis} .

δ_{p_1}, P_1 *Product thickness* referenced to free stream conditions on the high speed side. Mungal (1983) and Koochesfahani (1984) present

their product measurements in terms of this thickness and δ_{p_2}.
Mungal used the symbols P_1 and P_2 for δ_{p_1} and δ_{p_2} respectively.
For δ_{p_1} the reference concentration is the *high speed* free stream
value. It is the width of a top-hat profile whose height is the free-
stream concentration, C_{1o}, and whose area is the same as the
mean product concentration profile.

$$\delta_{p_1} = \frac{1}{C_{1o}} \int_{-\infty}^{\infty} \overline{c_p}(y)\, dy \qquad (2.4)$$

δ_{p_2}, P_2, P *Product thickness* referenced to free stream conditions on the low
speed side. This is the same as δ_{p_1} except the reference conditions
are on the *low speed* side.

$$\delta_{p_2} = \frac{1}{C_{2o}} \int_{-\infty}^{\infty} \overline{c_p}(y)\, dy \qquad (2.5)$$

δ_{p_2} is the same as P in Breidenthal's work and P_2 in Mungal's work.
In the present work, the marker fluid in all the shear layer experi-
ments was carried by the low speed fluid so when we speak of pro-
duct thickness we mean δ_{p_2}.

Chapter 3

Effects of Forcing on Shear Layer Structure and Mixing

In this chapter several experiments on the mixing layer are presented and discussed. Emphasis is on the effects of forcing. Changes in the large scale structure and in streamwise development are discussed for a large range of Reynolds numbers. The effects of forcing on the mixing characteristics of shear layers are discussed in detail.

Before discussing the effects of forcing, the basic structure and mixing phenomena in the unforced shear layers studied in this investigation are described. This provides a necessary reference for the discussion of the results obtained with forcing.

3.1. Reynolds Number Dependence of the Unforced Layer

A wide range of flow speeds was studied during the course of this work. For a fixed velocity ratio, the initial Reynolds number of the high speed boundary layer characterizes changes in flow conditions for changing speeds. This Reynolds number is defined as follows:

$$\text{Re}_{\theta_1} = \frac{U_1 \theta_1}{\nu} \tag{3.1}$$

where U_1 is the high speed velocity and θ_1 is the momentum thickness of the high speed boundary layer. This Reynolds number is obviously connected with initial conditions. Also useful is the unit Reynolds number defined as follows:

$$\text{Re}' = \frac{\Delta U}{\nu} \tag{3.2}$$

Re' has dimensions of inverse length and when multiplied by the vorticity thickness becomes the large-structure Reynolds number. The range of unit Reynolds number, Re', was from approximately $100\,cm^{-1}$ to $4340\,cm^{-1}$. Correspondingly, the range of initial Reynolds number which could be achieved varied over a range from 30 to 190. Photographs of shear layers at three different Reynolds numbers within this range are shown in Figure 3.1 (the y dimension of the test section in these photographs is 7 cm). They provide examples of the three flow regimes through which a shear layer developes with downstream distance, starting from an initially laminar state: (i) steady laminar flow; (ii) pre-mixing transition flow; and (iii) post-mixing transition flow.

In Figure 3.1a, the unit Reynolds number is low enough for the laminar part of the layer to extend over the whole field of view. The mixing occurs on a thin interface separating high speed and low speed fluid. The mean velocity profile for the flow in Figure 3.1a, measured with the LDV at a location $20\,cm$ downstream, is shown in Figure 3.2. At this location the maximum slope thickness of the profile is $8.6\,mm$ and the edge-to-edge thickness is approximately $12\,mm$, while the diffusion interface thickness in Figure 3.1a is less than $1\,mm$.

Of course, the diffusion layer will be much thinner than the vorticity layer because the former begins at the trailing edge of the splitter plate while the latter has developed from the boundary layers leaving the plate (estimated to have an edge-to-edge thickness of $4\,mm$). If the observed thickness of $12\,mm$ at $x = 20\,cm$ were to correspond to a shear layer beginning with zero thickness at the same origin as the diffusion layer, then the available similarity solution implies a diffusion layer thickness approximately equal to $\dfrac{12\,mm}{Sc^{\frac{1}{2}}}$, where

$Sc = \dfrac{\nu}{D}$ is the Schmidt number; for water, the diffusion layer thickness would be approximately $0.5\,mm$.

With increasing unit Reynolds number, instability appears at some point downstream. In Figure 3.1b that point is at the far left of the picture (a similar example may be seen in Figure 3.6a). Figure 3.1b displays another feature, the mixing transition, at about the midpoint of the picture. Thus this picture displays all three flow regimes defined above.

In Figure 3.1c the mixing transition (not well defined in this picture) is complete by about $x = 9\,cm$ (as estimated from results discussed in Section 3.3), while the transition from the steady regime, if any, has been squeezed into a small region near the splitter plate.

The above examples show that the unforced shear layer goes through two transitions. The first is the transition from steady, laminar flow to a two-dimensional flow with growing instabilities which eventually form vortices (as in Figure 3.6a). Above the Reynolds number where vortices form, no further change in primary structure takes place. The first transition is, therefore, a transition in structure. The second transition is a transition in mixing. The exact details of how this transition takes place are not well understood but it is associated with development of three-dimensional structure. It is known that an order of magnitude increase in mixing occurs in the high Schmidt number case, e.g., Breidenthal (1978).

The fact that the two transitions occur at different values of the Reynolds number means that three flow regimes exist. The first is the *laminar shear layer*. This occurs when the Reynolds number is smaller than both transition values. For the laminar shear layer, simple diffusion of vorticity and mass in the shear layer are the dominant phenomena. In the second regime the flow is a turbulent shear layer with Reynolds number smaller than that required for the mixing transition, i.e., the Reynolds number is larger than the structure-transition Reynolds number but is smaller than the mixing-transition Reynolds

number.

We shall refer to this as the *"pre-mixing-transition turbulent"* regime. Growth rate and momentum mixing by Reynolds stress are all well developed. Mixing is limited by diffusion over an interface in this case. The final case is the one where both transition Reynolds numbers are exceeded. This is the *"post-mixing-transition turbulent"* regime. Entrainment by inviscid, large-scale structures is the limiting process which determines mixing in this case.

3.2. Forced Shear Layer Structure — Visual Results

In this section, results obtained from photographs of reacting, forced shear layers are presented. Photographs provide a way to discern changes in large-scale structure, and, to a limited degree, changes in mixing that take place due to forcing.

Prior to discussion of the photographs, some terminology is needed to simplify the discussion. When the Reynolds number is larger than that required for the transition in structure, discussed above, we refer to the flow as "turbulent". When the Reynolds number is smaller than the structure transition value the flow is "laminar". To identify regions of the flow with respect to the mixing transition, we will use the terms "pre-" and "post-mixing-transition". Figure 3.1a is thus a laminar shear layer. Figure 3.1b is primarily a turbulent, pre-mixing-transition shear layer though the downstream half of the picture is post-mixing transitional. Figure 3.1c is a turbulent, post-mixing-transition shear layer.

Each shear layer, which is initially laminar when it leaves the splitter plate has an initial instability and roll-up frequency which will be called the "natural frequency". It is the passage frequency of the first, and smallest, organized structures in the mixing layer. Freymuth (1966) and Ho and Huang (1982) found that this frequency is predicted well by simple parallel-flow, linear

stability theory applied to the initial mean velocity profile; c.f., Michalke (1964) for the classical treatment of a hyperbolic tangent profile. Michalke's temporal theory implies that the most unstable wavelength, λ_0, is 28.5 times the momentum thickness, θ_1.

$$\lambda_0 = 28.5 \, \theta_1 \qquad (3.3)$$

The natural frequency, F_0, is equal to the convection velocity divided by the most unstable wavelength,

$$F_0 = \frac{U_c}{\lambda_0} \qquad (3.4)$$

Throughout the present work, the natural frequency was estimated using these relationships together with an estimate of θ_1 from Eq. (2.3) and $U_c = \dfrac{U_1 + U_2}{2}$.

For the later discussion of the effects of forcing, it is useful to recall some characteristics of the spectra of passage frequencies of the large vortical structures (Winant and Browand, 1974) or, equivalently, the probability distributions of their spacings (Brown and Roshko, 1974). Near the splitter plate, in the early stages of a shear layer developing from laminar boundary layers, the (nearly) fixed, natural frequency defines a spectral peak (or delta function in the wavelength or vortex-spacing distributions) (Ho and Huang, 1982). Eventually far downstream, in the "well developed" turbulent shear layer, a broad spectrum develops. Its maximum corresponds to the most probable passage frequency (or vortex spacing); it is close to the mean value (Brown and Roshko, 1974). Consistent with a linear growth rate for the shear layer, the local passage frequency decreases downstream as $\dfrac{1}{x}$.

The forced shear layer of Wygnanski and Oster, described in the Introduction, was in the latter, late stages of development (post-mixing-transition) while the

forcing experiments of Ho and Huang were mainly on a shear layer in its early stages of development, i.e., pre-mixing-transition.

The work of Ho and Huang (1982) focused mainly on $\frac{F}{F_0} \sim 1$ while Oster and Wygnanski (1982) studied $\frac{F}{F_0} \ll 1$. The present research covered the entire range and the observed effects of forcing on structure agree well with the findings of the above investigations. Much of what follows, therefore, may be found in the above works. The aim in this discussion is to unify the results, to present the necessary background for those unfamiliar with the previous research and, most important, to provide a reference for the effects of forcing on the large-scale structure and growth rate of the shear layers for which product measurements were made.

First consider the case when the forcing frequency equals the natural frequency, i.e., $\frac{F}{F_0} = 1$. In this case, vortices are shed from the splitter plate at the natural frequency and move downstream in an orderly fashion, without amalgamation, for an unnaturally long distance. Eventually, the growth of subharmonics of the input frequency causes pairings, triplings, etc., like those observed in the unforced layer. Figure 3.3 shows an example of a forced, pre-mixing-transition shear layer. Laser induced fluorescence was used to label pure fluid from the low speed side for this photograph. The forcing wavelength corresponds, in Figure 3.3, to the spacing between the initial structures on the left, i.e., the upstream side. The onset of a pairing is evident on the downstream end. Even though energy is being put into the flow at the initial roll-up frequency, the growth of subharmonics, available in the background, eventually causes a pairing.

Forcing at frequencies larger than the natural frequency, i.e., $\frac{F}{F_0} > 1$, causes no change in the behavior outlined above. Vortices form at the forcing frequency and move downstream without amalgamation until subharmonics grow sufficiently. The flow adjusts itself to the forcing in this case by a simple reduction of the flow scale to accommodate the input wavelength. There must exist an upper limit to the forcing frequency at which this is true. Linear stability theory predicts that the neutral-point frequency is roughly twice the natural frequency. High frequencies were difficult to achieve in the present experiments so this topic was not pursued.

Forcing at frequencies smaller than the natural frequency, $\frac{F}{F_0} < 1$, on the other hand, causes a variety of more interesting flow phenomena. In a sense, this is the more important case from an engineering standpoint since most shear layers of technical interest are large Reynolds number flows for which the natural frequency is very high and background, excitation spectra are more likely to contain lower frequencies; the initial roll-up frequency (F_0) can be so high in fact that forcing it may not be practical. Behavior of the structures for $\frac{F}{F_0} < 1$ is best understood by first considering forcing at integer subharmonics of the natural frequency, i.e., $\frac{F}{F_0} = \frac{1}{n}$ where n is an integer. The first subharmonic corresponds to $n = 2$, the second subharmonic to $n = 3$, etc.

If the flow is forced at exactly one-half of the natural frequency, $\frac{F}{F_0} = \frac{1}{2}$, a controlled pairing takes place. Vortices are shed from the splitter plate at the natural frequency and immediately undergo a pairing to form a larger vortex. The larger vortex moves downstream without interaction along with other vortices of the same type. In our facility, it was never obvious that these larger vortices would themselves undergo a pairing before they reached the end of the

test section. Figures 3.4a and 3.4b show the difference between forcing the natural frequency and the first subharmonic.

Amalgamations of more than two vortices can be caused by forcing at higher integer subharmonics of the natural frequency. Figure 3.4c and 3.4d show examples of controlled tripling and controlled quadrupling. The forcing frequency is one-third the natural frequency in Figure 3.4c and one-quarter the natural frequency in Figure 3.4d.

At this point, the effect of forcing on structure has been outlined for forcing at frequencies larger than or equal to the natural frequency and for forcing at integer subharmonics. Now consider what happens at intermediate frequencies. No new types of flow structure occur. Instead, rescaled versions of the flow patterns discussed above are the result.

This is best explained by example. Consider the case when the input frequency is less than the natural frequency but is greater than the first subharmonic. Recall that forcing at the natural frequency causes no amalgamations and forcing at the first subharmonic causes pairing. For forcing frequencies between the two, a rescaled version of the flow forced at the natural frequency occurs. This was first observed by Ho and Huang (1982) and is confirmed by the present research. The "response frequency" of the shear layer, a term introduced by Ho and Huang (1982), is the frequency at which vortices form at the splitter plate. When the forcing frequency is between the natural frequency and the first subharmonic, the "response frequency" equals the forcing frequency. All flows forced between the natural frequency and the first subharmonic, i.e., $\frac{1}{2} < \frac{F}{F_0} < 1$, thus have a flow structure that is a rescaled version of the flow resulting from forcing at the natural frequency. The rescaling is such that the spacing between the vortices shed from the splitter plate is equal to the

wavelength of the forcing. Hence, the scale of the flow is increased for $\frac{1}{2} < \frac{F}{F_0} < 1$.

In a similar manner, forcing between the first subharmonic and second subharmonic, $\frac{1}{3} < \frac{F}{F_0} < \frac{1}{2}$, causes a rescaled pairing flow pattern. In this case, the response frequency is twice the forcing frequency. The rescaling is such that spacing between the vortices shed from the splitter plate is equal to one-half the forcing wavelength. Similarly, forcing between the second subharmonic and third subharmonic causes a rescaled tripling flow pattern and so on.

From the foregoing discussion, one may be tempted to extend the findings to infinite subharmonics and, in so doing, develop a recipe for the flow resulting from any arbitrary frequency smaller than the natural frequency. For example, the recipe alluded to would imply that forcing at the 19th subharmonic causes a controlled amalgamation of 20 small vortices into a single large vortex. However, for large numbers of vortices, the amalgamation does not take place in a single event as it does when smaller numbers join. Depending on the availability of disturbances in the background, a series of pairing, tripling, etc., interactions may take place until a row of large vortices, in tune with the forcing frequency, is set up. This behavior is characteristic of the $\frac{F}{F_0} << 1$ regime and was the basic result of Wygnanski and Oster (1980). Ho and Huang (1982) refer to the case when large numbers of vortices come together in a single event as a "collective interaction" and state that large amplitudes are required to produce it. In this work, collective interactions were difficult to generate because the top and bottom of the test section limit the flow.

If consideration were limited to small amplitudes, which are more important from a practical standpoint, then the suggested recipe would be misleading

when the forcing frequency is very small compared to the natural frequency, $\frac{F}{F_0} \ll 1$. For this case, the results of Wygnanski and Oster (1980) show that a series of amalgamations occurs until vortices in tune with the input frequency are developed. This occurs at the downstream location where the mean local passage frequency of the large-scale structures in the unforced flow is, roughly, equal to the forcing frequency. Browand and Ho (1983) find that the growth rate upstream, in the interaction region, may be as much as twice that of the natural shear layer, depending on the amplitude of the forcing (see Figure 1.2). In this sense, one can say that the forcing causes the early amalgamations to occur at an unnaturally high rate. The upstream region of enhanced interaction is called Region I by Wygnanski and Oster (1980). The subsequent region, where the amalgamated vortices are in tune with the forcing, is referred to as Region II. The layer possesses basically no growth in Region II. Eventually, again depending on availability of disturbances in the background, the frequency-locked vortices begin to interact. Region III, as Wygnanski and Oster (1980) call it, is this downstream region where a relaxation to the unforced state takes place. Eventually, at far enough distances downstream, the original growth rate is achieved (see Browand and Ho (1983) or Figure 1.2).

To summarize, the effects of forcing on structure described above can be separated into two categories. The first case occurs when $\frac{F}{F_0}$ is near unity but not very small compared to unity. In this case, controlled amalgamations result. The second case occurs for $\frac{F}{F_0} \ll 1$. In this case, the flow can be divided into three regions, as shown in Figure 1.2. In the first region (I), the forcing causes an unnaturally high growth rate due to enhanced interactions of the vortices. In the second region (II), large scale vortices are locked to the forcing frequency. No amalgamations and virtually no growth characterize this

region. Finally, in the third region (III), the vortices from Region II begin to interact and the growth rate returns to the unforced value.

Examples of Forced Shear Layers for Various Reynolds Numbers. With the basic effects of forcing on structure having been outlined, the remainder of this section will be devoted to examples of the various flow regimes outlined above. The examples are taken from the many photographs of the flow recorded during the course of this research. The range of available forcing frequencies was limited to approximately 1 Hz to 20 Hz. Low Reynolds-number flows have low natural frequencies and high Reynolds numbers have high natural frequencies so, for the most part, low Reynolds-number flows fall into the $\frac{F}{F_0} \sim 1$ category while high Reynolds-number flows have $\frac{F}{F_0} << 1$. The examples will begin with the smallest Reynolds number studied and end with the largest value.

The first example is the steady laminar shear layer of Figure 3.1a. Figure 3.5 shows photographs of the same flow when forced at $F = 0.5\,Hz$. Although the shear layer in Figure 3.1a is not visibly oscillating, possibly because oscillations have not yet sufficiently amplified, an estimate of the initially most unstable or "natural" frequency can be made from equations 2.3, 3.3 and 3.4. Although the Reynolds number is low ($\frac{\Delta U \delta_\omega}{\nu} \approx 60$) the result from inviscid stability theory is good enough for our purposes. This gives $F_0 = 0.35\,Hz$, thus $\frac{F}{F_0} = 1.4$. Alternatively, using conditions further downstream, at $x = 20\,cm$, $\frac{F}{F_0} = 2.0$. Figure 3.5a shows simultaneous plan and side views of the flow while Figure 3.5b shows the view from above the plane of the layer looking upstream. The photographs show that forcing produces a wave-like distortion of the diffusion interface. The wave shape is approximately two-dimensional in the central part of the test section with wave crests, i.e., the dark sections in the plan view, parallel to the splitter

plate. Near the side walls, the crests split into symmetric sets of upstream and downstream tilted crests. The side wall interaction is due to the relatively thick side-wall boundary layers present in this low speed flow. A simple estimate of the side-wall boundary layer thickness is consistent with measurements taken from the photograph.

Figure 3.5 demonstrates that forcing alters the flow and might even enhance mixing. The fact that the crests are dark in the photograph indicates that possibly more product is present there. Whether or not forcing increases the mean product is speculative since product measurements were not made in this flow.

The next example is the previously cited Figure 3.3. The flow speeds for this case are roughly four times those for the laminar flow discussed above. The forcing frequency is greater than the first sub-harmonic so vortices form from the splitter plate at the forcing frequency and move downstream in an orderly fashion. The visualization technique is a non-reacting one in which pure high speed fluid is black and pure low speed fluid is white. The nearly vertical black lines in the white area are shadows caused by bubbles on the upper surface of the test section. Figure 3.3 shows quite clearly that the cores of the structures contain pure high speed fluid. Appendix B presents a model of this flow which reproduces many of the features of the photograph. The model is an extension of a model proposed by Jimenez (1980) in which the vorticity is modeled with point vortices and the interface is passive, i.e., contains no vorticity. Jimenez considered the case when the interface intersected the centers of the vortices and found that the resulting roll-up was symmetric. The model presented in Appendix B considers an off-center interface. The roll-up is non-symmetric for this case and the interface shapes are remarkably similar to Figure 3.3. Appendix B provides a complete presentation of the solution and more, in depth discussion of the results.

The next example is a turbulent, pre-mixing-transition shear layer. Figure 3.6 shows photographs of a reacting shear layer for several different forcing frequencies. The high speed velocity is $11.6\,cm/sec$ and the low speed velocity is $5.9\,cm/sec$ for all entries in Figure 3.6. From these, estimates of the other relevant parameters give $r = 0.51$, $U_c = 8.75\,cm/sec$, $\theta_1 = 0.66\,mm$, $F_0 = 4.7\,Hz$, $\dfrac{U_1\theta_1}{\nu} = 76$, and $\dfrac{\Delta U}{\nu} = 570\,cm^{-1}$. Each photograph contains simultaneous plan and side views of the flow. Only two-thirds of the plan view, including one wall, is shown. An inert dye was added to the lower free-stream so that pure high speed fluid appears grey in the photographs. Reacted fluid appears black in both side and plan views.

The changes in primary structure caused by forcing are evident in the photographs and are consistent with the description given earlier for the $\dfrac{F}{F_0} \sim 1$. Figures 3.6a, 3.6b, and 3.6d are all rescaled-natural-frequency type flows, i.e., vorticies form at the splitter plate at the same frequency as the forcing frequency. This is consistent with the earlier statement that the response frequency equals the forcing frequency for $\dfrac{1}{2} < \dfrac{F}{F_0} < 1$. Figure 3.6b shows that the frequency-locked vortices eventually begin to interact; a change in scale, caused by pairing of previously frequency-locked vortices, is evident in the middle of the side view. Figures 3.6e, 3.6f, and 3.6g are examples of controlled amalgamations. It is clear in these cases that the vortices which participate in the amalgamation are not of equal size. Figure 3.6f, for example, shows pairing of large vortices with smaller upstream vortices. In Figure 3.6g, the smaller vortex is more clearly visible while in Figure 3.6e, the smaller vortex is a mere kink in the braid connecting the larger vortices.

The development of three-dimensional instabilities is quite interesting in the series of pictures in Figure 3.6. The unforced case, Figure 3.6a, has three-

dimensional structure but it is hard to say whether this is caused by interaction with the thick side-wall boundary layers or if it represents the onset of the instability that leads to the streamwise vortices. The forced flows show a variety of interesting three-dimensional structure. In Figure 3.6b, the primary structures at the upstream end are seen to have a certain waviness even at the start. Notice also in this figure how the change in scale in the middle of the picture is accompanied by development of streamwise structures. Figures 3.6c and 3.6d show an interesting side wall effect which occured frequently for the low Reynolds number forced flows encountered during this research. The interaction of the primary vortices with the side-wall boundary layer produces three-dimensional motion which separates the flow into a wall region and a central region. In the central region, the primary structure is spanwise coherent while in the wall region, the vorticity gets tipped by the velocity defect of the boundary layer. The boundary between the two regions consists of a complicated three-dimensional motion which apparently mixes the two reactants efficiently. Another example of this type of flow, taken at similar conditions, is shown in Figure 3.7. Continuing with the plan views of Figure 3.6, it is seen that the side-wall influence is not as strong in 3.6e, 3.6f, and 3.6g. It appears, in 3.6g, that the forced pairing causes the development of streamwise vortices at the downstream end of the plan view. This may indicate that pairing of the primary structures triggers the development of the secondary structures.

In the previous example, the mixing transition is not an issue, i.e., the Reynolds number was small enough that the mixing transition did not occur in the test section. The next example, shown in Figure 3.8, is at a large enough Reynolds number for the mixing transition to occur near the downstream end of the test section. The speeds for this flow are $U_1 = 17.4\,cm/sec$ and $U_2 = 8.3\,cm/sec$ and implied by them are the following: $r = 0.48$, $\theta_1 = 0.54\,mm$, $F_0 = 8.3\,Hz$, $\dfrac{U_1\theta_1}{\nu} = 94$, and $\dfrac{\Delta U}{\nu} = 905\,cm^{-1}$. Black areas in the photographs

indicate regions where mixing occurs. However, the wedge-shaped dark area at the downstream end of the plan views is a shadow from an optical source. Quantitative measurements, presented later, do not extend that far downstream. Unlike the previous example, the optics were arranged to give the full wall-to-wall plan view of the test section. Changes in the primary structure for this case are very similar to those discussed earlier for Figure 3.6. Figures 3.8a, 3.8b, and 3.8c are rescaled natural frequency flows. Figures 3.8d and 3.8e show controlled pairing, Figures 3.8f and 3.8g show controlled tripling, and so on for the remaining entries in Figure 3.8. A rough feeling for the way forcing affects growth rate of the layer can be obtained from these photographs. The unforced layer demonstrates the expected linear growth rate while the forced layers each contain a region where there is virtually no growth. In each case, this region corresponds to the location where the passage frequency of the primary vortices equals the forcing frequency. As the frequency decreases for succesive photographs in Figure 3.8, the frequency-locked region moves further downstream.

As mentioned above, the mixing transition begins to occur in the unforced case at the downstream end of the photograph, Figure 3.8a. A picture alone is not enough to make such an assessment but product measurements, to be presented shortly, verify that this is the case. The clear presence of the secondary, streamwise vortices is a clue, however, that the mixing transition is imminent. Figure 3.9 is an enlargement of the photograph in Figure 3.8a which allows the three-dimensional structure of the unforced case to be more carefully scrutinized. Crude measurements of the streamwise structure spacing were obtained from this photograph and others like it. The result is that the ratio of the streamwise to spanwise structure spacing varied from 0.3 to 1.0 which is consistent with the range of values measured by Bernal(1981). It is clear, particularly in Figure 3.8g and 3.8h, that forcing can enhance the secondary vortices. Notice how clearly defined the streamwise structures are in these

two cases. An enlargement of Figure 3.8g is shown in Figure 3.10.

A final note with regard to the plan views of Figure 3.8 concerns the reduction in the side-wall influence compared to the previous example shown in Figure 3.6. The reason for this is not entirely clear. The speeds are roughly a factor of two larger for Figure 3.8 which means the side wall boundary layers are only 30% smaller than those in Figure 3.6. But the flow near the side-walls in the plan views is drastically different in the two cases. Perhaps the more fully developed three-dimensional structure in Figure 3.8 prevents the side-wall interaction from developing as strongly.

As a final example, a high Reynold-number shear layer will be discussed. This was the largest Reynolds number at which data were acquired. Figure 3.11 shows four side view photographs of fluorescent product; one unforced and three forced. Two cylindrical lenses were used to spread the laser beam; one in the spanwise direction and one in the streamwise direction. This produces a laser beam, normal to the shear layer, with dimensions $5\,cm$ spanwise and $40\,cm$ streamwise. The spanwise width was the same width used in the absorption measurements. One observes, in each picture, an instantaneous view of the spanwise averaged product in the center $5\,cm$ of the span. The actual height of the test section in each picture is $7\,cm$ and the flow is from left to right with the high speed side on top.

Figure 3.11a shows the unforced flow. Three forced shear layers and the value of $\dfrac{F}{F_0}$ for each are shown in Figure 3.11. Figure 3.11b shows the three regions of growth discussed earlier. At the left of the picture, two small vortices are pairing; they will later form a larger vortex in the frequency-locked region. Notice the apparent lack of structure in the recovery region (right side of the picture). It is expected that large scale structures would eventually emerge.

The time scale necessary for this to take place depends on the availability of background disturbances at long wavelengths and on the growth rate of instabilities associated with those wavelengths. It is not unreasonable for this time scale to be so long that we were unable to visualize the emergence of larger scales in the length of the test section.

Conditions in the frequency locked region correspond to the neutral point on the stability curve (Ho and Huerre, 1984). Figure 3.11b provides the necessary information to check this assertion. The thickness was measured in the locked-in region of Figure 3.11b by the method described in Chapter 2. This thickness along with the known forcing frequency and convection velocity, $U_c = 0.5\,(U_1 + U_2)$, imply a measured value of dimensionless wavelength, $\dfrac{F\,\delta_{vis}}{U_c}$, approximately equal to 0.62. This value is nearly equal to the value at the neutral stability point and is consistent with the results presented by Ho and Huerre (1984) if one assumes $\dfrac{\delta_{vis}}{\theta} \approx 8$. When the forcing frequency is at the neutral point, the first subharmonic is thus very near the most unstable frequency and is almost certain to emerge and cause amalgamation of frequency locked vortices. Such events occur at the begining of Region III.

Figure 3.11c shows the locked-in region most clearly. This picture is very similar to photographs by Wygnanski and Oster (1980) taken at Reynolds numbers ten times as high. Notice the penetration of unmixed fluid all the way across the layer in the third vortex from the left. This suggests that the flow is very nearly two-dimensional at this point; remember the picture is a spanwise average. The spiral arms of the structures are much longer and wrap around more of the core than in the unforced case.

Figure 3.11d gives a good example of the collective interaction of Ho and Huang (1982) which is typical for small forcing frequency and large enough amplitude. Six vortices, visible at the left of the picture, are wrapped-up into a single large vortex by the time they reach the downstream end. It is also evident in this picture that the bottom wall exerts an influence on the flow as the vortices actually run into it at the downstream end. Product measurements were restricted to the upstream 2/3 of these pictures.

Just below each of the forced flow pictures, a line is drawn to represent the forcing wavelength, λ, for the conditions under which the picture was taken. Wygnanski and Oster's scaling argument (see Browand and Ho (1983) or Figure 1.2) is qualitatively apparent. If the pictures were enlarged so as to make the wavelengths equal, the three forced flows would appear very similar in the frequency-locked region. This supports the hypothesis that the thickness of the forced shear layer scales with the forcing wavelength. One feature which would not appear similar in such a scaling is the number of vortices which amalgamate to make up the frequency locked structure. Initial conditions must determine that number, i.e., the number depends on $\frac{F}{F_0}$.

One-second duration time exposures of the phenolphthalein reaction are shown in Figure 3.12 for flow conditions identical to those in Figure 3.11. Figure 3.12a, the unforced flow, shows a more or less linear growth as expected while Figure 3.12b shows very clearly the three regions of growth characteristic of the forced shear layer.

The edge of the mixed fluid is fairly easy to identify in these photographs. Several points along these boundaries were selected and digitized as described in Chapter 2. The points selected for each picture in Figure 3.12 are shown in Figure 3.13. The horizontal and vertical scales are x and y in centimeters. The

line connecting the points on each edge is the function resulting from the least squares fit described in Chapter 2. The y distance between the fitting functions was measured and found to be roughly the same as the visual thickness, δ_{viz}, of Brown and Roshko (1974). The thickness was measured at sixteen x locations spaced $1.5\,cm$ apart.

The thickness was scaled with forcing wavelength and plotted against Wygnanski and Oster's non-dimensional downstream distance parameter. The result is shown in Figure 3.14. The case at the highest frequency, $F = 12\,Hz$, agrees well with Figure 1.2. The $F = 8\,Hz$ case has acceptable agreement though it is not as good as the higher frequency case. The $F = 4\,Hz$ data have a smaller growth rate for small X_{wo} than Figure 1.2 would predict. If the growth rate were as large as it "should" be, the structures would exceed the vertical extent of the test section. Thus, the test section restricts the growth in the $X_{wo} < 1$ region. It is possible that initial conditions are responsible for the small growth. However, the similarity growth hypothesis for the forced shear layer suggests that the beginning of the frequency-locked region is independent of initial conditions. Both Wygnanski's and Ho's data are consistent with this observation even though Wygnanski and Oster used small values of $\dfrac{F}{F_0}$ while Ho and Huang worked with values as high as 1. A recent review paper by Ho and Huerre (1984) presents forced shear-layer data plotted in the same dimensionless coordinates. There is a considerable amount of scatter in the results. The data in Figure 3.14 fall within the range of values in Ho and Huerre's plot. Another reason for the variation in the present data could be the use of visual thickness as a measure of width. In the unforced shear layer, the various measures of thickness are all proportional. The use of visual thickness, δ_{vis}, in the present case instead of integral thickness, θ, as Ho and Huerre, assumes, without justification, that this is also true in the forced layer.

Figure 3.14 also shows that flow at the end of the frequency-locked region for $F = 12\,Hz$ corresponds to conditions at the neutral point in a linear stability analysis as pointed out previously.

3.3. Product Thickness Measurements by Absorption

In this section we present the basic measurements of reaction product made by the absorption method described in Chapter 2. The first part describes the format in which the measurements will be presented and the remainder describes the results. While much of the material in the previous section on structure was discovered by previous investigators, the contents of the present section and those that follow represent, to the best of our knowledge, the first measurements of product in forced shear layers. Prior to these, it was not clear whether there was any correlation between the effects of forcing on growth rate and the effects on product production. The basic measurement presented in this section is the streamwise distribution of product thickness $\delta_p(x) = \int_\delta c_p(y)\,dy$ and its derivative, $\dfrac{d\,\delta_p}{dx}$, which will be called "the product growth rate". These give one measure of the mixing processes. Another and possibly better measure would be the product flux $\int_\delta \overline{c_p(y)u(y)}\,dy$; its derivative in the flow direction would give the local rate of chemical production. Since simultaneous measurements were not made of $c_p(y,t)$ and $u(y,t)$, it was not possible to determine this quantity, which can be written as the sum of the two terms $\int_\delta \overline{c_p}\,\overline{u}\,dy + \int_\delta \overline{c_p{}'u'}\,dy$. If the second term is neglected and the first one is written as $u_p\delta_p$, where u_p is a suitable mean velocity, then our product growth rate, $\dfrac{d\,\delta_p}{dx}$, multiplied by u_p, would be a measure of chemical production rate, provided u_p does not vary with x. While the quantity $\dfrac{d\,\delta_p}{dx}$ is not as precise a measure of chemical production rate, we believe it is a useful indicator of local mixing rates.

Eight data sets were recorded and analyzed. The results of each set are presented in Figures 3.15 to 3.22 in a standard format so that the reader may compare one set to another or to their own data. The main result of the analysis of each data set is the mean product thickness as a function of downstream distance. This plot appears in the center on the left side in the standard format. Figure 3.15 may be referred to at this time to better understand this description. The circles in the product thickness plot are the actual measured values while the solid line represents what is judged to be a reasonable smooth fit indicative of the trend of the measurements. Above the product thickness plot, the derivative of the solid line "fit" is shown. This represents the rate of change of product thickness with downstream distance or more simply stated, the product growth rate. Below the product thickness plot, is shown a photograph of the flow for which the measurements were taken. The photograph was enlarged in such a way that the scales agree with those on the plots, e.g. $x = 25 \, cm$ in the plots is the same as $x = 25 \, cm$ in the photograph and the origin in the plot is the tip of the splitter plate in the picture. In this way, one can compare the product thickness, its growth rate, and the visual information along a single vertical line in this standard format.

Finally, in the upper right, the various values of important parameters for the flow in question are presented. At the top of the list are the three basic parameters of the flow; U_1, the velocity of the high speed side; $r = \dfrac{U_2}{U_1}$, the velocity ratio; and F, the forcing frequency. The remaining entries in the list are derived quantities. θ_1 is the initial momentum thickness of the high speed boundary layer in millimeters. This allows, for example, the value of $\dfrac{x}{\theta_1}$ to be quickly estimated for a given x location. F_0 is the most unstable frequency from linear stability theory, which can be compared to the forcing frequency. The

next two entries in the list are the initial and unit Reynolds numbers respectively. The unit Reynolds number, when multiplied by some measure of the local thickness of the layer, provides an estimate of the large-structure Reynolds number. The last entry provides an estimate of the downstream location where the frequency-locked region begins. Recall, from Figure 1.2, that the frequency-locked region ends at roughly twice this value.

Data were recorded at two different Reynolds numbers. These will be referred to in the remainder of this section as simply "high" and "low" Reynolds number cases. In the high Reynolds number case, which will be considered first, the unforced flow and two forced flows will be presented. For the low Reynolds number case, the unforced flow and four forced flows will be considered. The photographs for the high Reynolds number flows have the high speed side on the bottom and an inert dye added to the high speed side. The low Reynolds number photographs have no inert dye and the high speed side is on top in the side view.

The high Reynolds number, unforced flow, Figure 3.15, represents the foundation of the present data since it was as close to the limiting case of an entirely post-mixing-transition flow as the facility and data acquisition methods would allow. The growth rate of product thickness is small for small x and increases monotonically with increasing x. The derivative plot shows that the slope of the product curve is constant beyond $x \approx 9\,cm$ with the value of the slope equal to approximately 0.04. The measurements are consistent with the information in the photograph. Notice that the beginning of the constant slope section corresponds well with increased amounts of mixed fluid in the photograph.

The beginning of the constant slope region at about $x = 9\,cm$ in Figure 3.15 apparently represents the beginning of the post-mixing transition region for this flow. The only data available for comparison are the data of Breidenthal (1978) which were taken in the same facility using the same method. The only

difference is that Breidenthal measured product at a single spanwise location while the present measurements gave a spanwise average. Breidenthal's measurements, shown in Figure 1.1, indicate the mixing transition is complete at this velocity ratio at $x \approx 20\,cm$. Hence, a discrepancy by a factor of two or more exists between Breidenthal's and the present measurements. The spanwise averaging in the present case might account for some of the difference but it is hard to believe, looking at the photograph in Figure 3.15, that it makes a difference of a factor of two. In the present work, it is the effect of forcing on mixing that is the main interest and from this stand point it makes sense to compare forced flows with unforced flows measured in the same way. For this reason, completion of the mixing transition at $x = 9\,cm$ for this unforced flow will be used as the reference value for comparison with forced flows in what follows.

Figure 3.16 shows the result of forcing the above flow at $F = 3.9\,Hz$. The frequency-locked region begins at $x = 27.6\,cm$, which is consistent with the visual information in the photograph. The product distribution, in this case, is not very different from that in the unforced case except at large x, where a noticeable increase in mean product and production rate are observed. For small values of x in this flow, the forcing causes a simple "flopping" of the layer from side to side, which does not increase mixing. However, the "flopping" eventually leads to a strong roll-up at approximately $x = 20\,cm$ which causes twice the asymptotic product growth rate of the unforced case.

Figure 3.17 shows one of the most interesting data sets obtained during this research. The forcing frequency in this case is $8\,Hz$ which means the frequency-locked region begins at $13.4\,cm$ and ends at $26.8\,cm$. The flow goes through the mixing transition in much the same way as the unforced case with the asymptotic value of production rate achieved by $x = 7\,cm$. However, the product

thickness stops growing at the begining of the frequency-locked region. Approximately half way into the frequency-locked region, the product begins to grow again at a rate slightly larger than the asymptotic unforced rate. The frequency-locking phenomenon thus causes a temporary zero product growth rate. The structures apparently convect and rotate without doing any mixing. Comparison with the unforced flow shows that forcing creates more product upstream of $x = 15\,cm$ and less product downstream of that point.

This concludes the presentation of the high Reynolds number data. The low Reynolds number case will now be addressed. The flow speeds for these data were roughly a factor of four smaller than in the previous flows so the initial Reynolds number is half the value for the above flows and the unit Reynolds number is one-quarter the previous value.

Figure 3.18 shows the unforced low Reynolds-number data. In this case, there is much less product than that measured for the high-Reynolds number case, which is consistent with pre-mixing transition conditions. At approximately $x = 20\,cm$ the production rate begins to rise sharply, indicating the beginning of the mixing transition.

The same flow, when forced at $F = 1.8\,Hz$ is shown in Figure 3.19. There is very little mixing until the beginning of the frequency-locked region. This is an interesting case since the beginning of the frequency-locked region here coincides with the location at which the mixing transition would begin in the unforced case. The product growth rate and the product thickness increase sharply at that point for the forced flow. The product growth rate actually exceeds the post-mixing transition value measured for the high Reynolds number unforced case. This implies that the product growth rate overshoots since it is expected that the unforced asymptotic value will be approached for sufficiently large x in Figure 3.19.

Figure 3.20 shows the low Reynolds number flow for a forcing frequency of 2.6 Hz. Here, as in the previous forced case, the product and the product growth rate both increase rapidly at the begining of the frequency-locked region. Unlike the high Reynolds-number forced flows, the product growth rate is largest in the frequency-locked region for these low Reynolds-number flows.

Figure 3.21 for a forcing frequency of 4.5 Hz once again shows the same behavior as seen in the previous two examples. The product and product growth rates are both small until the begining of the frequency-locked region. In this case, however, the product begins to level off and the product growth rate reduces at about $x = 20\,cm$. This is slightly downstream of the end of the frequency-locked region which occurs at $x = 16.2\,cm$ for this case.

Figure 3.22 shows the final low Reynolds number data set. Unfortunately, a photograph for this forcing frequency of 5.9 Hz was not obtained. The trends seen in the previous forced, low Reynolds-number flows are also true for this case. The product thickness and product growth rate increase at the begining of the frequency-locked region. After this the product thickness levels-off with corresponding low growth rate. This flow is particularly interesting since the actual product thickness at $x = 12\,cm$ is almost 5 times the unforced value at the same point. With regard to the missing photograph, pictures were obtained at forcing frequencies both higher and lower than 5.9 Hz and there was nothing unusual about them. The flow picture would look like a rescaled version of the photograph in Figure 3.21.

3.4. Product Thickness Fluctuations from Absorption Measurements

In this section, the fluctuating product thickness time series will be discussed. The mean product thickness, presented in the previous section, is the long-time average of a fluctuating signal which represents the product thickness as a function of time at a fixed x location. The product thickness fluctuates, of

course, due to the passage of the large-scale structures (as well as smaller ones). The shape of the waveforms give a indication, therefore, of the distribution of product carried by the structures.

Figure 3.23 shows three product-thickness time histories at x locations of $6\,cm$, $15\,cm$, and $24\,cm$ for the high Reynolds number, unforced case previously discussed in Figure 3.15. In the absorption experiments, 32 seconds of data were recorded. The long-time mean values were computed by taking the mean for the entire run. The time series shown for each x location represent only a 2 second portion of the data recorded at that location. The vertical scale in each plot is the product thickness in centimeters. In addition to the downstream location, x, and mean product thickness, δ_{P_2}, the root mean square of product thickness fluctuations, δ', is included in each plot. The signals in Figure 3.23 show that the presence of the large-scale structures causes a large fluctuation in the product thickness. Spectral analysis of these signals showed a rather broad peak with the frequency corresponding to the maximum decreasing like $\frac{1}{x}$, as expected. This change in frequency, or period, of the fluctuations is apparent in the plots of Figure 3.23. Note also that the ratio of rms product thickness to mean product thickness is approximately equal to 0.3 in the post-mixing-transition region.

Figures 3.24 and 3.25 show the time traces corresponding to the data sets presented in Figures 3.16 and 3.17 respectively. The $3.9\,Hz$ forced case, Figure 3.24, shows little change from the unforced case which is consistent with the similarity between the mean product-thickness distributions for the two cases. Figure 3.25, on the other hand, shows a strong response to the forcing frequency of $8\,Hz$. The period of the forcing corresponds well with time between peaks in the three traces. Recall that the high Reynolds-number, $8\,Hz$ flow had a zero production rate in the first part of the frequency-locked region, (c.f. Figure

3.17). The three traces in Figure 3.25 correspond to locations upstream, in the middle, and downstream of the zero growth region. The signals change very little through this region.

Figures 3.26 through 3.30 show examples of time traces corresponding to data sets presented in Figures 3.18 through 3.22 respectively. These are the low-Reynolds-number data sets. Note the change in the vertical scale from the high-Reynolds-number plots. Figure 3.26, for the unforced case, shows trends in mean product, rms product, and passage frequency similar to those discussed for the high Reynolds number unforced case. The actual values of mean and rms product are of course smaller.

Figures 3.27 and 3.28, corresponding to forcing frequencies of $1.8\,Hz$ and $2.6\,Hz$ respectively, show that large amplitude fluctuations are caused by forcing the flow in this frequency range. Notice that the ratio of rms to mean product is almost a factor of two larger, at the $x = 24\,cm$ location, than it is for the post-mixing transition region of the high Reynolds number unforced flow, c.f. Figure 3.23. This is due to the controlled amalgamation which takes place in these flows. When the vortices merge at the beginning of the frequency-locked region, their mixing is enhanced (see Figures 3.19 and 3.20) resulting in rather large regions of mixed fluid separated by large regions of unmixed fluid, c.f. photographs of the flows in Figures 3.19 and 3.20. This causes the large excursions in the product thickness seen in Figures 3.27 and 3.28.

Figure 3.29 shows time traces for the low Reynolds-number flow with a forcing frequency of $4.6\,Hz$. The $x = 6\,cm$ trace demonstrates an interesting signature of the large scale structures. This being a pre-mixing-transition case, the product resides in a thin interface which is wrapped up in the large scale vortices. When the interface is tangent to the laser sheet used for the measurement, the instantaneous product thickness is large and thus produces a spike in the time

trace. The number of spikes for a given structure is determined by the number of times the interface has wrapped around the vortex at an given x location. Another interesting point in Figure 3.29 is the small rms value of product thickness at the 15 cm location. This is the end of the frequency-locked region for this flow and, as was demonstrated in Figure 3.21, a location where the rate of change of product is high. The last trace in Figure 3.29 shows that the rms product thickness increases in the recovery region (region III) for this flow.

Figure 3.30 shows the low Reynolds-number, 5.9 Hz forced time traces. The spikes in product thickness, mentioned above, occur for the smallest x location and the other two traces show the increase in rms product and change in scale of the structures characteristic of the recovery region.

3.5. Product Measurements by Laser Induced Fluorescence

Results of product measurement by the method of laser induced fluorescence are presented in this section. The absorption measurements, presented above, are of integrated values across the layer. The product thickness is, in fact, an average of the y distribution of product concentration. The laser induced fluorescence technique, employed in the present experiments, allows the details of this distribution in y to be measured. In this sense, the present section presents more detailed information on the flows discussed previously. Specifically, it is the variation of product concentration in the y direction that is of interest.

Measurements of laser induced fluorescence were conducted on four high-Reynolds-number and four low-Reynolds-number shear layers at the conditions described earlier. For all these measurements, fluorescence of reacted fluid was measured, i.e., it was the product of a chemical reaction that was measured. All of the measurements were made for a single downstream location at $x = 25 cm$. For the high-Reynolds-number flows, the unforced flow and forced flows with

$F = 8\,Hz$, $12\,Hz$, and $20\,Hz$ were studied. For the low-Reynolds-number flows, the unforced flow and forced flows at $F = 1.5\,Hz$, $2.5\,Hz$, and $5.0\,Hz$ were studied. Methods described in Chapter 2 were used to compute the product concentration at 256 equally spaced points across the layer. A single one of these points is referred to as a pixel. The concentration time histories were averaged for the length of the run (approximately 20 seconds of data) to obtain the mean product concentration profiles.

Product Concentration Profiles. The product concentration profiles for the high-Reynolds-number cases are shown in Figure 3.31. Only every fifth measurement is shown in this plot. y is expressed in this plot in pixels; one pixel is $0.37\,mm$ so $1\,cm \approx 25\,pixels$ in this plot. The high speed side is on the left and the low speed side is on the right.

The width at 1% of the maximum concentration, called δ_1, is nearly equal to the visual thickness, δ_{vis}, as defined by Brown and Roshko (1974). Values of δ_1, for each profile in Figure 3.31, are presented in Table 3.1 below along with corresponding values of X_{wo}.

TABLE 3.1

Frequency	$\dfrac{\varepsilon x F}{U_c}$	δ_1	δ_{p_2}	$\dfrac{\delta_{p_2}}{\delta_1}$
unforced	- -	5.2 cm	7.2 mm	0.14
8 Hz	1.9	4.2 cm	4.8 mm	0.12
12 Hz	2.8	4.1 cm	5.4 mm	0.13
20 Hz	4.6	4.4 cm	5.6 mm	0.13

Returning to the profiles in Figure 3.31, it is interesting that the product-concentration profiles appear similar in shape even though the local structure is quite different for the different forcing frequencies. The greatest effect on the profiles occurs on the low speed side (high pixel number). Recall that the forcing is applied only to the high speed stream.

The product thickness, δ_{p_2} in Table 3.1, is the area under the product concentration profile. It is apparent that forcing reduces the amount of product at $x = 25\,cm$ in this shear layer, for the frequencies measured, which is consistent with results of absorption measurements on the same flows.

The mean concentration profiles for the low-Reynolds-number runs are shown in Figure 3.32. The profiles show that a considerable change in the shape results from forcing, in contrast to the situation at high Reynolds number (Fig. 3.31) where all profiles are of roughly similar shape. The mean quantities, implied by the profiles, are collected in Table 3.2 below.

TABLE 3.2

Frequency	$\dfrac{\varepsilon x F}{U_c}$	δ_1	δ_{p_2}	$\dfrac{\delta_{p_2}}{\delta_1}$
Unforced	--	4.2 cm	2.6 mm	0.06
5.0 Hz	3.1	3.0 cm	3.5 mm	0.12
2.5 Hz	1.6	4.4 cm	3.7 mm	0.08
1.5 Hz	0.9	4.9 cm	3.7 mm	0.08

In contrast to the high-Reynolds-number results, all of the low-Reynolds-number forced shear layers had more product than the natural flow. The 5 Hz

forcing produced a 29% decrease in visual thickness but a 35% increase in product thickness. At 2.5 Hz forcing, the product is larger by 42% and the layer is thicker by 5%. Finally at 1.5 Hz forcing the layer is 17% thicker and contains 42% more product.

Time Traces. The signals, whose average values produce the mean concentration profiles, will now be examined. For the high-Reynolds-number flow, product concentration as a fuction of time, at five selected pixels on the array, is shown in Figure 3.33 for the unforced flow and in Figure 3.34 for the 8 Hz forced case. The five pixels selected are spaced 20 pixels apart in each figure, i.e., approximately 8 mm. The center trace in each figure is at the location of the maximum in the mean concentration profile, which was arbitrarily choosen to be the origin in y. The value of y/δ_{vis} for each of the other traces in both figures is indicated. These traces display information equivalent to the temperature time series obtained by Mungal (1983) in a gas flow and are precisely the same as the product time histories obtained by Koochesfahani (1984) in a liquid flow.

The boundaries of structures are identified in these plots by product concentration jumps from relatively low values (outside the structure) to a higher value (inside). It is seen, in the traces, that the product concentration within the structure is independent of y, i.e., the duration of passage of the mixed areas decreases near the edges of the layer but the concentration level within the mixed regions does not change significantly with y location. This is true for forced as well as unforced flow. Mungal (1982) and Koochesfahani (1984) drew similar conclusions from their data on unforced flows. Comparing the unforced time histories, Figure 3.33, to the 8 Hz forced case, Figure 3.34, shows that the product concentration inside the structures is lower for the forced flow indicating that the composition of mixed fluid is altered by forcing. This point will be discussed in more detail later.

In the low-Reynolds-number case, time traces of the measured product concentration on the centerline for three of the data sets presented in Table 3.2 are shown in Figure 3.35. The time series for unforced flow demonstrates that mixing occurs primarily on large-structure interfaces and that there is very little small-scale structure in this shear layer. Notice how the signal contains many spikes, each corresponding to an interface passing through the measuring station. Comparison of the unforced trace with the traces in the high-Reynolds-number layer, Figure 3.33, shows that there are more of the spikes in the low-Reynolds-number flow than in the high-Reynolds-number flow or, more accurately, that the low-Reynolds-number interfaces are more resolvable than are the high-Reynolds-number interfaces. The time trace of the $F = 5\,Hz$ data has rather large sections of time when no product is present on the centerline. At first, it was thought that these blank spots occur between structures and that the mixed regions correspond to the cores of the structures. It was found that the opposite is true, i.e., the unmixed regions correspond to the cores of the structures and the mixed regions occur in the braids. This fact will be obvious later when the "flow images" are introduced. The $F = 2.5\,Hz$ data in Figure 3.35 contain the same type of spikes as those observed in the natural case. The interfaces in this case appear thicker than those in the unforced case.

Flow Images. Perhaps the best way to display time-series data obtained in the experiments is with the so-called "flow image". This is essentially an inversion of the process that was used to take the data. The data were obtained from intensity information along a line in the flow. The process can be inverted by translating the data into intensity information along a line on a video screen. Moreover, since successive scans were recorded, the corresponding intensity lines on the video screen can be placed in proper sequence to obtain a "picture" called the "flow image". It is not an instantaneous spatial picture as one would obtain with a camera in the laboratory but rather it is a $y-t$ diagram of the

product concentration along a fixed line in the flow as the vortices in the shear layer pass by that line. The difference between the flow image and a photograph is best realized by considering the conditions under which the two might be identical. If the Taylor hypothesis is valid, namely if the vortices pass by the measuring station in a "frozen" state, then the flow image is the same as a spatial photograph. The structures are, of course, rotating and growing as well as translating so strictly speaking the Taylor hypothesis does not hold. For more discussion on the flow image the reader is referred to Koochesfahani (1984).

Once the data are translated into intensity on a video screen in the form of the flow image, a variety of image processing tricks can be performed. One very illuminating technique is pseudo-color assignment. The idea here is to assign different colors to different intensity levels such that relative concentration levels are easy to indentify. One could, for example, assign blue to the low intensity levels and identify blue areas in the resulting image as regions of low product concentration.

Flow images for the four high-Reynolds-number runs, discussed earlier, are shown in Figure 3.36. Side-view photographs of the same flows are shown in Figure 3.5. Time in these flow images increases from *right to left* and each image contains 512 consecutive scans. Thus, approximately a one second portion of the data for each run is shown. The appearance of the large-scale structure in the unforced case, Figure 3.36a, is very similar to the structure at $x = 25\,cm$ in Figure 3.5a; i.e., two-thirds of the distance downstream in Figure 3.5a. Figure 3.36b shows the $F = 8\,Hz$ flow image and it is apparent that the forcing organizes the vortices in this case. Comparing Figure 3.36a and 3.36b, it is seen that the unforced flow possesses more small scale turbulence than the $F = 8\,Hz$ case. The braids in Figure 3.36b are thicker than those typically found in the natural case.

Both flow images in the recovery region (Figures 3.36c and 3.36d) look very much like the unforced case. The $F = 12\,Hz$ case (Figure 3.36c) for which $X_{\pi o} = 2.8$, appears to be at an intermediate mixed condition between the frequency-locked structure of Fig. 3.36b and the new, larger-scale structure at the unlocked conditions of Fig. 3.36d. As regards small scale motion, the $12\,Hz$ and $20\,Hz$ data look very similar to those in the unforced case but rather different from that in the locked region.

The intensity transformation table, which displays the color assignments for Figure 3.36, is shown in Figure 3.37. Note that low product concentrations are labeled blue, medium levels are green, and high levels are red. Comparing the unforced flow, Figure 3.36a, with the 8 Hz forced case, Figure 3.36b, indicates that the forced flow contains more low concentration areas than the natural flow (i.e., Figure 3.36b has more blue and green area than Figure 3.36a). It is obvious, in the natural case, that the composition varies from vortex to vortex. One structure in Figure 3.36a contains a considerable amount of red while another, at the extreme right, has almost no red and little yellow. The $8\,Hz$ case does not show as strong a variation; each vortex looks more or less like any other. The $20\,Hz$ image, Figure 3.36d, also shows little variation from structure to structure but has more red areas than the $8\,Hz$ case. Notice the thin braids in Figure 3.36d compared to those in Figure 3.36b.

Monocolor flow images, in which grey level is proportional to concentration, for the low-Reynolds-number data are shown in Figure 3.38. Comparing these images with the high-Reynolds-number images, it is seen how mixing takes place on a contorted interface in the present case. Comparing the $2.5\,Hz$ and $1.5\,Hz$ data (Figure 3.38c and 3.38d) with the unforced flow (Figure 3.38a) suggests that the increased mixing is due to an increase in the amount of interface. Both these flows apparently benefit, as regards mixing, from the enhanced vortex

activity upstream of the measuring station which is responsible for more stretching of the mixing interface. In Figure 3.38c the Wygnanski-Oster parameter is $X_{wo} = 1.6$, i.e., the data were acquired in the middle of the frequency-locked region. For 1.5 Hz data (Figure 3.38d) $X_{wo} = 0.9$ and a pairing can be observed. At 5 Hz forcing (Figure 3.38b) the flow has a very unusual structure. The Wygnanski-Oster parameter for this case is 3.1 so we expect these data to be in the recovery region. The vortices in this case contain hollow cores, as indicated previously, with no mixed fluid in them while the braids are greatly accentuated and contain most of the product.

Concentration Histograms. The concentration histogram is another method of displaying the information from the experiments. It is a plot of probability versus concentration and cross-stream coordinate, y; i.e., the concentration histogram is a surface in a three-dimensional space in which height is probability, width is concentration, and depth is y location. Such a surface is shown for the unforced, high-Reynolds-number case in Figure 3.39 and for the 8 Hz forced case in Figure 3.40. The unforced concentration histogram has little variation in the y direction. The forced case, Figure 3.40, also shows little variation in the y direction in the central part of the layer where the vortex cores exist. The edges, on the other hand, do have y variation which is consistent with the earlier observation that the braids contain a larger amount of low concentration fluid than does the unforced layer.

A less complicated form of presentation is obtained by integrating in the y direction to produce a plot of probabilty versus concentration. Figure 3.41 shows the y-averaged concentration histogram for each of the high-Reynolds-number data sets. Averaging in the y direction produces a "total histogram". The probability is expressed in thousands of occurences (25 on the plot means 25,000 realizations) and concentration has been normalized so that pure high

speed fluid is zero and pure low speed fluid is one, i.e., the concentration axis is $\frac{c_p}{c_{p\,max}}$. Comparison of Figure 3.41a, the unforced case, with Figure 3.41b, the 8 *Hz* forced case, shows a shift to the left in the forced flow. The probability peak in the natural case is much less prominent in the 8 *Hz* data. This forced flow, Figure 3.41b, shows a definite increase in the amount of fluid with normalized concentration between 0.0 and 0.15. This is consistent with the increased amount of low concentration fluid in the braids for the forced flow as discussed earlier. The histograms for the other forced cases, Figure 3.41c and Figure 3.41d, differ only slightly from the natural concentration histogram. The peak in Figure 3.41c is not as strong as in the natural case while the one in Figure 3.41d, and the entire histogram for that matter, appears very similar to that for the natural flow.

The y-averaged concentration histograms for the low-Reynolds-number flows are shown in Figure 3.42. The peaks observed at high Reynolds numbers do not occur for these data. It is interesting that all four concentration histograms in Figure 3.42 look almost the same even though the structure, evident in the flow images, is so different.

3.6. Summary of Forcing Effects on Mixing

The measurements of product thickness obtained by the absorption method (section 3.3) and from integration of the laser induced fluorescence concentration profiles (section 3.5) are collected in what may be called "enhancement plots" in Figures 3.43a and 3.44a. The effects of forcing on reaction product are demonstrated by plotting the *ratio* of forced product thickness to natural product thickness as a function of dimensionless downstream distance, X_{wo}. Similar plots for the ratio of product growth rates are given in Figures 3.43b and 3.44b. In these plots a value greater than one indicates that forcing causes

enhancement in either product thickness or product growth rate.

The high-Reynolds-number enhancement plots are shown in Figures 3.43a and 3.43b for product and product growth rate respectively. Recall that points which fall above the dotted line in Figures 3.43 represent flows in which product was enhanced by forcing. It is clear in Figure 3.43 that product is increased in the region below $X_{wo} = 1.0$ (i.e., the enhanced growth region). The forced-growth plot of Figure 1.2 suggests that the shear layer growth rate is twice as large in this region so it might be expected that twice as much product would result. The data show values even greater than two. This is due in part to the fact that the enhanced growth region in this particular flow is undergoing the mixing transition so the natural flow has a small product thickness. The low-frequency, high-Reynolds-number data are suspect because the visual growth rate was smaller than what it should have been indicating that the top and bottom of the test section may have been limiting growth. Figure 3.43b shows that the production rate is enhanced in the enhanced growth region with values greater than two near the splitter plate. More important, however, is the result that forcing stops production entirely in the frequency-locked region.

Broadly speaking, the results show that the frequency-locking phenomenon in forced shear layers serves to inhibit mixing in high Reynolds-number flows.

The enhancement plots for the low-Reynolds number data are shown in Figures 3.44a and 3.44b for product and product growth rate respectively. The trend in these plots is quite different from the high-Reynolds-number case. Both product and product growth rate are enhanced in the frequency-locked region. The reason for this is not entirely clear but, since enhancement by the the primary structures is suppressed, it must be connected with the modification of the secondary structure. The secondary structure is just begin-ing to form in these flows at the downstream location where the frequency-

locking occurs. Photographs of the flow (Figure 3.8) show that the secondary structure is influenced by the forcing. However, the connection between details of the secondary structure and improved mixing are not well understood.

To summarize, in contrast to the high-Reynolds-number case, the frequency-locking phenomenon produced more mixing in the low-Reynolds number flows. The results indicate that this is caused by the effect of forcing on the secondary structure rather than the primary, two-dimensional structure.

3.7. Discussion

The dramatic effect of periodic forcing on the downstream development of the thickness of the shear layer is demonstrated by the plot of Browand and Ho, shown in Figure 1.2. In this plot, both growth rate and downstream distance are made dimensionless with the forcing frequency, i.e., $\theta F/U_c$ is taken to be a function of $x \alpha F/U_c \equiv X_{wo}$. That plot is influenced heavily by the original results of Oster and Wygnanski, obtained at high values of unit Reynolds number, i.e., for $\dfrac{F}{F_0} \ll 1$ and the mixing transition very close to the splitter plate. In general, however, the Reynolds number (through its effect on initial thickness), as well as the dimensionless group $\dfrac{F}{F_0}$, are parameters of the flow as discussed earlier, c.f. section 1.3. Thus one can expect that in the $(\theta F/U_c , x \varepsilon F/U_c)$ plane there will be a *family* of curves, as in our Figure 3.14. The asymptotic condition represented by the Browand-Ho plot provides a useful reference. In our experiments, the experiment which most closely approaches the asymptotic, high Reynolds number state and yet displays a sufficiently large range of X_{wo} is the one summarized in Figure 3.17, with $\dfrac{F}{F_0} = 0.13$. It is compared with the Browand-Ho reference curve in Figure 3.14, where the ordinates have been rescaled from $\dfrac{\theta F}{U_c}$ to $\dfrac{\delta_{vis} F}{U_c}$, assuming $\delta_{vis} = 8\,\theta$. Our results are simi-

lar to but lie somewhat above the Browand-Ho curve. Part of the discrepancy may be connected with the rescaling of the thickness.

One of the main goals of this research was to describe the effects of forcing on the distribution of reaction product along the layer and to compare that with the unforced case. It was found that these effects of forcing could not be described simply, due to the role of the additional parameters discussed above. In particular, the upper Reynolds number limit of our facility made it difficult to isolate the mixing transition effects from the forcing effects. The broad, qualitative results, however, may be summarized as follows: for post-mixing-transition shear layers, in which the length of the pre-mixing-transition region is small, initial part of the flow forcing reduces the amount of mixing and of reaction product formed; for shear layers which are predominantly pre-mixing-transitional, forcing appreciably increases the amount of product. In the post-mixing-transition case, the reduction of product must be due mainly to reduced entrainment in the locked-in region and beyond. In the pre-mixing-transition case, the increased product may be partly due to the enhanced growth rate of the vorticity thickness and whatever enhanced entrainment that produces, but this cannot account for the increases observed and we conclude that there are important effects from changes in the developing secondary structure.

Coming back to the simpler, post-mixing-transition case, the relation of enhanced growth rate and entrainment to the product can be illustrated as follows. Dimotakis (1983) has shown that the particular mixture ratio inside the shear layer, which depends on the ratio of entrainment from the two sides, is a function of growth rate. In an unforced, linearly growing, self-similar layer this mixture ratio will therefore be invariant with x. The non-linear growth rate along a driven layer implies varying entrainment ratio, according to Dimotakis' model, and thus varying mixture ratio. However, the mixture ratio indicated by

the amount of product at any downstream station is an integrated measure dependent on all the events up to that point. Comparing the forced case of Figure 3.17, at $F = 8\,Hz$, with the unforced flow at the same Reynolds number, we note that the interaction region I, which has twice the unforced growth rate, has an entrainment ratio of 1.73, compared to 1.31 for the unforced layer, according to Dimotakis' theory. Further downstream in the locked-in region (II) the growth rate is zero and so the entrainment *ratio* is 1, according to Dimotakis' model, but the actual *level* of entrainment is zero. Weighing the contributions of these two regions (which are of equal length) to the product at the end of the locked-in region, predicts 34% less product than in the unforced layer. This agrees well with the measured 32% reduction.

A further demonstration of the effect of forcing on composition mixture is given in Figure 3.45; a photograph from the "disappearing vortex" experiment. The strength of acid in the low speed stream was increased such that a larger amount of high speed fluid was required before the mixed fluid appeared red; i.e., before the mixed fluid reached the pH at which phenolphthalein changes from transparent to red. Figure 3.45 shows photographs of natural flow and of the $8\,Hz$ flow for condition in which the acid was strong enough to require five parts high speed fluid to one part low speed fluid for reaction to occur. Thus, dark areas in the photographs are mixed regions where there is at least five times as much high speed fluid as low speed fluid. The unforced flow shows virtually no product, indicating that the composition of mixed fluid never exceeds five-to-one in favor of high-speed fluid. In the forced flow, on the other hand, the cores are reacted in the early part of the frequency-locked region but disappear as they move downstream. This experiment was therefore named the "disappearing vortex" experiment. It shows that the vortices start out with at least five times more high-speed fluid than low-speed fluid in the mixed cores and, furthermore, that the composition ratio of the mixed fluid reduces as the

vortices move downstream.

Chapter 4

Effects of Forcing on Wake Structure and Mixing

4.1. Structure and Mixing in the Unforced Wake

A wake, in the context of these experiments, is created by setting the flow speeds of the two streams equal to each other. The shear flow in the test section then reflects the fact that the splitter plate has drag and it is, therefore, a wake in the truest sense. A Reynolds number for the wake can be defined as

$$\mathrm{Re}_{\theta_w} = \frac{U_\infty \theta_w}{\nu} \tag{4.1}$$

where

$$U_\infty = U_1 = U_2 \tag{4.2}$$

and

$$\theta_w = \theta_1 + \theta_2. \tag{4.3}$$

θ_w is the sum of the momentum thicknesses of the boundary layers on the two sides of the splitter plate.

At very low speeds, the flow is steady with mixing only on a thin interface between the two fluids. Photographs of the phenolphthalein reaction for $U_\infty = 2\,cm/sec$ (implying $\theta_w = 3.2\,mm$ and $\mathrm{Re}_{\theta_w} = 63$) are indistinguishable from the picture in Figure 3.1a of the steady laminar shear layer. A mean velocity profile was not obtained for this flow but it is clear that it would show that the wake thickness is considerably larger than the product thickness as was the case for the laminar shear layer.

An example of an unforced wake at a higher Reynolds number, where periodic oscillations have appeared in the flow, is shown in Figure 4.1 for $U_\infty = 12\,cm/sec$, implying $\theta_w = 1.3\,mm$ and $\mathrm{Re}_{\theta_w} = 160$. The photograph shows that this wake is strongly affected by the side-walls of the test section (Figure 4.1a). A wedge shaped contamination region observed on both side walls contains most of the mixed fluid. The cross-section view (Figure 4.1b), made with the laser induced fluorescence technique, shows that the structure along the center plane of this flow, away from the side-wall regions, looks like a two-dimensional Karman vortex street with mixing on a thin interface which is distorted by the vortices. The cusped wave pattern produced in the interfacial boundary by the action of the vortices is similar to those observed experimentally and in a computer simulation for a mixing layer (see Figure 3.3 and Figures B.1 and B.3 in Appendix B). The mixing mechanism is similar to that in the premixing transition shear layers discussed in Chapter 3.

At sufficiently high speeds, the wake becomes "turbulent" as in the example shown in Figure 4.2, for which $U_\infty = 50\,cm/sec$, thus $\theta_w = 0.64\,mm$ and $\mathrm{Re}_{\theta_w} = 320$ and it is clear that a transition has occurred. In contrast to the case at lower Reynolds number, the wake structure here is basically three-dimensional even at the largest scale, as evident from the plan view in Figure 4.2. This is consistent with results of Cimbala (1984) who found that the far wakes of circular cylinders appear fundamentally three-dimensional in plan view at sufficiently high Reynolds number. Also relevant are the experiments of Breidenthal (1980) who demonstrated the tendency of large vortical structures to be three-dimensional in wakes, c.f. two-dimensional in mixing layers.

For the flow which comes off a splitter plate, as in Figure 4.2, there would appear to be less tendency to form an initially two-dimensional vortex street as in wakes behind bluff bodies. Here the three-dimensional structure appears to

develop from the beginning.

If the initial wave length and frequency are simply scaled with the rules $\text{Re} \sim U\delta \sim U^{\frac{1}{2}} ; \lambda \sim U^{-\frac{1}{2}} ; F \sim U/\delta \sim U^{\frac{3}{2}}$, then the ratios of initial wave lengths and frequencies in the flows in Figures 4.2 and 4.1 are 0.5 and 8, respectively. Comparing the photos one can discern this change of scale, suggesting that, as in the examples of Breidenthal and Cimbala, the "vortex street" scaling laws may be extended to higher Reynolds number even when the spanwise instability that contributes to the three dimensionality of the primary structure is very strong.

The unforced wake of a flat plate, then, has basically three Reynolds-number regimes: steady laminar flow at low Reynolds number; "turbulent" flow with three-dimensional large structure at high Reynolds number; and a transitional, non-steady, periodic, flow between.

4.2. Effects of Forcing on Structure of the Wake — Visual Results

This section is devoted to presentation of the visual results from forced wake experiments. The changes in structure brought about by forcing are discussed as are effects on mixing (though photographs allow only a qualitative assessment of mixing). The results are presented in order of increasing Reynolds number.

Forced Laminar Wake. Figure 4.3 shows plan, side, and oblique views of the steady laminar wake subjected to 0.5 Hz forcing. Like the laminar shear layer, the laminar wake responds to the two-dimensional forcing with a very three-dimensional wavy interface. The wake does not respond with as large an amplitude as the shear layer indicating that the shear layer is more unstable than the wake at these low Reynolds numbers. The finite width of the test section and the thick side wall boundary layers at low speeds are probably responsible for the

three-dimensional response. It would be interesting to repeat these low Reynolds number experiments with a wider test section to see if the response is three-dimensional in the center of the test section, away from side wall influence.

Structure in a Forced Wake at $Re_{\theta_w} = 160$. The $Re_{\theta_w} = 160$ wake showed a great variety of interesting changes in structure when forced. These flows were first investigated, in the present work, with the laser induced fluorescence technique. Photographs of the flow field for several forcing frequencies are shown in Figure 4.4. The acid-quenched fluorescein was slightly fluorescent even in the "off" state so pure fluid from one side appears black, pure fluid from the other side appears grey, and the mixed fluid is white in a black-and-white picture. The laser sheet was aligned along the center plane of the test section normal to the shear layer, for these photographs.

The photographs in Figure 4.4 are all for the same flow speed. Only the frequency varies from one case to another. As can be seen, forcing drastically changes structure and mixing in this flow. The unforced flow is shown in Figure 4.4a. The basic structure is a somewhat tenuous Karman vortex street with mixing occurring on a thin interface. When the flow is forced at a frequency equal to the naturally occuring frequency ($F_0 = 5\,Hz$) a more organized version of the natural flow results as seen in Figure 4.4b. Apparently, the forcing creates stronger vortices since the interface is wrapped up more in the driven case. Forcing at less than the natural frequency, $F = 1.7\,Hz$, produces a peculiar "double Karman vortex street" as seen in Figure 4.4c. This corresponds to forcing at a subharmonic in the shear layer. The flow forms structures at or near the natural frequency with a "modulation" at the forcing frequency. In the shear layer, the modulation leads to an amalgamation but the wake adopts the double vortex street configuration without any tendency toward amalgamation

within the length of the test section.

When the wake is forced at frequencies greater than the natural frequency, the initial Karman vortex street which is formed is frequency-locked to the input disturbance. However, at large downstream distances a breakdown of the initial street is observed. In Figure 4.4d, which is at a forcing frequency of 6.45 Hz, the breakdown or rearrangement can be seen. Notice the small mushroom-like blobs of pure fluid from one side that jet out into the opposite stream on each side. At a forcing frequency of 9.8 Hz (Fig. 4.4e) the breakdown of the initial street is accompanied by a dramatic increase in mixing, which will be discussed later. Increasing the frequency further to 10.75 Hz produced the photograph shown in Figure 4.4f. The emergence of a new, larger scale, Karman vortex street following the breakdown is clearly visible. Notice that vortices of like-sign contain uniformly mixed cores and those above the wake centerline have a core concentration different from those below the centerline.

Close inspection of the photographs in Figure 4.4 reveals that there is a change in the spacing ratio of the initial vortex street with change of forcing frequency. Figure 4.5 shows how the lengths a and b are defined for a Karman vortex street. The wavelength, a, was measured from each of the photographs in Figure 4.4 and compared with the forcing wavelength, U_∞ /F. The agreement was very good in every case. The separation, b, was also measured from each photograph in Figure 4.4 and values for the spacing ratio, $\frac{b}{a}$, were calculated. Figure 4.5 shows how the spacing ratio varies with forcing frequency (the abscissa is forcing frequency made dimensionless by the natural frequency in the unforced case, $F_0 = 5\,Hz$). The spacing ratio is close to 0.5 for all forcing frequencies except the frequency that causes the "highly mixed wake" of Figure 4.4e. Intriguingly, the spacing ratio for the highly mixed wake is nearly equal to the theoretical Karman spacing ratio of 0.281.

Simultaneous side and plan views of the same flow using reacting phenol-phthalein visualization are shown in Figure 4.6 for several of the frequencies included in Figure 4.4. It is obvious in these pictures that the side wall influence is strong at this Reynolds number. The reasons for this will be discussed in detail latter in connection with a model for the effect. What is seen in Figure 4.6 is that forcing significantly affects the mixing in this particular wake. Notice that the low frequency forced wakes mix primarily along the side-walls (which was also the case without forcing as shown in Figure 4.1) while the high frequency forcing causes mixing primarily in the center of the test section.

Secondary (Streamwise) Structure in Forced Wakes. Photographs of the phenolphthalein reaction are shown for a $Re_{\theta_w} = 220$ wake in Figure 4.7. The sidewall influence is not as strong at this Reynolds number as it is for $Re_{\theta_w} = 160$. The photographs show that this wake responds to forcing by assuming a two-dimensional Karman vortex street configuration and that three-dimensional secondary instabilities form on the spanwise vortices. The secondary instabilities lead to formation of streamwise vortices with a topology different from the streamwise vortices in the shear layer (Bernal, 1981).

It was found that larger forcing amplitude in a similar flow ($Re_{\theta_w} = 200$) caused the formation of strong streamwise vortices. This wake, when forced at an amplitude of 5% of the free-stream speed, is shown in Figure 4.8. The unforced flow is shown for reference in Figure 4.8a; note the side wall influence at this Reynolds number is similar to the $Re_{\theta_w} = 160$ wake. Figure 4.8b shows the flow forced near the natural frequency with the larger amplitude. It is seen, in the central part of the plan view, that the secondary instabilities form strong, closely spaced, streamwise vortices in this flow. The secondary-to-primary wavelength ratio is smaller for this forced wake than it is for the natural shear layer, e.g. Bernal (1981) found a ratio of approximately 0.5 for the mixing layer

while the secondary-to-primary spacing ratio measured from Figure 4.8b is 0.12, a factor of four smaller.

Structure in a Forced Turbulent Wake. Figure 4.9 shows the flow of Figure 4.2 being forced at an amplitude of 2% at various frequencies which are much lower than the natural initial frequency ($F_0 = 40\,Hz$) as estimated above. The wake reponds strongly to these low forcing frequencies; in each case the forced wave length is U_∞/F, compared to the natural initial wave length $U_\infty/40\,Hz$. The response is strongest at $F = 9.1\,Hz$ for which, in the plan view, the wave appears to have developed into a vortex street at the forcing wave length. The initial structure at the natural frequency $F_0 = 40\,Hz$ appears to be simply incorporated into the larger, forced structure, in a process analogous to the "collective interaction" described by Ho for mixing layers forced at low frequencies. Comparing with the forced-mixing-layer regimes of Figures 3.11 to 3.14 , the regimes visible in these pictures would appear to correspond to the enhanced growth region rather than to the later, locked-in region of no growth. The amount of product is seen to be larger than in the unforced case but, unfortunately, no quantitative measurements of it were made.

4.3. Side-Wall Effects at Moderate Reynolds Number

It has been shown that the side-walls of the test section have a strong influence on the $Re_{\theta_w} = 160$ wake flow discussed earlier (see Figure 4.4 and Figure 4.6). This flow and the side-wall effect in it will be discussed in detail in this section.

When this work was begun it was hoped that we would find we could increase mixing by forcing. This was the case for the flow shown in Figure 4.4e where an obvious increase in mixing occurs. The same flow, when viewed with the phenolphthalein technique, was found to have a highly three-dimensional structure.

Simultaneous side and plan views of this case with the side-wall interaction causing strong mixing are shown in Figure 4.10. The highly mixed region is concentrated in the center of the test section and the side-wall influence in the upstream Karman vortex street is substantial. Further insight into the structure of this flow were obtained by looking at sectional views of the type Bernal (1981) first obtained. The laser sheet was placed perpendicular to the free-stream flow direction and photographed from underneath the test section looking upstream. Ideally, a picture of a cross-section through the flow at a fixed x location is obtained. The Bernal section at $x = 12\,cm$ for the highly mixed wake is shown in Figure 4.11. The picture shows that the flow at this downstream location possesses streamwise vorticity in the form of counter-rotating vortex pairs.

The photographs suggest that the structure of the highly mixed wake is caused by the interaction of the Karman vortex street with the side-walls of the test section. The vortices in the forced street convect with the local velocity so their ends will be tipped in the upstream direction by the velocity defect in the side wall boundary layers as shown in Figure 4.12. The effect is shown, in Figure 4.12, for only one vortex. This tipping of course also occurs for shear layers, where vorticity of only one sign exists. But in the wake, which has vortices of both signs, the tipping has more serious effects. It will set up counter-rotating vortex pairs in the streamwise direction, along the sides of the test section walls, whose mirror images and mutual induction will tend to make them lift off the walls. The vortices are observed in the Bernal section (Figure 4.11). As the vortices propagate toward the center from the two sides they tend to churn up the fluid they encounter. At the same time, the three-dimensional instability in the central part of the flow is enhanced. This and possibly smaller-scale structure greatly enhances mixing. Note, in Figure 4.10, how the vortices propagate rapidly at first but slow down as the pair from the other side approach until

they cease to propagate any more in the z direction.

Figure 4.13 demonstrates a simplified model of how this process takes place. (It was suggested by L. Sigurdson in a private communication). The views in Figure 4.13 are from downstream looking upstream such that the free stream flow is perpendicular to and out of the plane of the page, i.e. same as the Bernal section view. Figure 4.13a represents an x location near the splitter plate where the tipping has occured and the streamwise vortices are established. The images of the streamwise vortices in the side walls are indicated. Actually, the image system extends cyclically to infinity in both directions though only the first set of images is shown. The induced velocities on each vortex are indicated. The counter-rotating pairs lift off the side walls and propagate toward the center of the test section until the equilibrium condition in Figure 4.13c is reached. At this point, the configuration is steady. Notice that the spacing between the streamwise vortices in the equilibrium configuration is twice the distance from either pair to the side wall from which it originated. This is consistent with the observed equilibrium spacing seen in Figure 4.10 and in the Bernal section (Figure 4.11).

An experiment was conducted to test the effect of the thickness of the side-wall boundary layer on the highly mixed wake. A false side-wall was inserted in the test section. A triangular notch was cut in the false wall into which the splitter plate fit so that the boundary layer on the false wall had developed over $3\,cm$ at the splitter plate tip. This should be compared to the boundary layer on the real side-wall which had developed over the entire contraction length of approximately $60\,cm$. The resulting flow, forced at the high mixing frequency and viewed with the phenolphthalein reaction, is shown in Figure 4.14. The flow is not perfectly symmetric in the wider passage but the tipping process and inward propagation alluded to above still occurs. Hence, it is only necessary

that the no-slip condition be present on the side walls for the high-mixing wake structure to occur. The thickness of the side-wall boundary layers is of secondary importance.

4.4. Mixing Measurements in the Moderate Reynolds Number Wake

In order to quantify the increased mixing in the highly mixed wake, measurements of laser induced fluorescence were conducted. The data were taken for a non-reacting case in which fluorescein was used to mark pure fluid from one side. This is referred to as a dilution experiment. Eight different frequencies were studied at a downstream location $x = 25\,cm$. Flow images of the data are shown in Figure 4.15. The color assignment for the images labels pure fluid from one side as blue and pure fluid from the other as red. Mixed fluid appears yellow and green. Figure 4.15a is the unforced case and the weak Karman vortex street structure is observed, with mixing only on a thin interface. Figure 4.15b shows the subharmonic forcing with its double Karman street structure. It is interesting to note that one wavelength in this flow contains five vortices; two sets of counter rotating pairs and one extra. The reason for this is not clear; it is possibly connected with weak harmonics in the forcing. The remaining images display different stages of the frequency-locked Karman vortex street and downstream breakdown discussed earlier. Figure 4.15d demonstrates that a nearly perfect vortex street can be produced by forcing at or near the natural frequency. Figure 4.15e shows the begining of breakdown of the initial street. Notice how "tongues" of pure fluid from one side extend into the opposite stream and also take note of the jet-like flow between the vortex rows. Figure 4.15f demonstrates the reformation process in which small vortices from the upstream street begin to rearrange themselves into a larger scale Karman vortex street. Figure 4.15g is the highly mixed wake flow discussed earlier; the increase in mixed fluid is evident in the flow image. Finally, at high frequencies (see Figure 4.15h), the emergence of a new street from the upstream, small-

scale street is observed.

The increased mixing in Figure 4.15g was measured from a concentration histogram of mixed fluid. Histograms for the natural wake and for the highly mixed wake are shown in Figure 4.16. It can be shown that the product thickness is the first moment of the histogram from a dilution experiment when the free stream delta functions are removed, e.g. Koochesfahani (1984). The narrow spike at the left in Figure 4.16a corresponds to pure fluid from one side and the broader peak on the right corresponds to pure fluid from the other side. Figure 4.16a shows, therefore, exactly what is obvious in the image; namely, there is very little measureable mixed fluid in the unforced case. Figure 4.16b, the histogram for the highly mixed wake, has the same peaks corresponding to unmixed fluid but now has another, broad peak in the middle corresponding to mixed fluid. Not surprisingly, most of the mixed fluid occurs at a 50-50 mixture of fluid from the two sides. Computation of the first moment of these histograms shows that there is more than an order-of-magnitude increase in mixing on the centerline due to forcing.

4.5. Discussion

First, as regards the change of flow regime with Reynolds number for the unforced wakes, it is interesting to compare with corresponding developments in the wakes of bluff bodies, especially circular cylinders, for which considerable information is available. For bluff bodies, the reference length is the cylinder diameter d , which for the flat plate is, ideally, zero. Momentum thickness is related to d by $C_D d = 2\theta_w$ where C_D is the drag coefficient of the cylinder. Thus, if we base the cylinder wake Reynolds number on $\frac{1}{2}C_D d$ we might expect to observe a rough correspondence between critical Reynolds numbers in the two flows.

For a circular cylinder, it is known that the wake is steady up to about $Re_d = 40$, i.e., $Re_{\theta_w} = 34$ (calculated with $C_D = 1.7$) while for the splitter plate the flow was still steady at $Re_{\theta_w} = 63$. For the circular cylinder, the nonsteady wake is pure periodic from $Re_d = 40$ to 160 (Roshko, 1954), i.e., $Re_{\theta_w} = 34$ to 100 , then passes an "irregular" or transitional range, and settles down to regular but "turbulent" vortex shedding at about $Re_d = 300$ or $Re_{\theta_w} = 180$. A similar course of development is described by Sato and Kuriki (1961) for the wake of a thin flat plate (but they did not cite specific Reynolds numbers). The splitter-plate wake in our experiments seems to have settled down to a "turbulent" regime (Figure 4.2) by $Re_{\theta_w} = 320$. Thus the Reynolds-number range in which the flat-plate wake makes its transition from steady to turbulent, periodic flow ($63 < Re_{\theta_w} < 320$) differs somewhat from that for the circular cylinder which is not surprising, considering the considerable differences in initial vorticity distribution. For the flat-plate wake, Breidenthal determined the beginning of the mixing transition, where product rate begins to increase dramatically, at about $Re_{\theta_w} = 100$, i.e., in the middle of the transition range; it probably corresponds to the onset of "irregular" fluctuation in the cylinder wakes. The end of the mixing transition observed by Breidenthal for the flat-plate wake was at about $Re_{\theta_w} = 800$; thus the flow in Figure 4.2 may still be undergoing the mixing transition although it appears to have a well developed three dimensional structure.

The wake-flow regimes, then, can also be labelled as "steady", "pre-mixing-transition" and "post-mixing-transition", as for the mixing-layer flows. In the mixing layer the changes from one regime to the next develop in downstream distance, which is also the direction of increasing Reynolds number. The wake Reynolds number, on the other hand, is invariant with downstream distance, to first approximation, and the regime changes occur over the whole wake, so to speak, at the appropriate changes of the (uniform) wake Reynolds number.

Although local Reynolds number does not change with downstream distance in the wake, a rescaling of the large vortex structure does occur, as seen in the pictures in Figure 4.4. For the unforced case shown in Figure 4.4a, the "breakdown" or rescaling occurs at $x/\theta_w \approx 200$, which is the same as the values found by Cimbala for natural, circular-cylinder wakes. When forced at frequencies higher than natural the breakdown occurs earlier, for example, at $x/\theta_w \approx 70$ in Figure 4.4f. This smaller distance corresponds to the smaller initial scale induced by the higher forcing frequency.

To close this chapter, a note on the case of anomalously high mixing (Figure 4.4e) is in order. First, it is clear from the various photographs in this chapter that the wake flows are more strongly influenced by side-wall boundary-layer interference than are the shear layers. The difference is connected with the fact that in the shear layer the vortices have only one sign while in the wake the presence of vortices of opposite signs make possible the strong side-wall interaction after their deflection by the no-slip condition. This difference in primary vortex structure is also thought to be connected with the greater tendency to form three-dimensional structure in the wake (Roshko, 1976; Breidenthal, 1980; Robinson and Saffman, 1982). While the details of the mechanism leading to the greatly enhanced mixing in the central part of the flow, away from the side-wall contamination region, are not clear, it seems plausible that the events are associated with the susceptibility of the wake vortex system to spanwise instability. The side wall effects are strongest and enhancement of mixing is greatest for the flow in which the forced initial vortex spacing has its smallest value, which turns out to be close to the well known Karman value. Smaller vortex spacing implies, from the model in Figure 4.13, higher propagation speed away from the wall. Whether this is the only effect in the enhanced mixing or whether there are additional ones, e.g., strengthening of the vortices, is not clear.

From an engineering stand point, the highly mixed wake may be very useful in a real combustion situation. Not only does the amount of mixing increase as a result of forcing, but the mixing occurs in the center of the test section rather than along the side-walls as it does in the same flow without forcing. This means that heat generated from combustion can be localized in the center of the combustor rather than along the sides were heat transfer to the walls may degrade performance.

Chapter 5

Conclusions

The effects of a periodic disturbance, applied to one of the free streams, on large-scale structure and mixing processes in chemically reacting shear layers and wakes were investigated. A wide range of Reynolds numbers, encompassing three different flow regimes was examined. Two different methods were employed to measure the amount of chemical product and thus the extent of molecular scale mixing. Absorption by reacted phenolphthalein provided cross-stream average product thickness and laser induced fluorescence intensity provided the product concentration distribution. These methods, in addition, provided very effective flow visualization of the large-scale structures and of their response to the periodic forcing. Following is a summary of the results.

1. The effects of periodic forcing on structure of the shear layer may be summarized as follows. For $\frac{F}{F_0} \ll 1$ and Re_{θ_1} large the forced shear layer possesses a frequency-locked region (II) in which vortices were spaced at the forced wavelength and amalgamations do not occur. Upstream, a region (I) of enhanced interaction exists and downstream, a region (III) of recovery to the unforced state occurs. For $\frac{F}{F_0} \sim 1$ but not small compared to 1, the interaction region (I) consists of controlled amalgamations, i.e. pairings, triplings, etc. , of vortices formed at the splitter plate. The present measurements of the distribution of thickness in forced shear layers agree with results obtained by previous investigators. The results confirm and, to a some degree, unify the

previous results of Wygnanski and Oster (1980) and Ho and Huang (1982).

2. The effects of periodic forcing on the distribution of mixing product in shear layers is different at high and low Reynolds numbers. At high Reynolds number, in post-mixing-transition shear layers, the most prominent result is that mixing is greatly reduced or even completely stopped in the frequency-locked region (II). Upstream, in region I, the mixing is enhanced. The net result is a reduction of product at the end of region II. The results at low Reynolds number, in pre-mixing-transition shear layers, are more varied, depending on $\dfrac{F}{F_0}$ and Re_{θ_1}. The most prominent result is that for some cases there is a large enhancement of mixing in the frequency-locked region.

3. More limited measurements were made on wake flows, which were obtained by setting equal flow velocities on the two sides of the splitter plate. An important difference between the shear-layer and wake flow was discovered, namely the much greater susceptibility of the wakes to test-section side-wall influence. The difference is attributed to the fact that the wake has vortices of *both* signs which, when swept backward in the sidewall boundary layers, interact strongly. A model based on this picture accounts fairly well for the strong sidewall effects observed at particular forcing frequencies. Less clear is why under these conditions, the mixing is greatly increased, by almost an order of magnitude, in the central part of the wake, away from the side-wall contamination region; it almost certainly is connected with effects on the secondary structure.

The most surprising result was the measured effect of forcing on mixing in the frequency-locked region of the shear layer at high Reynolds number. For a particular frequency it was observed that mixing in that region was complete stopped. Oster and Wygnanski had previously demonstrated that the growth of the shear layer is stopped and, even more, that Reynolds stresses are reversed in this region, but it was not anticipated that mixing could be reduced to zero. While large-scale entrainment is stopped, the secondary and possibly smaller turbulent structure still exists at these Reynolds numbers and it is not clear why it makes no contribution to chemical mixing product.

In contrast, at low Reynolds numbers, under what would be pre-mixing-transition conditions in the unforced layer, forcing enhances mixing in the frequency locked region. In this case the secondary structure must evidently be prominent in contributing to the mixing.

An equally surprising finding was the anomalous structure of forced wakes under some conditions. The strong side-wall effects can be explained but the reasons for the remarkable increase of mixing away from the sidewalls is not yet clear.

Appendix A

Notes on Laser Absorption

A.1. Spanwise Average of Absorption in a Sheet

Breidenthal (1978) used absorption of light along a beam to measure product in a turbulent shear layer. The measurement was an average in the cross-stream direction (i.e., the y direction) and, when referenced to a free-stream concentration, was expressed as a length called the product thickness.

In the present investigation, a laser beam was spread into a sheet and passed through the test section perpendicular to the plane of the shear layer. A bar photodiode (Quantrad model LL - 4 diffused junction silicon photodiode) was used as a detector to monitor the transmitted light intensity. The device is a solid piece of semiconductor with a light sensitive area 0.1 inches wide and 4 inches long. Ideally, the current from the diode is proportional to the total power incident on the sensitive area. As such, the measurement is a spanwise (i.e., z direction) as well as cross-stream average. The relationship, derived below, between product thickness and photodiode current is the basis for the measurement method.

A.2. Relation Between Photodiode Current and Product Thickness

The exponential relationship between incident and transmitted power along a ray is the basis for calculating the product thickness from absorption. The input power is a function of spanwise coordinate z as is the output power. Their ratio is

$$\frac{P_{out}(z)}{P_{in}(z)} = e^{-\alpha L(z)} \qquad \text{(A.1)}$$

where α is the absorption coefficient and $L(z)$ is the local value of the product thickness. The photodiode current is converted to a voltage with a standard operational amplifier circuit. The output voltage, V, is proportional, therefore, to the integral of $P_{out}(z)$ across the sheet.

$$V = \frac{\beta \mu}{W} \int_0^W P_{out}(z)dz \qquad \text{(A.2)}$$

where W is the width of the sheet, β is the conversion constant for the current to voltage converter with units of volts/amp, and μ is the sensitivity of the photodiode in amps/watt. Assuming $P_{in}(z)$ is a constant, Equations (A.1) and (A.2) imply

$$V = \frac{\beta \mu P_{in}}{W} \int_0^W e^{-\alpha L(z)}dz . \qquad \text{(A.3)}$$

Now, the spanwise average product thickness, $\bar{L}$, is the average of $L(z)$;

$$\bar{L} = \frac{1}{W} \int_0^W L(z)dz . \qquad \text{(A.4)}$$

A relationship is desired between the measured quantity, V, and the spanwise average product thickness $\bar{L}$. In order to achieve this a linearization in (A.3) is clearly necessary. Introduce L_{max} as the largest value $L(z)$ ever achieves and non-dimensionalize in the following way:

$$L^{*}(z^{*}) = \frac{L(Wz^{*})}{L_{\max}}, \tag{A.5}$$

$$z^{*} = \frac{z}{W} , \quad \alpha^{*} = \alpha L_{\max} . \tag{A.6}$$

Then L^{*} has a maximum value of 1 and (A.3) becomes

$$V = \beta\mu P_{in} \int_{0}^{1} e^{-\alpha^{*}L^{*}(z^{*})} dz^{*} . \tag{A.7}$$

Assume $0 < \alpha^{*} << 1$ and expand the integrand in (A.7).

$$\frac{V}{\beta\mu P_{in}} = \int_{0}^{1} \left[1 - \alpha^{*}L^{*}(z^{*}) + O(\alpha^{*2}) \right] dz^{*} \tag{A.8}$$

or in terms of $\bar{L}$

$$\frac{V}{\beta\mu P_{in}} = 1 - \alpha^{*} \frac{\bar{L}}{L_{\max}} + O(\alpha^{*2}) . \tag{A.9}$$

$\beta\mu P_{in}$ is the voltage when no product is present; i.e.

$$V_{in} = \beta\mu P_{in} . \tag{A.10}$$

Finally,

$$\bar{L} = \frac{1}{\alpha} \left[1 - \frac{V}{V_{in}} + O(\alpha^{*2}) \right] . \qquad (A.11)$$

Since

$$1 - \frac{V}{V_{in}} = O(\alpha^*) \qquad (A.12)$$

the error in $\bar{L}$ is of order α^* if the higher order terms in (A.11) are neglected. In the experiment, a molar concentration of 3×10^{-6} gave an absorption coefficient of $0.1 \ cm^{-1}$. One centimeter is a reasonable estimate for L_{max}, so α^* would be 0.1 and the error would be 10%.

A.3. Calibration of Phenolphthalein as an Absorbing Medium

Experiments were conducted to determine the absorption coefficient, α, for phenolphthalein. Mixtures were prepared according to the recipe given by Breidenthal (1978); alcohol and soft water plus phenolphthalein for one reactant and soft water plus sodium hydroxide for the other. The base was mixed so as to produce a pH of 11.7 and the phenolphthalein was mixed to concentrations of 1.0×10^{-6} , 3.33×10^{-6} , and 1.0×10^{-5} molar to test the effect of concentration on α. A beam of laser light was passed through a test cell consisting of three 1 cm cuvette cells. First, one of the cells was filled with a pH 11.3 mixture of the two reactants and the other two were filled with clear water. The output voltage of the detector was recorded. Next, two cells were filled with reacted fluid and one with water to obtain absorption for a 2 cm path length. Finally, all three cells were filled with reacted fluid. The results are shown in Figure A.1 for the three different phenolphthalein concentrations tested. Equation (A.1) is applicable since calibration was done with a beam and, appropriately, Figure A.1 shows the natural logarithm of the ratio of output to input power as a function

of path length. Apparently, the absorption coefficient is a linear function of concentration. The results in Figure (A.1) imply the empirical relation

$$\alpha = (constant) \times concentration$$

where

$$(constant) = 3.0 \times 10^4 \ cm^{-1}$$

and it is understood that *concentration* refers to the molar concentration of phenolphthalein.

Another set of experiments were conducted to determine the effect of base concentration on the absorption coefficient. Figure A.2 shows the absorption curves for three different base concentrations. The absorption coefficient is weakly dependent on base pH for the range of values shown in this plot. The weak dependence demonstrated in Figure A.2 was not a factor in the experiments since accurate measurement of the volume of concentrated base that was added to the soft water was not difficult. The volume was of the order of a liter for a pH 11.7 solution. The range of pH values shown in Figure A.2 corresponds to a factor of 25 variation in the volume of concentrated base, i.e., from 1/5 liter to 5 liters of concentrate. The pH of the base in all the experiments varied only from 11.6 to 11.8. Each "batch" of fluids was calibrated at run time, in the way described above, and the resulting value of α for that "batch" was used to determine the product thickness.

A.4. Data Reduction

The first time the laser sheet power was measured with the bar photodiode, a substantial 60 *Hz* component was discovered which was due, most likely, to the laser power supply. In any case, it was removed by recording both the input and output power as functions of time. Since the product thickness is proportional

to the difference between input and output power, within the assumptions given above, the common 60 *Hz* components cancelled each other.

Data were digitized with an 8-bit computer. In order to take advantage of the full dynamic range of the computer, the D.C. levels were subtracted out and gain was applied to the remainder. The gains and D.C. levels were recorded for each run as was the absorption coefficient for the fluids used. Later, with the computer, the original signals were recovered by applying the proper (inverse) gain and restoring the D.C. levels. The spanwise average product thickness as a function of time was computed on a point by point basis using equation (A.11) with higher order terms neglected.

Appendix B

Roll-Up of a Passive Interface by Rows of Point Vortices

B.1. Introduction

The motivation for the model presented here was, for the most part, the work of Jimenez (1980). He presented models for the visual growth of the turbulent shear layer which bare a striking resemblence to photographs of pre-mixing-transition shear layers taken during the course of the present study, e.g., the photo of the forced flow in Figure 3.3.

One of Jimenez's models concerns the roll-up of a thin vortex sheet. An initially flat vortex sheet is disturbed and allowed to roll-up under the action of its own induced velocity. The resulting shape of the vortex sheet is qualitatively similar to photographs of a chemically reacting liquid flow; specifically, a spiral type roll-up occurs.

Another of Jimenez's models concerns the roll-up of a passive interface by a row of point vortices. In this model all of the vorticity, within a given wavelength in the initial sheet, is concentrated into a single point vortex. The rest of the sheet contains no vorticity but still represents a material surface separating fluid above from fluid below. The interface moves with the fluid and, as such, will roll-up under the action of a row of point vortices with the given spacing.

Surprisingly, the two models produce similar interface even though physically the models represent opposite ends of the spectrum, so to speak. All that matters, apparently, is the net vorticity, not how it is distributed; at least as far as the distortion of a material surface between high and low speed fluid is concerned. The advantage of the point vortex model is that it is a significantly

simpler problem to solve. For this reason, we shall investigate Jimenez's point vortex model more deeply.

When examined in detail, several features of the passive interface solution do not agree with experimentally observed flow structures. There is difficulty with an interface that intersects a point vortex since the velocity singularity at the vortex center causes infinite distortion. Experimentally, it is known that the centers of the large-scale structures contain pure high speed fluid for pre-mixing-transition flow and that there exists a decided asymmetry in the spiral roll-up. Figure 3.3 shows both features quite clearly; the centers of the stuctures are pure black and the roll-up is not symmetric. Jimenez's point vortex model is entirely symmetric with equal amounts of high-speed and low-speed fluid within the spiral.

To alleviate these inconsistencies, it is presently proposed that a passive interface which does not intersect the vortices, but rather, one that is displaced intially toward the low speed side will better agree with Figure 3.3 . The infinite distortion is, thus, obviously eliminated and it is likely that cores of pure high speed fluid will result. The problem is with justification of such a model. It is hard enough to accept concentration of all the vorticity in a given wavelength into a single point on the interface but concentrating it to a point off the inter-face seems even more removed from reality. A simple justification is that the vorticity of the "correct" sign comes from the high speed boundary layer. It seems locigal, therefore, that the emerging vortices should exist above the material line originating from the splitter plate.

Koochesfahani (1984) made an observation, based on linear stability theory for the spatially growing layer, about the roll-up process. He found that the vor-ticity contour that is spaced 20% of the boundary layer thickness toward the low speed side resembles the experimentally observed interface quite closely. This

confirms the supposition that the center of vorticity is above the material line separating the two fluids. From a physical standpoint, linear stability theory preserves more of the physics of the problem than our model but with added compuational complexity. Linear stability theory is only valid for small disturbances to a basically parallel flow so it is not capable of predicting what happens at downstream distances where substanial vorticity concentration has taken place. For that regime, some simplifications are necessary. The present model retains the basic elements suggested by Koochesfahani's observation without the computational difficulty.

Cantwell (1981) found a difference between vorticity maxima and particle path spiral singularities. His study of transition in the axisymmetric jet showed that an off-axis spiral point develops even though the vorticity is a maximum on the axis of symmetry.

B.2. Statement of the Problem

The fluid motion is assumed two-dimensional, inviscid, and incompressible and as such satisfies the Euler equations:

$$\frac{\partial u}{\partial x} + \frac{\partial v}{\partial y} = 0 \tag{B.1}$$

$$\frac{\partial u}{\partial t} + u \frac{\partial u}{\partial x} + v \frac{\partial u}{\partial y} = -\frac{1}{\rho} \frac{\partial p}{\partial x} \tag{B.2}$$

$$\frac{\partial v}{\partial t} + u \frac{\partial v}{\partial x} + v \frac{\partial v}{\partial y} = -\frac{1}{\rho} \frac{\partial p}{\partial y} . \tag{B.3}$$

The x and y components of the vorticity vector are identically zero and the z component, ω, is given by

$$\omega = \frac{\partial v}{\partial x} - \frac{\partial u}{\partial y} . \tag{B.4}$$

When the vorticity is concentrated in isolated singularities the complex potential can be used to obtain solutions to the system (B.1) (B.2) (B.3) in the usual way. Given the velocity field, the interface location is found by solving an initial value problem. Denote the coordinates of a point on the interface by $(\xi(t),\eta(t))$. This point moves with the fluid and is therefore also a fluid particle whose motion is given by

$$\frac{d\xi}{dt} = u(\xi,\eta,t) \tag{B.5}$$

$$\frac{d\eta}{dt} = v(\xi,\eta,t) . \tag{B.6}$$

Initial conditions for (B.5) (B.6) are

$$\xi(t_0) = \xi_0 , \quad \eta(t_0) = \eta_0 . \tag{B.7}$$

Two different types of interface patterns can be generated from solutions of the system (B.5) (B.6) (B.7). The two will be referred to as temporal and spatial interfaces. The temporal interface is the locus of solution points for all possible values of ξ_0, when t_0 and η_0 are fixed. Physically, this represents the distortion of an interface which at $t = t_0$ is a straight line $y = \eta_0$. The spatial interface, on the other hand, is the locus of solution points for all values of t_0, when ξ_0 and η_0 are fixed. As such, it is the streakline originating from the point $(x,y) = (\xi_0, \eta_0)$.

The goal in the present approach is to take simple, known solutions to the Euler equations which contain vorticity and integrate equations (B.5) and (B.6) to determine the interface distortion.

B.3. Analytical Solution for Stuart's Velocity Field

Introduce the streamfunction, ψ, such that

$$u(x,y,t) = \frac{\partial \psi}{\partial y}, \quad v(x,y,t) = -\frac{\partial \psi}{\partial x}.$$

(B.8)

The Euler equations can then be written as

$$\frac{\partial \omega}{\partial t} + \frac{\partial \psi}{\partial y}\frac{\partial \omega}{\partial x} - \frac{\partial \psi}{\partial x}\frac{\partial \omega}{\partial y} = 0$$

(B.9)

$$\frac{\partial^2 \psi}{\partial x^2} + \frac{\partial^2 \psi}{\partial y^2} + \omega = 0.$$

(B.10)

Stuart (1967) found a solution to (B.9) and (B.10) which can be used to model the coherent structures of the turbulent shear layer. His exact solution is

$$\psi(x,y,t) = U_c y + \frac{\Delta U h}{2}\ln\left[\cosh\left[\frac{y}{h}\right] + A\cos\left[\frac{x - U_c t}{h}\right]\right].$$

(B.11)

ΔU is the velocity difference across the layer and h is proportional to the vortex spacing. The vortices move with speed U_c in the positive x direction. The non-dimensional parameter, A, is a vorticity concentration parameter. $A = 0$ corresponds to a parallel flow with hyperbolic tangent velocity profile and $A = 1$ corresponds to the flow due to an infinite row of potential vortices. For further properties of the solution (B.11), the reader is referred to Stuart's paper.

Using (B.11) in (B.8) the velocity field is found

$$u(x,y,t) = U_c + \frac{\Delta U}{2} \frac{\sinh\left[\frac{y}{h}\right]}{\cosh\left[\frac{y}{h}\right] + A\cos\left[\frac{x - U_c t)}{h}\right]} \qquad (B.12)$$

$$v(x,y,t) = \frac{\Delta U}{2} \frac{A\sin\left[\frac{x - U_c t}{h}\right]}{\cosh\left[\frac{y}{h}\right] + A\cos\left[\frac{x - U_c t}{h}\right]} . \qquad (B.13)$$

Inserting this velocity field into the particle path equations of the previous section yields the following problem for the interface solution:

$$\frac{d\xi}{dt} = U_c + \frac{\Delta U}{2} \frac{\sinh\left[\frac{\eta}{h}\right]}{\cosh\left[\frac{\eta}{h}\right] + A\cos\left[\frac{\xi - U_c t}{h}\right]} \qquad (B.14)$$

$$\frac{d\eta}{dt} = \frac{\Delta U}{2} \frac{A\sin\left[\frac{\xi - U_c t}{h}\right]}{\cosh\left[\frac{\eta}{h}\right] + A\cos\left[\frac{\xi - U_c t}{h}\right]} \qquad (B.15)$$

$$\xi(t_0) = \xi_0 , \quad \eta(t_0) = \eta_0 . \qquad (B.16)$$

Introduce non-dimensional variables in the following way:

$$\widehat{x} = \frac{\xi - U_c t}{h} \ , \ \widehat{y} = \frac{\eta}{h} \ , \ \widehat{t} = \frac{\Delta U}{2h} t \tag{B.17a}$$

$$\widehat{x}_0 = \frac{\xi_0 - U_c t_0}{h} \ , \ \widehat{y}_0 = \frac{\eta_0}{h} \ , \ \widehat{t}_0 = \frac{\Delta U}{2h} t_0 \ . \tag{B.17b}$$

Equations (B.14),(B.15), and (B.16) then become

$$\frac{d\widehat{x}}{d\widehat{t}} = \frac{\sinh \widehat{y}}{\cosh \widehat{y} + A \cos \widehat{x}} \tag{B.18}$$

$$\frac{d\widehat{y}}{d\widehat{t}} = \frac{A \sin \widehat{x}}{\cosh \widehat{y} + A \cos \widehat{x}} \tag{B.19}$$

$$\widehat{x}(\widehat{t}_0) = \widehat{x}_0 \ , \ \widehat{y}(\widehat{t}_0) = \widehat{y}_0 \ . \tag{B.20}$$

Dividing equation (B.19) by (B.18) yields

$$\frac{d\widehat{y}}{d\widehat{x}} = \frac{A \sin \widehat{x}}{\sinh \widehat{y}} \tag{B.21}$$

which implies

$$\sinh \widehat{y} \, d\widehat{y} - A \sin \widehat{x} \, d\widehat{x} = 0 \ . \tag{B.22}$$

Integration of (B.22) gives

$$\cosh \widehat{y} + A \cos \widehat{x} = \text{constant} ,\qquad\text{(B.23)}$$

Initial conditions, (B.20), determine the constant of integration. Introduce $\widehat{\psi}$ such that

$$e^{\widehat{\psi}} = \cosh \widehat{y} + A \cos \widehat{x} = \cosh \widehat{y}_0 + A \cos \widehat{x}_0 .\qquad\text{(B.24)}$$

This simply shows that the interface point moves on the streamline $\widehat{\psi}$ determined by initial conditions. The function $\widehat{\psi}$ is independent of time. From (B.24) and (B.18) it is seen that

$$\frac{d\widehat{x}}{d\widehat{t}} = e^{-\widehat{\psi}} \sinh \widehat{y} .\qquad\text{(B.25)}$$

Since $\sinh \widehat{y} = \sqrt{\cosh^2 \widehat{y} - 1}$, Equation (B.24) can be used to write (B.25) as

$$\frac{d\widehat{x}}{d\widehat{t}} = \left[(1 - A\, e^{-\widehat{\psi}} \cos \widehat{x})^2 - e^{-2\widehat{\psi}} \right]^{\frac{1}{2}}\qquad\text{(B.26)}$$

or

$$d\widehat{t} = \frac{d\widehat{x}}{\left[(1 - A\, e^{-\widehat{\psi}} \cos \widehat{x})^2 - e^{-2\widehat{\psi}} \right]^{\frac{1}{2}}}\qquad\text{(B.27)}$$

Integrating (B.27) produces

$$\widehat{t} - \widehat{t}_0 = \int_{\widehat{x}_0}^{\widehat{x}} \frac{dx}{\sqrt{1 - a \cos x)^2 - b^2}}\qquad\text{(B.28)}$$

where

$$a = A e^{-\hat{\psi}}, \quad b = e^{-\hat{\psi}} . \tag{B.29}$$

a and b are constants. The solution is found by determining $\hat{x}(\hat{t})$ from (B.28) and then $\hat{y}(\hat{t})$ from (B.24).

Physically, it is known that there is a critical value of the non-dimensional streamfunction, $\hat{\psi}$, corresponding to the boundary of the so called "cat's eye". This value is easily found,

$$\hat{\psi} = \ln(1 + A) . \tag{B.30}$$

Outside the cat's eye boundary $e^{\hat{\psi}} > 1 + A$ and the quantity inside the square root in (B.28) is positive for all real values of x. Inside the cat's eye $e^{\psi} < 1 + A$ and the denominator of the integrand in (B.28) possesses zeros for certain real x. A change in integration variable will put (B.28) into a form where the above behavior is more apparent. Let

$$\zeta = \tan \frac{x}{2} , \quad x = 2 \arctan \zeta . \tag{B.31}$$

With this substitution

$$dx = \frac{2d\zeta}{1 + \zeta^2} , \quad \cos x = \frac{1 - \zeta^2}{1 + \zeta^2} .$$

After some manipulation (B.28) becomes

$$\hat{t} - \hat{t}_0 = \frac{2}{\sqrt{(1 + a + b)(1 + a - b)}} \int_{\zeta_0}^{\hat{\zeta}} \frac{d\zeta}{\sqrt{(\zeta^2 + \alpha^2)(\zeta^2 - \beta^2)}} \tag{B.32}$$

where

$$\hat{\zeta} = \tan \frac{\hat{x}}{2} , \quad \hat{\zeta}_0 = \tan \frac{\hat{x}_0}{2} \tag{B.33a}$$

$$\alpha = \left[\frac{1-a+b}{1+a+b} \right]^{\frac{1}{2}} , \quad \beta = \left[\frac{a+b-1}{a-b+1} \right]^{\frac{1}{2}} . \tag{B.33b}$$

Inside the cat's eye

$$1-A < e^{\hat{\psi}} < 1+A \tag{B.34}$$

which implies

$$1-a < b < 1+a . \tag{B.35}$$

Hence α and β are positive real numbers. Outside the cat's eye

$$e^{\hat{\psi}} > 1+A \tag{B.36}$$

which implies

$$b < 1-a . \tag{B.37}$$

Once again α is positive real but now β is positive and purely imaginary.

The integral in (B.32) is in a form that allows the solution to be expressed easily in terms of Jacobian elliptic functions. The fundamental relation defining these functions is the following:

$$f = \int\limits_{0}^{y} \frac{dt}{\sqrt{(1-t^2)(1-k^2t^2)}} \; . \tag{B.38}$$

y, considered as a function of f and k, is expressed as

$$y = sn(f,k) \; . \tag{B.39}$$

Two other functions are defined in terms of sn,

$$cn(f,k) = \sqrt{1-y^2}$$
$$dn(f,k) = \sqrt{1-k^2y^2} \; .$$

Reciprocals of these three functions are denoted as follows:

$$ns(f,k) = \frac{1}{sn(f,k)} \; , \quad nc(f,k) = \frac{1}{cn(f,k)} \; , \quad nd(f,k) = \frac{1}{dn(f,k)} \; .$$

Byrd and Friedman (1971) give a complete development of the Jacobian elliptic functions and of their properties. The similarity between (B.38) and the integral in (B.32) establishes the connection between the desired solution and Jacobian elliptic functions.

B.4. Exact Solution Inside the Cat's Eye Boundary

Since the streamlines inside the cat's eye are closed orbits we expect $\hat{x}$ to be a periodic function of $\hat{t}$ in (B.28). The period of one revolution around the vortex center can be shown to be

$$T = \frac{8\,K(s)}{\sqrt{(1+a+b)(1+a-b)(\alpha^2+\beta^2)}} \qquad (B.40)$$

where

$$s = \frac{\alpha}{\sqrt{\alpha^2+\beta^2}} \qquad (B.41)$$

and $K(s)$ is the complete elliptic integral of the first kind.

Since $\hat{t}$ and $\hat{t}_0$ are known, determination of the number of complete revolutions, which have occured, is possible. Let this quantity be denoted by N.

$$N = INT\left[\frac{\hat{t}-\hat{t}_0}{T}\right] . \qquad (B.42)$$

The symbol $INT(x)$ was borrowed from Fortran. It simply means to truncate x after the decimal point. For example

$$INT(2.123) = 2 ,$$

the result being a simple integer.

The function $\hat{x}(\hat{t})$ is bounded above and below in a predictable way. Define a quantity x^* such that

$$\cos x^{\bullet} = \frac{1-b}{a} .$$
(B.43)

Then

$$x^{\bullet} < \hat{x}(\hat{t}) < 2\pi - x^{\bullet} .$$
(B.44)

With the above information, the solution needs to be separated into four different cases corresponding to initial locations in one of four quadrants about the vortex center. The four cases are as follows:

1) $\hat{y}_0 < 0$, $x^{\bullet} < \hat{x}_0 < \pi$ (B.45a)

2) $\hat{y}_0 > 0$, $x^{\bullet} < \hat{x}_0 < \pi$ (B.45b)

3) $\hat{y}_0 > 0$, $\pi < \hat{x}_0 < 2\pi - x^{\bullet}$ (B.45c)

4) $\hat{y}_0 < 0$, $\pi < \hat{x}_0 < 2\pi - x^{\bullet}$.   (B.45d)

For each case, it will turn out, five sub-cases are needed, so twenty separate formulas represent the complete solution. More development will be given for Case 1 in (B.45a). The other cases follow in a similar manner.

Consider Case 1. Define the time $t^{\bullet}$ as

$$t^{\bullet} = \int_{x^{\bullet}}^{\hat{x}_0} g(\xi) d\xi$$
(B.46)

where

$$g(\xi) = [(1 - a \cos \xi)^2 - b^2]^{-\frac{1}{2}} .$$
(B.47)

Given the number of periods, N from (B.42), we can define five separate possibilities. They are

$$a) \quad 0 < (\hat{t} - \hat{t}_o) - NT < t^* \tag{B.48a}$$

$$b) \quad t^* < (\hat{t} - \hat{t}_o) - NT < t^* + \frac{1}{4}T \tag{B.48b}$$

$$c) \quad t^* + \frac{1}{4}T < (\hat{t} - \hat{t}_o) - NT < t^* + \frac{1}{2}T \tag{B.48c}$$

$$d) \quad t^* + \frac{1}{2}T < (\hat{t} - \hat{t}_o) - NT < t^* + \frac{3}{4}T \tag{B.48d}$$

$$e) \quad t^* + \frac{3}{4}T < (\hat{t} - \hat{t}_o) - NT < T \ . \tag{B.48e}$$

Take Case 1a for example. Equation (B.28) implies

$$\hat{t} - \hat{t}_0 - NT = \int_{\hat{x}}^{\hat{x}_0} g(\xi)d\xi \tag{B.49}$$

with restrictions

$$0 < (\hat{t} - \hat{t}_0) - NT < t^* \ , \quad \hat{y} < 0 \ , \quad x^* < \hat{x} < \hat{x}_0 \ . \tag{B.50}$$

Equation (B.49) implies

$$\hat{t} - \hat{t}_0 - NT = \int_{x^*}^{\hat{x}_0} g(\xi)d\xi - \int_{x^*}^{\hat{x}} g(\xi)d\xi \ .$$

Using (B.46)

$$\hat{t} - \hat{t}_0 - NT = t^* - \int_{x^*}^{\hat{x}_0} g(\xi)d\xi \ .$$

Using (B.47), (B.31), (B.33), and (B.43) the above can be written as

$$\hat{t} - \hat{t}_0 - NT = t^* - \frac{2}{\sqrt{\sigma}} \int\limits_{\beta}^{\tan\frac{\hat{x}}{2}} \frac{d\zeta}{\sqrt{(\zeta^2 + \alpha^2)(\zeta^2 - \beta^2)}} \qquad (B.51)$$

where

$$\sigma = (1 + a + b)(1 + a - b) .$$

Manipulation aimed at obtaining a form similar to equation (B.38) will eventually produce

$$\frac{1}{\beta} \tan\left[\frac{1}{2} \hat{x}(\hat{t}) \right] = nc \left[\frac{1}{2} \sqrt{\sigma(\alpha^2 + \beta^2)} (t^* - \hat{t} + \hat{t}_0 + NT) , \frac{\alpha}{\sqrt{\alpha^2 + \beta^2}} \right] \qquad (B.52)$$

which defines the solution $\hat{x}(\hat{t})$ in terms of the Jacobian elliptic function $nc\,(f,k)$ where f and k are the complicated expressions in square brackets above. The twenty formulas mentioned earlier, of which (B.52) is one, are collected together in section B.6.

B.5. Exact Solution Outside the Cat's Eye Boundary

A fluid particle that starts outside the cat's eye boundary will remain outside and simply move over, or under, the vortex centers depending on whether the particle starts above, or belo,w the boundary. Equation (B.28) may be written then, for the outside flow, as

$$above: \hat{t} - \hat{t}_0 = \int\limits_{\hat{x}_0}^{\hat{x}} g(\xi)d\xi , \quad \hat{x} > \hat{x}_0 , \quad \hat{y} > 0 \qquad (B.53a)$$

$$below: \quad \hat{t} - \hat{t}_0 = \int\limits_{\hat{x}}^{\hat{x}_0} g(\xi)d\xi \ , \quad \hat{x} < \hat{x}_0 \ , \quad \hat{y} < 0 \qquad (B.53b)$$

where $g(\xi)$ is given in equation (B.47).

The characteristic time for the outside flow is

$$\tau = \int\limits_{0}^{2\pi} g(\xi)d\xi \qquad (B.54)$$

which is analogous to the period, T, for the inside flow. Physically, it is the time it takes a particle to travel from a location directly above one stagnation point to a location directly above the next stagnation point. The methods used previously allow τ to be found.

$$\tau = \frac{4\,K(r)}{\alpha\sqrt{(1+a+b)(1+a-b)}} \qquad (B.55)$$

where

$$r = \frac{\sqrt{\alpha^2-\gamma^2}}{\alpha} \qquad (B.56a)$$

$$\alpha = \left[\frac{1-a+b}{1+a+b}\right]^{\frac{1}{2}} \ , \quad \gamma = \left[\frac{1-a-b}{1+a-b}\right]^{\frac{1}{2}} \ . \qquad (B.56b)$$

Following a strategy similar to that used for the inside problem, the number of vortex centers traversed can be defined as

$$M = INT\left[\frac{\hat{t} - \hat{t}_0}{\tau}\right] .$$

(B.57)

Now define new coordinates with the effect of non-zero M subtracted out. Denote these by a prime.

$$\hat{t}' = \hat{t} - \hat{t}_0 - M\tau , \quad 0 < \hat{t}' < \tau$$

(B.58a)

$$\hat{x}'_a = \hat{x} - \hat{x}_0 - 2\pi M , \quad 0 < \hat{x}'_a < 2\pi , \quad \hat{y} > 0$$

(B.58b)

$$\hat{x}'_b = \hat{x}_0 - \hat{x} - 2\pi M , \quad 0 < \hat{x}'_b < 2\pi , \quad \hat{y} < 0$$

(B.58c)

The subscripts, a and b, refer to above and below the boundary; a for $\hat{y} > 0$ and b for $\hat{y} < 0$. It is useful to define an origin $\hat{x}_{00}$. Above the boundary, $\hat{x}_{00}$ is taken to be the $\hat{x}$ coordinate of the first stagnation point to the left of $\hat{x}_0$. Below, it is the first stagnation point to the right.

$$\hat{y} > 0, \quad \hat{x}_{00} = 2\pi M_0 , \quad M_0 = \begin{cases} INT\left[\dfrac{\hat{x}_0}{2\pi}\right] & , \quad \hat{x}_0 > 0 \\[3mm] -1 + INT\left[\dfrac{\hat{x}_0}{2\pi}\right] & , \quad \hat{x}_0 < 0 \end{cases}$$

(B.59a)

$$\hat{y} < 0, \quad \hat{x}_{00} = 2\pi M_0 , \quad M_0 = \begin{cases} 1 + INT\left[\dfrac{\hat{x}_0}{2\pi}\right] & , \quad \hat{x}_0 > 0 \\[3mm] INT\left[\dfrac{\hat{x}_0}{2\pi}\right] & , \quad \hat{x}_0 < 0 \end{cases}$$

(B.59b)

then

$$\hat{y} > 0, \quad 0 < \hat{x}_0 - \hat{x}_{00} < 2\pi \qquad \text{(B.60a)}$$

$$\hat{y} < 0, \quad 0 < \hat{x}_{00} - \hat{x}_0 < 2\pi \qquad \text{(B.60b)}$$

Consider $\hat{y} > 0$; $\hat{y} < 0$ will be very similar. Equation (B.53) can be written, using (B.58) and (B.59), as

$$\hat{t}' = \int_{\hat{x}_0}^{\hat{x}_a' + \hat{x}_0} g(\xi) d\xi = \int_{\hat{x}_0 - \hat{x}_{00}}^{\hat{x}_a' + \hat{x}_0 - \hat{x}_{00}} g(\xi) d\xi$$

$$\hat{t}' = \int_{0}^{\hat{x}_a' + \hat{x}_0 - \hat{x}_{00}} g(\xi) d\xi - \int_{0}^{\hat{x}_0 - \hat{x}_{00}} g(\xi) d\xi \qquad \text{(B.61)}$$

The inequalities in (B.58) and (B.60) imply

$$0 < \hat{x}_a' + \hat{x}_0 - \hat{x}_{00} < 4\pi \qquad \text{(B.62a)}$$

$$0 < \hat{x}_0 - \hat{x}_{00} < 2\pi . \qquad \text{(B.62b)}$$

Define a time, τ_0, as the time for a particle to travel from $\hat{x}_{00}$ to $\hat{x}_0$. Then

$$\tau_0 = \int_{0}^{\hat{x}_0 - \hat{x}_{00}} g(\xi) d\xi . \qquad \text{(B.63)}$$

Putting τ_0 into the elliptic function form, using (B.31), produces

$$\tau_0 = \frac{2F(\varphi_a, r)}{\alpha \sqrt{(1+a+b)(1+a-b)}} , \quad 0 < \hat{x}_0 - \hat{x}_{00} < \pi \qquad \text{(B.64a)}$$

$$\tau_0 = \tau - \frac{2F(\theta_a, r)}{\alpha \sqrt{(1+a+b)(1+a-b)}} , \quad \pi < \hat{x}_0 - \hat{x}_{00} < 2\pi \qquad \text{(B.64b)}$$

where

$$\tan \varphi_a = \frac{1}{\gamma} \tan \left[\frac{\hat{x}_0 - \hat{x}_{00}}{2} \right] \qquad \text{(B.65a)}$$

$$\tan \theta_a = \frac{1}{\gamma} \tan \left[\frac{2\pi + \hat{x}_0 - \hat{x}_{00}}{2} \right] \qquad \text{(B.65b)}$$

and $F(\varphi, k)$ is the incomplete elliptic integral of the first kind. Putting (B.65) into (B.61) yields

$$\hat{t}' + \tau_0 = \int_0^{\hat{x}_a' + \hat{x}_0 - \hat{x}_{00}} g(\xi) d\xi . \qquad \text{(B.66)}$$

Just as was the case in the inside problem, separate cases need to be studied, depending upon the value of $\hat{t}' + \tau_0$. They are

$$1) \quad 0 < \hat{t}' + \tau_0 < \frac{1}{2}\tau , \quad 0 < \hat{x}_a' + \hat{x}_0 - \hat{x}_{00} < \pi \qquad \text{(B.67a)}$$

$$2) \quad \frac{1}{2}\tau < \hat{t}' + \tau_0 < \tau , \quad \pi < \hat{x}_a' + \hat{x}_0 - \hat{x}_{00} < 2\pi \qquad \text{(B.67b)}$$

$$3) \quad \tau < \hat{t}' + \tau_0 < \frac{3}{2}\tau , \quad 2\pi < \hat{x}_a' + \hat{x}_0 - \hat{x}_{00} < 3\pi \qquad \text{(B.67c)}$$

4) $\frac{3}{2}\tau < \hat{t}' + \tau_0 < 2\tau$, $\quad 3\pi < \hat{x}_a' + \hat{x}_0 - \hat{x}_{00} < 4\pi$ $\hfill$ (B.67d)

Consider Case 1. Straightforward manipulation of (B.66) gives

$$\hat{t}' + \tau_0 = \frac{2F(\varphi'_a, r)}{\alpha \sqrt{(1+a+b)(1+a-b)}} \hfill \text{(B.68)}$$

where

$$\tan \varphi'_a = \frac{1}{\gamma} \tan \left[\frac{\hat{x}_a' + \hat{x}_0 - \hat{x}_{00}}{2} \right] \hfill \text{(B.69)}$$

Using properties of elliptic functions, (B.68) and (B.69) imply

$$\cot \left[\frac{\hat{x}_a' + \hat{x}_0 - \hat{x}_{00}}{2} \right] = \frac{c(\hat{t}')}{\gamma} \left[\frac{1}{1 - c^2(\hat{t}')} \right]^{\frac{1}{2}}. \hfill \text{(B.70)}$$

where

$$c(\hat{t}') = cn \left[\frac{\alpha}{2} \sqrt{(1+a+b)(1+a-b)} \, (\hat{t}' + \tau_0) \, , \, r \right] \hfill \text{(B.71)}$$

Equation (B.70) defines $\hat{x}_a'$ and hence $\hat{x}$ as a function of $\hat{t}'$ and hence of $\hat{t}$. $\hat{x}(\hat{t})$ is the desired solution. The other three cases follow in similar fashion as does the solution below the cat's eye boundary.

B.6. Complete Solution

For the record, the complete solution to the problem (B.18) (B.19) (B.20) is given below. $\hat{x}_0, \hat{y}_0, \hat{t}_0,$ and $\hat{t}$ are given and $\hat{x}$ and $\hat{y}$ are desired. The formulas for $\hat{x}(\hat{t})$ will be given realizing that those for $\hat{y}(\hat{t})$ are obtained from equation (B.24).

Inside Solution:

Case 1: $x^* < \hat{x}_0 < \pi$, $\hat{y}_0 < 0$

1a) $0 < \hat{t} - \hat{t}_0 - NT < t^*$, $x^* < \hat{x} < \hat{x}_0$, $\hat{y} < 0$

$$\frac{1}{\beta} \tan \left[\frac{\hat{x}}{2} \right] = nc \left[\frac{\sqrt{\alpha^2 + \beta^2}}{\kappa} (t^* - \hat{t} + \hat{t}_0 + NT) , s \right]$$

1b) $t^* < \hat{t} - \hat{t}_0 - NT < t^* + \frac{1}{4}T$, $x^* < \hat{x} < \pi$, $\hat{y} > 0$

$$\frac{1}{\beta} \tan \left[\frac{\hat{x}}{2} \right] = nc \left[\frac{\sqrt{\alpha^2 + \beta^2}}{\kappa} (\hat{t} - \hat{t}_0 - NT - t^*) , s \right]$$

1c) $t^* + \frac{1}{4}T < \hat{t} - \hat{t}_0 - NT < t^* + \frac{1}{2}T$, $\pi < \hat{x} < 2\pi - x^*$, $\hat{y} > 0$

$$\frac{1}{\beta} \tan \left[\frac{2\pi - \hat{x}}{2} \right] = nc \left[\frac{\sqrt{\alpha^2 + \beta^2}}{\kappa} (t^* + \frac{1}{2}T - \hat{t} + \hat{t}_0 + NT) , s \right]$$

1d) $t^* + \frac{1}{2}T < \hat{t} - \hat{t}_0 - NT < t^* + \frac{3}{4}T$, $\pi < \hat{x} < 2\pi - x^*$, $\hat{y} < 0$

$$\frac{1}{\beta} \tan\left[\frac{2\pi - \hat{x}}{2}\right] = nc\left[\frac{\sqrt{\alpha^2 + \beta^2}}{\kappa}\,(\hat{t} - \hat{t}_0 - NT - t^* - \frac{1}{2}T)\,,\ s\right]$$

1e) $t^* + \frac{3}{4}T < \hat{t} - \hat{t}_0 - NT < T$, $\hat{x}_0 < \hat{x} < \pi$, $\hat{y} < 0$

$$\frac{1}{\beta} \tan\left[\frac{\hat{x}}{2}\right] = nc\left[\frac{\sqrt{\alpha^2 + \beta^2}}{\kappa}\,(t^* + T - \hat{t} + \hat{t}_0 + NT)\,,\ s\right]$$

Case 2: $x^* < \hat{x}_0 < \pi$, $\hat{y}_0 > 0$

2a) $0 < \hat{t} - \hat{t}_0 - NT < \frac{1}{4}T - t^*$, $\hat{x}_0 < \hat{x} < \pi, \hat{y} > 0$

$$\frac{1}{\beta} \tan\left[\frac{\hat{x}}{2}\right] = nc\left[\frac{\sqrt{\alpha^2 + \beta^2}}{\kappa}\,(\hat{t} - \hat{t}_0 - NT + t^*)\,,\ s\right]$$

2b) $\frac{1}{4}T - t^* < \hat{t} - \hat{t}_0 - NT < \frac{1}{2}T - t^*$, $\pi < \hat{x} < 2\pi - x^*$, $\hat{y} > 0$

$$\frac{1}{\beta} \tan\left[\frac{2\pi - \hat{x}}{2}\right] = nc\left[\frac{\sqrt{\alpha^2 + \beta^2}}{\kappa}\,(\frac{1}{2}T - t^* - \hat{t} + \hat{t}_0 + NT)\,,\ s\right]$$

$2c)$ $\frac{1}{2}T - t^* < \hat{t} - \hat{t}_0 - NT < \frac{3}{4}T - t^*$, $\pi < x < 2\pi - x^*$, $\hat{y} < 0$

$$\frac{1}{\beta} \tan\left[\frac{2\pi - \hat{x}}{2}\right] = nc\left[\frac{\sqrt{\alpha^2 + \beta^2}}{\kappa}(\hat{t} - \hat{t}_0 - NT + t^* - \frac{1}{2}T), \ s\right]$$

$2d)$ $\frac{3}{4}T - t^* < \hat{t} - \hat{t}_0 - NT < T - t^*$, $x^* < \hat{x} < \pi$, $\hat{y} < 0$

$$\frac{1}{\beta} \tan\left[\frac{\hat{x}}{2}\right] = nc\left[\frac{\sqrt{\alpha^2 + \beta^2}}{\kappa} + (T - t^* - \hat{t} + \hat{t}_0 + NT), \ s\right]$$

$2e)$ $T - t^* < \hat{t} - \hat{t}_0 - NT < T$, $x^* < \hat{x} < \hat{x}_0$, $\hat{y} > 0$

$$\frac{1}{\beta} \tan\left[\frac{\hat{x}}{2}\right] = nc\left[\frac{\sqrt{\alpha^2 + \beta^2}}{\kappa}(\hat{t} - \hat{t}_0 - NT - T + t^*), \ s\right]$$

Case 3: $\pi < \hat{x}_0 < 2\pi - x^*$, $\hat{y}_0 > 0$

$3a)$ $0 < \hat{t} - \hat{t}_0 - NT < t^*$, $\hat{x}_0 < \hat{x} < 2\pi - x^*$, $\hat{y} > 0$

$$\frac{1}{\beta} \tan\left[\frac{2\pi - \hat{x}}{2}\right] = nc\left[\frac{\sqrt{\alpha^2 + \beta^2}}{\kappa}(t^* - \hat{t} + \hat{t}_0 + NT), \ s\right]$$

3b) $t^* < \hat{t} - \hat{t}_0 - NT < t^* + \frac{1}{4}T$, $\pi < \hat{x} < 2\pi - x^*$, $\hat{y} < 0$

$$\frac{1}{\beta} \tan \left[\frac{2\pi - \hat{x}}{2} \right] = nc \left[\frac{\sqrt{\alpha^2 + \beta^2}}{\kappa} \, (\hat{t} - \hat{t}_0 - NT - t^*) \,, \; s \right]$$

3c) $t^* + \frac{1}{4}T < \hat{t} - \hat{t}_0 - NT < t^* + \frac{1}{2}T$, $x^* < \hat{x} < \pi$, $\hat{y} < 0$

$$\frac{1}{\beta} \tan \left[\frac{\hat{x}}{2} \right] = nc \left[\frac{\sqrt{\alpha^2 + \beta^2}}{\kappa} \, (t^* + \frac{1}{2}T - \hat{t} + \hat{t}_0 + NT) \,, \; s \right]$$

3d) $t^* + \frac{1}{2}T < \hat{t} - \hat{t}_0 - NT < t^* + \frac{3}{4}T$, $x^* < \hat{x} < \pi$, $\hat{y} > 0$

$$\frac{1}{\beta} \tan \left[\frac{\hat{x}}{2} \right] = nc \left[\frac{\sqrt{\alpha^2 + \beta^2}}{\kappa} \, (\hat{t} - \hat{t}_0 - NT - t^* - \frac{1}{2}T) \,, \; s \right]$$

3e) $t^* + \frac{3}{4}T < \hat{t} - \hat{t}_0 - NT < T$, $\pi < \hat{x} < \hat{x}_0$, $\hat{y} > 0$

$$\frac{1}{\beta} \tan \left[\frac{2\pi - \hat{x}}{2} \right] = nc \left[\frac{\sqrt{\alpha^2 + \beta^2}}{\kappa} \, (t^* + T - \hat{t} + \hat{t}_0 + NT) \,, \; s \right]$$

Case 4: $\pi < \hat{x}_0 < 2\pi - x^*$, $\hat{y}_0 < 0$

$4a$) $0 < \hat{t} - \hat{t}_0 - NT < \frac{1}{4}T - t^{\cdot}$, $\pi < \hat{x} < \hat{x}_0$, $\hat{y} < 0$

$$\frac{1}{\beta} \tan \left[\frac{2\pi - \hat{x}}{2} \right] = nc \left[\frac{\sqrt{\alpha^2 + \beta^2}}{\kappa} (\hat{t} - \hat{t}_0 - NT + t^{\cdot}) , s \right]$$

$4b$) $\frac{1}{4}T - t^{\cdot} < \hat{t} - \hat{t}_0 - NT < \frac{1}{2}T - t^{\cdot}$, $x^{\cdot} < \hat{x} < \pi$, $\hat{y} < 0$

$$\frac{1}{\beta} \tan \left[\frac{\hat{x}}{2} \right] = nc \left[\frac{\sqrt{\alpha^2 + \beta^2}}{\kappa} (\frac{1}{2}T - t^{\cdot} - \hat{t} + \hat{t}_0 + NT) , s \right]$$

$4c$) $\frac{1}{2}T - t^{\cdot} < \hat{t} - \hat{t}_0 - NT < \frac{3}{4}T - t^{\cdot}$, $x^{\cdot} < \hat{x} < \pi$, $\hat{y} > 0$

$$\frac{1}{\beta} \tan \left[\frac{\hat{x}}{2} \right] = nc \left[\frac{\sqrt{\alpha^2 + \beta^2}}{\kappa} (\hat{t} - \hat{t}_0 - NT + t^{\cdot} - \frac{1}{2}T) , s \right]$$

$4d$) $\frac{3}{4}T - t^{\cdot} < \hat{t} - \hat{t}_0 - NT < T - t^{\cdot}$, $\pi < \hat{x} < 2\pi - x^{\cdot}$, $\hat{y} > 0$

$$\frac{1}{\beta} \tan \left[\frac{2\pi - \hat{x}}{2} \right] = nc \left[\frac{\sqrt{\alpha^2 + \beta^2}}{\kappa} (T - t^{\cdot} - \hat{t} + \hat{t}_0 + NT) , s \right]$$

$4e$) $T - t^{\cdot} < \hat{t} - \hat{t}_0 - NT < T$, $\hat{x}_0 < \hat{x} < 2\pi - x^{\cdot}$, $\hat{y} < 0$

$$\frac{1}{\beta} \tan \left[\frac{2\pi - \hat{x}}{2} \right] = nc \left[\frac{\sqrt{\alpha^2 + \beta^2}}{\kappa} (\hat{t} - \hat{t}_0 - NT - T + t^{*)}) , s \right]$$

Above Outside Solution: $\hat{y}_0 > 0$, $\hat{y} > 0$

Case 1: $0 < \hat{t}' + \tau_0 < \frac{1}{2}\tau$, $0 < \hat{x}'_a + \hat{x}_0 - \hat{x}_{00} < \pi$

$$\cot \left[\frac{\hat{x}'_a + \hat{x}_0 - \hat{x}_{00}}{2} \right] = \frac{1}{\gamma} F \left\{ cn \left[\frac{\alpha}{\kappa} (\hat{t}' + \tau_0) , r \right] \right\}$$

Case 2: $\frac{1}{2}\tau < \hat{t}' + \tau_0 < \tau$, $\pi < \hat{x}'_a + \hat{x}_0 - \hat{x}_{00} < 2\pi$

$$\cot \left[\frac{2\pi + \hat{x}_{00} - \hat{x}'_a - \hat{x}_0}{2} \right] = \frac{1}{\gamma} F \left\{ cn \left[\frac{\alpha}{\kappa} (\tau - \hat{t}' - \tau_0) , r \right] \right\}$$

Case 3: $\tau < \hat{t}' + \tau_0 < \frac{3}{2}\tau$, $2\pi < \hat{x}'_a + \hat{x}_0 - \hat{x}_{00} < 3\pi$

$$\cot \left[\frac{\hat{x}'_a + \hat{x}_0 - \hat{x}_{00} - 2\pi}{2} \right] = \frac{1}{\gamma} F \left\{ cn \left[\frac{\alpha}{\kappa} (\hat{t}' + \tau_0 - \tau) , r \right] \right\}$$

Case 4: $\frac{3}{2}\tau < \hat{t}' + \tau_0 < 2\tau$, $3\pi < \hat{x}'_a + \hat{x}_0 - \hat{x}_{00} < 4\pi$

$$\cot\left[\frac{4\pi+\widehat{x}_{00}-\widehat{x}_a'-\widehat{x}_0}{2}\right] = \frac{1}{\gamma}\,\mathrm{F}\left\{cn\left[\frac{\alpha}{\kappa}\,(2\tau-\widehat{t}'-\tau_0)\,,\ \tau\right]\right\}$$

Below Outside Solution: $\widehat{y}_0 < 0$, $\widehat{y} < 0$

Case 1: $0 < \widehat{t}'+\tau_0 < \frac{1}{2}\tau$, $0 < \widehat{x}_b'+\widehat{x}_{00}-\widehat{x}_0 < \pi$

$$\cot\left[\frac{\widehat{x}_b'+\widehat{x}_{00}-\widehat{x}_0}{2}\right] = \frac{1}{\gamma}\,\mathrm{F}\left\{cn\left[\frac{\alpha}{\kappa}\,(\widehat{t}'+\tau_0)\,,\ \tau\right]\right\}$$

Case 2: $\frac{1}{2}\tau < \widehat{t}'+\tau_0 < \tau$, $\pi < \widehat{x}_b'+\widehat{x}_{00}-\widehat{x}_0 < 2\pi$

$$\cot\left[\frac{2\pi+\widehat{x}_0-\widehat{x}_b'-\widehat{x}_{00}}{2}\right] = \frac{1}{\gamma}\,\mathrm{F}\left\{cn\left[\frac{\alpha}{\kappa}\,(\tau-\widehat{t}'-\tau_0)\,,\ \tau\right]\right\}$$

Case 3: $\tau < \widehat{t}'+\tau_0 < \frac{3}{2}\tau$, $2\pi < \widehat{x}_b'+\widehat{x}_{00}-\widehat{x}_0 < 3\pi$

$$\cot\left[\frac{\widehat{x}_b'+\widehat{x}_{00}-\widehat{x}_0-2\pi}{2}\right] = \frac{1}{\gamma}\,\mathrm{F}\left\{cn\left[\frac{\alpha}{\kappa}\,(\widehat{t}'+\tau_0-\tau)\,,\ \tau\right]\right\}$$

Case 4: $\frac{3}{2}\tau < \widehat{t}'+\tau_0 < 2\tau$, $3\pi < \widehat{x}_b'+\widehat{x}_{00}-\widehat{x}_0 < 4\pi$

$$\cot\left[\frac{4\pi+\hat{x}_0-\hat{x}_b'-\hat{x}_{00}}{2}\right] = \frac{1}{\gamma}\,\mathrm{F}\left\{cn\left[\frac{\alpha}{\kappa}(2\tau-\hat{t}'-\tau_0)\,,\ \tau\right]\right\}$$

Auxiliary Formulas:

$$a = A\,e^{-\hat{\psi}}\,,\quad b = e^{-\hat{\psi}}\,,\quad \hat{\psi} = \ln(\cosh\hat{y}_0 + A\cos\hat{x}_0)$$

$$\hat{\psi} = \ln(1+A)\,,\ on\ cat's\ eye\ boundary$$
$$e^{\hat{\psi}} > 1+A\quad,\ outside\ boundary$$
$$e^{\hat{\psi}} < 1+A\quad,\ inside\ boundary$$

$$\alpha = \left[\frac{1-a+b}{1+a+b}\right]^{\frac{1}{2}},\quad \beta = \left[\frac{a+b-1}{1-b+1}\right]^{\frac{1}{2}},\quad \gamma = \left[\frac{1-a-b}{1+a-b}\right]^{\frac{1}{2}}$$

$$s = \frac{\alpha}{\sqrt{\alpha^2+\beta^2}}\,,\quad \tau = \frac{\sqrt{\alpha^2-\gamma^2}}{\alpha}$$

$$\kappa = 2\left[(1+a+b)(1+a-b)\right]^{-\frac{1}{2}}$$

$$T = \frac{4\kappa}{\sqrt{\alpha^2+\beta^2}}\,K(s)\,,\quad \tau = \frac{2\kappa}{\alpha}\,K(\tau)$$

$$N = INT\left[\frac{\hat{t}-\hat{t}_0}{T}\right],\quad M = INT\left[\frac{\hat{t}-\hat{t}_0}{\tau}\right]$$

$$\hat{t}' = \hat{t}-\hat{t}_0 - M\tau$$

$$\hat{x}_a' = \hat{x}-\hat{x}_0 - 2\pi M\ \ for\ \hat{y} > 0$$

$$\hat{x}_b' = \hat{x}_0-\hat{x} - 2\pi M\ \ for\ \hat{y} < 0$$

$$\cos x^* = \frac{1-b}{a}\,,\quad \hat{x}_{00} = 2\pi M_0$$

$$M_0 = \begin{cases} INT\left[\dfrac{\widehat{x}_0}{2\pi}\right] & ;\ \widehat{x}_0 > 0\,,\ \widehat{y}_0 > 0 \\[2ex] -1 + INT\left[\dfrac{\widehat{x}_0}{2\pi}\right] & ;\ \widehat{x}_0 < 0\,,\ \widehat{y}_0 > 0 \\[2ex] 1 + INT\left[\dfrac{\widehat{x}_0}{2\pi}\right] & ;\ \widehat{x}_0 > 0\,,\ \widehat{y}_0 < 0 \\[2ex] INT\left[\dfrac{\widehat{x}_0}{2\pi}\right] & ;\ \widehat{x}_0 < 0\,,\ \widehat{y}_0 < 0 \end{cases}$$

$$\mathbf{F}\big(\Theta\big) = \left[\frac{\Theta^2}{1 - \Theta^2}\right]^{\frac{1}{2}}$$

B.7. Numerical Solution and Interface Patterns

B.7.1. *Numerical Methods.* Equations (B.5)(B.6) and (B.7) can be solved directly numerically by Euler integration. The differential equations are approximated as difference equations for a small time step, Δt. Starting at t_0, the solution (ξ, η) is found at $t_0 + \Delta t$. Using this solution as initial conditions the solution at $t_0 + 2\Delta t$ is found and so on until the final time t is reached. This method will work, with no additional complication, for any velocity field even if exact integration is not possible. The disadvantage is that it is computationally very slow since high accuracy requires a small time step. A PDP 11/44 computer took as long as 5 hours to compute a typical interface of interest.

The exact solution of the previous section can be evaluated numerically as an alternative to Euler integration. The Jacobian elliptic functions are approximated by taking the first several terms of their Fourier series expansions. is The interface pattern computed in 5 hours by Euler integration takes only 6 minutes to compute when the exact solution is evaluated.

B.7.2. *Results of Numerical Evaluation of Exact Solution.* Results for the spatial interface problem introduced earlier will be presented first. Recall that the interface in this case is the same as the streakline that originates from a point (x_0, y_0). From the discussion in Section B.1, our interest is in the case when x_0 is the x coordinate of the splitter plate tip and y_0 is small and negative. For demonstration purposes, suppose $U_1 = 10\ cm/sec$, $U_2 = 5\ cm/sec$, and take the forced wavelength to be $\pi\ cm$. The interface pattern for A = 1.0 and $y_0 = -0.55\ cm$ is shown in Figure B.1a. The similarity between this computed interface and the observed interface for turbulent pre-mixing transition shear layers is quite remarkable; c.f., Figure 3.3. As expected, an origin below the splitter plate produces cores of pure high speed fluid. A cusp forms which rolls around the vortex center as it moves downstream. Inside the cat's eye

boundary, the interface forms a double spiral, the two spiral arms terminating at the cusp. A second cusp forms along the low speed edge. This cusp occurs in the outside flow, using the terminology of the previous sections. The formation of these cusps can be understood by looking at the temporal roll-up for a moment. The streamlines, which are fixed for all time, are shown in Figure B.2 along with the initial interface. Point (a) moves around on its streamline while points (b) and (c) move on their streamline. The period for (a) to orbit the vortex center is less than that for points (b) and (c) because (a) is closer to the vortex. Point (a), being at the mid-point between vortex centers, will orbit in a shorter time than any other point, between (d) and (e), on the interface and thus will be the cusp point. In the outside flow, point (f) takes less time to move from one vortex to another than any other between (d) and (g). Point (f) is, therefore, the cusp point in the outside flow. These cusps are observed in the real flow, Figure 3.3.

Figure B.1 demonstrates the effect of vorticity concentration on the interface pattern. Figure B.1a is the solution for $A=1.0$, the potential flow solution, while Figures B.1b, B.1c, B.1d are the solutions for smaller values of A and hence, for less concentrated vortices. The release point is fixed for all four figures at $y_0 = -0.55 \ cm$. Recall that the streamline pattern does not change significantly with A. The width of the cat's eye at its widest point decreases with decreasing A. If we take

$$\psi(x,y) = \ln(\cosh y + A \cos x) \qquad (B.72)$$

then the width of the cat's eye divided by the spacing of the vortices is

$$\frac{w}{2\pi} = \frac{1}{\pi} \ln\left[(1+2A) + \sqrt{(1+2A)^2-1)}\right].$$ (B.73)

This function is given in the table below for various values of A.

TABLE B.1

A	1.0	0.8	0.6	0.4	0.2	0.0
$\frac{w}{2\pi}$	0.6807	0.5123	0.4537	0.3797	0.2480	0.0

The width decreases monotonically with decreasing A. This effect is visible in Figure B.1 by comparing the width of the last vortex on the right in Figures B.1a, B.1b, and B.1c. In Figure B.1d the cat's eyes are so narrow that the $y_0 = -0.55$ release point places the interface entirely in the outside flow. The conclusion from Figure B.1 is that A does not effect the qualitative properties of the interface. As long as part of the interface falls inside the cat's eye boundary, the cusp and spiral arms will form. Qualitatively speaking then, there is no difference between a concentrated point vortex and a vortex with non-zero core size as far as the shape of the interface is concerned.

The effect of release point for fixed vorticity concentration is demonstrated in Figure B.3. When the release point is near the x-axis, as in Figure B.3a, most of the interface is inside the cat's eye so the spiral arms are longer and wrap around the vortex center more times than would be the case for y_0 further from the x-axis. Notice also how the cusp in the outside flow changes with y_0. In Figure B.1a it is much sharper than in B.1d. The time for the cusp to form, however, is not a strong function of release point.

B.7.3. *Numerical Solution by Euler Integration.* The lack of qualitative

changes in the interface pattern with vorticity concentration in the foregoing discussion suggests that it is sufficient to limit further consideration to point vortices where the analysis is simplified by complex variable theory. In fact, this simplification allows an extension of the model to include effects of a vortex pairing on the interface. Jimenez (1980) presented an exact solution for orbiting rows of point vortices which will be used to model the pairing process. This solution is briefly reviewed in what follows.

The complex potential for two infinite rows of point vortices with spacing l is

$$w(z) = \frac{i\gamma_1}{2\pi} \ln \sin \frac{\pi}{l}(z - z_1) + \frac{i\gamma_2}{2\pi} \ln \sin \frac{\pi}{l}(z - z_2). \qquad \text{(B.74)}$$

z_1 and z_2 label the position of the two rows while γ_1 and γ_2 are the strengths of the vortices in row 1 and row 2 respectively. z_1 and z_2 are functions of time determined by the condition that each vortex moves with the induced velocity of all others. This implies

$$\frac{dz_1}{dt} = \frac{i\gamma_2}{2l} \cot \frac{\pi}{l}(z_1 - z_2) \qquad \text{(B.75)}$$

$$\frac{dz_2}{dt} = \frac{i\gamma_1}{2l} \cot \frac{\pi}{l}(z_2 - z_1) . \qquad \text{(B.76)}$$

If we let

$$\zeta = z_1 - z_2 \qquad \text{(B.77)}$$

$$\gamma = \gamma_1 + \gamma_2 \qquad \text{(B.78)}$$

Then

$$\frac{d\zeta}{dt} = \frac{i\gamma}{2l} \cot \frac{\pi \zeta}{l} . \tag{B.79}$$

Separating (B.79) into real and imaginary parts will produce a system of equations very similar to equations (B.18)(B.19)(B.20) of Section B.3. Without loss in generality, choose $l = \frac{\pi}{2}$ and $\gamma = \frac{\pi}{2}$ and let $\zeta = \xi + i\eta$. Assuming $\gamma_1 = \gamma_2$, some manipulation leads to the following system of equations.

$$\frac{dx}{dt} = \frac{1}{2} \frac{\sinh (y - \eta)}{\cosh (y - \eta) - \cos (x - \xi)} + \frac{1}{2} \frac{\sinh (y + \eta)}{\cosh (y + \eta) - \cos (x + \xi)} \tag{B.80}$$

$$\frac{dy}{dt} = -\frac{1}{2} \frac{\sin (x - \xi)}{\cosh (y - \eta) - \cos (x - \xi)} - \frac{1}{2} \frac{\sin (x + \xi)}{\cosh (y + \eta) - \cos (x + \xi)} \tag{B.81}$$

$$\frac{d\xi}{dt} = \frac{1}{2} \frac{\sinh 2\eta}{\cosh 2\eta - \cos 2\xi} \tag{B.82}$$

$$\frac{d\eta}{dt} = -\frac{1}{2} \frac{\sin 2\xi}{\cosh 2\eta - \cos 2\xi} \tag{B.83}$$

with initial conditions

$$y(0) = x_0, \ y(0) = y_0, \ \xi(0) = \xi_0, \ \eta(0) = 0 . \tag{B.84}$$

Physically the system (B.80) through (B.84) represents the following problem. Start with an infinite row of point vortices with spacing π and strength $\frac{\pi}{2}$. At t = 0, select pairs and displace them from their equilibrium location toward each other by an amount ξ_0. The vortices will move since they are no longer at their

equilibrium location. The developing interface is described by the system (B.80) through (B.84) with (ξ,η) reflecting the vortex locations and (x,y) the interface location. The system of equations is easily solved by Euler integration.

As a check, $\xi_0 = 0$ should produce the same interface pattern as was seen earlier since no displacement initially will leave the vortices at their equilibrium positions for all time. Figure B.4 shows the developing temporal interface for such a case. The cusp and spiral arm behavior discussed earlier is apparent and the result checks with the $\xi_0 = 0$ limit.

Jimenez (1980) describes the interface we speak of as being like a rubber band that is attached to fluid particles at time equals zero and forced to stretch or compress as dictated by the prescribed fluid motion. Even for steady flow the rubber band shape will continuously change with time. It is interesting to see how much the rubber band gets stretched and where it gets stretched the most. The impression one gets from Figure B.4 is that a great deal of stretching takes place. Strain is an important consideration if this model is taken a step further by treating the interface as a strained diffusion flame. Such an extension would allow computation of the product of a chemical reaction between two species separated by the interface. This problem is not solved in this work. However, the strain on the interface is computationally simple to find. Consider two points on the interface; points (a) and (b) in Figure B.2 for example. Let the distance between (a) and (b) be L at $t = 0$. At some later time, (a) and (b) will be some other distance apart, say L_1. The strain is the new length divided by the original length. Now consider many points all with the same L. At a later time the spacing between the initially equidistant points is proportional to the local strain. This strain is displayed in Figure B.5 for the interface roll-up in Figure B.4.

The data in Figure B.5 are computed starting with 300 equally spaced points extending over four wavelengths. This means the points are 0.04189 apart at $t = 0$. Each plot in Figure B.5 shows the spacing between points as a function of point number for a certain elapse time. Figure B.5a, at the upper left, is the first time step shown and time increases to the right and downward. Note the frequent rescaling of the plots. Figure B.5a shows that at first there are almost equal amounts of stretching and compressing. The minimum in the strain corresponds to the cusp point inside the cat's eye. As time transpires (i.e., moving from plot to plot in Figure B.5) you see that a net stretching begins to occur. Two local maxima occur corresponding to locations on the two spiral arms on opposite sides of the inside cusp point. The apparent "turbulence" in these plots is most likely due to the numerics since nothing in the flow could cause this kind of randomness. The true strain would probably look like a smoothed out version of the curves in Figure B.5.

At some definite time, a change in the strain takes place. In Figure B.5g (third row, first column) a peak is observed at the extreme left. Subsequent frames show this peak increases rapidly until, for the last plot, it dominates all others. This strain maximum occurs at the point where the interface intersects the cat's eye boundary; point (d) in Figure B.2. Consider two points very near point (d); one inside the cat's eye and one outside. Point (d) moves toward the stagnation point with time and eventually ends up at the stagnation point in infinite time. The point inside the boundary also moves toward the stagnation point at first but will make a sharp turn to the right at some time. Similarly, the point outside the boundary will move toward the stagnation point at first turning sharply to the left at some later time. Thus, the two points which were initially very close together remain close to each other for a while and then separate by large distances at a time associated with point (d) approaching the stagnation point. The outside point will leap-frog from vortex-to-vortex to the

left while the inside point will orbit around the vortex above point (a) in Figure B.2. For infinite time, the points will become infinitely far apart. Jimenez (1980) refers to this process as a production of interface at the stagnation points. In his solutions, $y_0 = 0$, so the stretching occurs instantly. In our model, $y_0 < 0$ and it takes a finite amount of time for the strong stretching to occur.

B.7.4. *Results for the Case of Pairing Rows.* Consider the system (B.80) through (B.84) when the vortices are displaced initially from their equilibrium position; i.e., $\xi_0 \neq 0$. The developing temporal interface is shown in Figure B.6. Once again, the interface pattern looks very much like the pictures of the actual flow; c.f., pairing vortices at the downstream end of Figure 3.3. The cusp behavior, outlined earlier for $\xi_0 = 0$, is similar for the pairing vortices. A cusp forms in the inside flow for both vortices involved in the pairing as do the spiral arm pairs. The outside flow, below the vortices, develops cusps also with the right vortex possessing a more pronounced one than the left vortex. Something new shows up in the last two frames of Figure B.6. A cusp forms on the other side of the vortex which started on the left. For the steady row, $\xi_0 = 0$, this can never occur. In that problem, the portion of the initially straight interface that is outside the cat's eye is either entirely above or entirely below. In other words, the outside problem was separable into two problems; an above problem and a below problem. Once a particle started above, it remained above and likewise for the below problem. When the flow is unsteady, such as for $\xi_0 \neq 0$, this is not the case. Figure B.6 is an example of the effect of unsteady flow. The interface, outside the instantaneous cat's eye at $t = 0$, is entirely below. The new cusp, seen in the last two frames, suggests that part of the interface has crossed the boundary to become part of the above flow since that is the only place such a cusp could form.

B.8. Summary

The roll-up of a passive interface by rows of point vortices has been studied for the case when the interface initially starts below the vortex centers. Many features of the real, forced, pre-mixing transition shear layer, shown in Figure 3.3, appear in the solutions. Moreover, these features exist only for the off-axis interface and not for the symmetric case of Jimenez (1980).

Cores of pure high speed fluid were found as were the cusp and spiral arm features evident in Figure 3.3. In addition, cusp development in the braids also occured which matched well with the picture. Study of the strain on the interface showed that it took a finite length of time for the large strain associated with the stagnation point flow to exert an influence on the interface. In Jimenez's solution, the influence was instantaneous because the interface intersected the stagnation point at $t = 0$. Study of orbiting rows of point vortices showed interface patterns similar to those observed for pairing vortices in the real shear layer. Specifically, a cusp forms on the high-speed-side like those visible in Figure 3.3.

REFERENCES

BERNAL, L. P. (1981) *The Coherent Structure of Turbulent Mixing Layers. I. Similarity of the Primary Vortex Structure, II. Secondary Streamwise Vortex Structure* , Ph.D. Thesis, California Institute of Technology.

BREIDENTHAL, R. E. (1980) *Response of Plane Shear Layers and Wakes to Strong Three-Dimensional Disturbances* , *Physics of Fluids 23 (10)* , 1929-1934.

BREIDENTHAL, R. E. (1978) *A Chemically Reacting Turbulent Shear Layer* , Ph.D. Thesis, California Institute of Technology. Also *J. Fluid Mech. 109* , (1981), 1-24.

BROADWELL, J. E. and BREIDENTHAL, R. E. (1981) "A Simple Model of Mixing and Chemical Reaction in a Turbulent Shear Layer", GALCIT Report FM 81-10, California Institute of Technology. Also *J. Fluid Mech. 125* , (1982), 397-410.

BROWAND, F. E. and HO, C.-M. (1983) "The Mixing Layer: An Example of Quasi Two-dimensional Turbulence", *Journal de Mecanique theorique et appliquee Numero special* , 99-120.

BROWN, G. L. and ROSHKO, A. (1971) "The Effect of Density Difference on the Turbulent Mixing Layer", *Turbulent Shear Flows* , AGARD-CP-93, Paper No. 23, 23-1-23-12.

BROWN, G. L. and ROSHKO, A. (1974) "On Density Effects and Large Structure in Turbulent Mixing Layer", *J. Fluid Mech. 64(4)*, 775-816.

BYRD, P. F. and FRIEDMAN, M. D. (1971) *Handbook of Elliptic Integrals for Engineers and Scientists*, Second Edition, Springer-Verlag.

CANTWELL, B. J. (1981) "Transition in the Axisymmetric Jet", *J. Fluid Mech. 104*, 369-386.

CIMBALA, J. M. (1984) *Large Structure in the Far Wakes of Two-Dimensional Bluff Bodies*, Ph.D. Thesis, California Institute of Technology.

CIMBALA, J., NAGIB, H. and ROSHKO, A. (1981) "Wake Instability Leading to New Large Scale Structures Downstream of Bluff Bodies", *Bull. Am. Phys. Soc. 26(9)*, 1256.

DIMOTAKIS, P. E. (1983) "Entrainment into a Fully Developed, Two-dimensional Shear Layer", GALCIT Internal Report, California Institute of Technology. Also AIAA Paper No. 84-0368.

DIMOTAKIS, P. E., MIAKE-LYE, R. C., and PAPANTONIOU, D. A. (1982) *Structure and Dynamics of Round Turbulent Jets*, invited lecture XV International Symposium of Fluid Mechanics, Jachranka Poland, 7-12, September 1981. Also in *Phys. Fluids 26 (11)*, (1983) 3185-3192.

FREYMUTH, P. (1966) "On Transition in a Separated Laminar Boundary Layer", *J. Fluid Mech. 25(4)*, 683-704.

HO, C.-M. and HUANG, L.-S. (1982) "Subharmonics and Vortex Merging in Mixing Layers", *J. Fluid Mech. 119* , 443-473.

HO, C.-M. and HUERRE, P. (1984) "Perturbed Free Shear Layers", *Ann. Rev. Fluid Mech.* , 365-424.

JIMENEZ, J. (1980) "On the Visual Growth of a Turbulent Mixing Layer", *J. Fluid Mech. 96* , 447-460.

KOOCHESFAHANI, M. M. (1984) *Experiments on Turbulent Mixing and Chemical Reactions in a Liquid Mixing Layer* , Ph.D. Thesis, California Institute of Technology.

KOOCHESFAHANI, M. M., DIMOTAKIS, P. E. and BROADWELL, J. E. (1983) "Chemically Reacting Shear Layers", AIAA Paper No. 83-0475.

KONRAD, J. H. (1976) *An Experimental Investigation of Mixing in Two-dimensional Turbulent Shear Flows with Applications to Diffusion-Limited Chemical Reactions* , Ph.D. Thesis, California Institute of Technology, and Project SQUID Technical Report CIT-8-PU, December 1976.

LOEHRKE, R. I. and NAGIB, H. M. (1976) "Control of Free-Stream Turbulence by Means of Honeycombs: A Balance between Suppression and Generation", *J. of Fluids Eng. 98(3)* , 342.

MATSUI, T. and OKUDE, M. (1980) "Rearrangement of Karman Vortex Street at Low Reynolds Numbers", XVth International Congress of Theoretical

and Applied Mechanics, Univ. of Toronto, August, 1-27.

MICHALKE, A. (1964) "On the Inviscid Instability of the Hyperbolic Tangent Velocity Profile", *J. Fluid Mech. 19* , 543-556.

MUNGAL, M. G. (1983) *Experiments on Mixing and Combustion with Low Heat Release in a Turbulent Shear Flow* , Ph.D. Thesis, California Institute of Technology.

NOSENCHUCK, D. M. (1982) *Passive and Active Control of Boundary Layer Transition* , Ph.D. Thesis, California Institute of Technology.

OSTER, D. and WYGNANSKI, I. (1982) "The Forced Mixing Layer between Parallel Streams", *J. Fluid Mech. 123* , 91-130.

ROBINSON, A. C. and SAFFMAN, P. G. (1982) "Three-Dimensional Stability of Vortex Arrays", *J. Fluid Mech. 125* , 411-427.

ROSHKO, A. (1954) "On the Development of Turbulent Wakes from Vortex Streets", NACA Report 1191.

SATO, H. and KURIKI, K. (1961) "The Mechanism of Transition in the Wake of a Thin Flat Plate Placed Parallel to a Uniform Flow", *J. Fluid Mech. 11 (3)* , 321-352.

STUART, J. T. (1967) "On Finite Amplitude Oscillations in Laminar Mixing Layers", *J. Fluid Mech. 29* , 417-440.

TANEDA, S. (1959) "Downstream Development of Wakes Behind Cylinders", *J. Phys. Soc. Japan, 14 (6)* , 843-848.

WINANT, C. D. and BROWAND. F. K. (1974) "Vortex Pairing: The Mechanism of Turbulent Mixing Layer Growth at Moderate Reynolds Number", *J. Fluid Mech. 63* , 237-255.

WYGNANSKI, I. and OSTER, D. (1980) "The Mixing Layer Between Two Parallel Streams: A Test Case for the Importance of Initial Conditions", Tel-Aviv University. Also reported in *J. Fluid Mech. 93* , (1979), 325-335 and *J. Fluid Mech. 123* , (1982), 91-130.
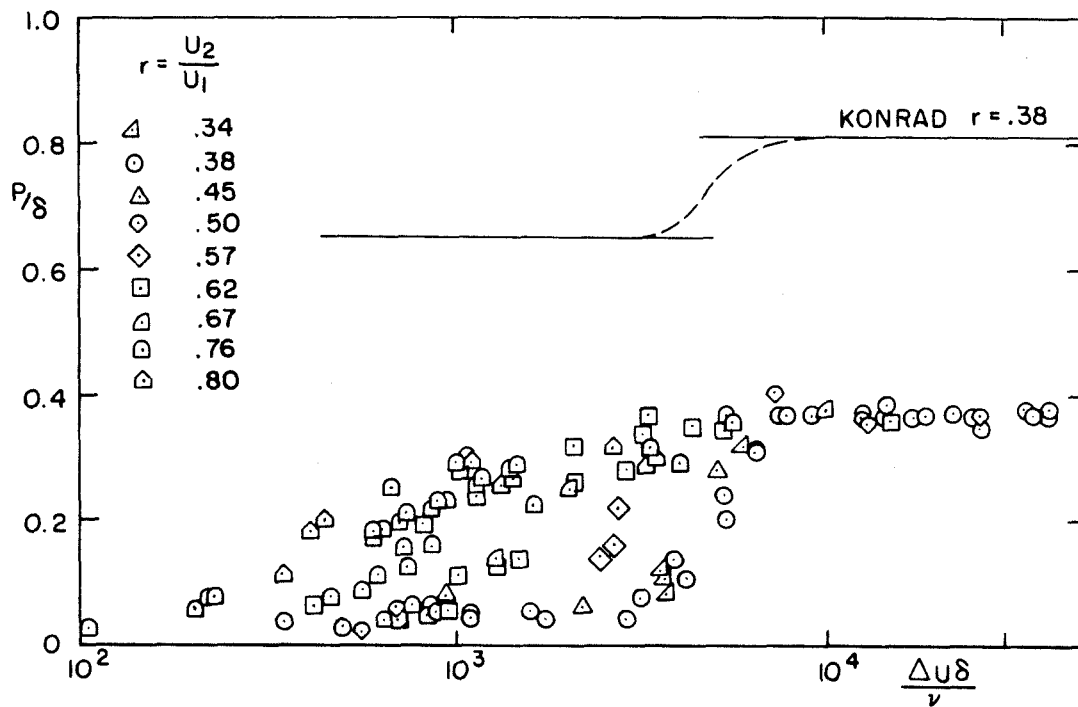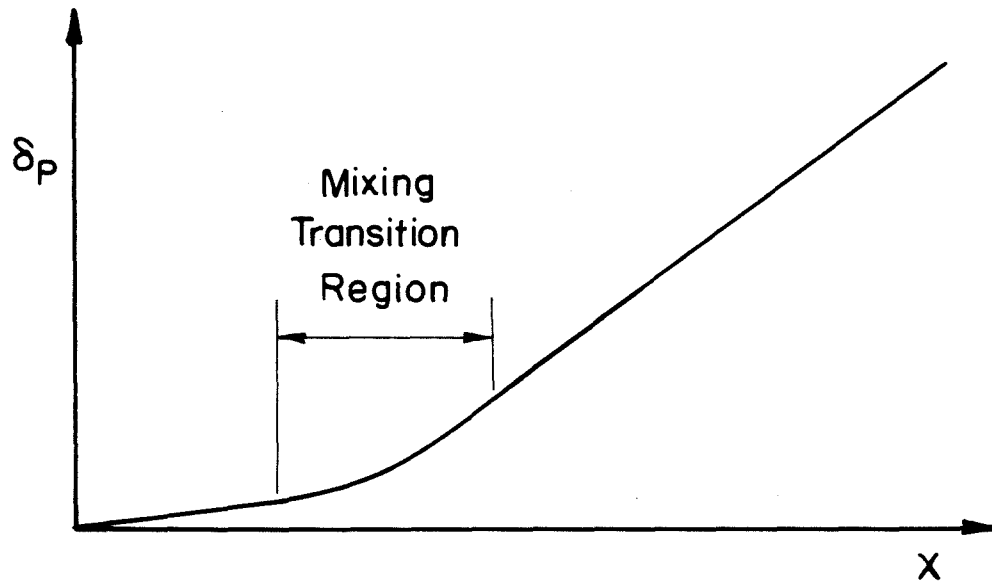
Figure 1.1 : Breidenthal's Product Measurements (unforced flow)
P = Product Thickness , δ = Vorticity Thickness
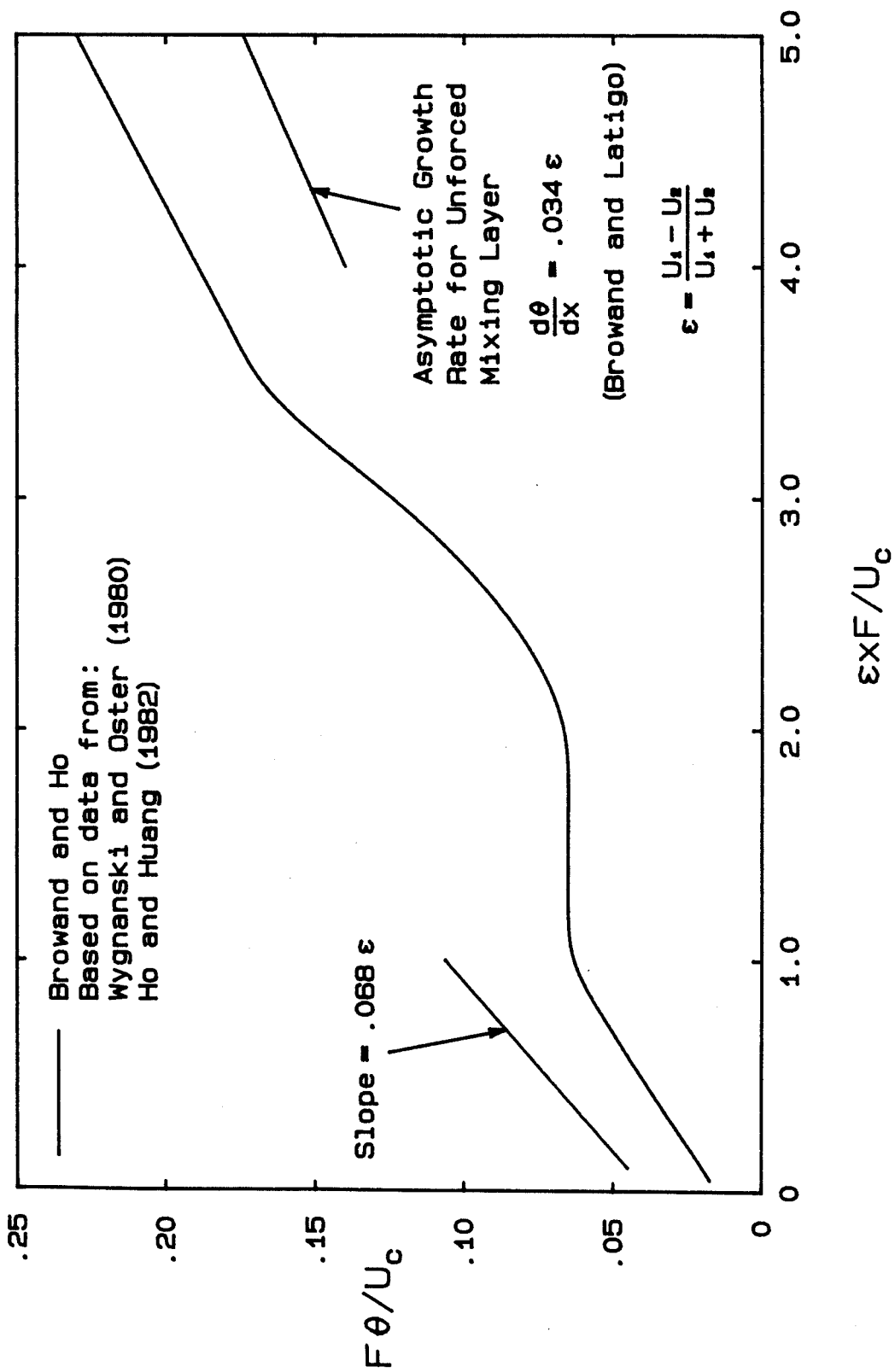
Figure 1.2: Growth Law for the Forced Shear Layer (from Browand)
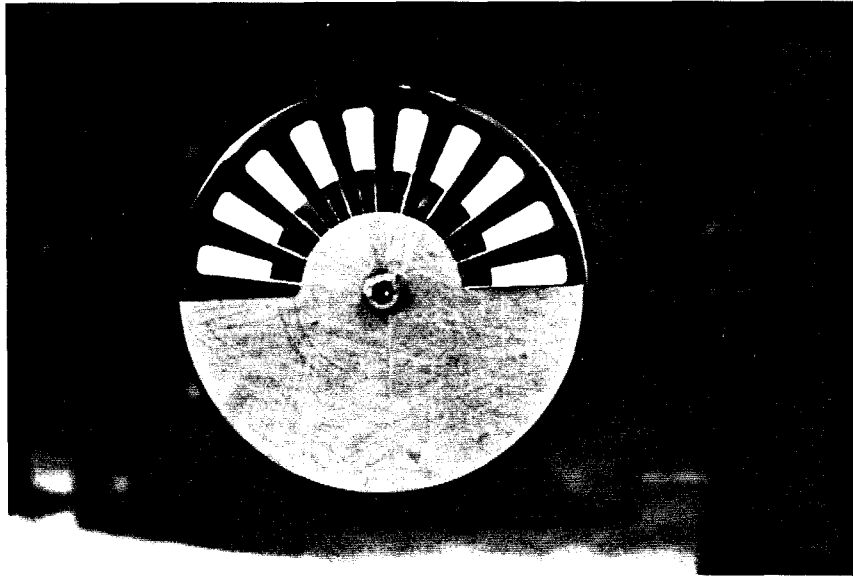
(a) Valve in Maximum Open Position
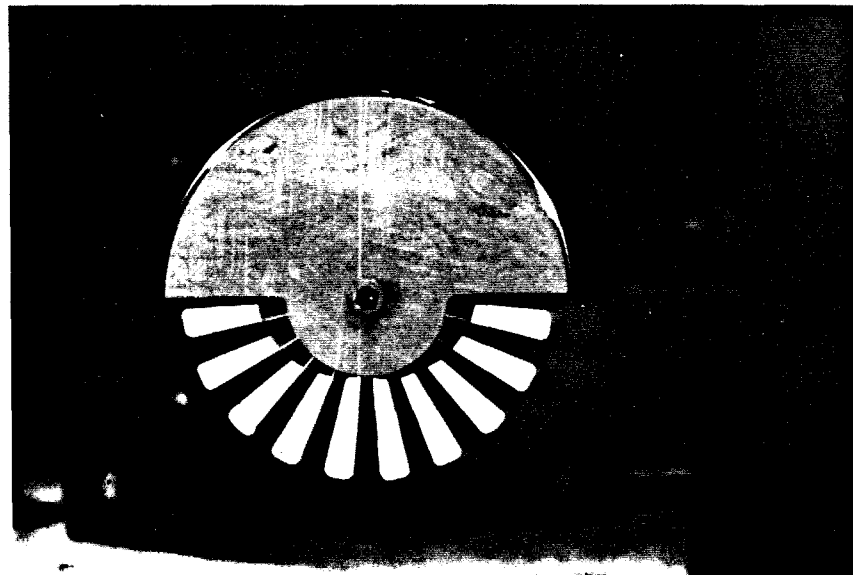
(b) Valve in Minimum Open Position

Figure 2.1 : Forcing Meachanism Rotor and Stator
(a) Maximum Open Area
(b) Minimum Open Area
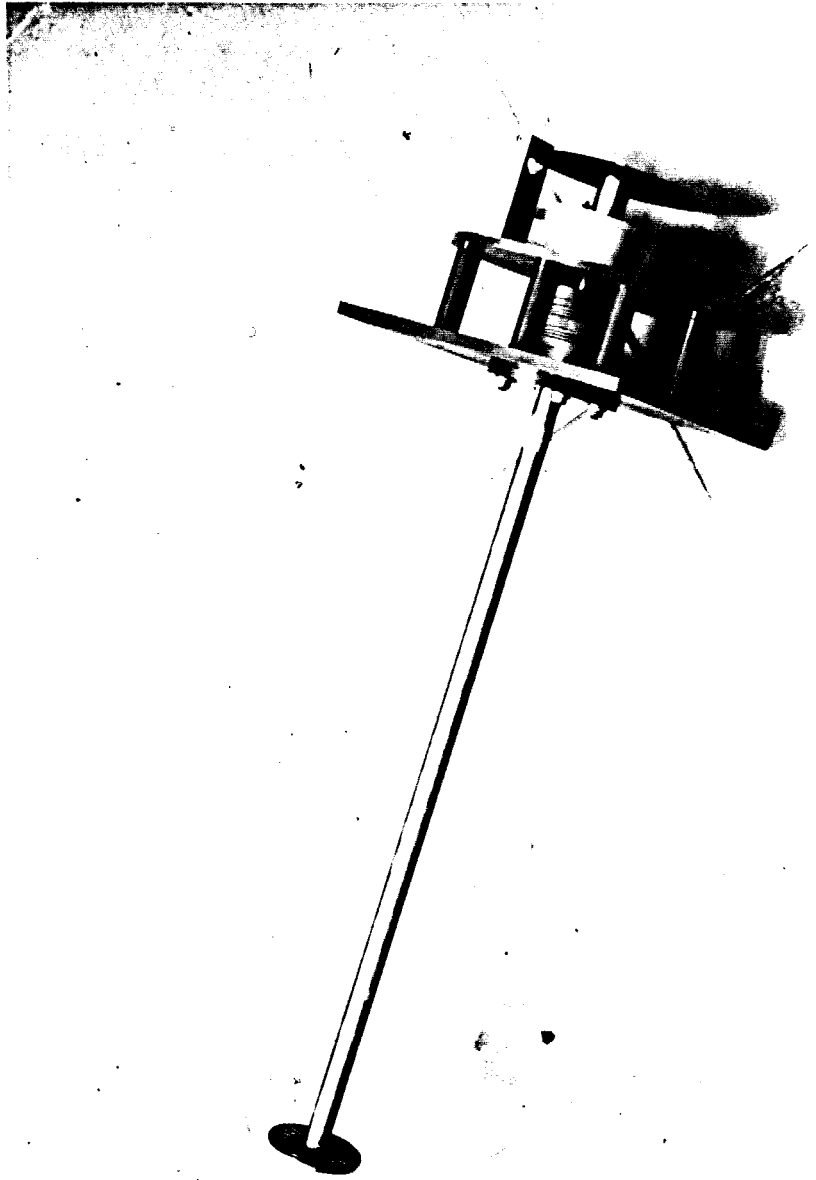
Figure 2.2: Complete Forcing Mechanism
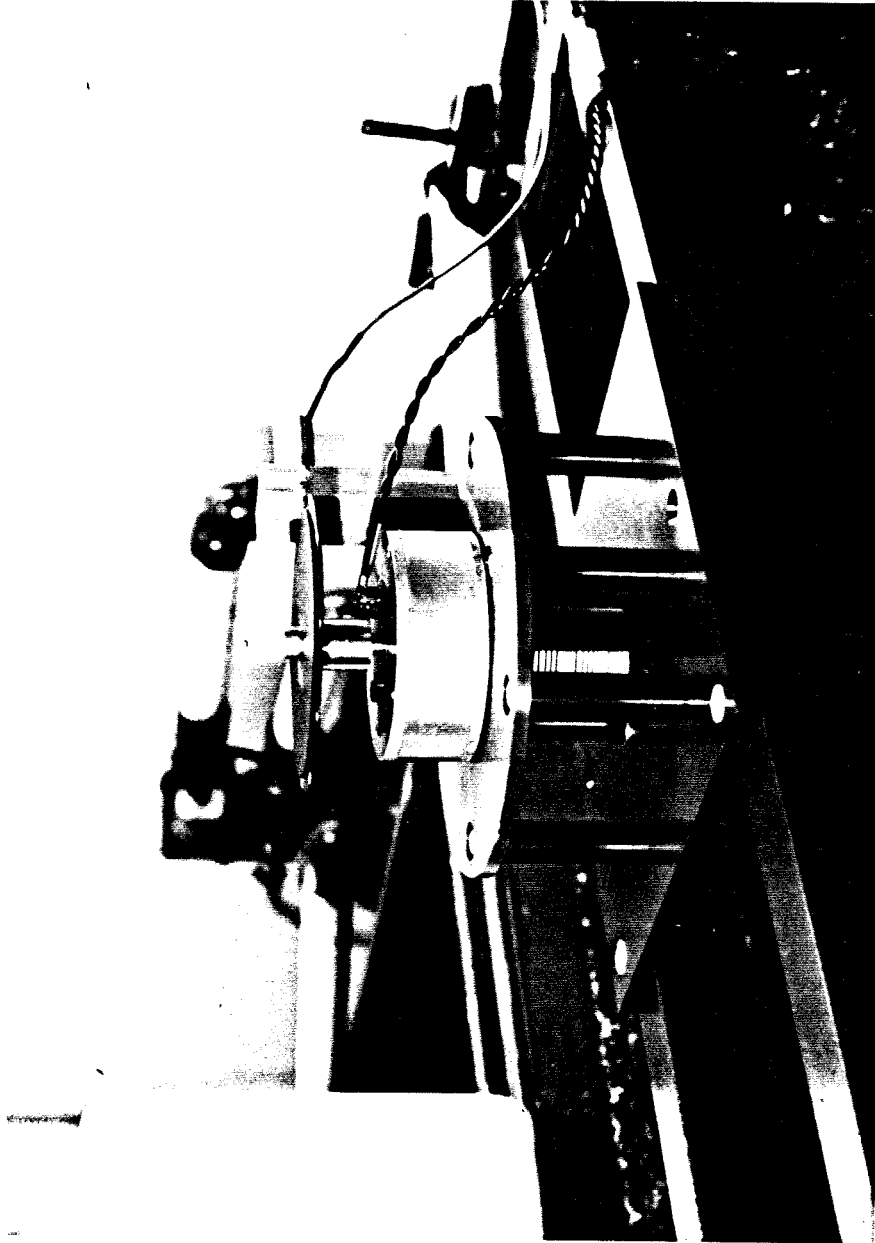
Figure 2.3: Installed Forcing Mechanism
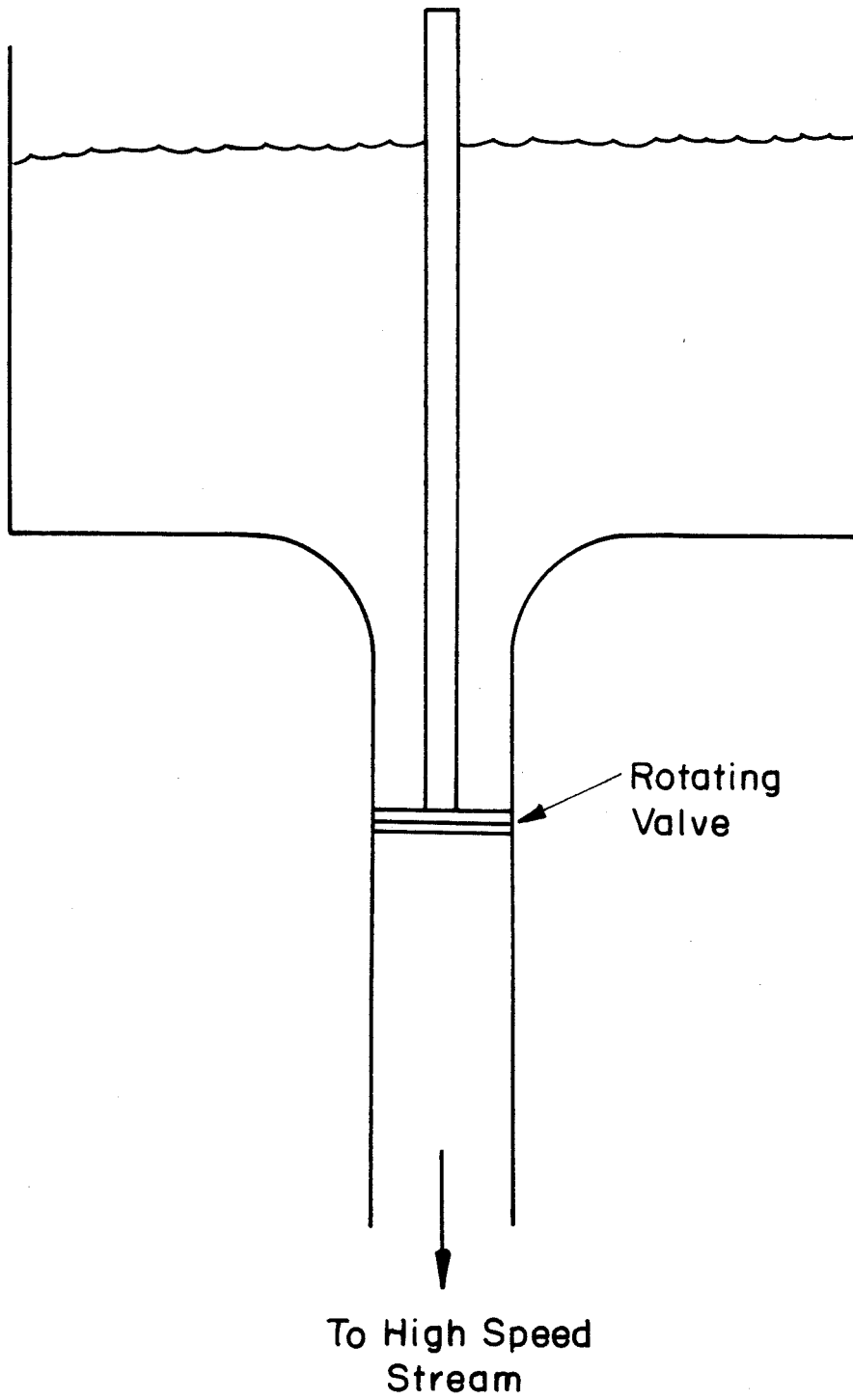
Figure 2.4 : Schematic of Forcing Mechanism
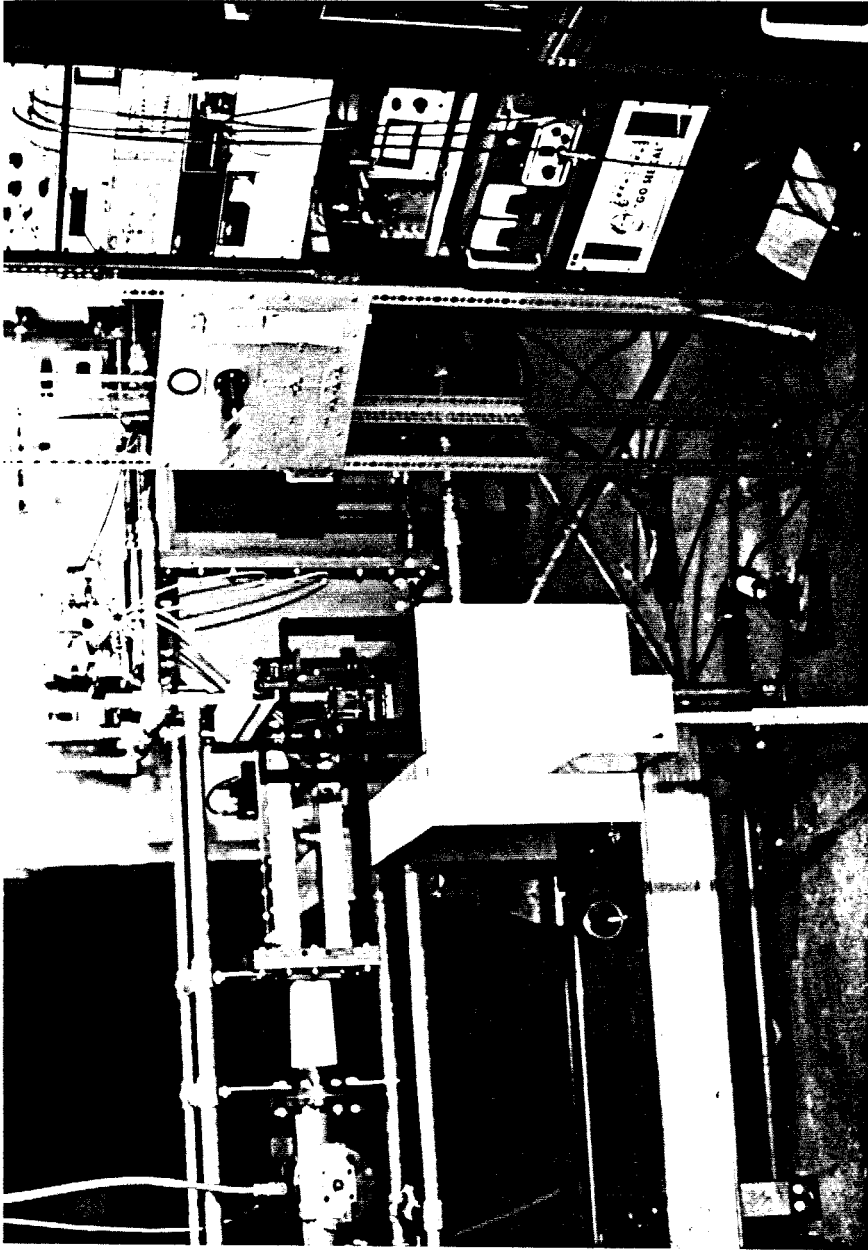
Figure 2.5: Photograph of the Laboratory

(a) $U_1 = 2.0$ cm/sec , $U_2 = 1.0$ cm/sec , $Re_{\theta_1} = 31$

(b) $U_1 = 14.8$ cm/sec , $U_2 = 8.6$ cm/sec , $Re_{\theta_1} = 86$

(c) $U_1 = 56.1$ cm/sec , $U_2 = 21.9$ cm/sec , $Re_{\theta_1} = 170$
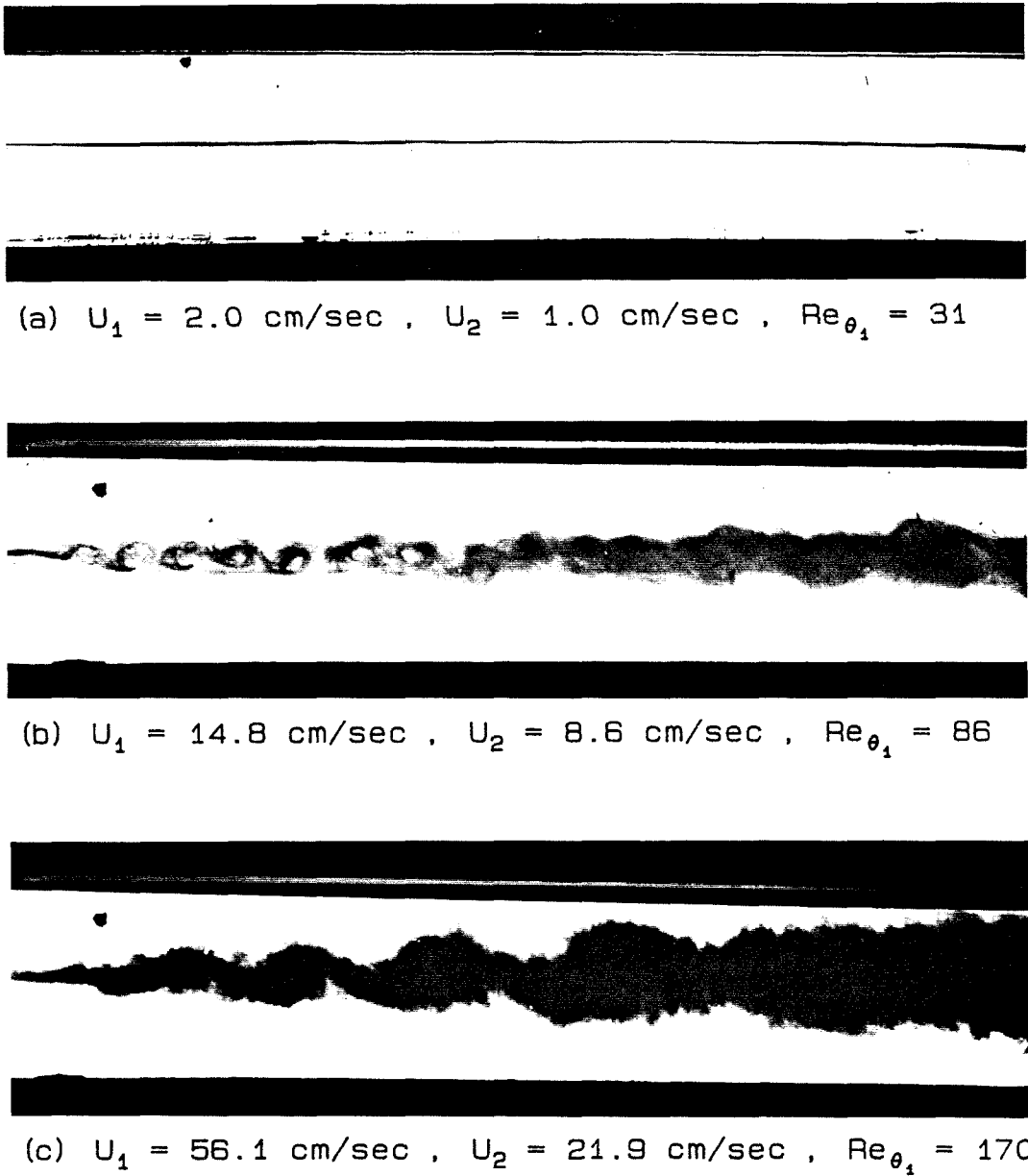
Figure 3.1 : Three Flow Regimes of the Unforced Shear Layer
(a) Laminar , (b) Transitional , (c) Turbulent
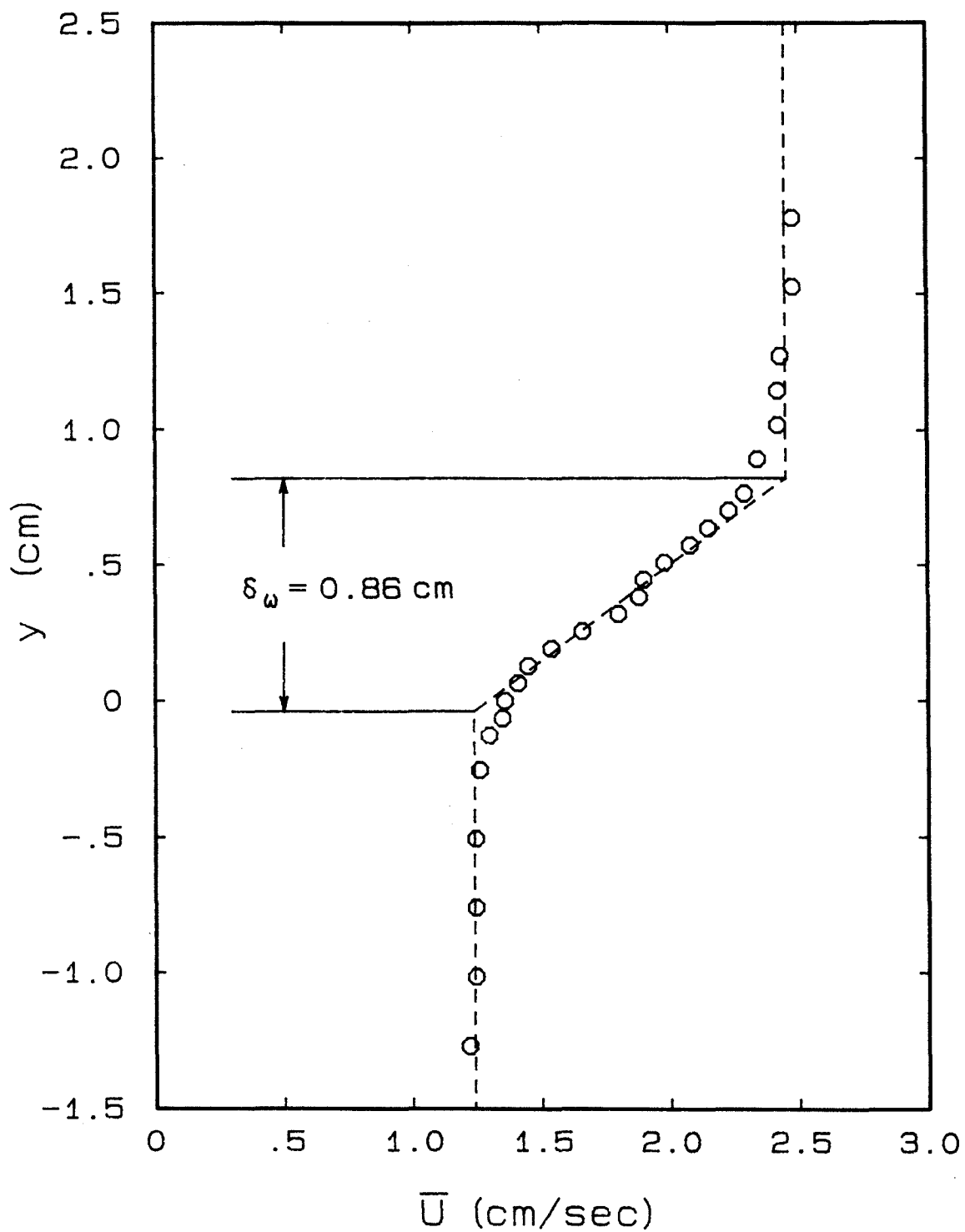
Figure 3.2 : Mean Velocity Profile in the Laminar
Shear Layer at x = 20 cm.
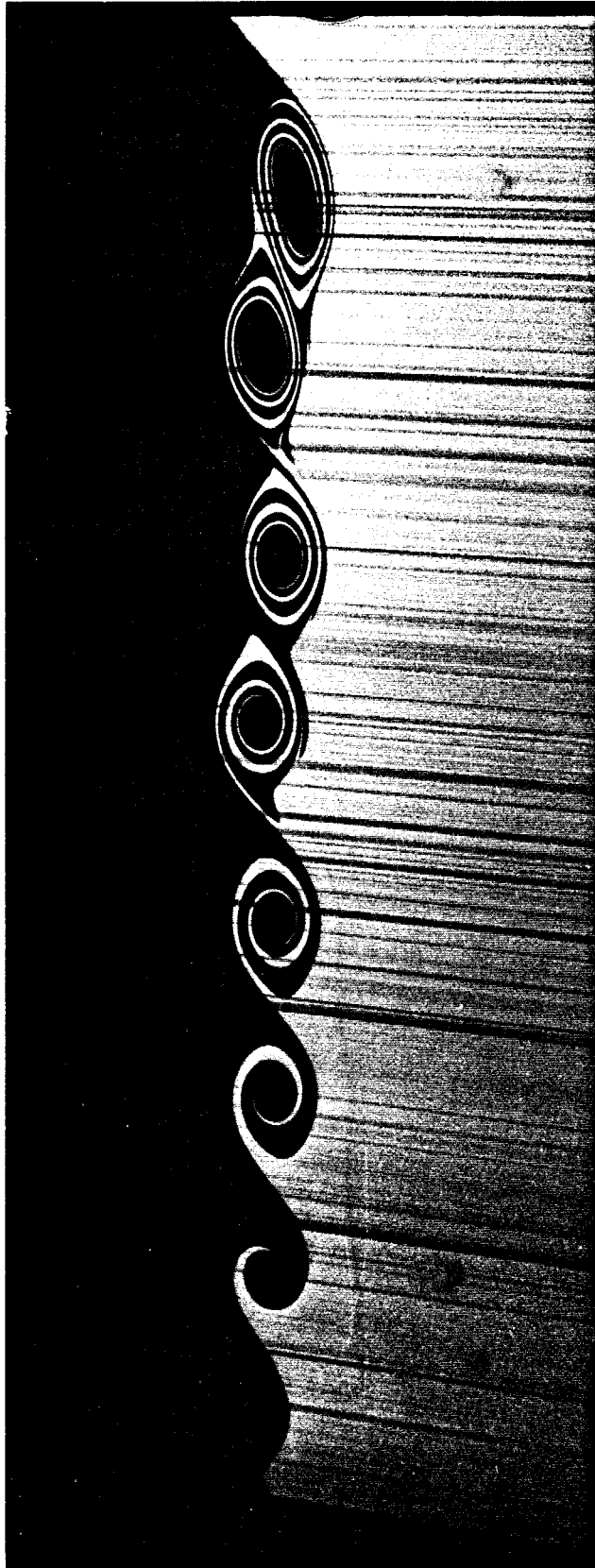
Figure 3.3: Non-reacting L.I.F. Photograph of a Forced Transitional Shear Layer, $U_1 \approx 8$ cm/sec, $U_2 \approx 5$ cm/sec

(a) forced at natural frequency

(b) forced pairing

(c) forced tripling

(d) forced quadrupling

Figure 3.4 : Controlled Amalgamation by Subharmonic Excitation
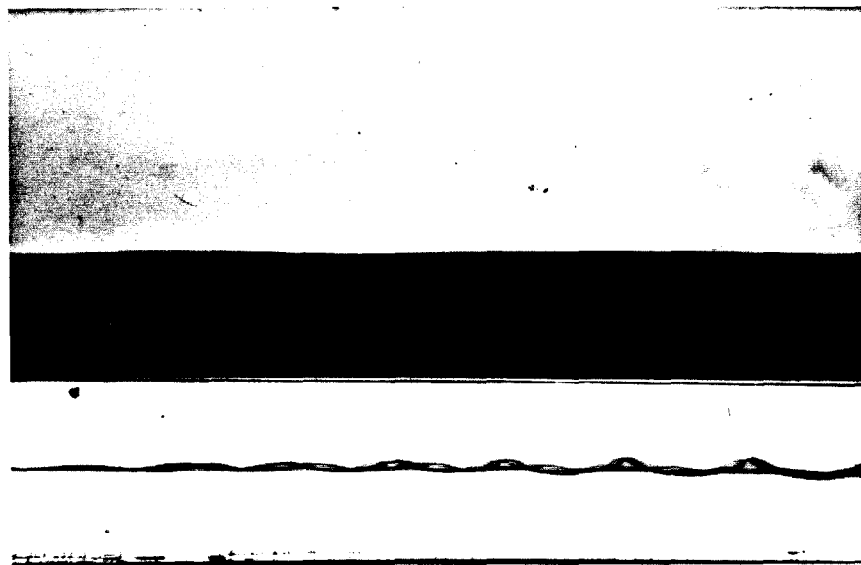
(a) Plan and Side Views
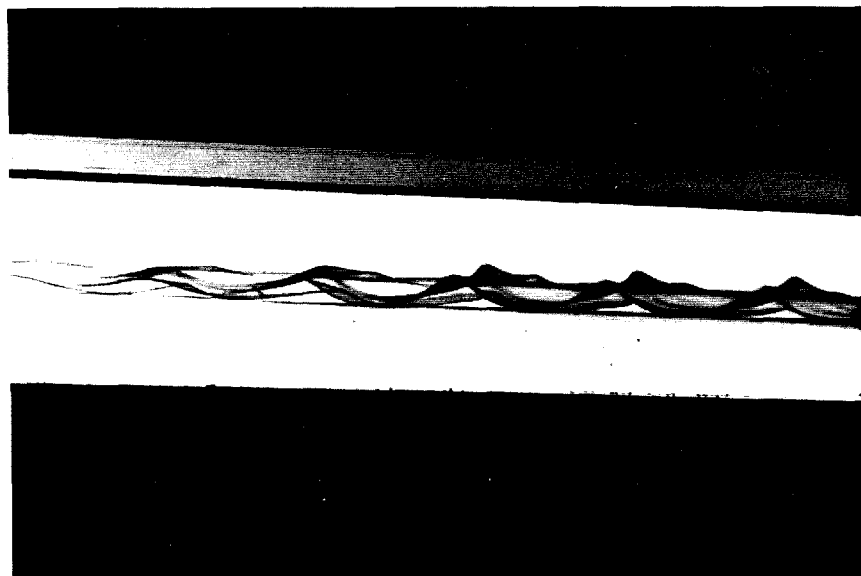
(b) Oblique View

Figure 3.5 : Effects of F = 0.5 Hz forcing on a Laminar Shear Layer
U_1=2 cm/sec , U_2=1 cm/sec , (a) Simultaneous Plan and
Side Views (b) Oblique View looking down and upstream

(a) unforced flow
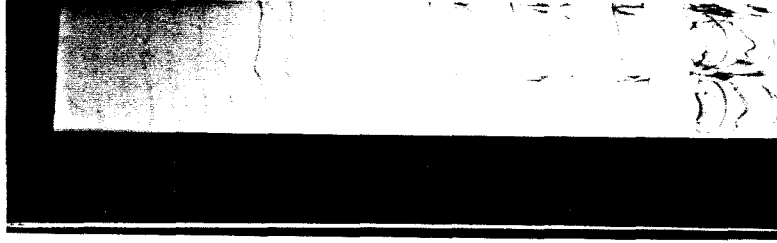
(b) F = 3.8 Hz
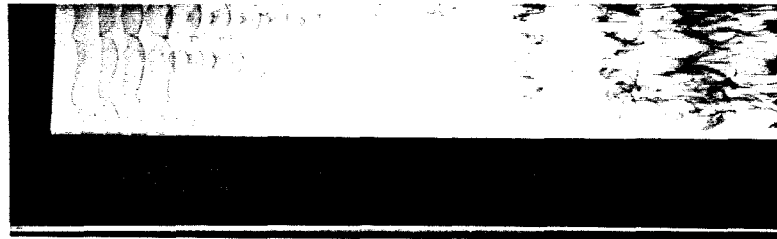
(c) F = 2.9 Hz

(d) F = 2.4 Hz

Figure 3.6 : Effects of Forcing on Shear Layer Structure for
U_1 = 11.6 cm/sec and U_2 = 5.8 cm/sec (part 1)

(e) F = 2.2 Hz
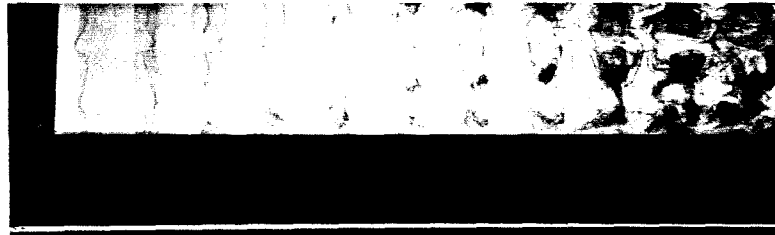
(f) F = 1.4 Hz
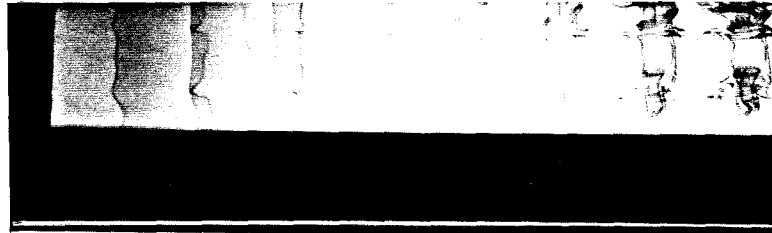
(g) F = 1.1 Hz
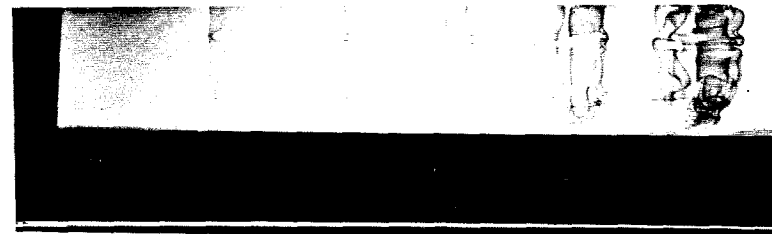
$r = 0.51, \quad \theta_1 = 0.66 \text{ mm}, \quad F_m = 4.7 \text{ Hz}, \quad \dfrac{U_1 \theta_1}{\nu} = 76, \quad \dfrac{\Delta U}{\nu} = 570 \text{ cm}^{-1}$

Figure 3.6 : Effects of Forcing on Shear Layer Structure for
$U_1 = 11.6$ cm/sec and $U_2 = 5.9$ cm/sec (part 2)
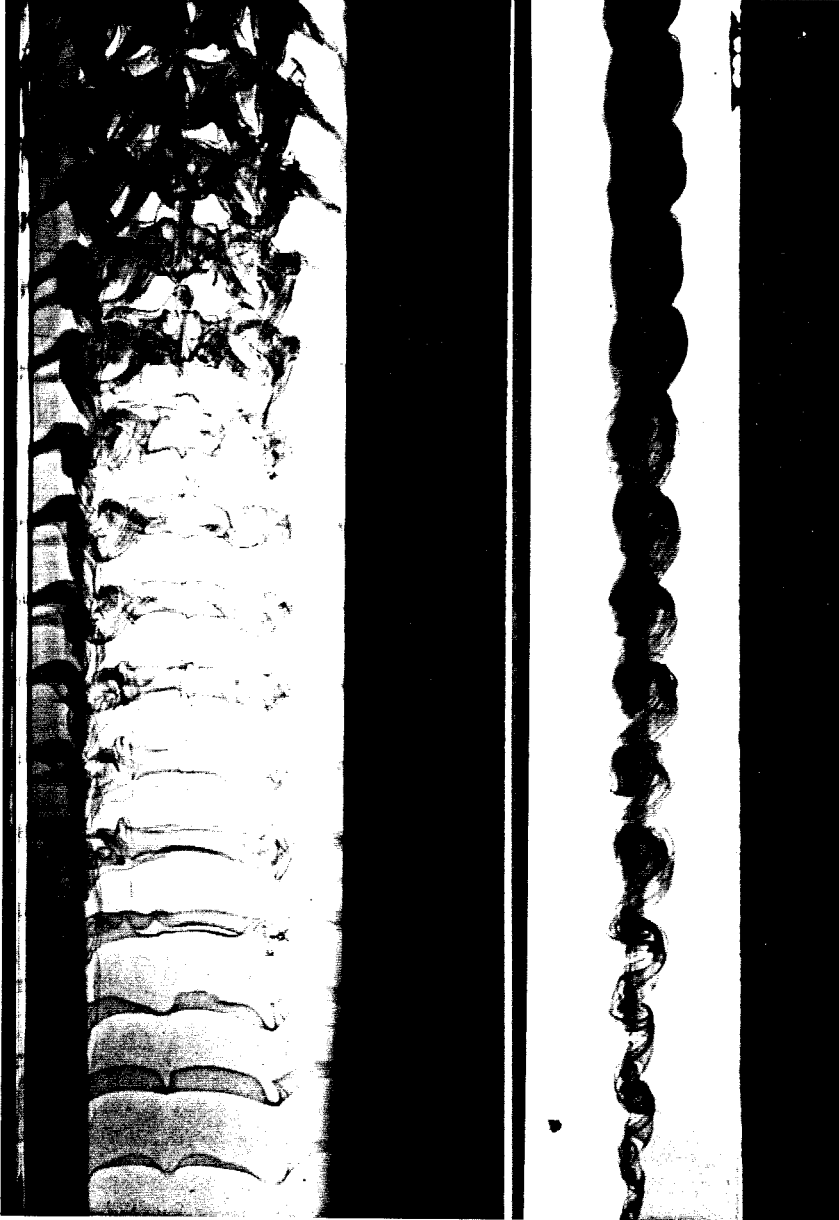
Figure 3.7 : Side Wall Interaction for a Transitional Shear Layer
$U_1 = 18$ cm/sec , $U_2 = 13$ cm/sec , $r = 0.72$, $Re_{\theta_1} = 90$

(a) unforced flow
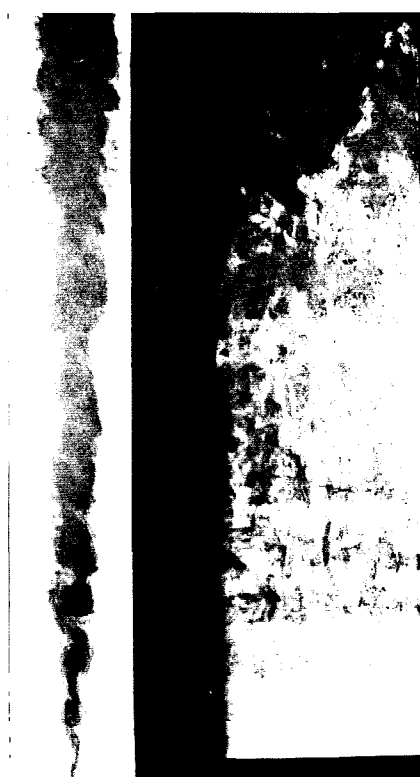
(b) F = 7.3 Hz

(c) F = 4.7 Hz

(d) F = 3.9 Hz

Figure 3.8: Effects of Forcing on Shear Layer Structure for
$U_1 = 17.4$ cm/sec and $U_2 = 8.3$ cm/sec (part 1)
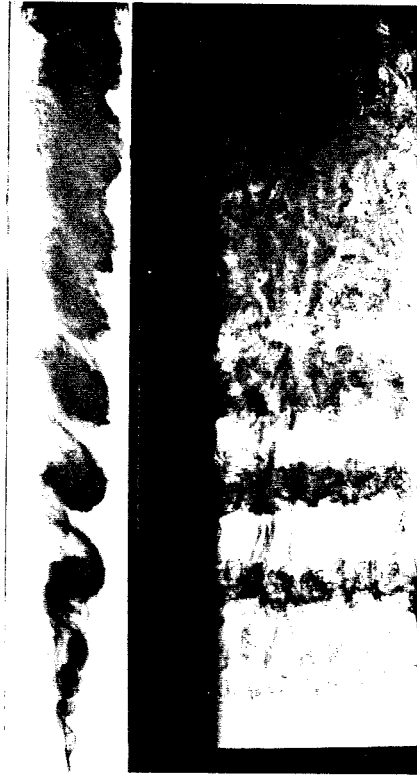
141

(e) F = 3.2 Hz

(f) F = 2.9 Hz

(g) F = 2.4 Hz

(h) F = 2.2 Hz

Figure 3.8: Effects of Forcing on Shear Layer Structure for
$U_1 = 17.4$ cm/sec and $U_2 = 8.3$ cm/sec (part 2)

142

(j) F = 1.3 Hz

(i) F = 1.8 Hz

(k) F = 1.0 Hz

$U_1 = 17.4 \text{ cm/sec}$

$r = 0.48$

$\theta_1 = 0.54 \text{ mm}$

$F_m = 8.3 \text{ Hz}$

$\dfrac{U_1 \theta_1}{\nu} = 94$

$\dfrac{\Delta U}{\nu} = 905 \text{ cm}^{-1}$

Figure 3.8: Effects of Forcing on Shear Layer Structure for
$U_1 = 17.4$ cm/sec and $U_2 = 8.3$ cm/sec (part 3)

Figure 3.9: Simultaneous Plan and Side Views of the Unforced Transitional Shear Layer. $U_1 = 17$ cm/sec, $U_2 = 8$ cm/sec

Figure 3.10: Simultaneous Plan and Side Views of a Transitional Shear Layer Forced at 2.4 Hz. $U_1 = 17$ cm/sec. $U_2 = 8$ cm/sec

(a) unforced flow
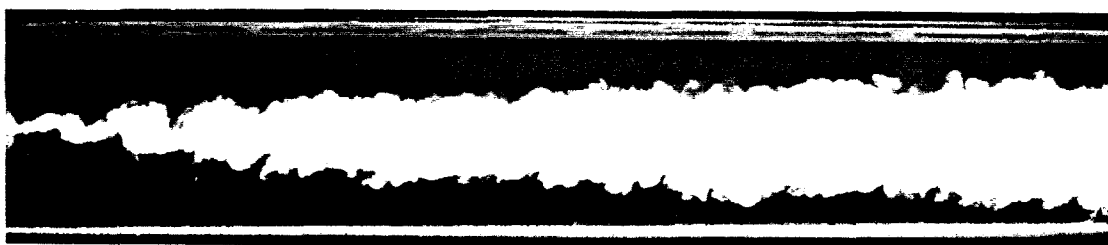
(b) F = 12 Hz , F/F$_0$ = 0.19 , λ = 4 cm

(c) F = 8 Hz , F/F$_0$ = 0.13 , λ = 6 cm

(d) F = 4 Hz , F/F$_0$ = 0.06 , λ = 12 cm

Figure 3.11 : Reacting L.I.F. Photographs of a Forced Turbulent
Shear layer , U$_1$ = 70 cm/sec , U$_2$ = 27 cm/sec

(a) unforced flow
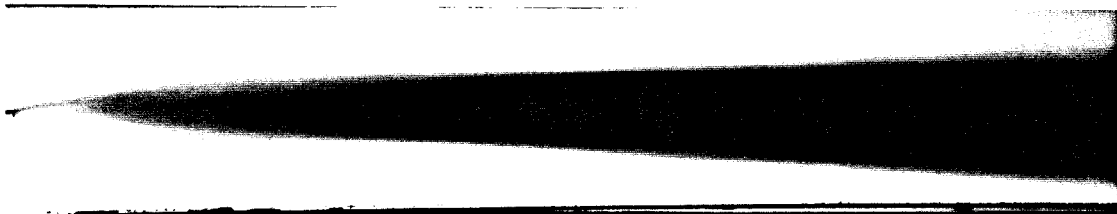
(b) F = 12 Hz , $F/F_0 = 0.19$, λ = 4 cm
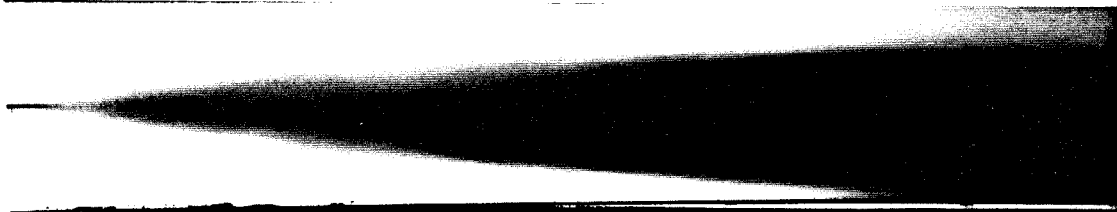
(c) F = 8 Hz , $F/F_0 = 0.13$, λ = 6 cm
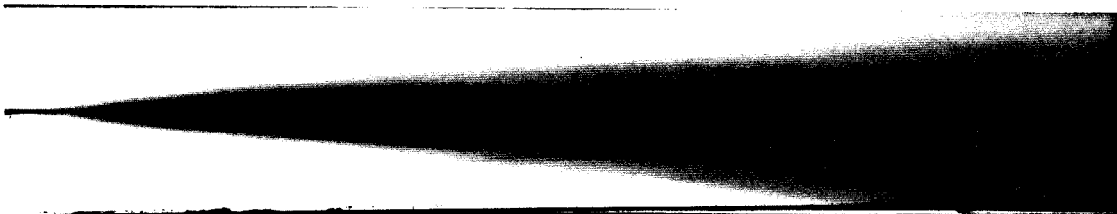
(d) F = 4 Hz , $F/F_0 = 0.08$, λ = 12 cm

Figure 3.12 : Time Exposures of the Phenolphthalein Reaction
U_1 = 70 cm/sec , U_2 = 27 cm/sec
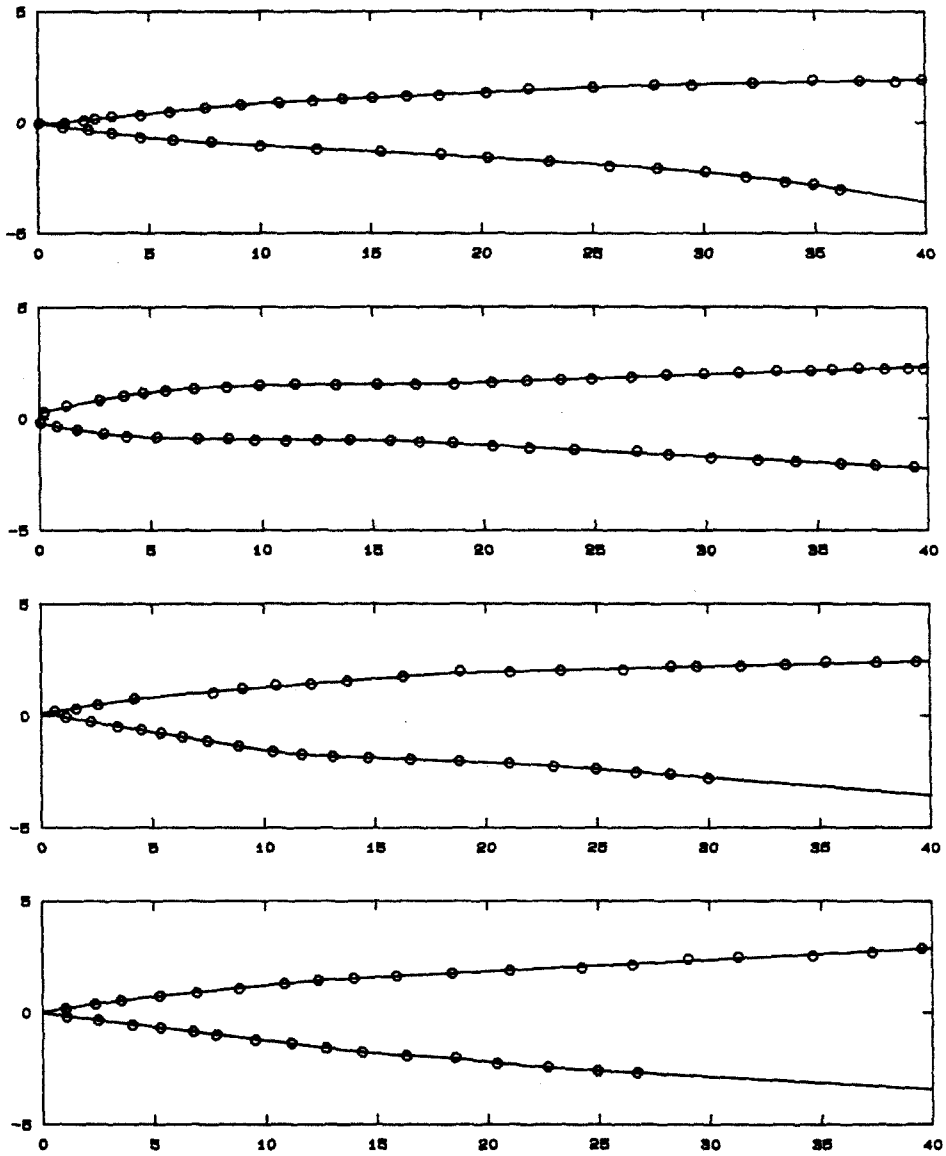
Figure 3.13 : Digitized Boundary of the Mixed Region from Time Exposures in **Figure 3.12**
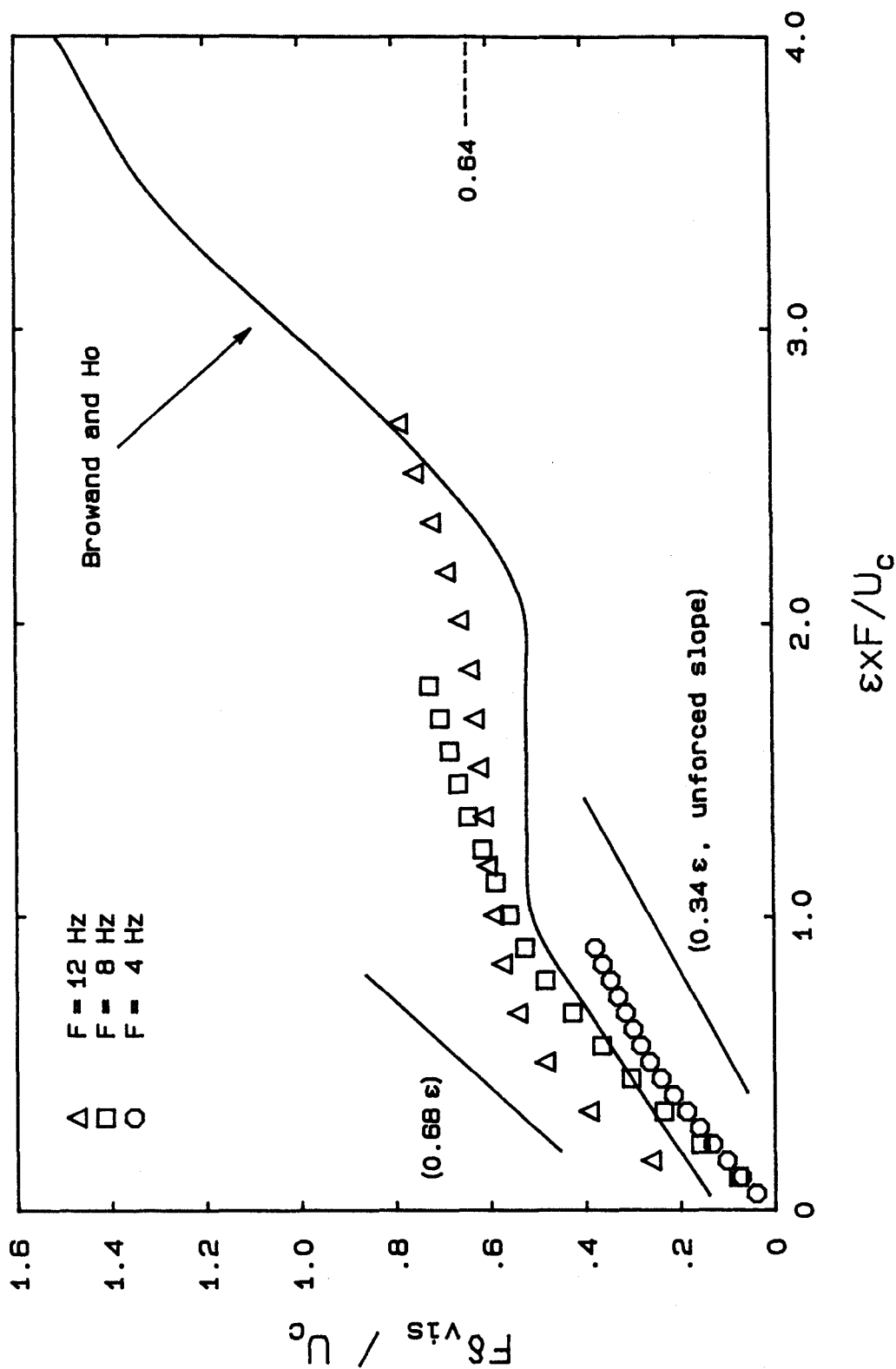
Figure 3.14: Visual Growth in Dimensionless Coordinates. Numbers in brackets are slopes. The 0.84 refers to the neutral stability point.
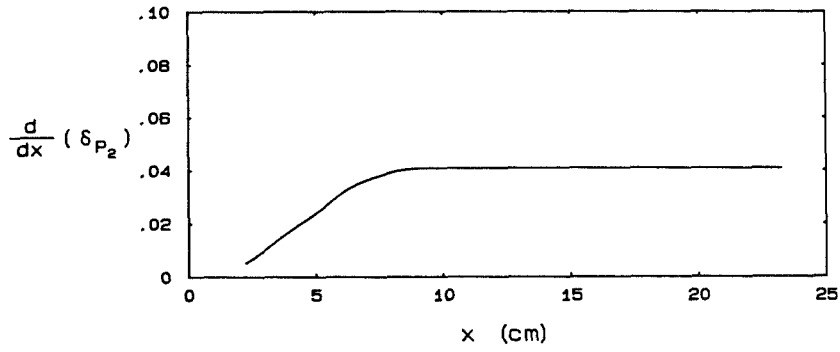
$$U_1 = 70 \text{ cm/sec}$$

$$r = 0.38$$

$$F = \text{unforced}$$

$$\theta_1 = 0.27 \text{ mm}$$

$$F_0 = 62.7 \text{ Hz}$$

$$\frac{U_1 \theta_1}{\nu} = 187$$

$$\frac{\Delta U}{\nu} = 4340 \text{ cm}^{-1}$$

$$\frac{U_c}{\varepsilon F} = \text{unforced}$$
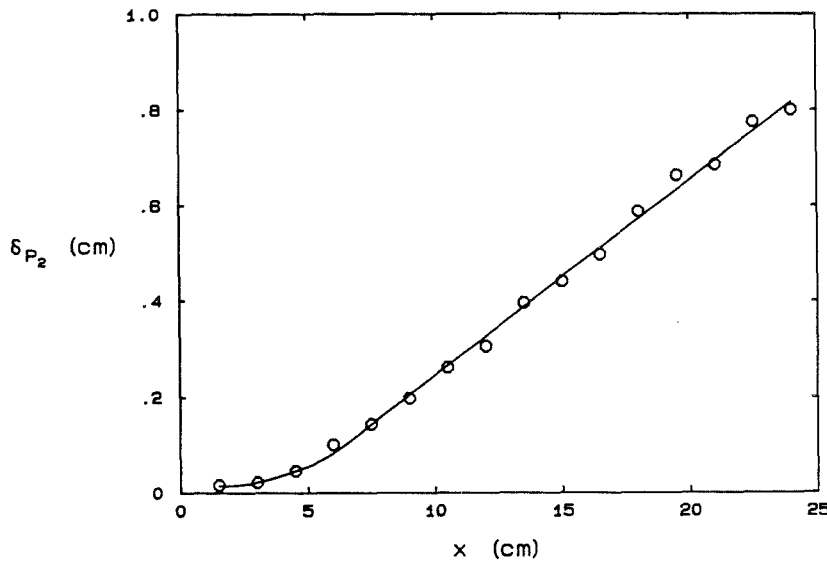
Figure 3.15 : Product Thickness and Growth Rate from Absorption Measurement -- High Reynolds Number , Unforced
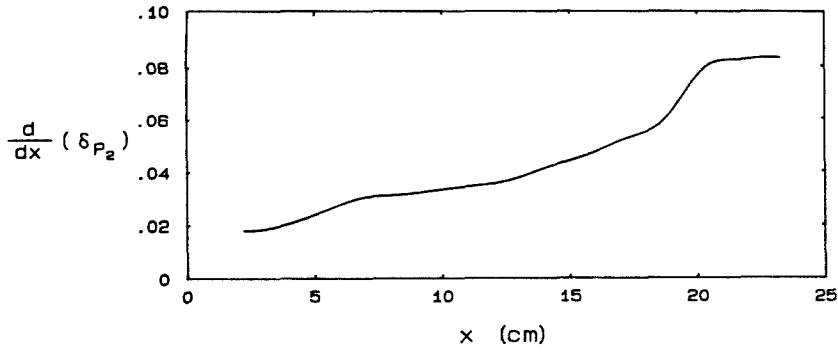
$U_1 = 70 \text{ cm/sec}$

$r = 0.38$

$F = 3.9 \text{ Hz}$

$\theta_1 = 0.27 \text{ mm}$

$F_0 = 62.7 \text{ Hz}$

$\dfrac{U_1 \theta_1}{\nu} = 187$

$\dfrac{\Delta U}{\nu} = 4340 \text{ cm}^{-1}$

$\dfrac{U_c}{\varepsilon F} = 27.6 \text{ cm}$
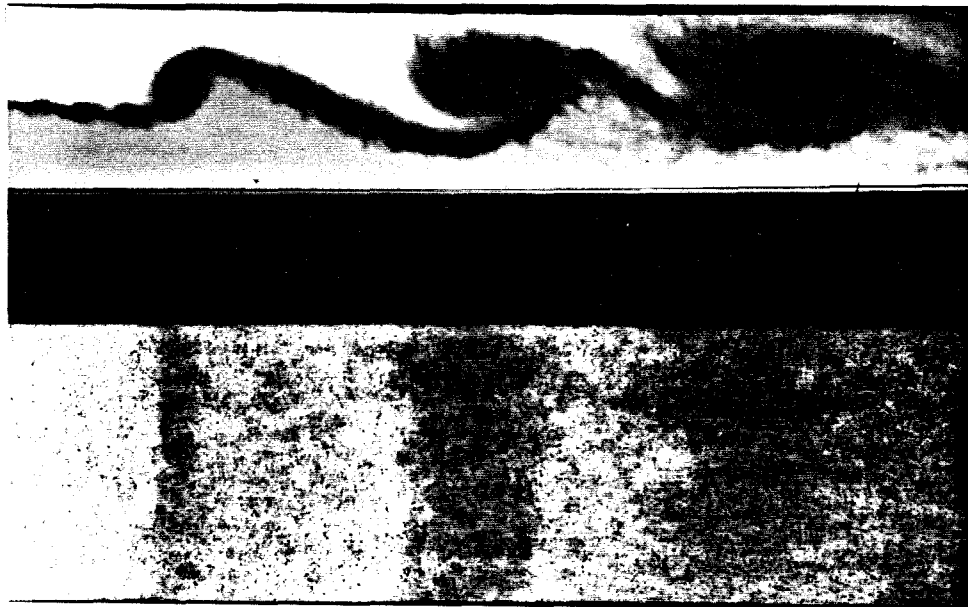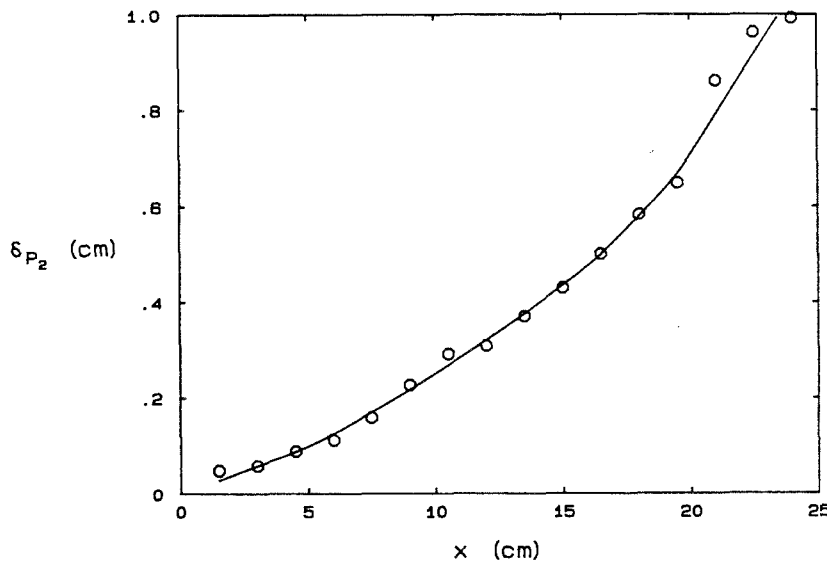
Figure 3.16 : Product Thickness and Growth Rate from Absorption
Measurement — High Reynolds Number , F = 3.9 Hz
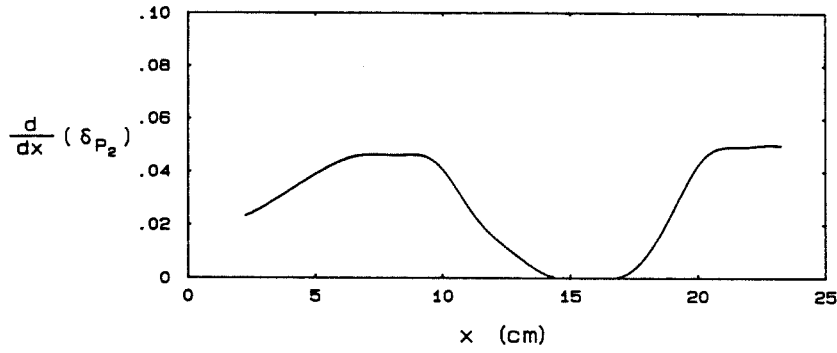
$$U_1 = 70 \text{ cm/sec}$$

$$r = 0.38$$

$$F = 8.0 \text{ Hz}$$

$$\theta_1 = 0.27 \text{ mm}$$

$$F_0 = 62.7 \text{ Hz}$$

$$\frac{U_1 \theta_1}{\nu} = 187$$

$$\frac{\Delta U}{\nu} = 4340 \text{ cm}^{-1}$$

$$\frac{U_c}{\varepsilon F} = 13.4 \text{ cm}$$
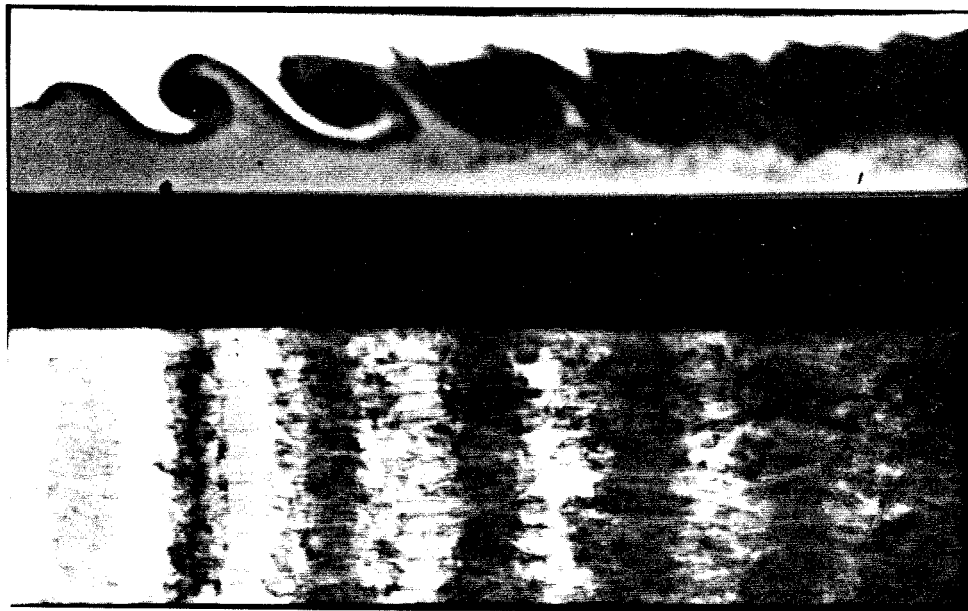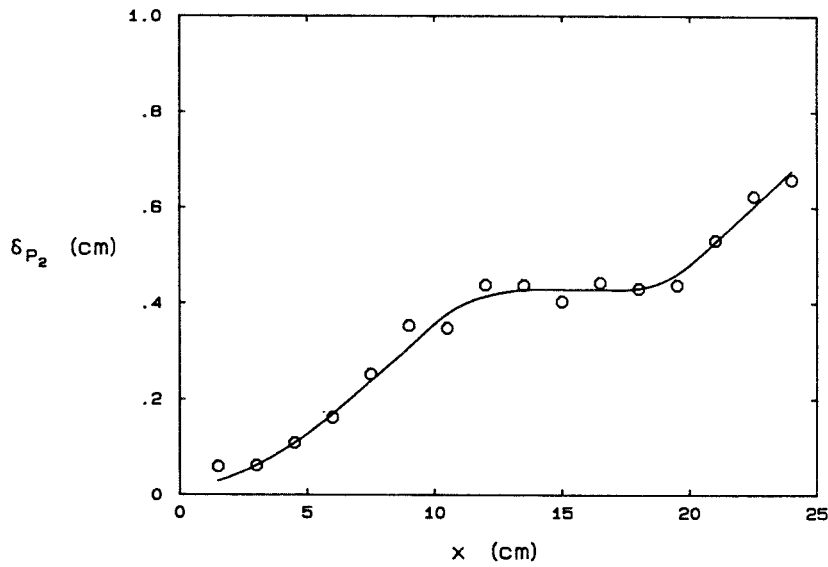
Figure 3.17 : Product Thickness and Growth Rate from Absorption
Measurement -- High Reynolds Number , F = 8.0 Hz
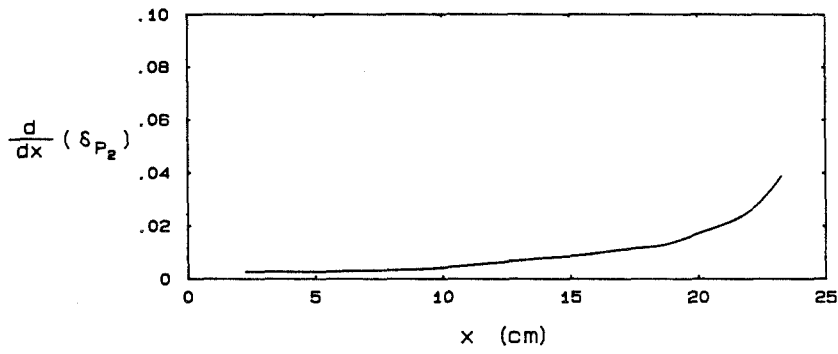
$$U_1 = 17.4 \text{ cm/sec}$$

$$r = 0.48$$

$$F = \text{unforced}$$

$$\theta_1 = 0.54 \text{ mm}$$

$$F_0 = 8.3 \text{ Hz}$$

$$\frac{U_1 \theta_1}{\nu} = 94$$

$$\frac{\Delta U}{\nu} = 905 \text{ cm}^{-1}$$

$$\frac{U_c}{\varepsilon F} = \text{unforced}$$
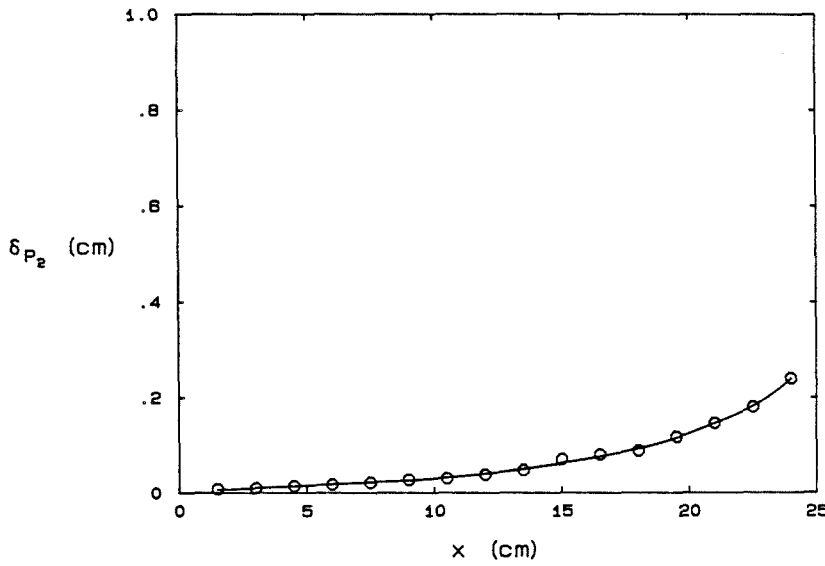
Figure 3.18 : Product Thickness and Growth Rate from Absorption
Measurement -- Low Reynolds Number , Unforced
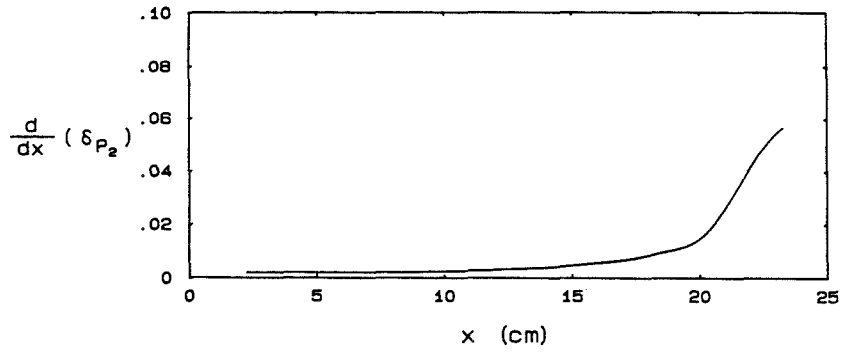
$U_1 = 17.4 \, \text{cm/sec}$

$r = 0.48$

$F = 1.8 \, \text{Hz}$

$\theta_1 = 0.54 \, \text{mm}$

$F_0 = 8.3 \, \text{Hz}$

$\dfrac{U_1 \theta_1}{\nu} = 94$

$\dfrac{\Delta U}{\nu} = 905 \, \text{cm}^{-1}$

$\dfrac{U_c}{\varepsilon F} = 20.4 \, \text{cm}$
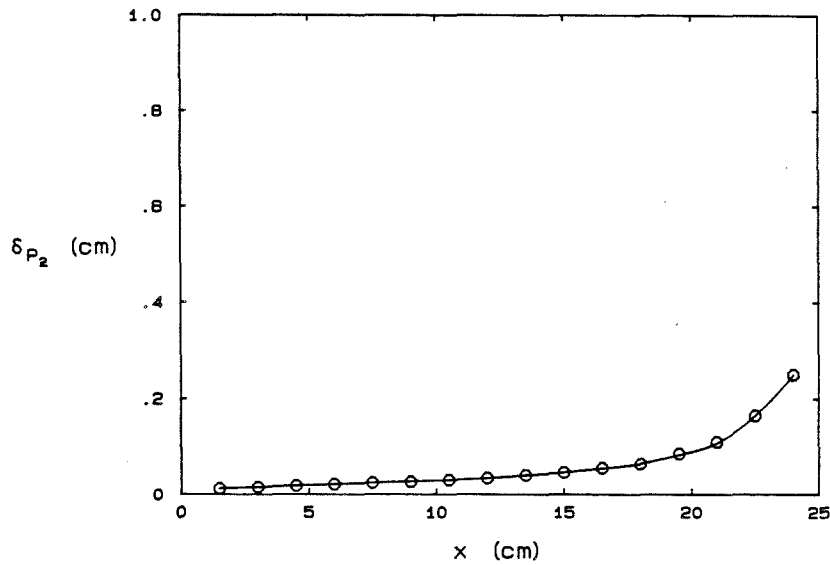
Figure 3.19 : Product Thickness and Growth Rate from Absorption
Measurement -- Low Reynolds Number , F = 1.8 Hz
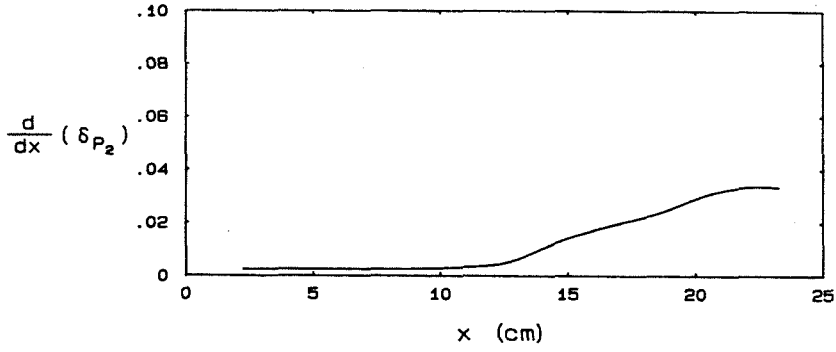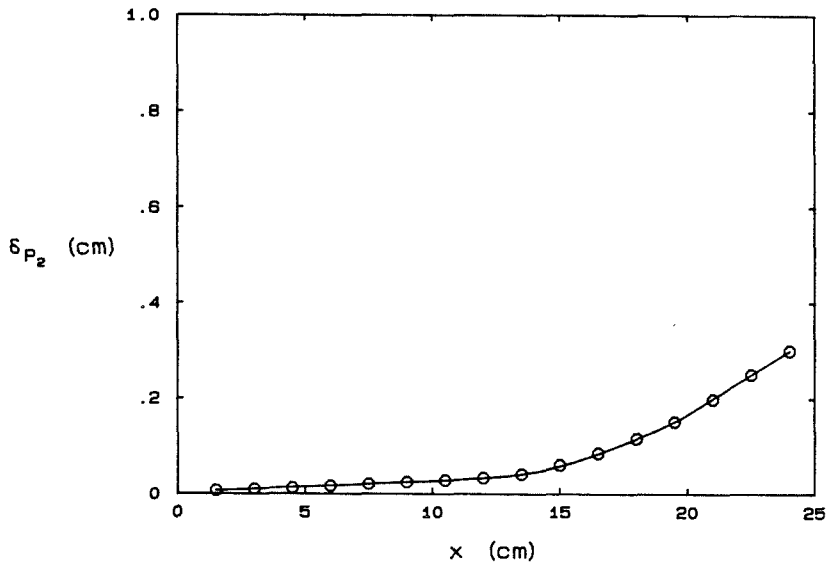
Figure 3.20 : Product Thickness and Growth Rate from Absorption
Measurement -- Low Reynolds Number , F = 2.6 Hz
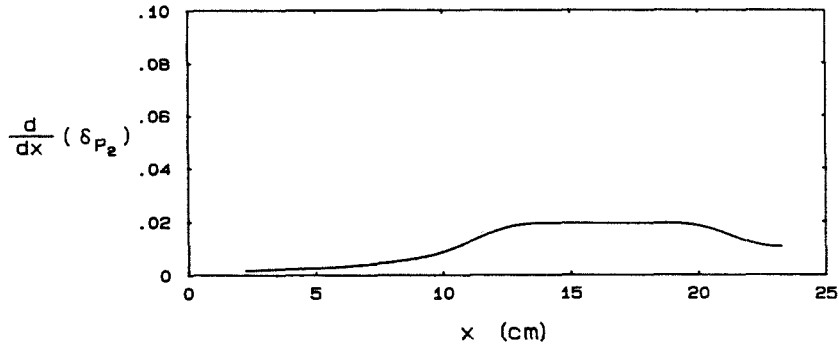
$U_1 = 17.4$ cm/sec

$r = 0.48$

$F = 4.5$ Hz

$\theta_1 = 0.54$ mm

$F_0 = 8.3$ Hz

$\dfrac{U_1 \theta_1}{\nu} = 94$

$\dfrac{\Delta U}{\nu} = 905$ cm^{-1}

$\dfrac{U_c}{\varepsilon F} = 8.1$ cm
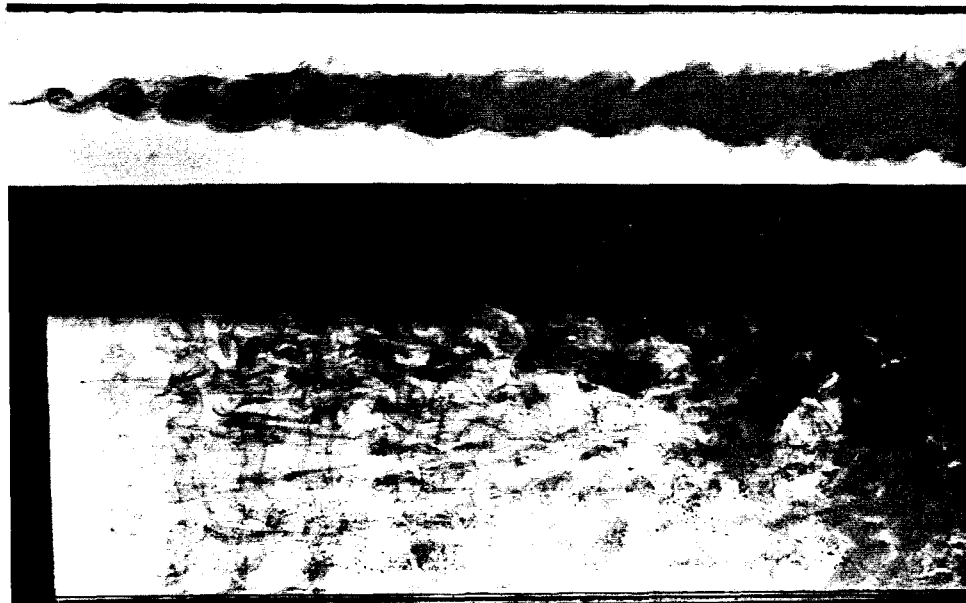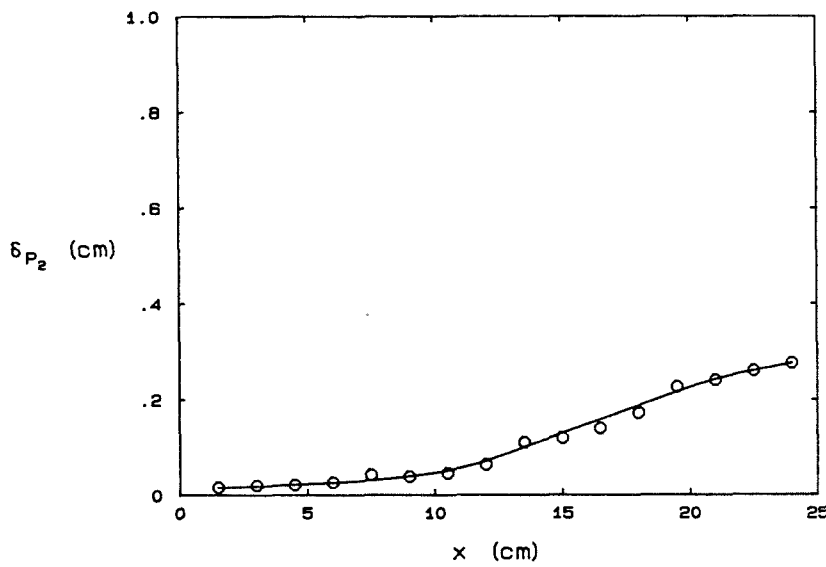
Figure 3.21 : Product Thickness and Growth Rate from Absorption
Measurement -- Low Reynolds Number , F = 4.5 Hz
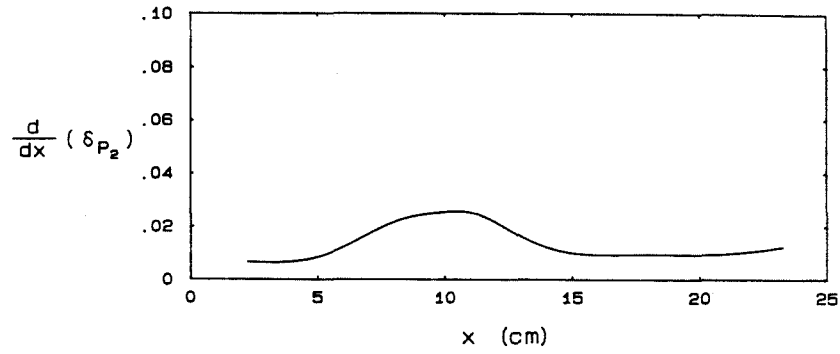
$U_1 = 17.4\,\text{cm/sec}$

$r = 0.48$

$F = 5.9\,\text{Hz}$

$\theta_1 = 0.54\,\text{mm}$

$F_0 = 8.3\,\text{Hz}$

$\dfrac{U_1 \theta_1}{\nu} = 94$

$\dfrac{\Delta U}{\nu} = 905\,\text{cm}^{-1}$

$\dfrac{U_c}{\varepsilon F} = 6.2\,\text{cm}$
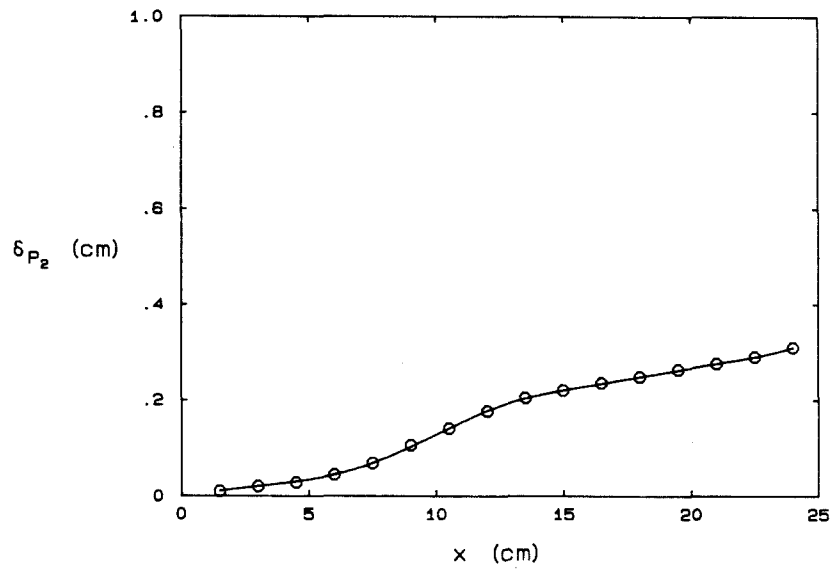
Figure 3.22 : Product Thickness and Growth Rate from Absorption
Measurement -- Low Reynolds Number , F = 5.9 Hz

x = 6 cm

δ_{p_2} = 0.11 cm

δ' = 0.027 cm
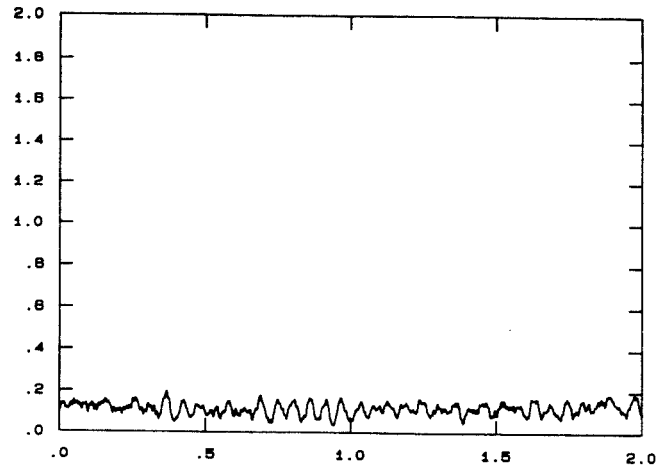
x = 15 cm

δ_{p_2} = 0.44 cm

δ' = 0.12 cm
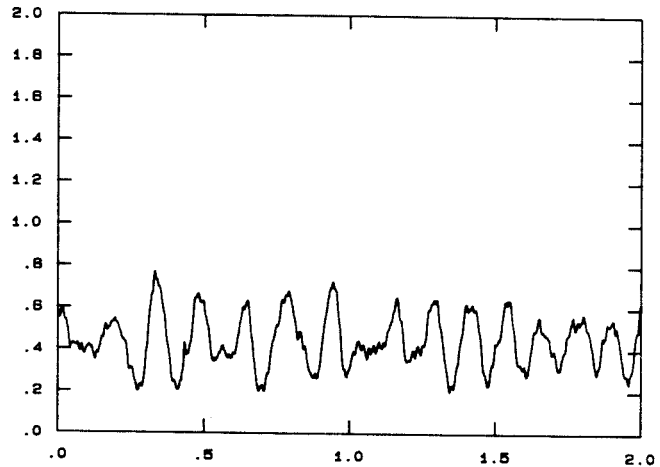
x = 24 cm

δ_{p_2} = 0.84 cm
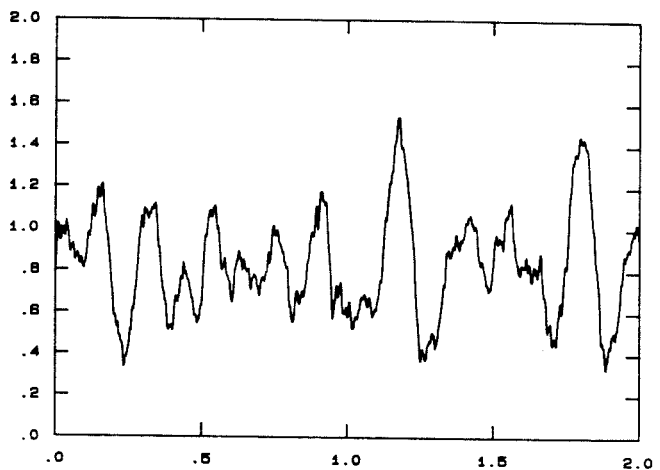
δ' = 0.25 cm

Figure 3.23 : Product Thickness Fluctuation from Absorption Product
Measurement -- High Reynolds Number , Unforced

x = 6 cm

δ_{p_2} = 0.11 cm

δ' = 0.025 cm
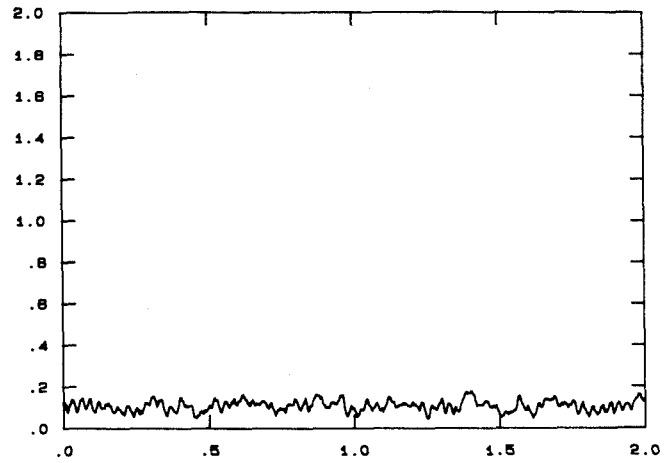
x = 15 cm

δ_{p_2} = 0.43 cm

δ' = 0.17 cm
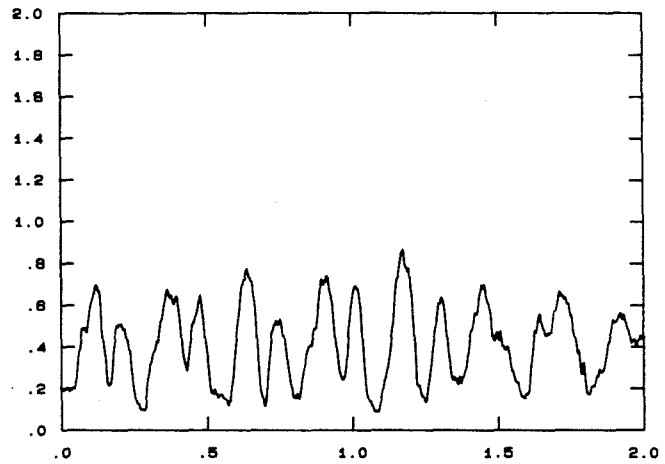
x = 24 cm

δ_{p_2} = 0.99 cm

δ' = 0.26 cm
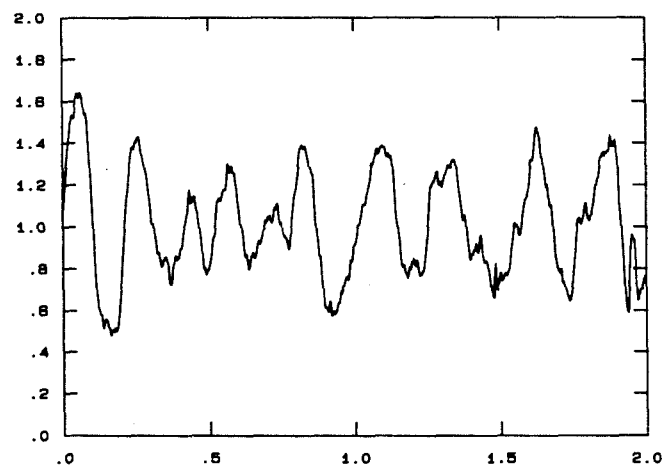
Figure 3.24 : Product Thickness Fluctuation from Absorption Product
Measurement -- High Reynolds Number , F = 3.9 Hz

x = 9 cm

$\delta_{p_2} = 0.35$ cm

$\delta' = 0.073$ cm
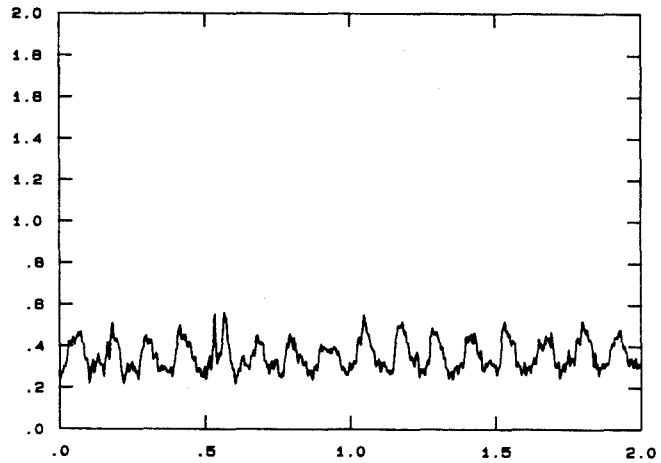
x = 15 cm

$\delta_{p_2} = 0.40$ cm

$\delta' = 0.11$ cm
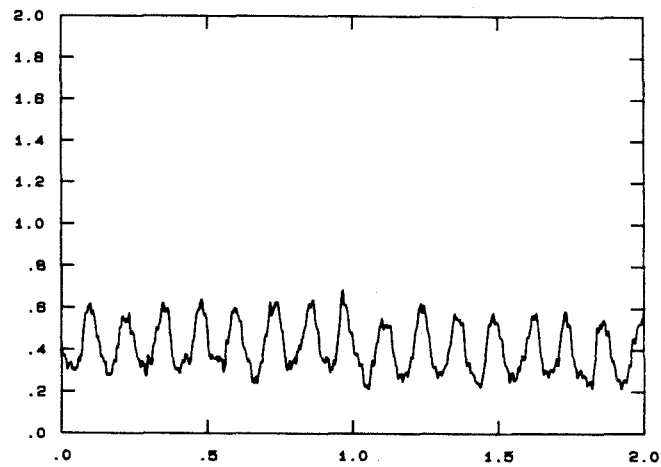
x = 24 cm

$\delta_{p_2} = 0.66$ cm

$\delta' = 0.11$ cm
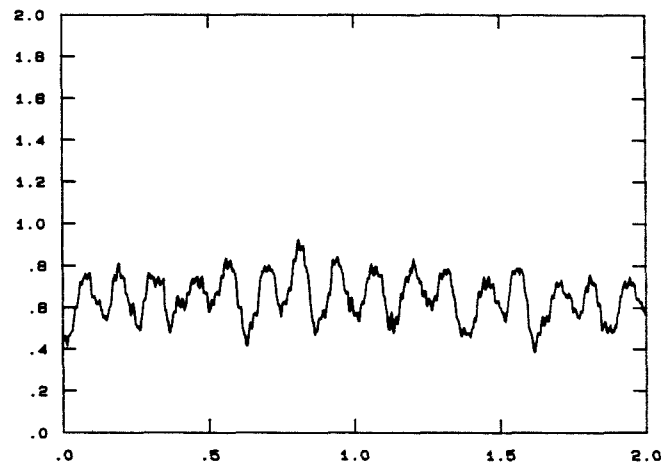
Figure 3.25 : Product Thickness Fluctuation from Absorption Product
Measurement -- High Reynolds Number , F = 8.0 Hz

x = 3 cm

δ_{p_2} = 0.01 cm

δ' = 0.002 cm
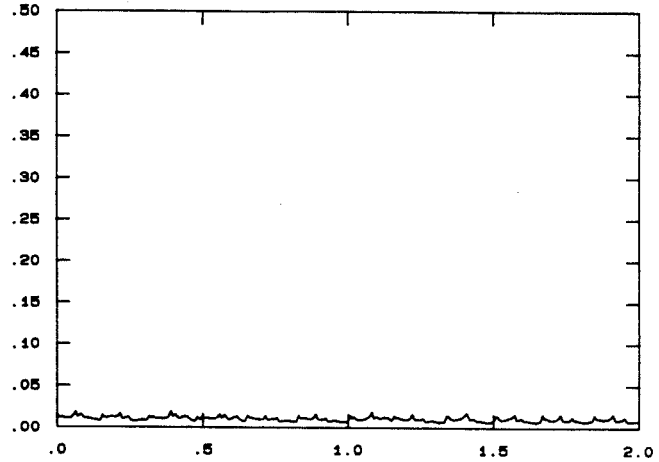
x = 15 cm

δ_{p_2} = 0.07 cm

δ' = 0.013 cm
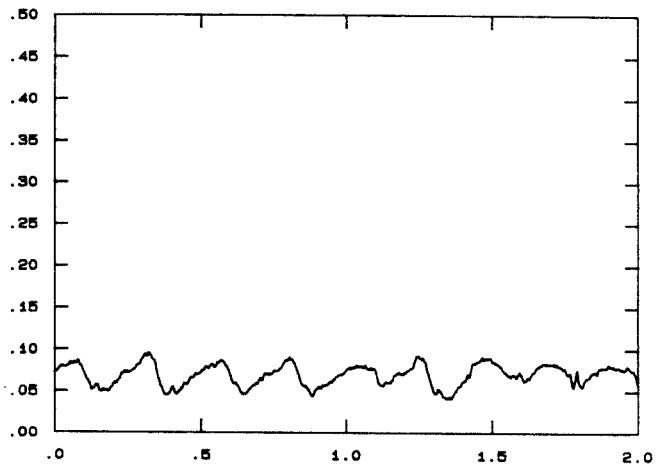
x = 24 cm

δ_{p_2} = 0.24 cm

δ' = 0.06 cm
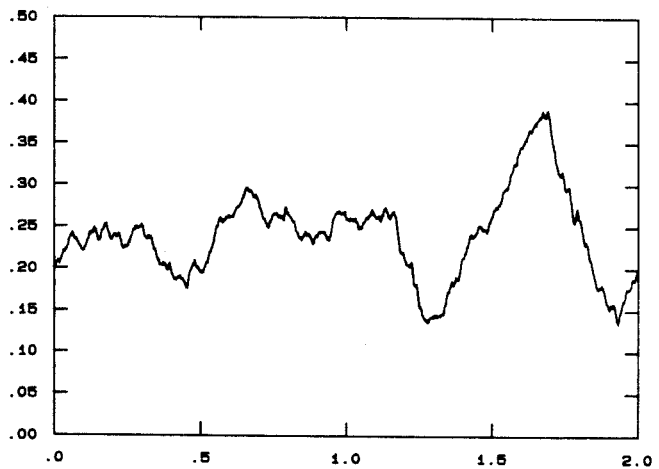
Figure 3.26 : Product Thickness Fluctuation from Absorption Product
Measurement -- Low Reynolds Number , Unforced

x = 6 cm

$\delta_{p_2} = 0.021$ cm

$\delta' = 0.009$ cm
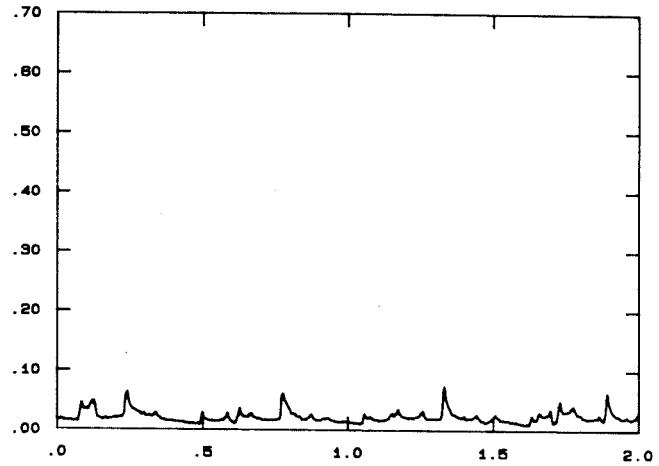
x = 15 cm

$\delta_{p_2} = 0.046$ cm

$\delta' = 0.036$ cm
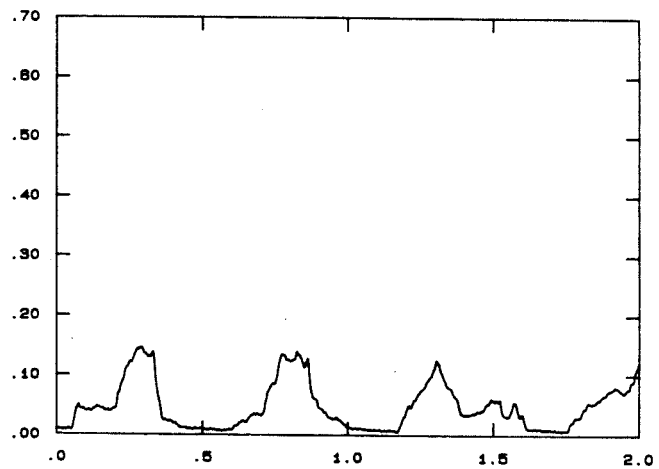
x = 24 cm

$\delta_{p_2} = 0.25$ cm

$\delta' = 0.13$ cm
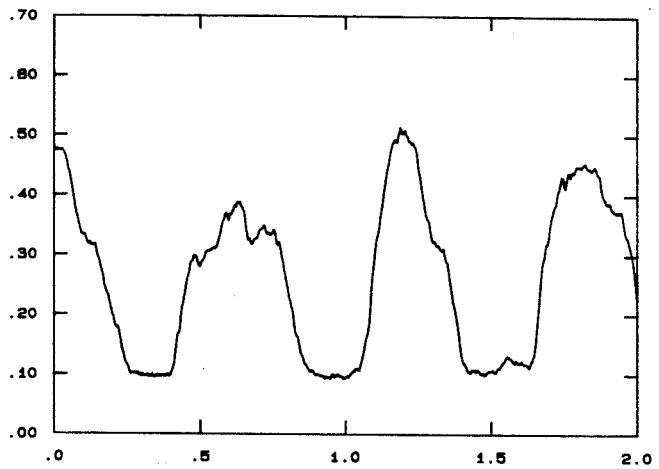
Figure 3.27 : Product Thickness Fluctuation from Absorption Product
Measurement -- Low Reynolds Number , F = 1.8 Hz

162

$x = 6$ cm

$\delta_{p_2} = 0.016$ cm

$\delta' = 0.005$ cm
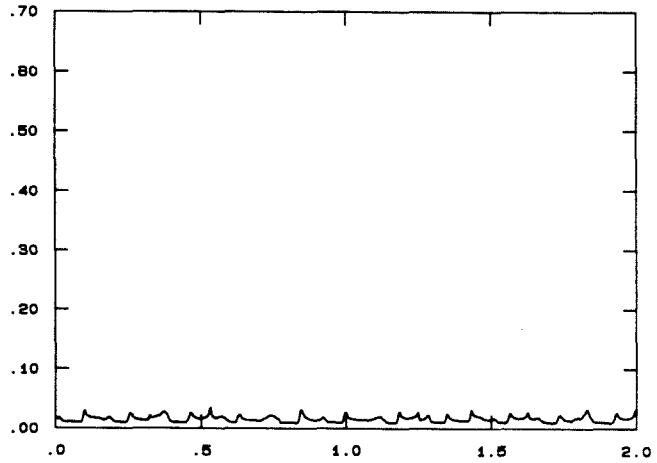
$x = 15$ cm

$\delta_{p_2} = 0.060$ cm

$\delta' = 0.013$ cm
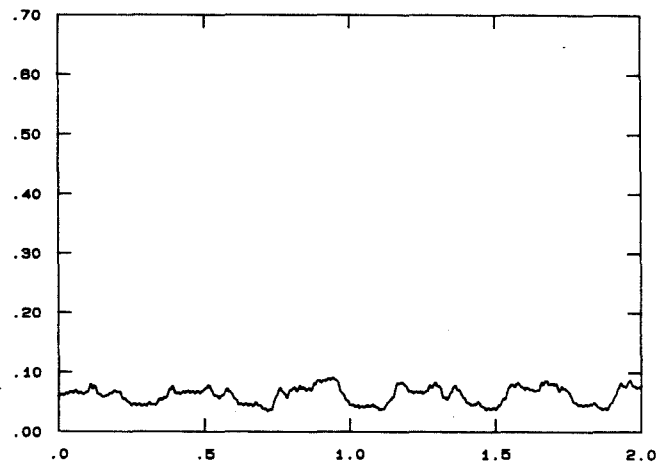
$x = 24$ cm

$\delta_{p_2} = 0.30$ cm

$\delta' = 0.18$ cm
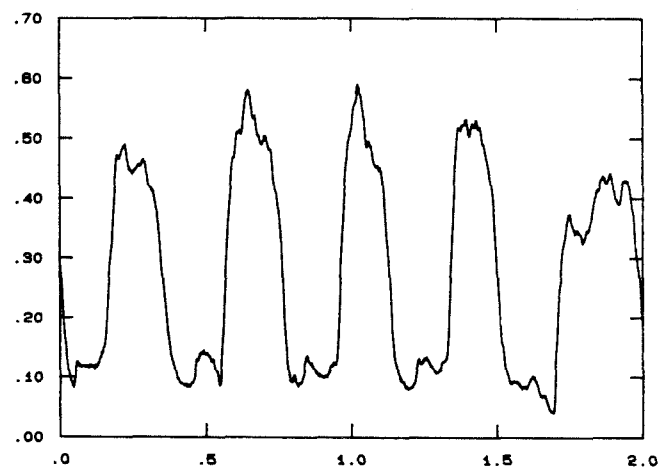
Figure 3.28 : Product Thickness Fluctuation from Absorption Product
Measurement -- Low Reynolds Number , F = 2.8 Hz

x = 6 cm

δ_{p_2} = 0.026 cm

δ' = 0.008 cm
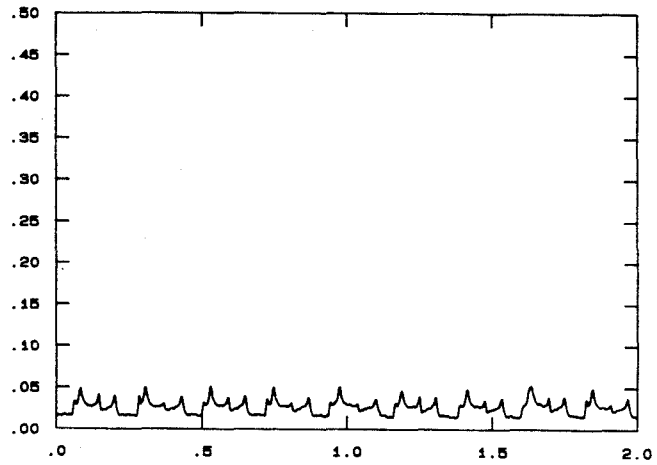
x = 15 cm

δ_{p_2} = 0.12 cm

δ' = 0.009 cm
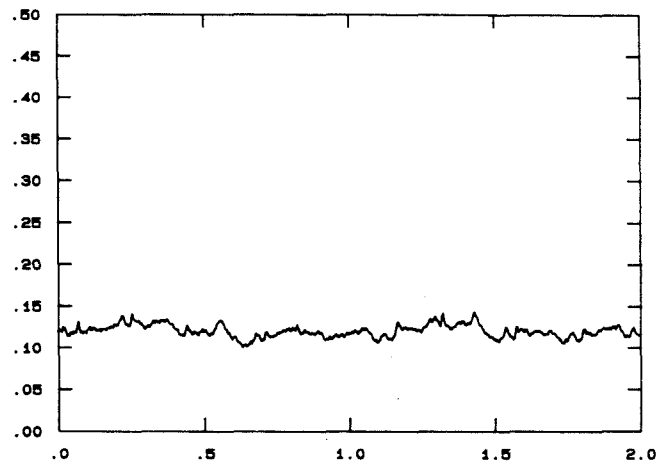
x = 21 cm

δ_{p_2} = 0.24 cm
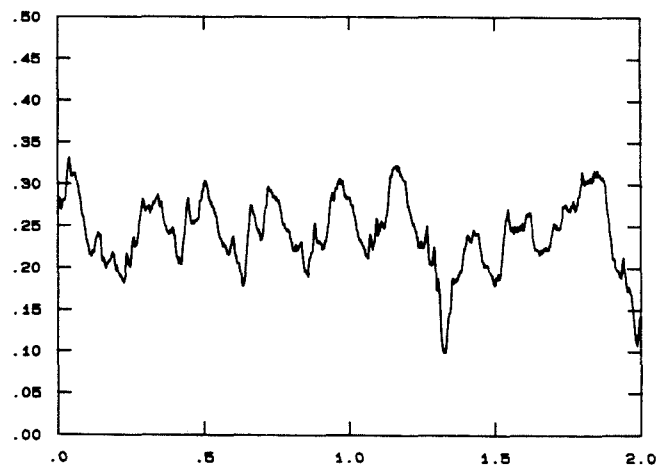
δ' = 0.044 cm

Figure 3.29 : Product Thickness Fluctuation from Absorption Product
Measurement -- Low Reynolds Number , F = 4.5 Hz

x = 6 cm

δ_{p_2} = 0.044 cm

δ' = 0.013 cm
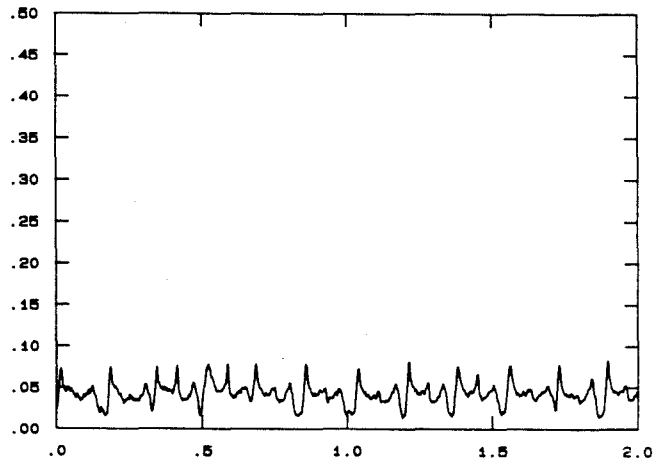
x = 15 cm

δ_{p_2} = 0.22 cm

δ' = 0.058 cm
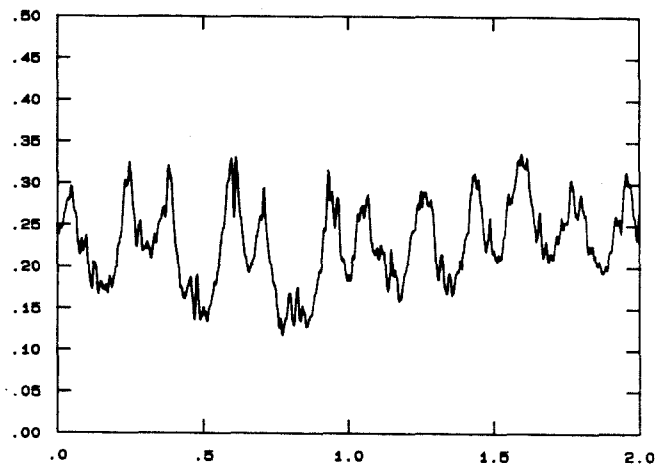
x = 24 cm

δ_{p_2} = 0.31 cm

δ' = 0.057 cm
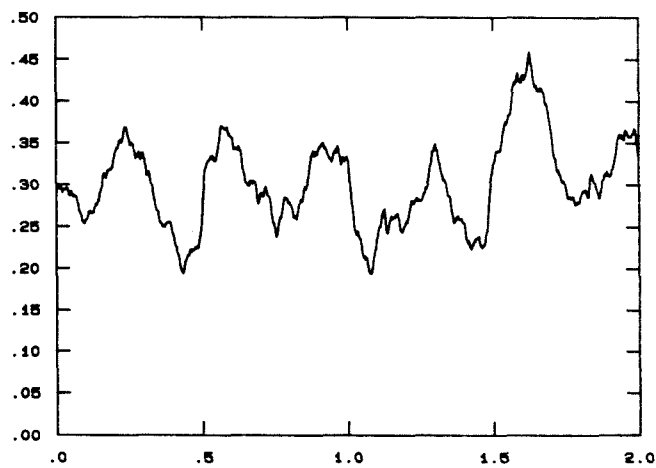
Figure 3.30 : Product Thickness Fluctuation from Absorption Product
Measurement -- Low Reynolds Number , F = 5.9 Hz
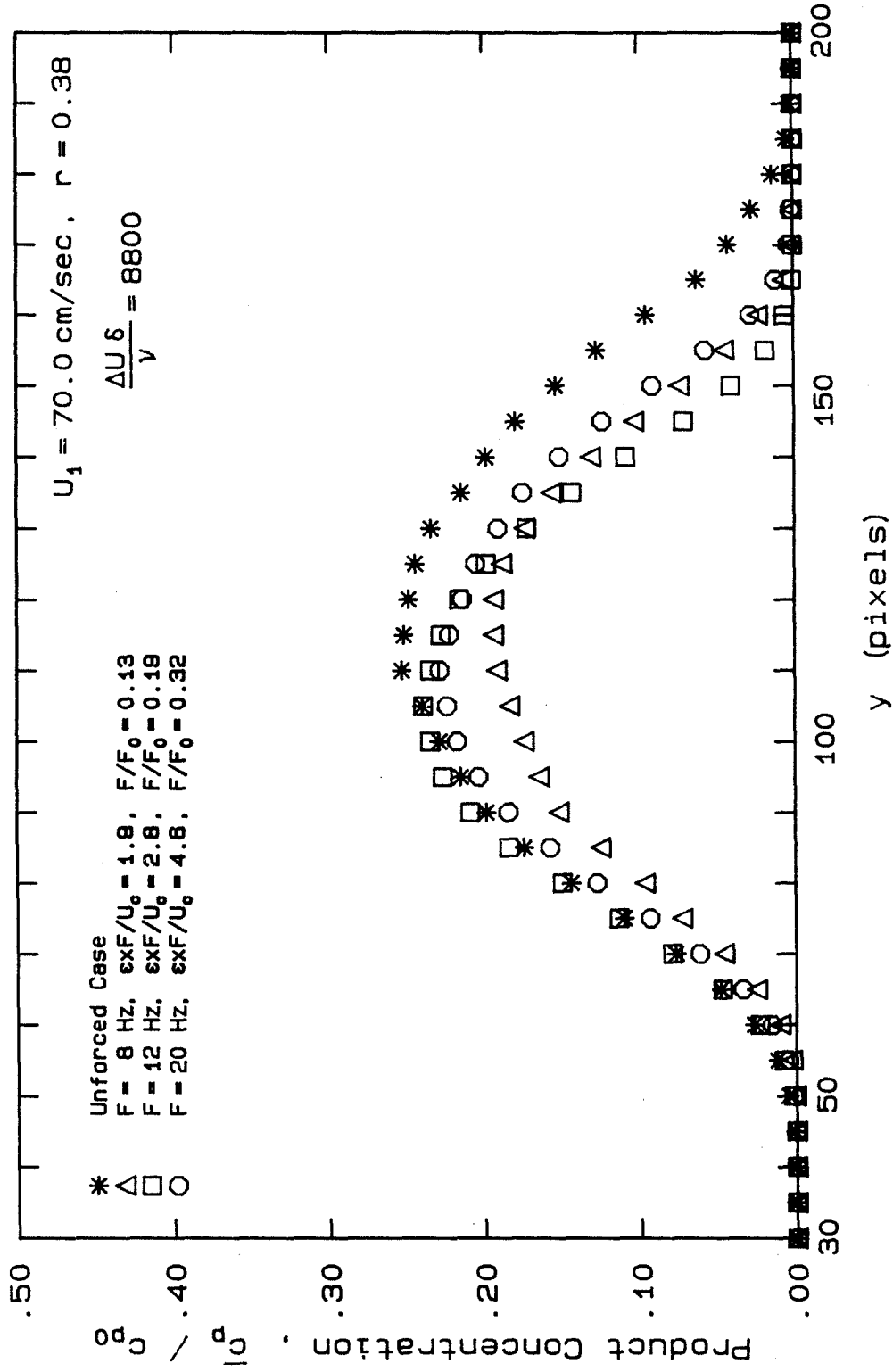
Figure 3.31 : Mean Product Concentration Profiles for a Turbulent Shear Layer
$U_1 = 70$ cm/sec, $U_2 = 27$ cm/sec, 1 pixel ≈ 0.37 mm
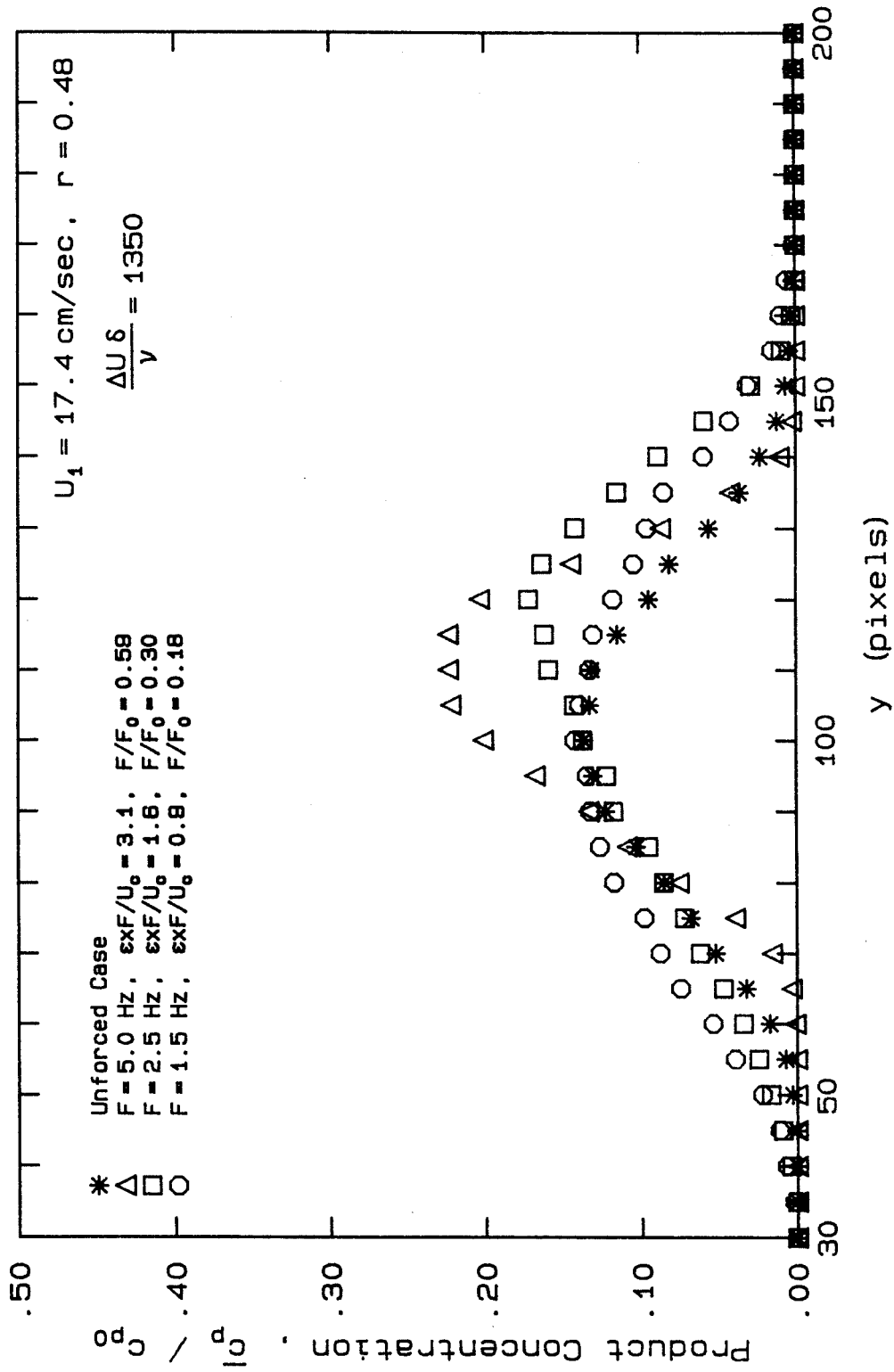
Figure 3.32 : Mean Product Concentration Profiles for a Transitional Layer
$U_1 = 17.4 \, cm/sec, \; U_2 = 8.3 \, cm/sec$
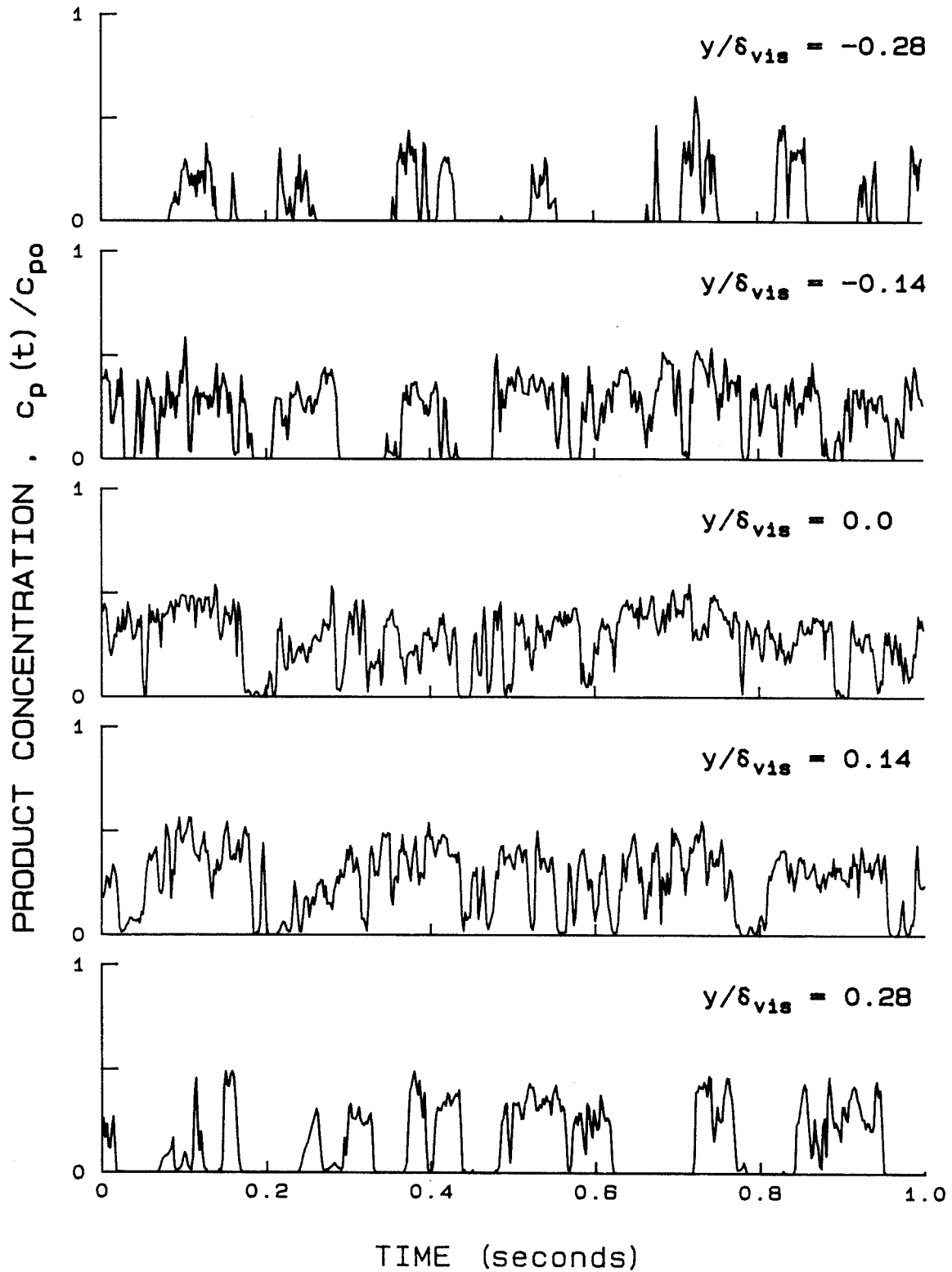
Figure 3.33 : Time Series of Product Concentration in the Unforced Flow
U_1 = 70 cm/sec , U_2 = 27 cm/sec
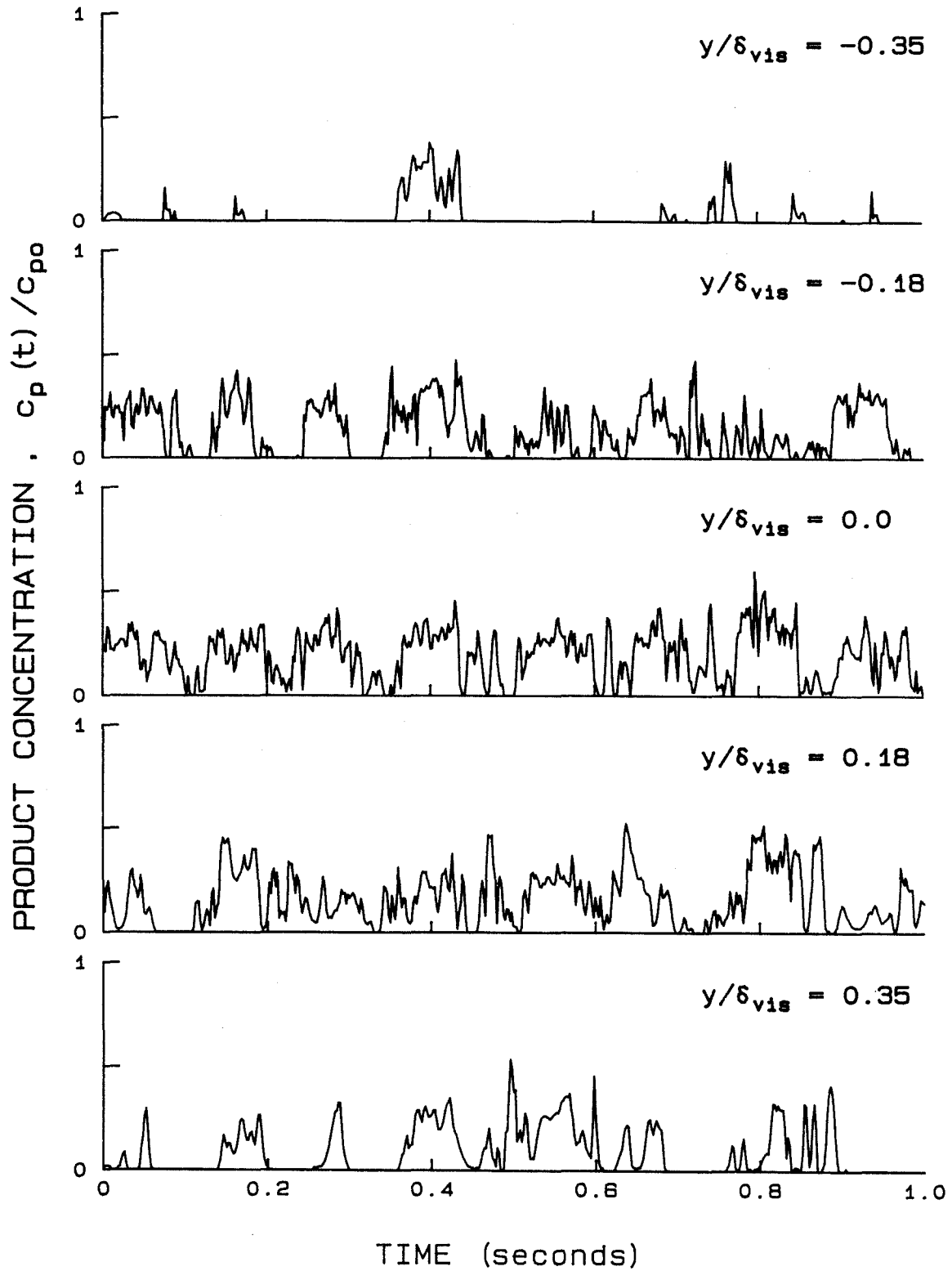
Figure 3.34 : Time Series of Product Concentration in a Forced Layer
F = 8 Hz , U_1 = 70 cm/sec , U_2 = 27 cm/sec
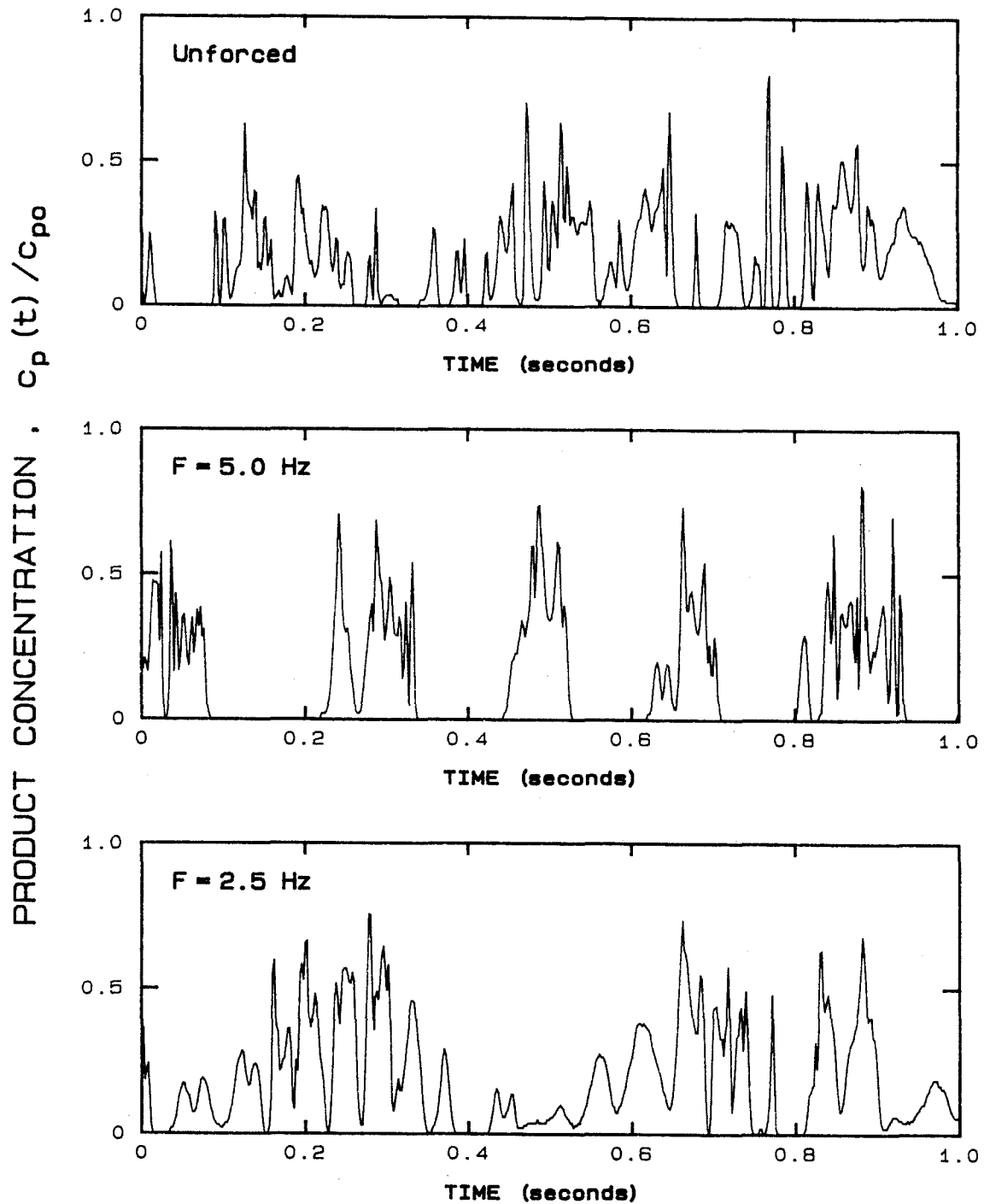
Figure 3.35 : Time Traces of Product Concentration in a Transitional Layer Data shown are for the y location of maximum mean product. U_1 = 17.4 cm/sec , U_2 = 8.3 cm/sec
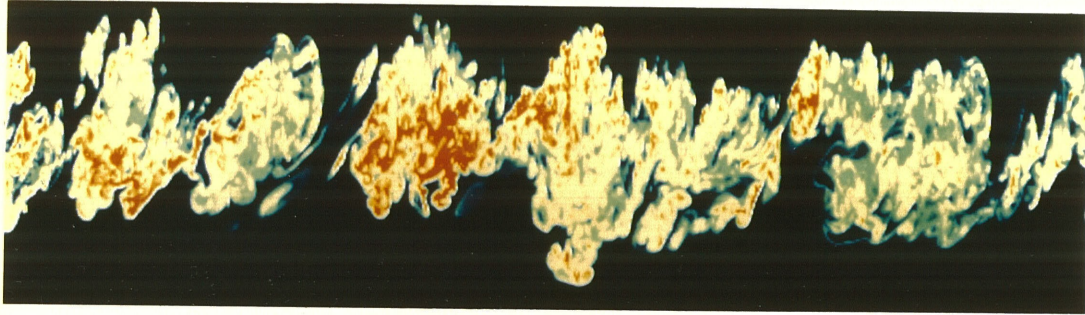
(a) unforced flow

(b) F = 8 Hz X_{wo} = 1.9
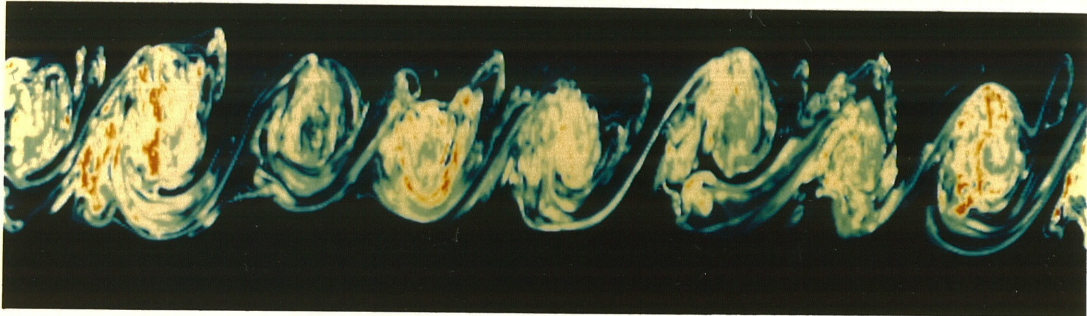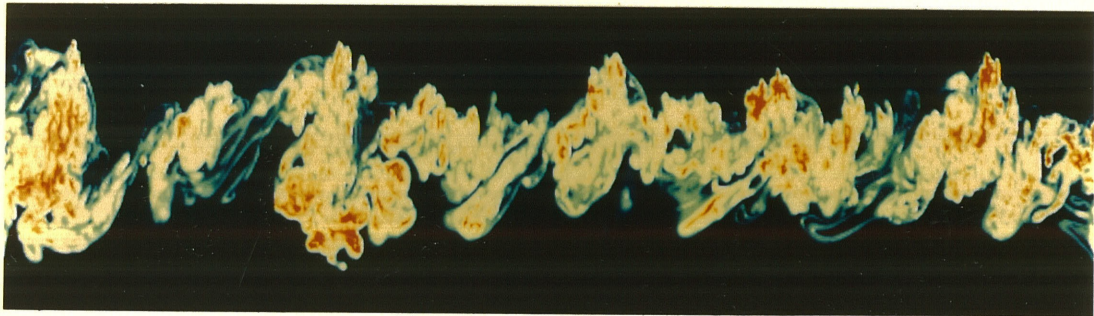
(c) F = 12 Hz X_{wo} = 2.8
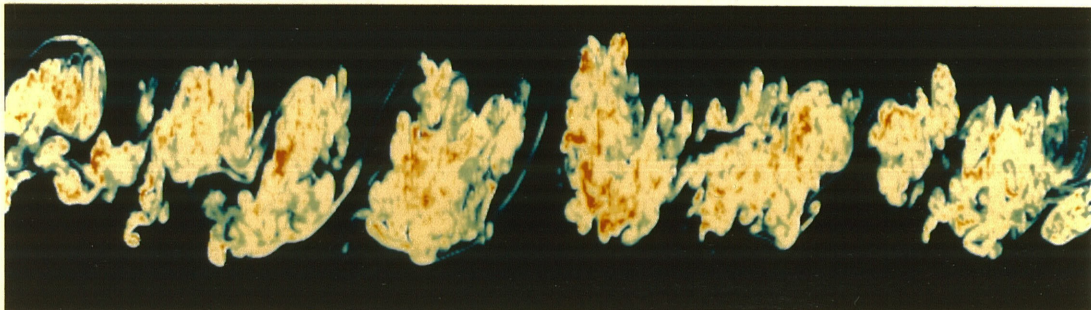
(d) F = 20 Hz X_{wo} = 4.6

Figure 3.36 : Pseudo-color Flow Images from L.I.F. Measurements
U_1 = 70 cm/sec , U_2 = 27 cm/sec
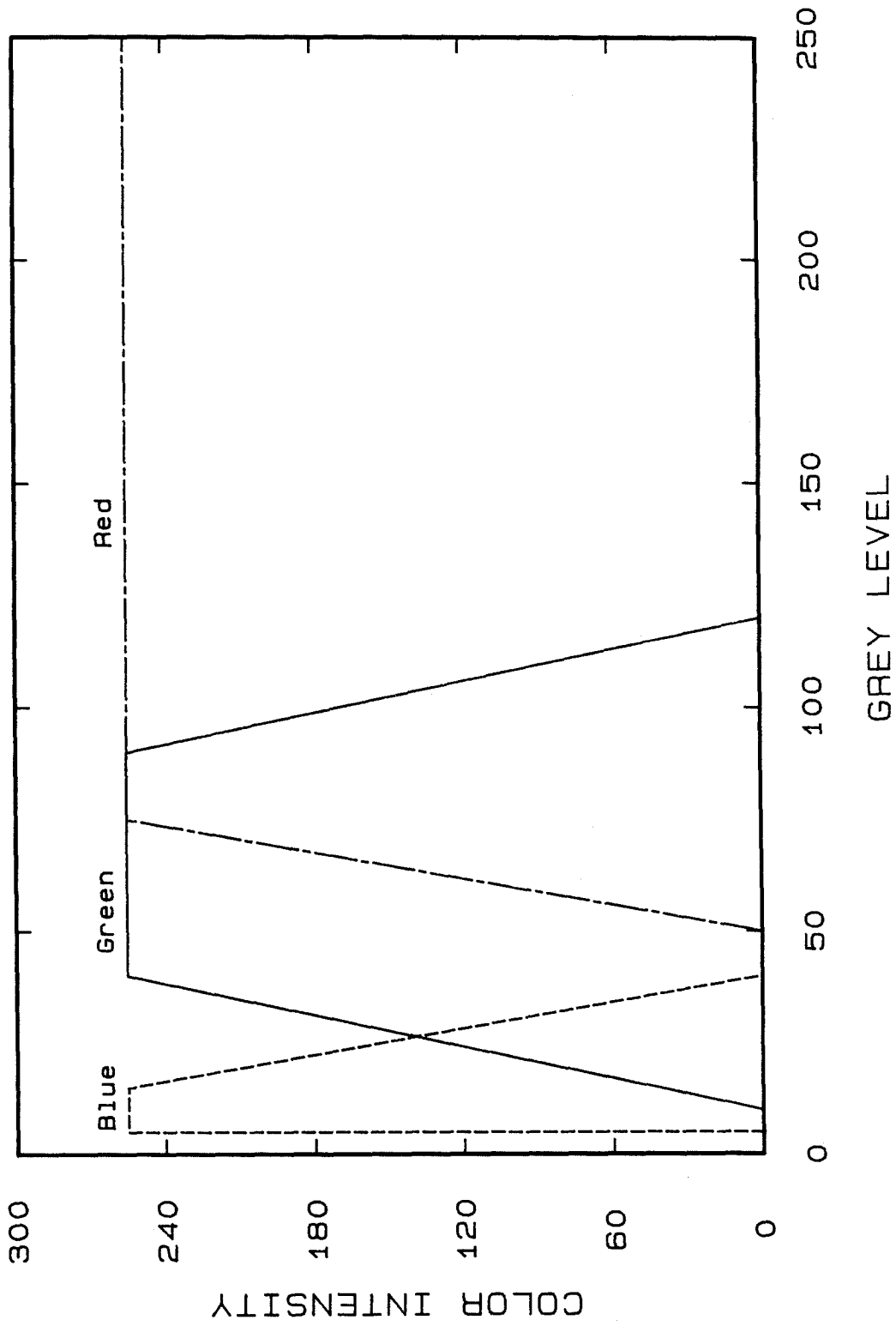
Figure 3.37 : Intensity Transformation Table used for Figure 3.36

(a) unforced flow

(b) F = 5.0 Hz X_{wo} = 3.1

(c) F = 2.5 Hz X_{wo} = 1.6

(d) F = 1.5 Hz X_{wo} = 0.9

Figure 3.38 : Flow Images from L.I.F. Measurements in a Transitional Layer
U_1 = 17.4 cm/sec , U_2 = 8.3 cm/sec
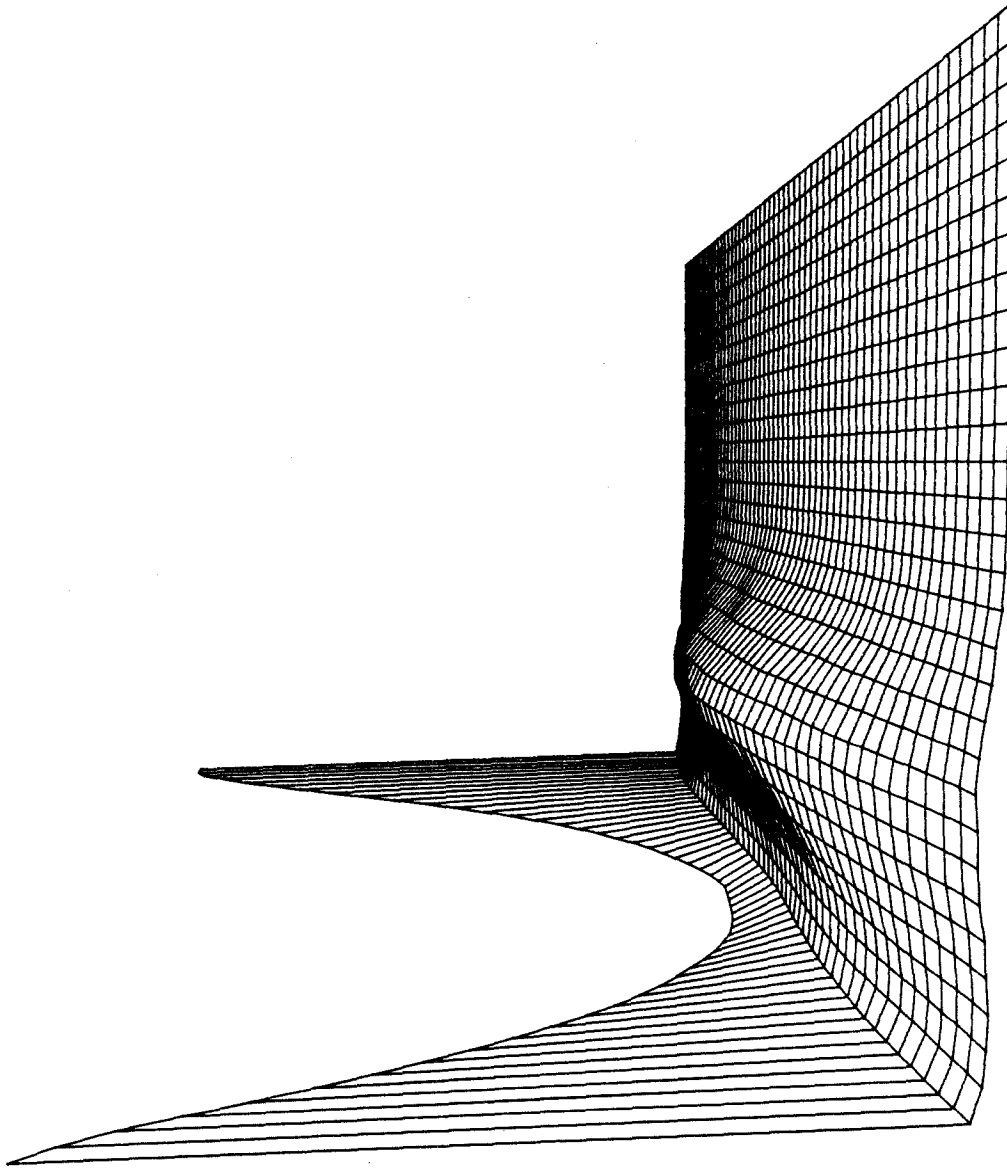
Figure 3.39: Concentration Histogram in the Unforced Flow from L.I.F.
Measurements at X = 25 cm. Width = concentration.
Height = probability, and Depth = y
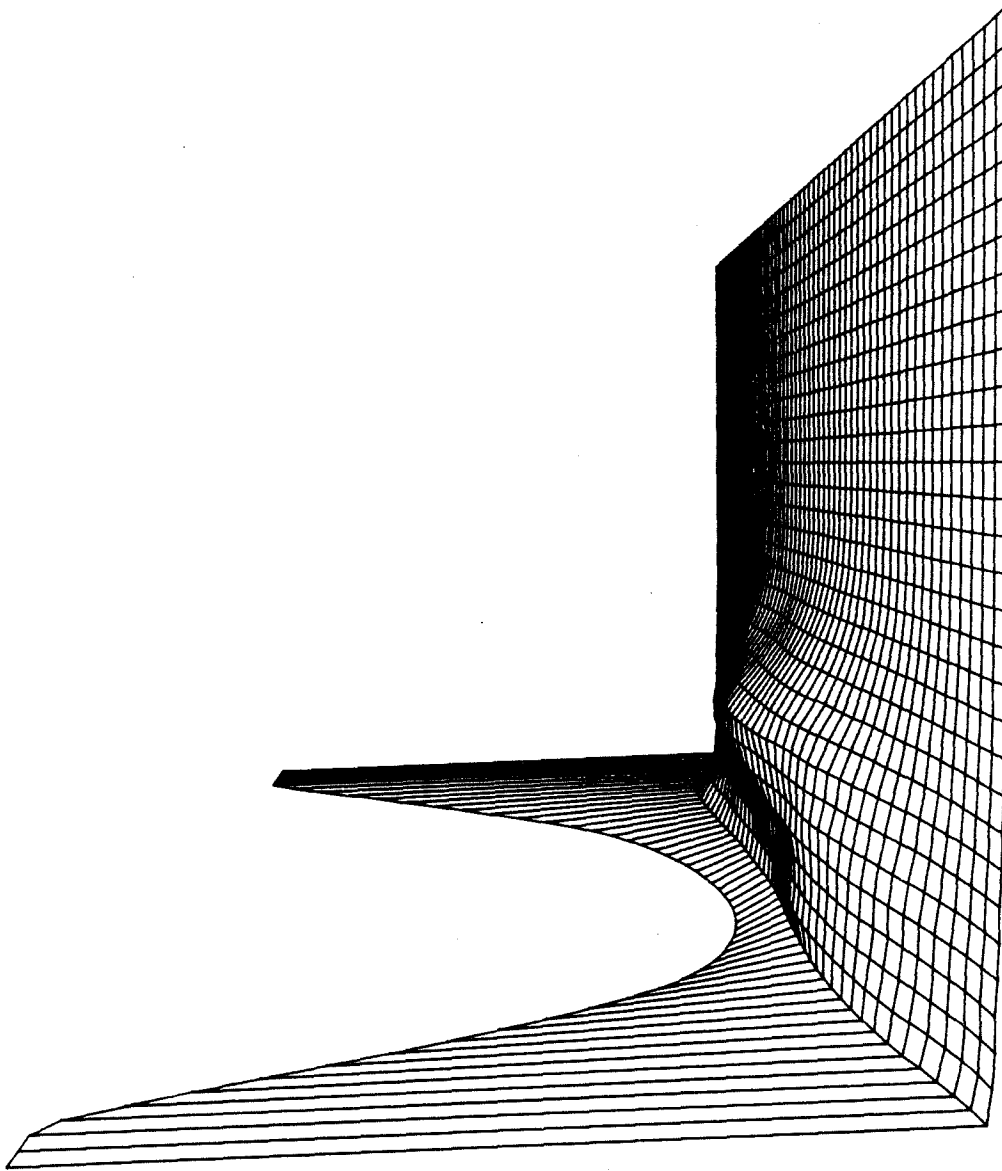
Figure 3.40: Concentration Histogram for F = 8 Hz Forced Flow from L.I.F. Measurements at X = 25 cm. Width = concentration. Height = probability, and Depth = y
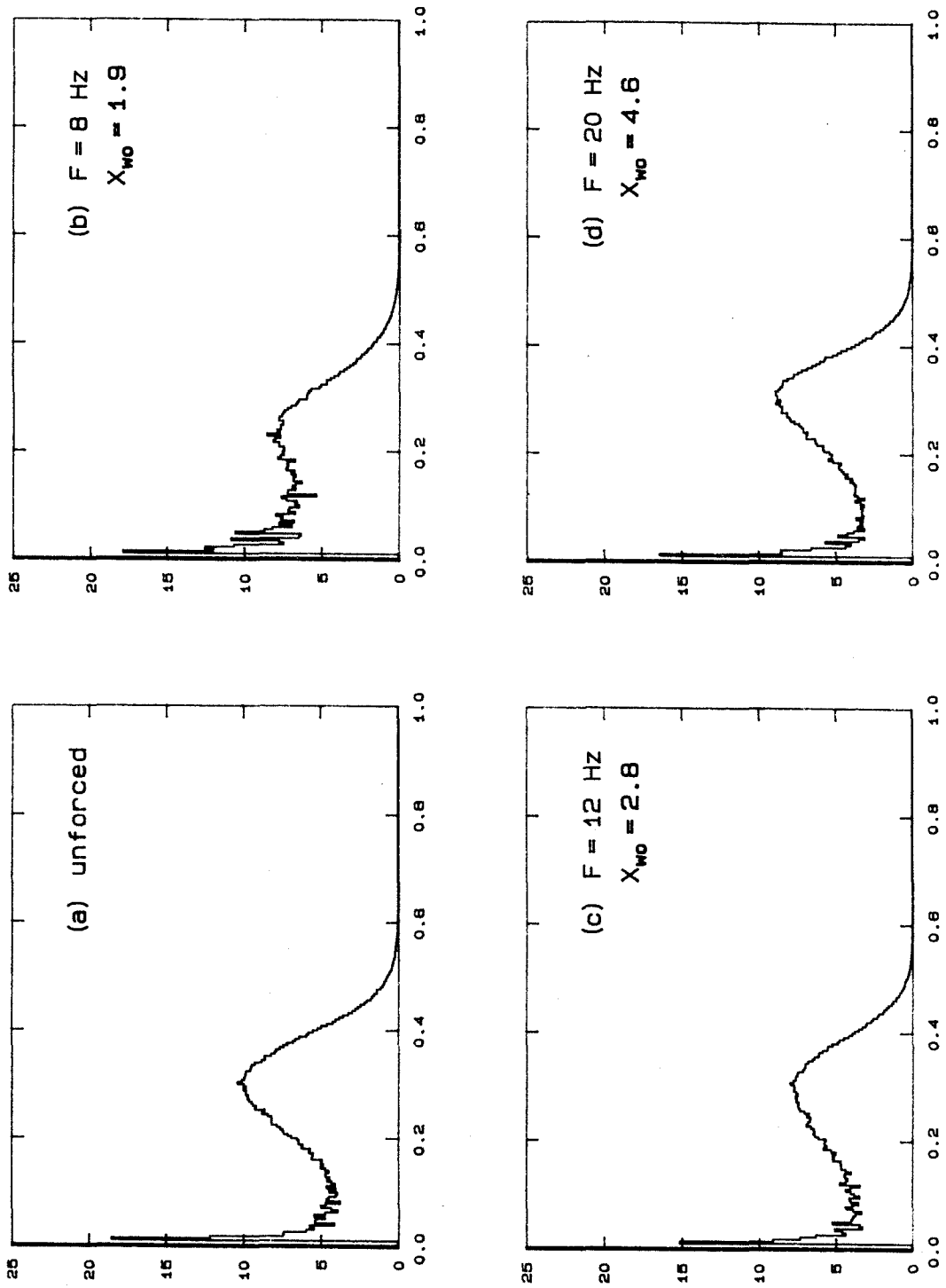
Figure 3.41: Mean Histograms. $U_1 = 70$ cm/sec, $U_2 = 27$ cm/sec, $x = 25$ cm
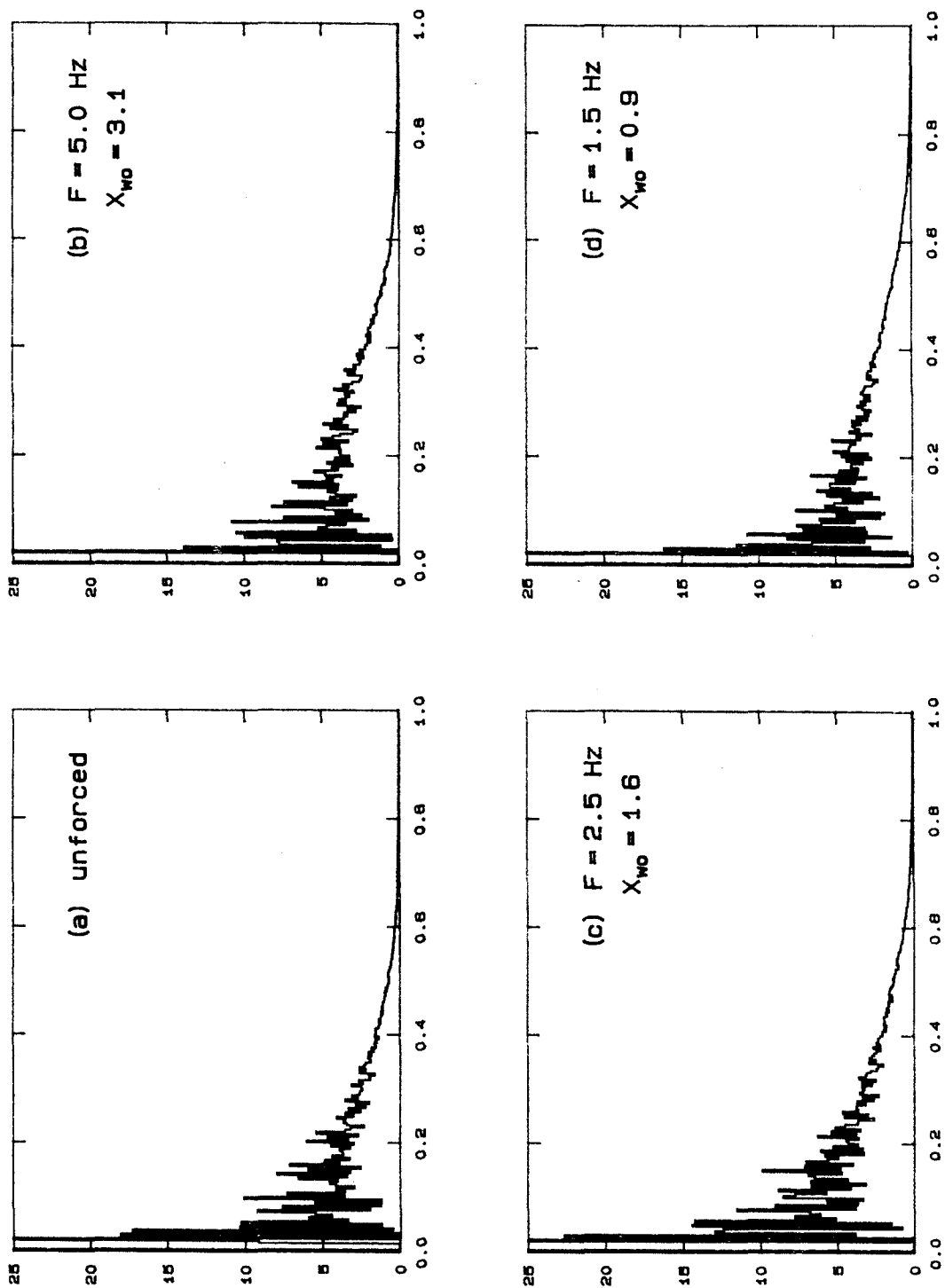
Figure 3.42: Mean Histograms, $U_1 = 17.4$ cm/sec, $U_2 = 8.3$ cm/sec, $x = 25$ cm
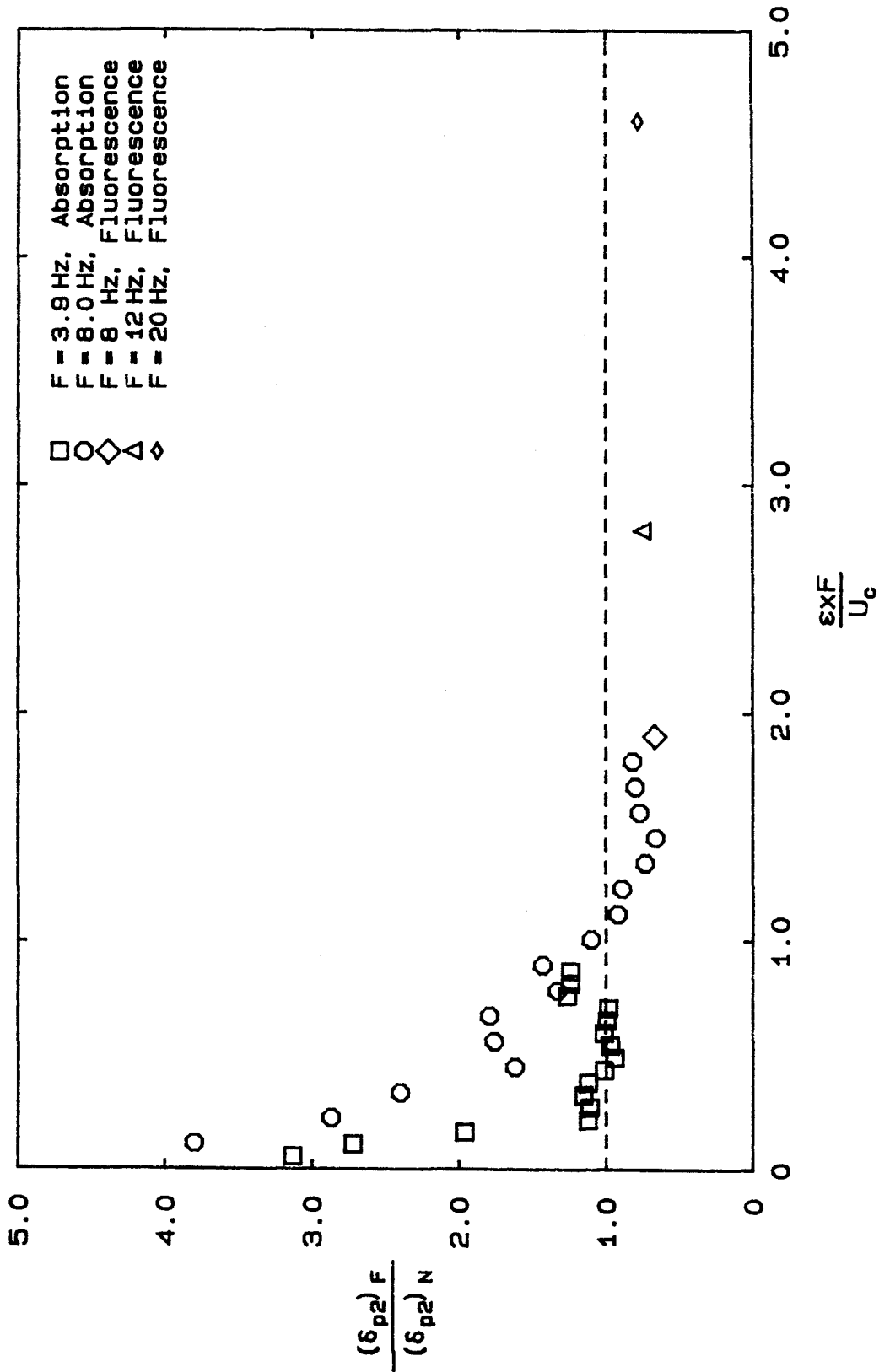
Figure 3.43a : Ratio of Forced Product Thickness to Natural Product Thickness
as a Function of Dimensionless Downstream Distance, X_{wo}.
High Reynolds Number Results.
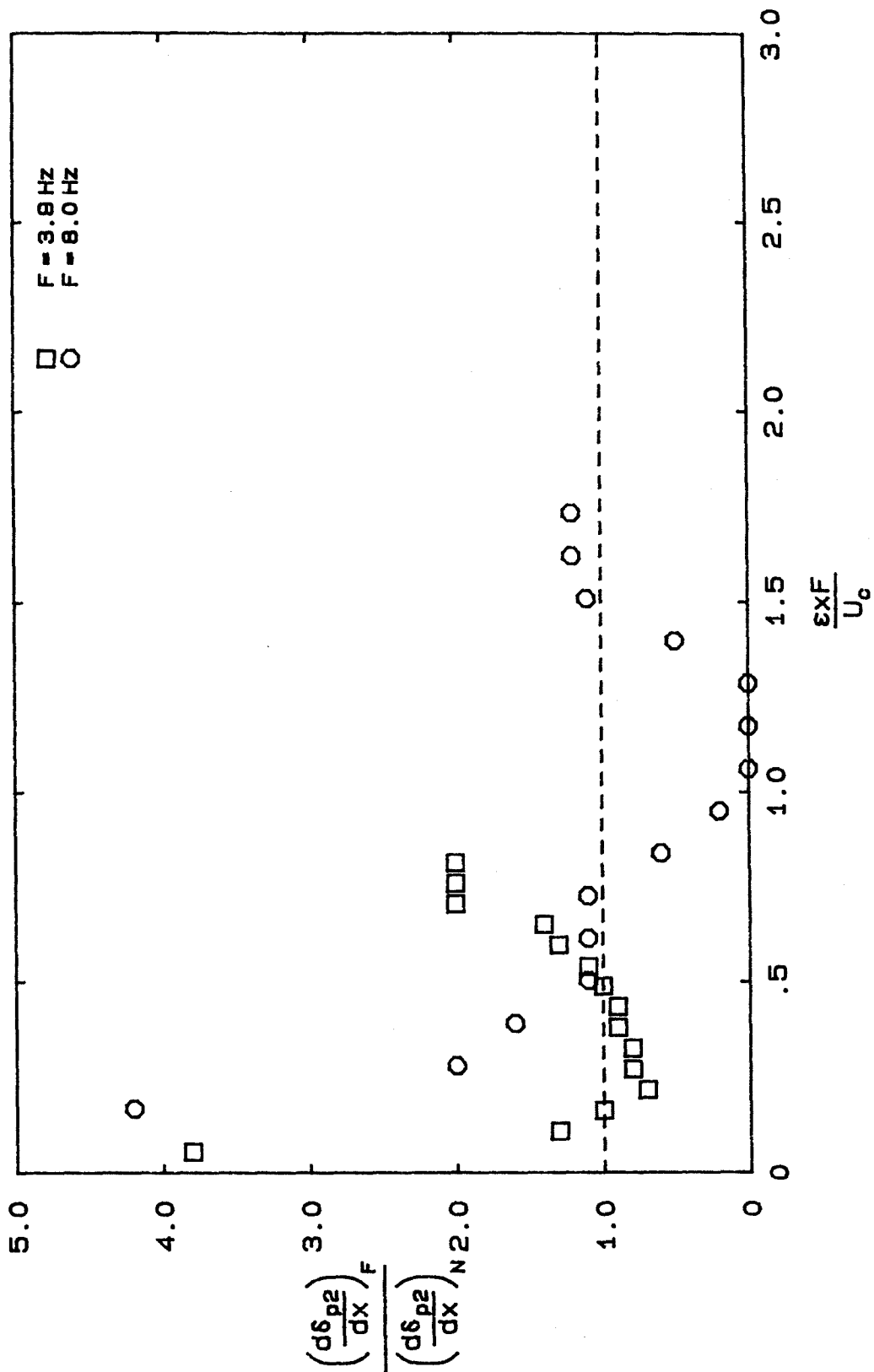
Figure 3.43b: Ratio of Forced Product Growth Rate to Natural Product Growth Rate as a Function of Dimensionless Downstream Distance, X_{wo} High Reynolds Number Results.
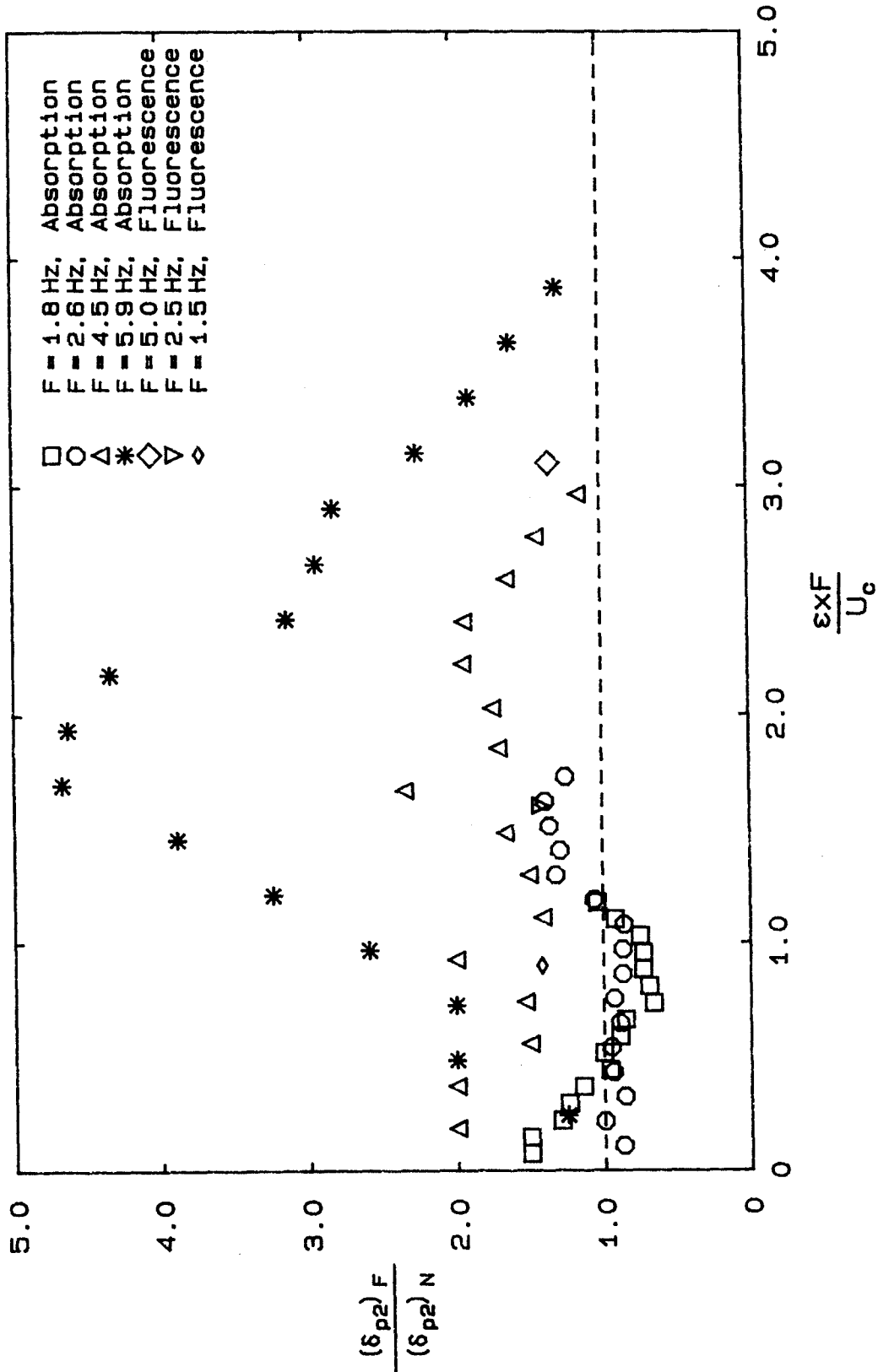
Figure 3.44a : Ratio of Forced Product Thickness to Natural Product Thickness as a Function of Dimensionless Downstream Distance, X_{wo}. Low Reynolds Number Results.
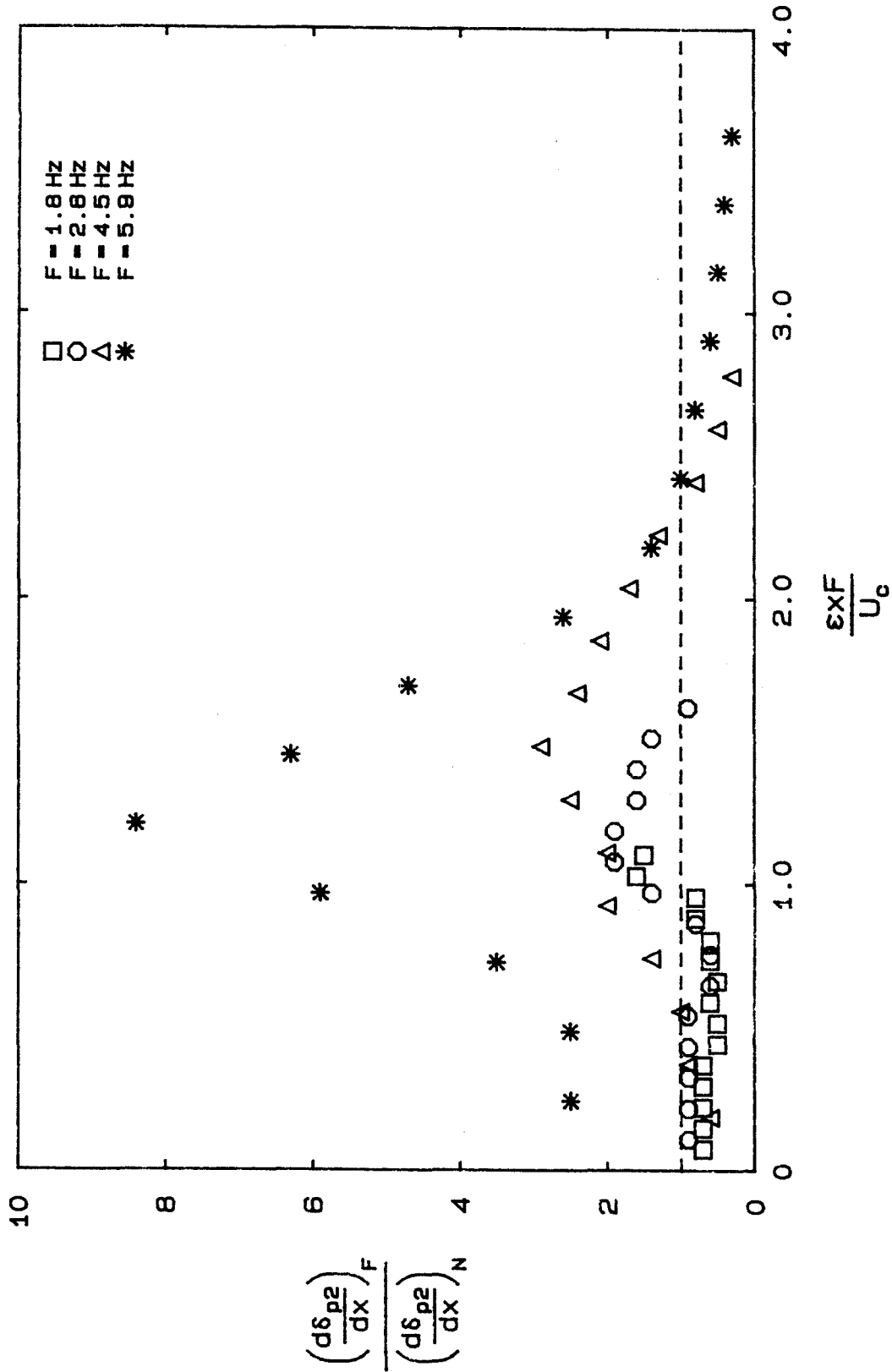
Figure 3.44b : Ratio of Forced Product Growth Rate to Natural Product Growth
Rate as a Function of Dimensionless Downstream Distance, X_{wo}
Low Reynolds Number Results.

Unforced Flow
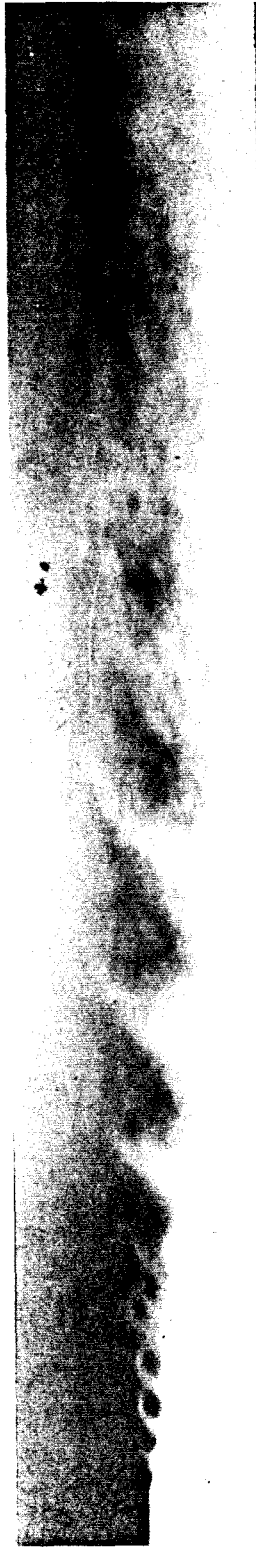
F = 8 Hz
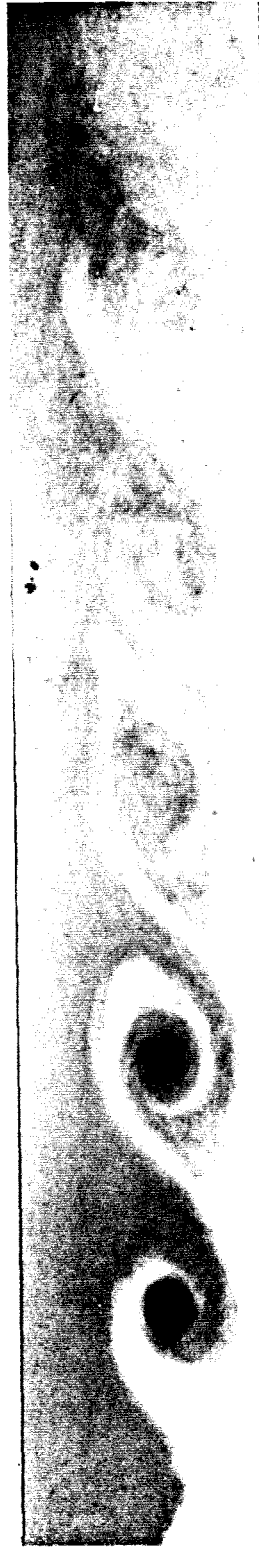
Figure 3.45 : The "Disappearing Vortex" Experiment. $U_1 = 70$ cm/sec. $U_2 = 27$ cm/sec. Reacted fluid is black only when the ratio of high-speed to low-speed fluid in the mixed region is greater than five.
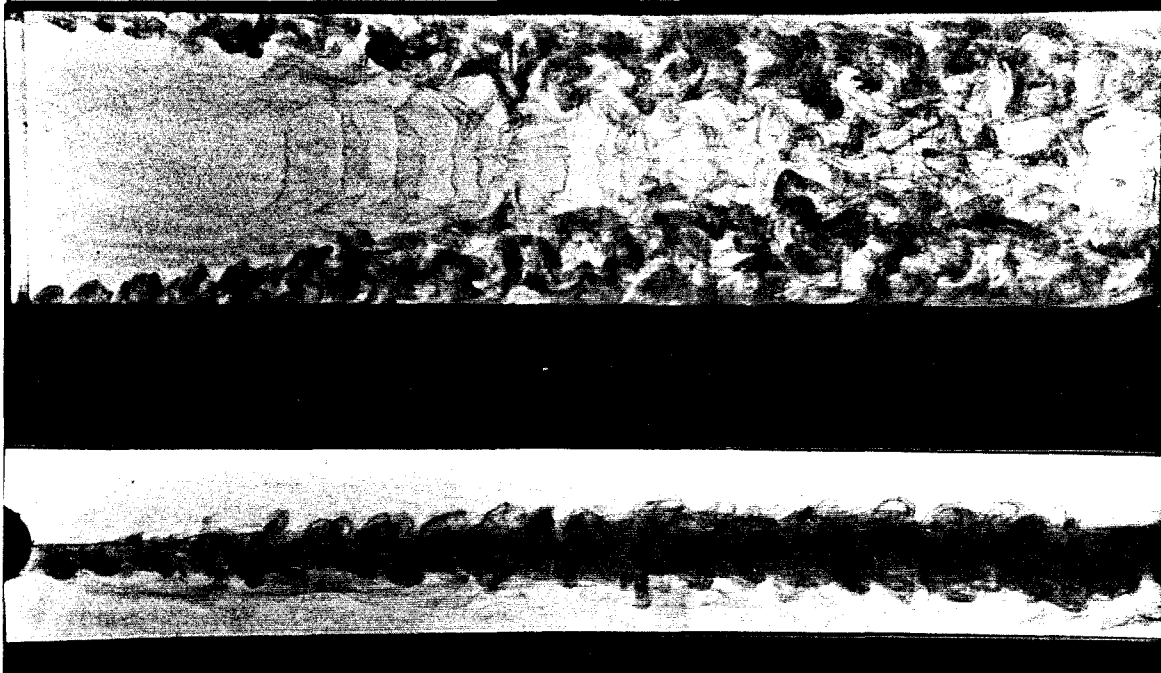
(a) Side and Plan Views of Phenolphthalein Reaction

(b) Reacting L.I.F. Cross-section. Scale different than (a).

Figure 4.1 : Unforced Wake at a Reynolds Number of 160
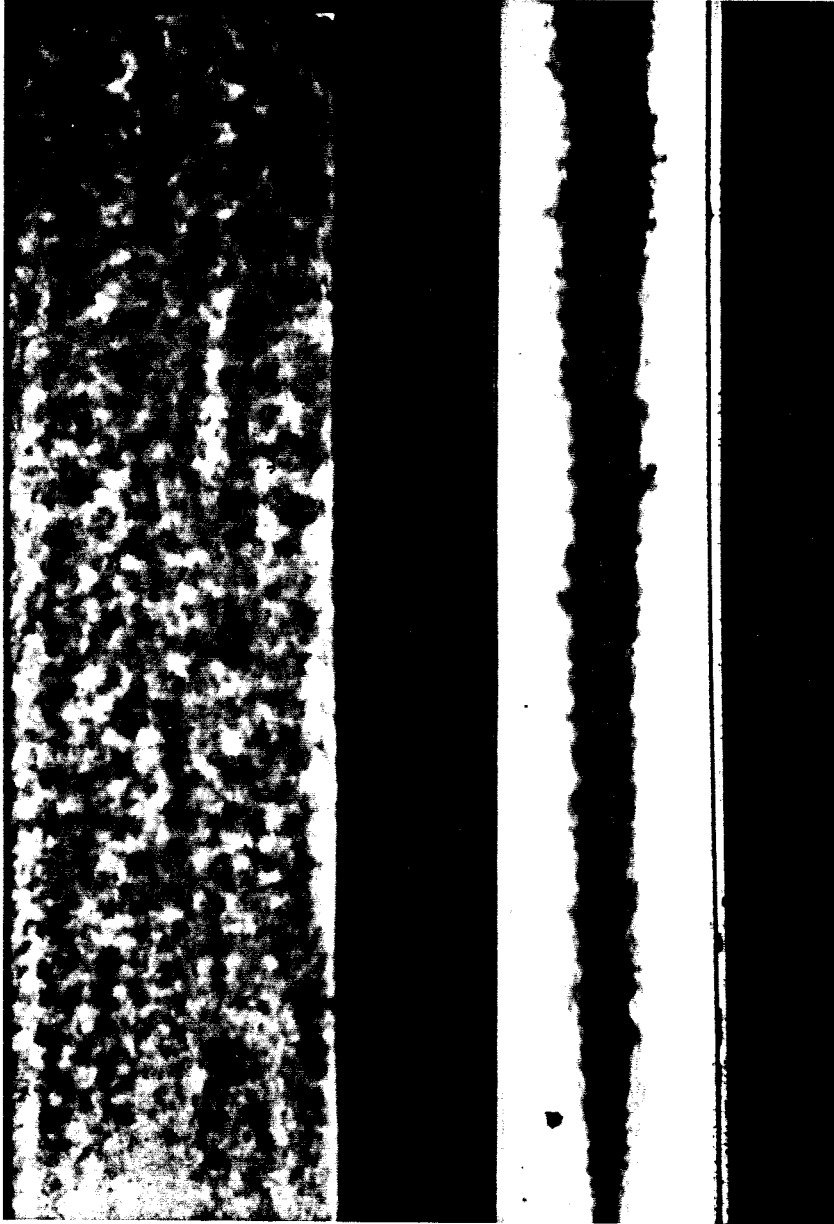
Figure 4.2: Simultaneous Plan and Side Views of a Turbulent Wake
$U_\infty = 50$ cm/sec, Unforced
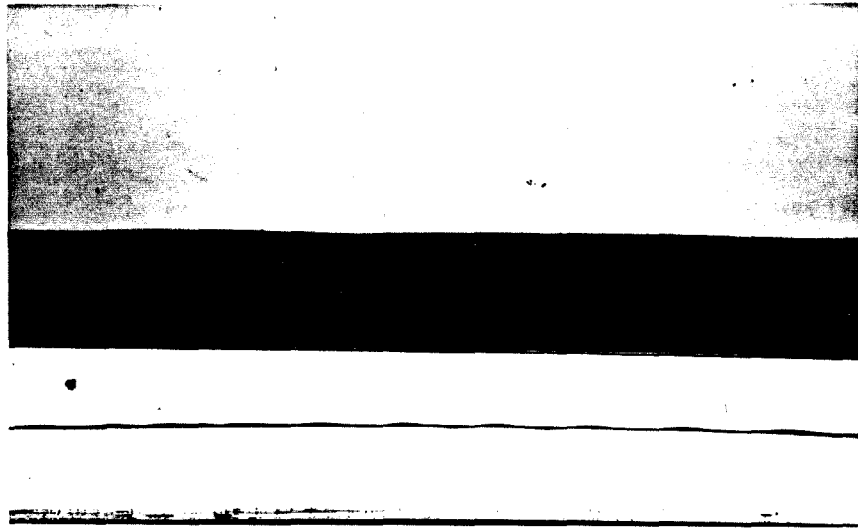
(a) Plan and Side Views
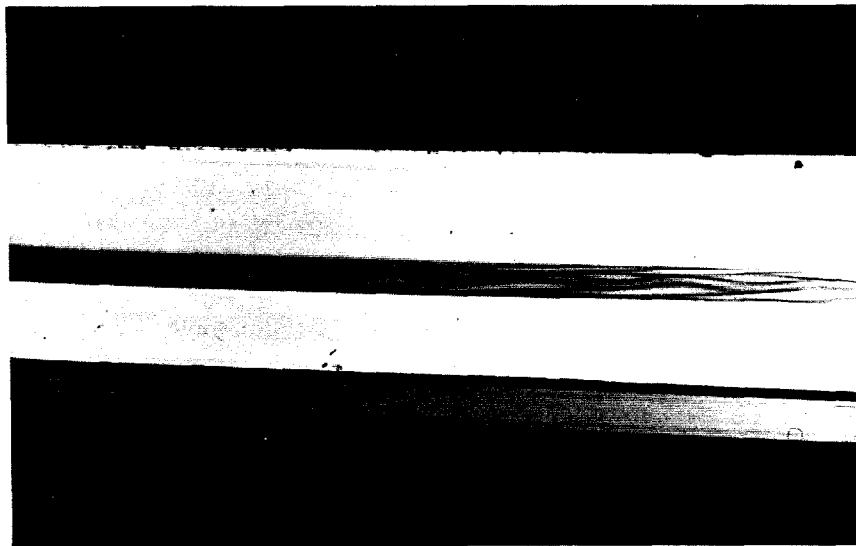
(b) Oblique View

Figure 4.3 : Effects of Forcing on a Laminar Wake (F = 0.5 Hz , U_∞ = 2 cm/s)
(a) Simultaneous Plan and Side Views   (b) Oblique View
-- looking down and slightly upstream
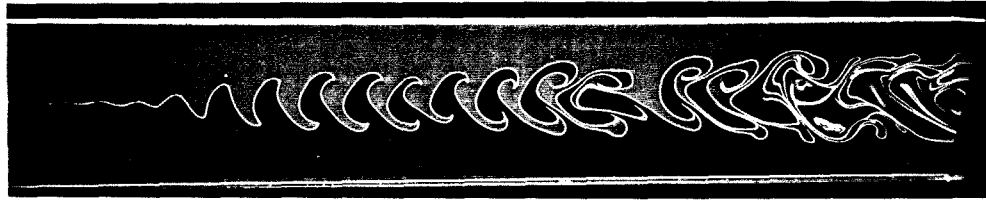
(a) Unforced flow

(b) F = 4.4 Hz

(c) F = 1.7 Hz
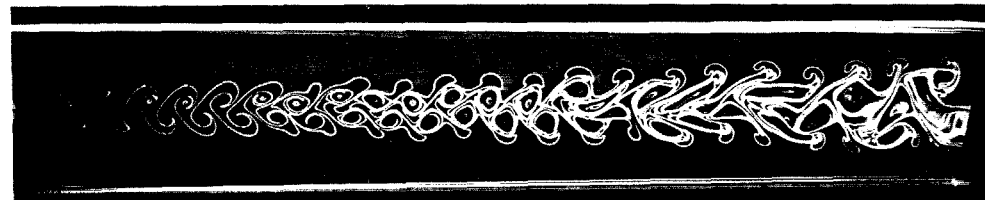
(d) F = 6.5 Hz

(e) F = 9.8 Hz

(f) F = 10.8 Hz

Figure 4.4 : Effects of Forcing on a Transitional Wake
$U_\infty = 12$ cm/sec , $Re_{\theta_w} = 160$
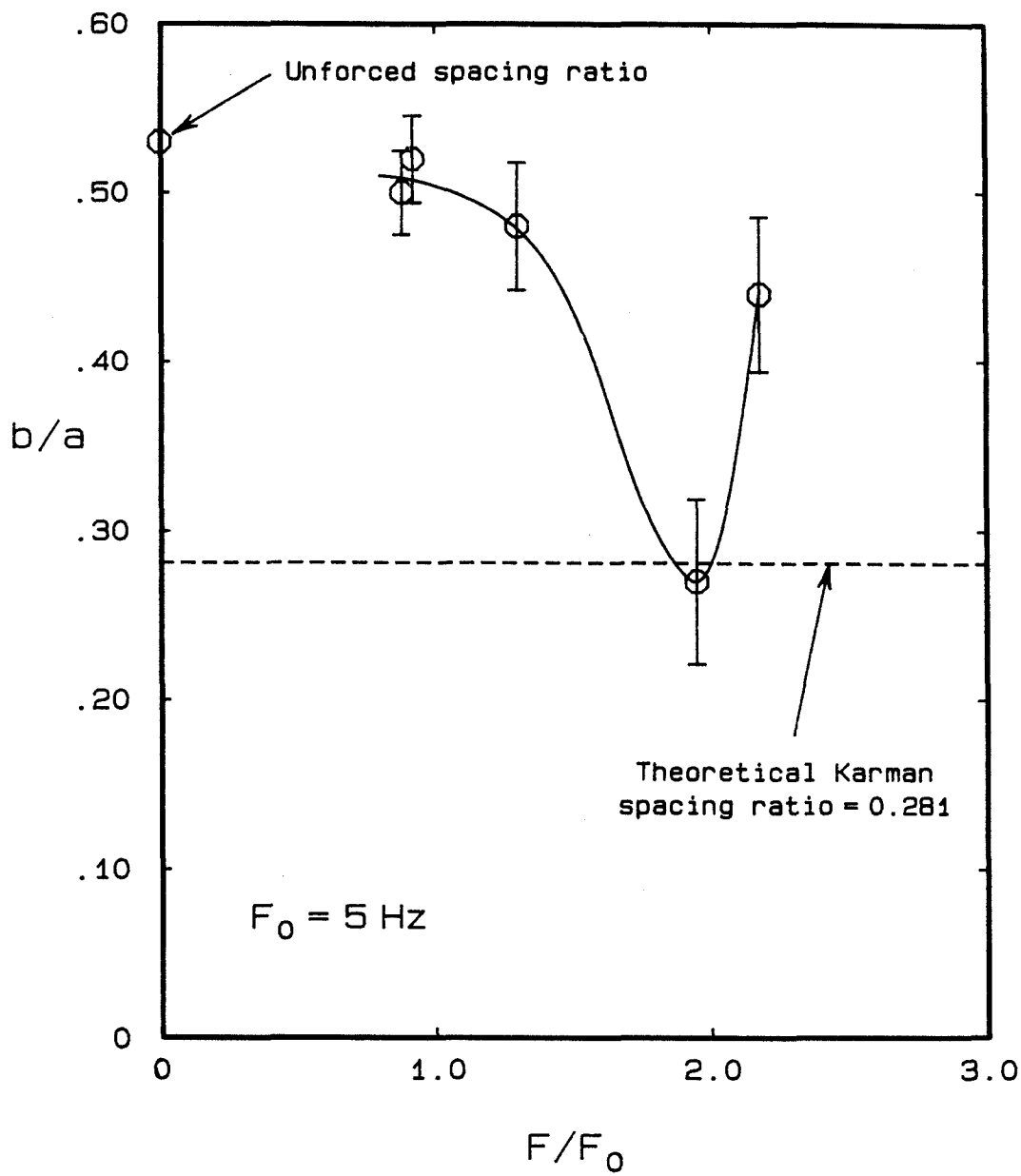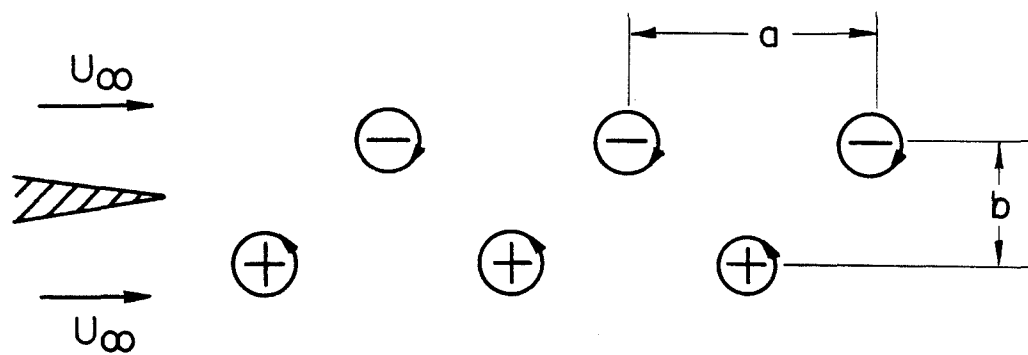
Figure 4.5 : Effect of Forcing on Spacing Ratio in the Initial Karman
Vortex Street of a Transitional Wake (U_∞ = 12 cm/sec)
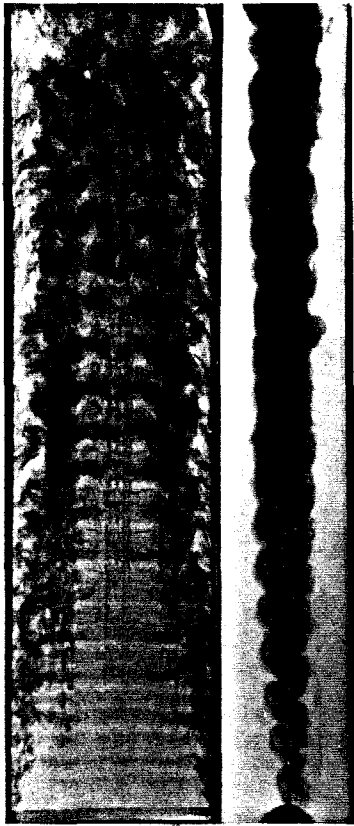
(a) F = 1.8 Hz

(b) F = 6.5 Hz
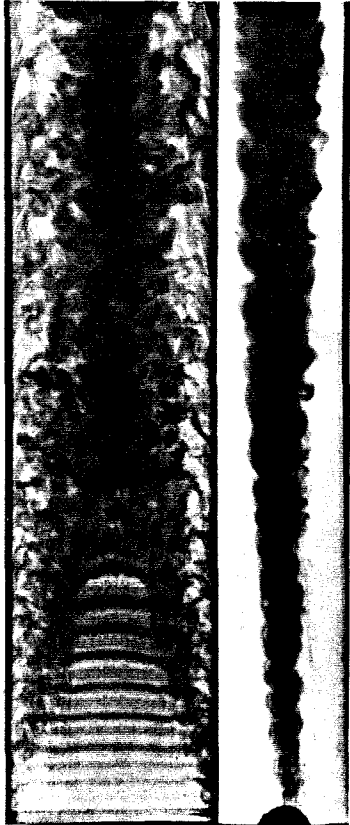
(c) F = 9.3 Hz

(d) F = 10.3 Hz

Figure 4.6: Reacting Phenolphthalein Pictures of the $Re_{\theta_w} = 160$ wake.
$U_\infty = 12$ cm/sec, $\theta_w = 1.3$ mm

(a) unforced

(b) F = 11.5 Hz

(c) F = 7.5 Hz

(d) F = 5.3 Hz

(e) F = 4.2 Hz

(f) F = 3.2 Hz

(g) F = 2.2 Hz

U_∞ = 24 cm/sec

θ_W = 0.9 mm

Re_{θ_W} = 220
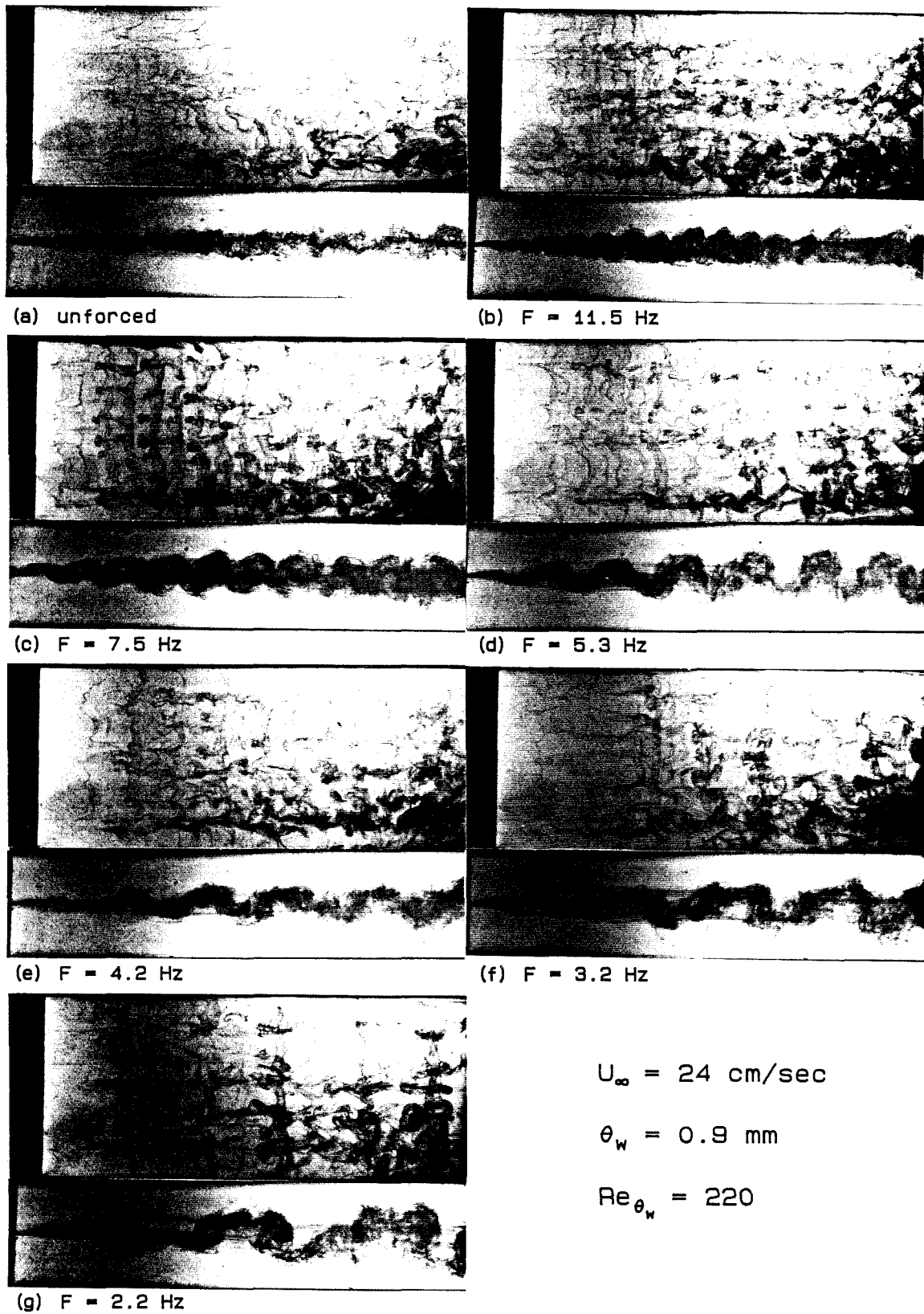
Figure 4.7 : Effects of Forcing on a Re_{θ_W} = 220 Wake.
Side and Plan Views of Reaction Product.

(a) unforced flow

(b) F = 5.9 Hz

Figure 4.8 : Effects of Forcing on a Re_{θ_w} = 200 Wake.
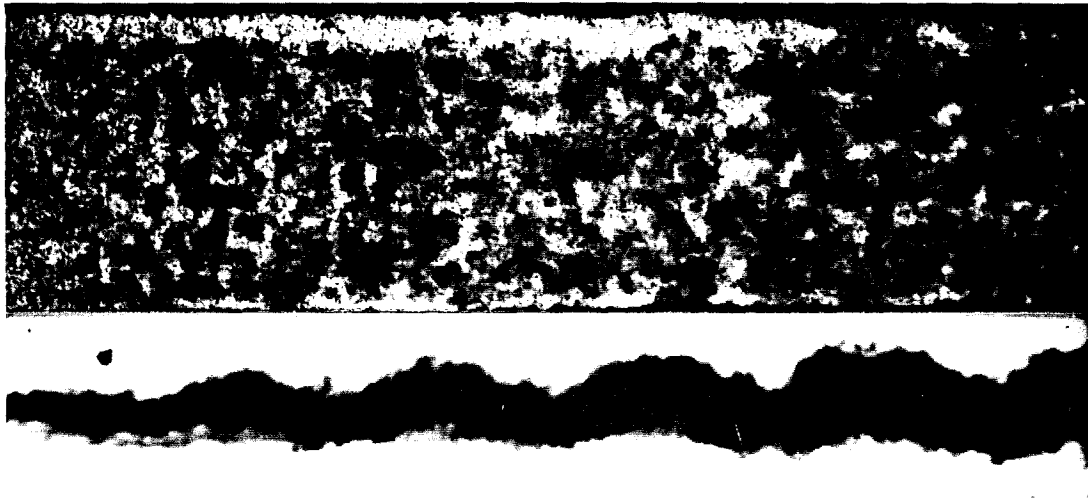
(a) F = 12.5 Hz
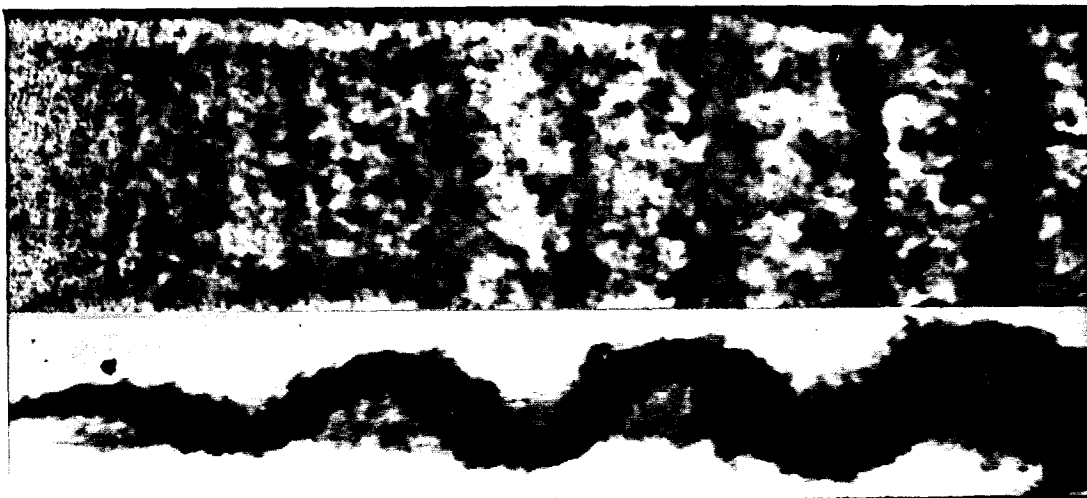
(b) F = 9.1 Hz

Figure 4.9 : Photographs of a Forced "Turbulent" Wake ($Re_{\theta_w} = 320$).

(c) F = 7.1 Hz

(d) F = 5.9 Hz

Figure 4.9 : (continued) Forced "Turbulent" Wake (Re_{θ_M} = 320) .
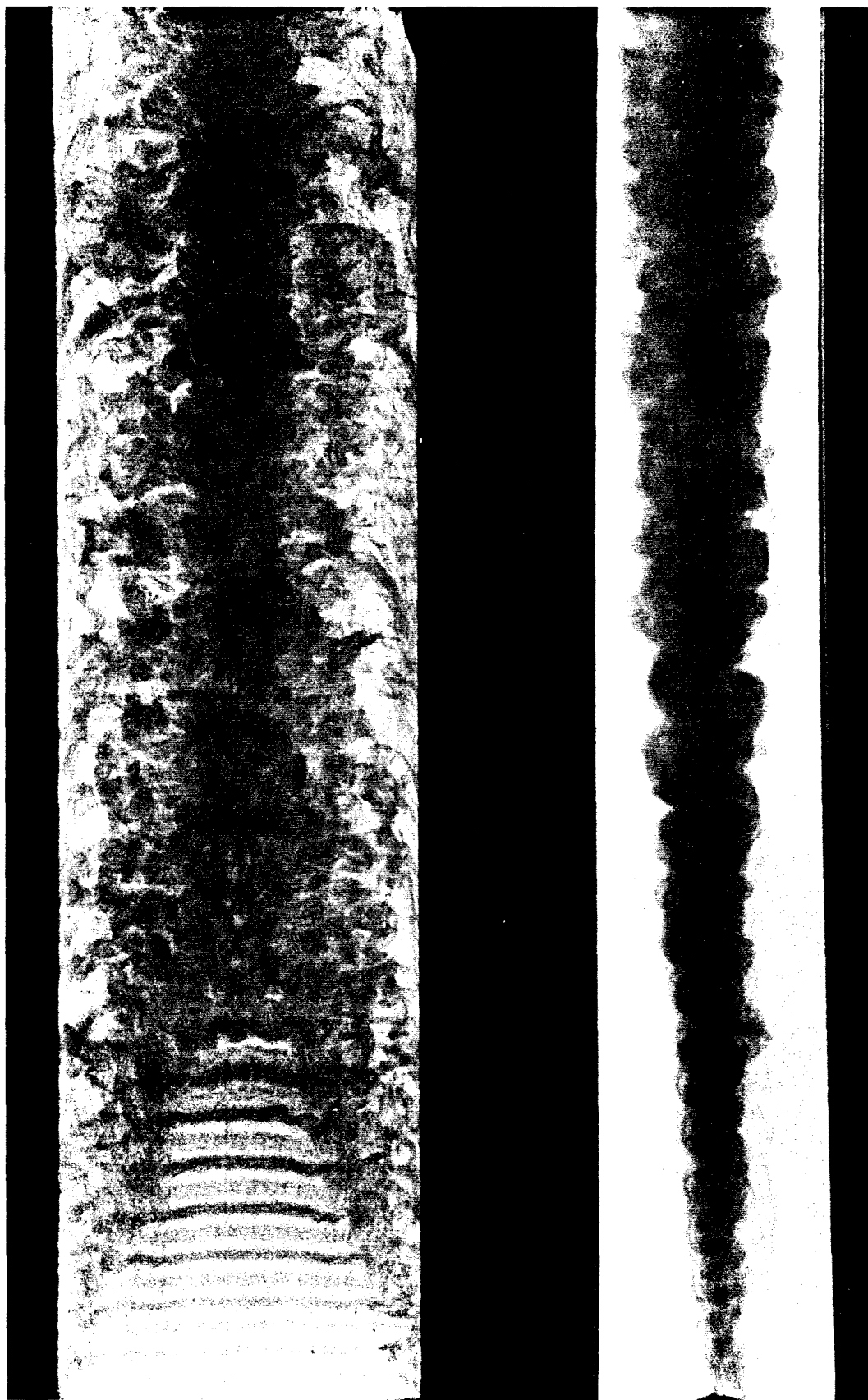
Figure 4.10 : Simultaneous Plan and Side Views of the Highly Mixed Wake
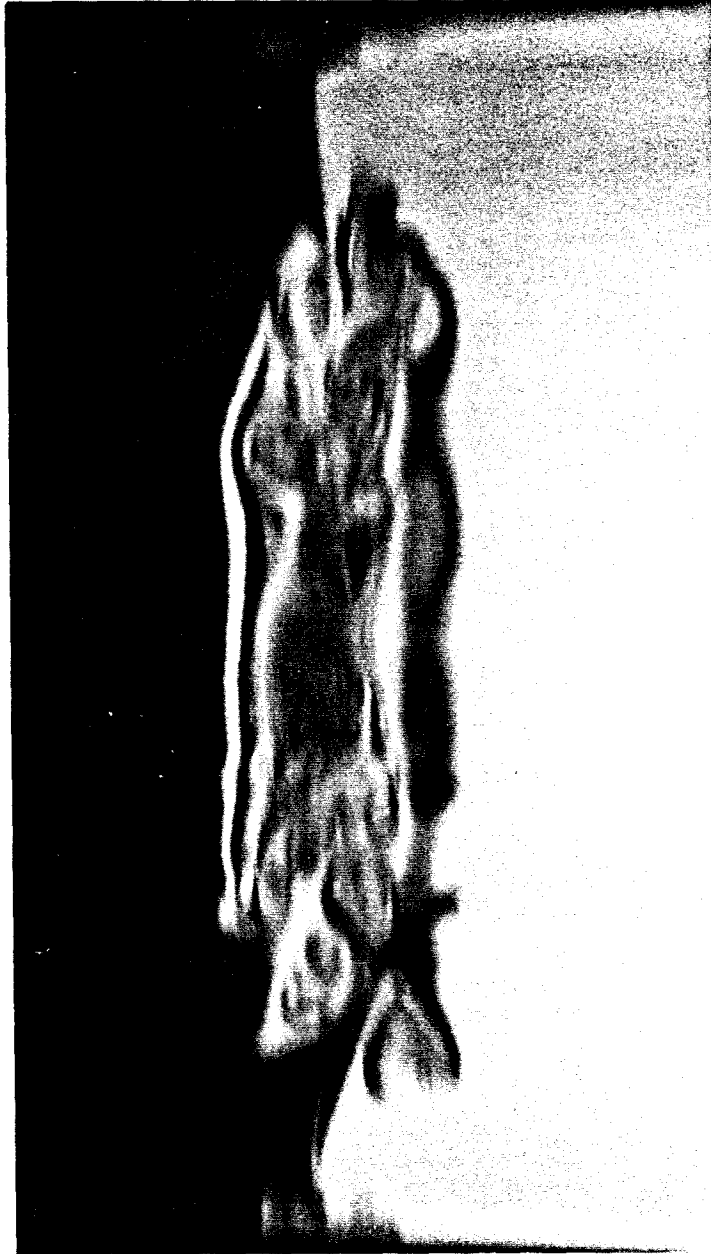
Figure 4.11 : Cross-section View of the Highly Mixed Wake using
Non-Reacting L.I.F. Visualization
x = 12 cm
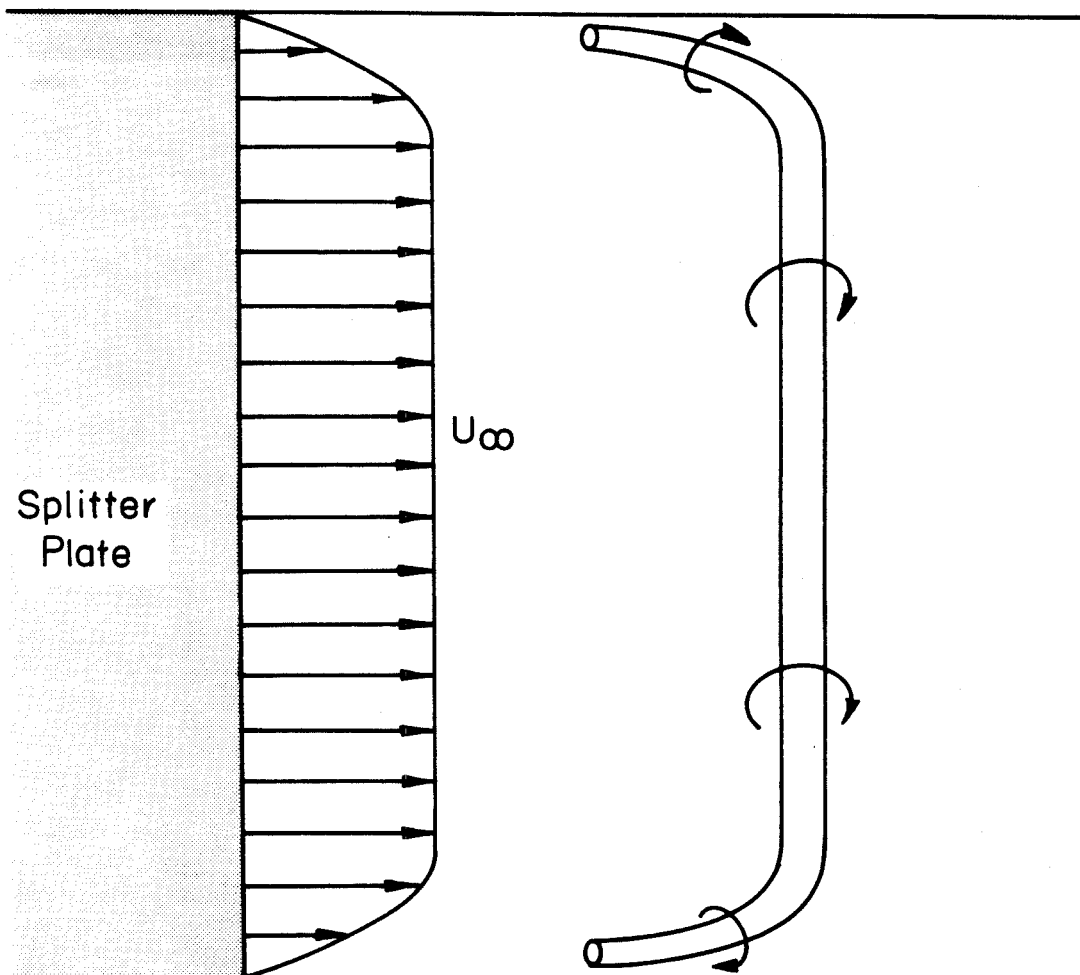
Figure 4.12 : "Tipping" of Spanwise Vorticity by the No-Slip Condition
on the Test Section Side-Walls.

195
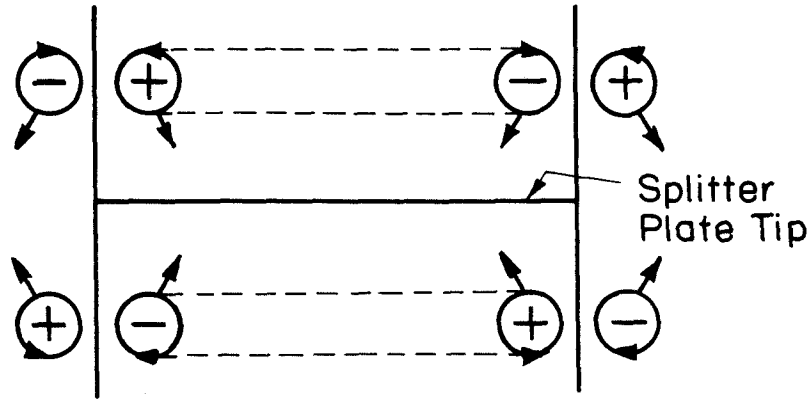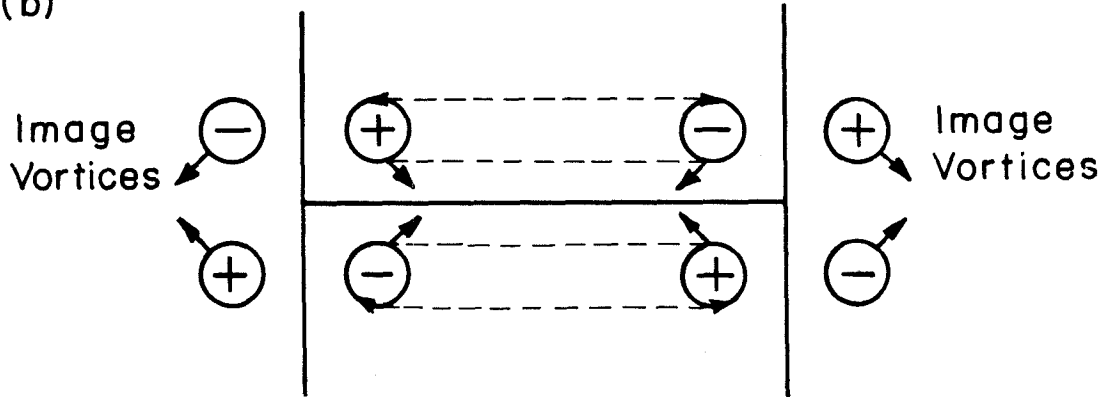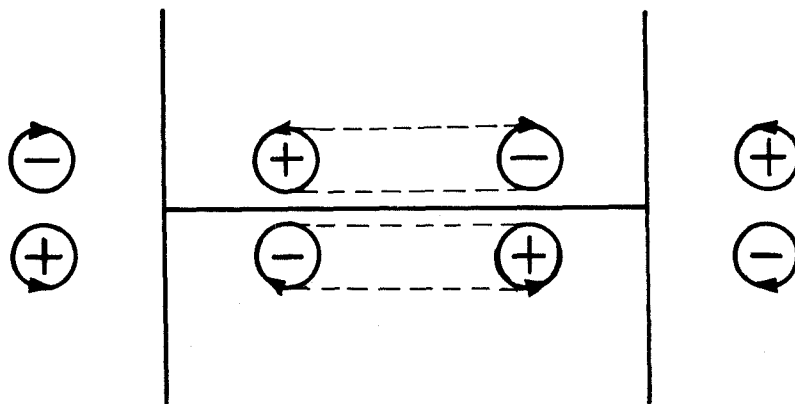
Figure 4.13 : Model for Motion of the Streamwise Vortices in the Highly Mixed Wake . The view point is from downstream looking upstream. (a) near splitter plate (b) intermediate stage (c) steady equilibrium configuration

Figure 4.14 : Effect of a "False Wall" on the Highly Mixed Wake
Simultaneous Plan and Side Views

(a)

(b)

(c)

(d)
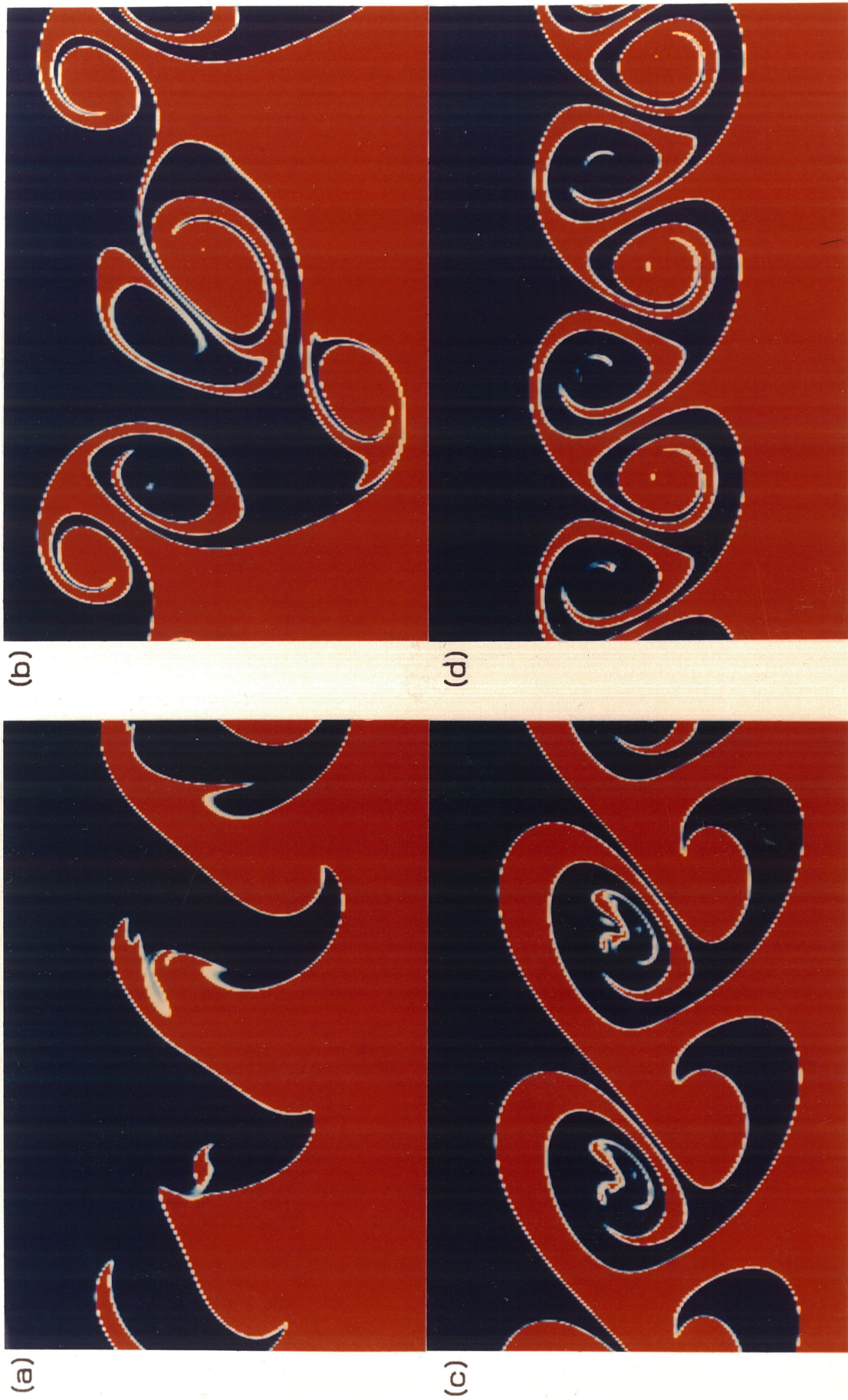
Figure 4.15 : Flow Images from Non-Reacting L.I.F. Measurements in the
Transitional Wake, $U_\infty = 12$ cm/sec, x = 25 cm, (a) Unforced
(b) F = 1.6 Hz (c) F = 3.1 Hz (d) F = 3.9 Hz
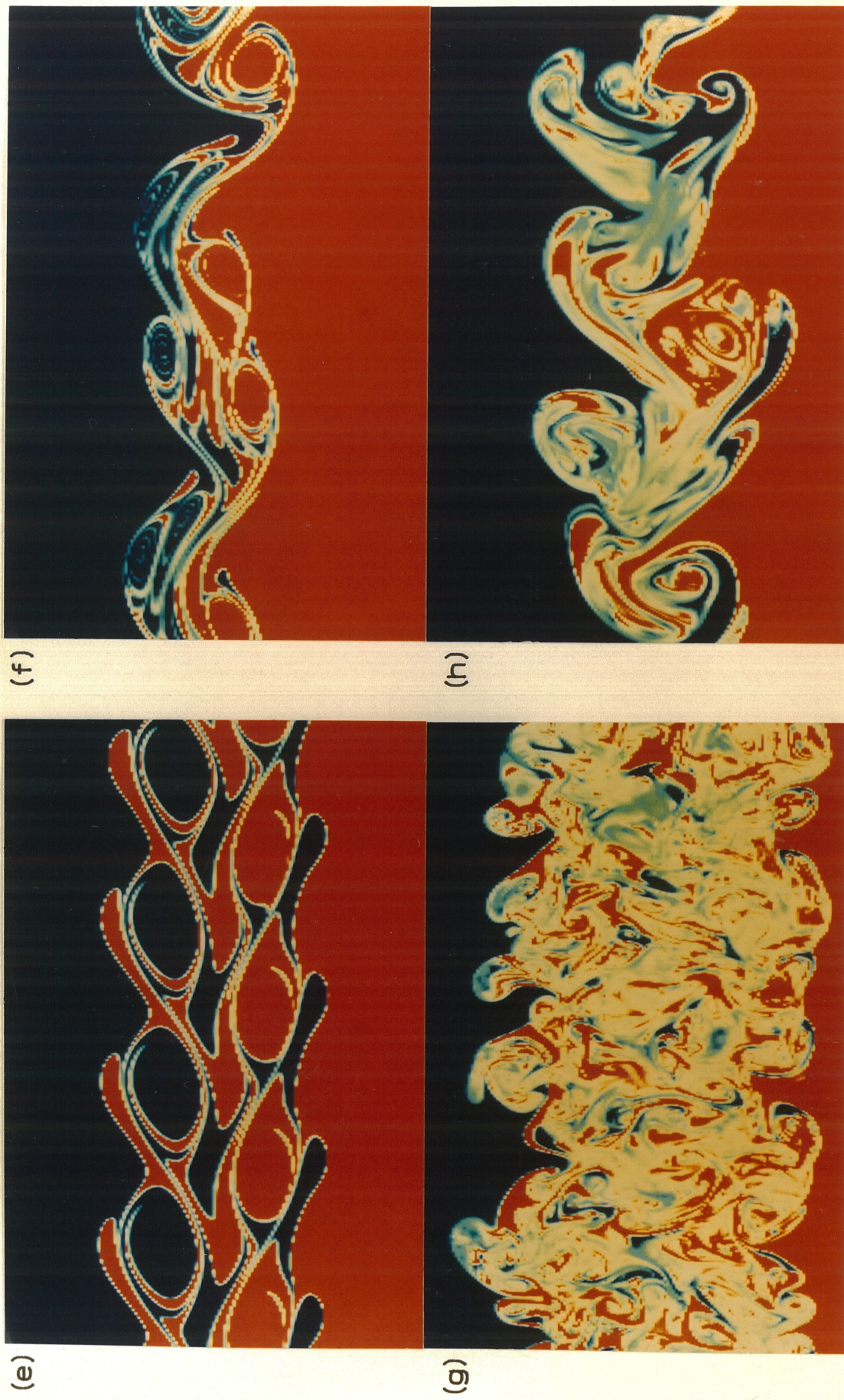
(f)

(h)

(e)

(g)

Figure 4.15 (continued) : (e) F=4.8 Hz (f) F=6.9 Hz (g) F=9.5 Hz
(h) F=12.2 Hz
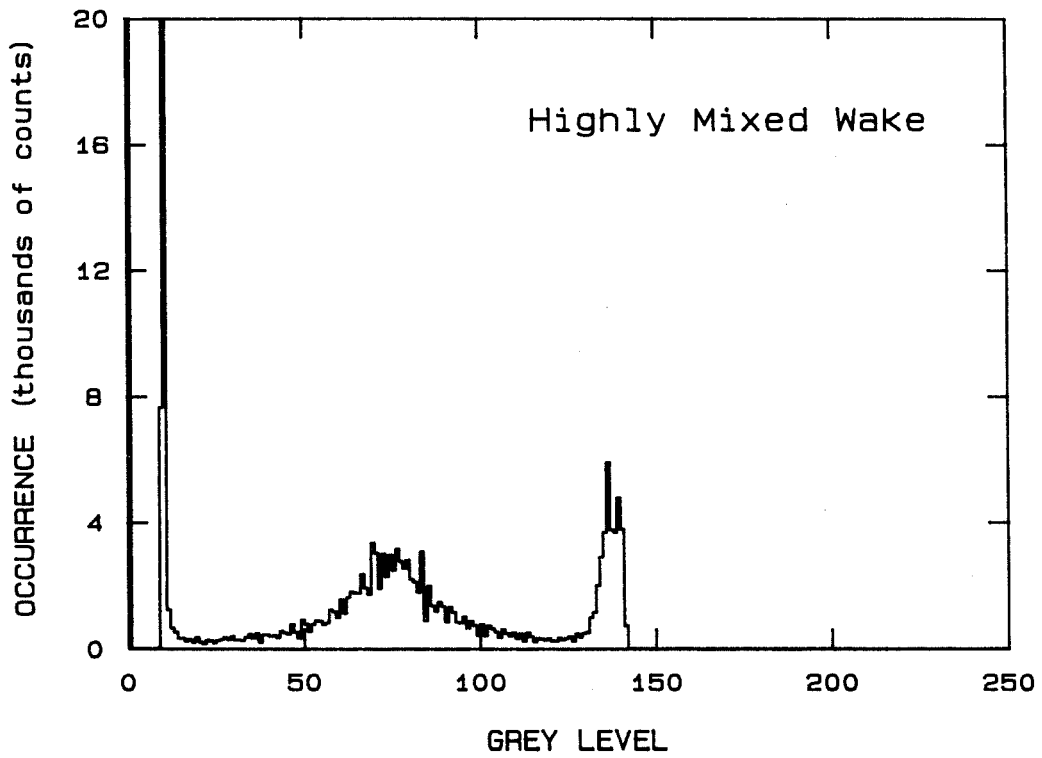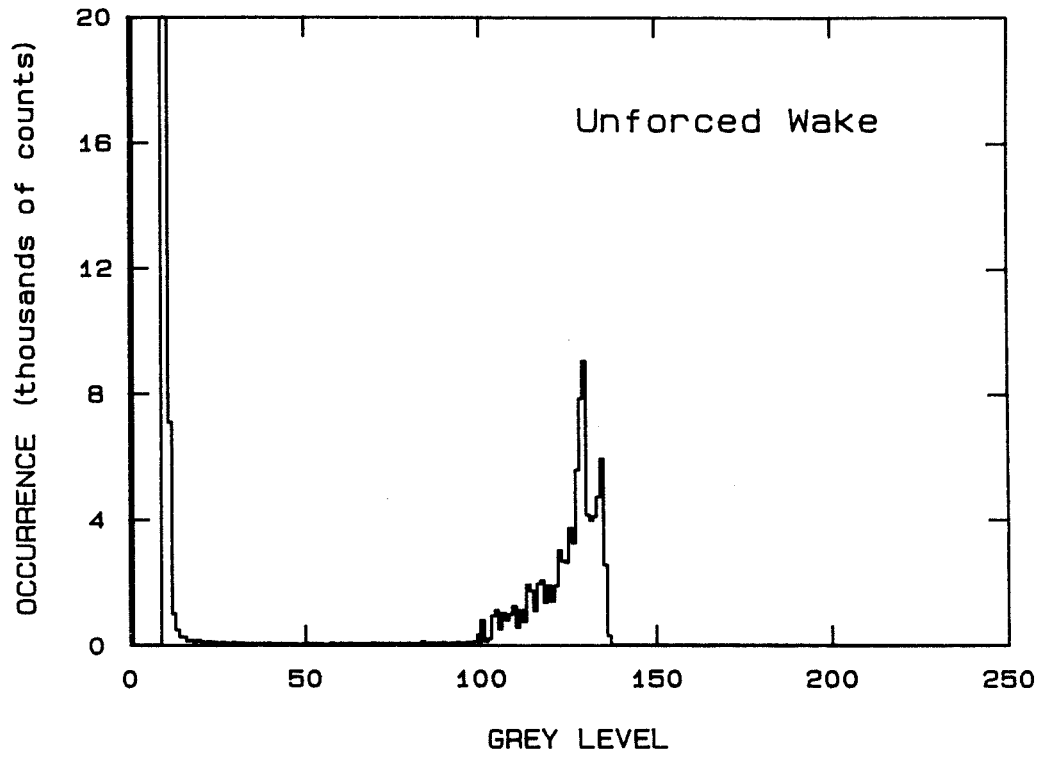
Figure 4.16 : Mean PDF from Non-Reacting L.I.F. Measurements
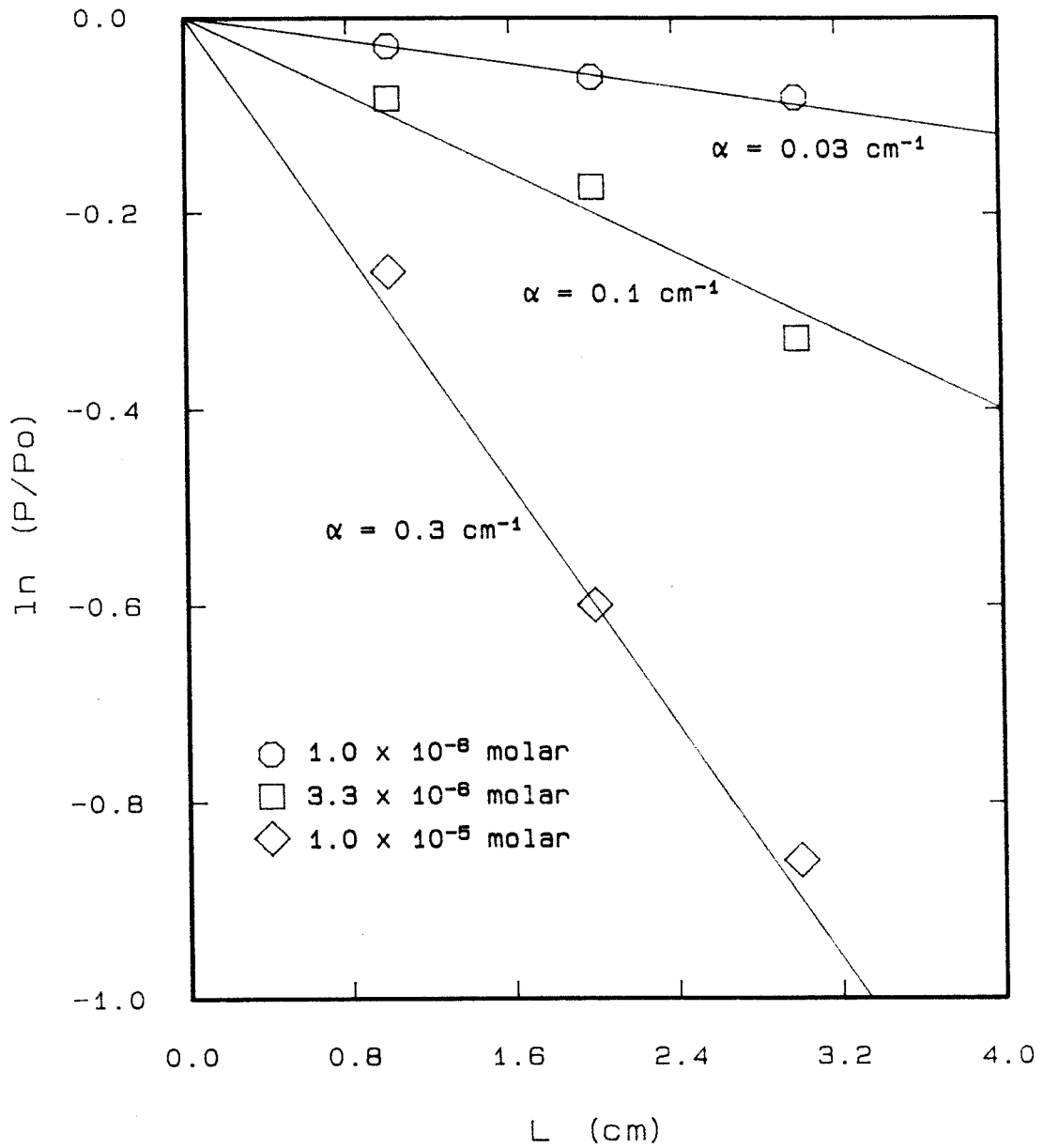
Figure A.1 : Calibration of Phenolphthalein as an Absorbing Medium
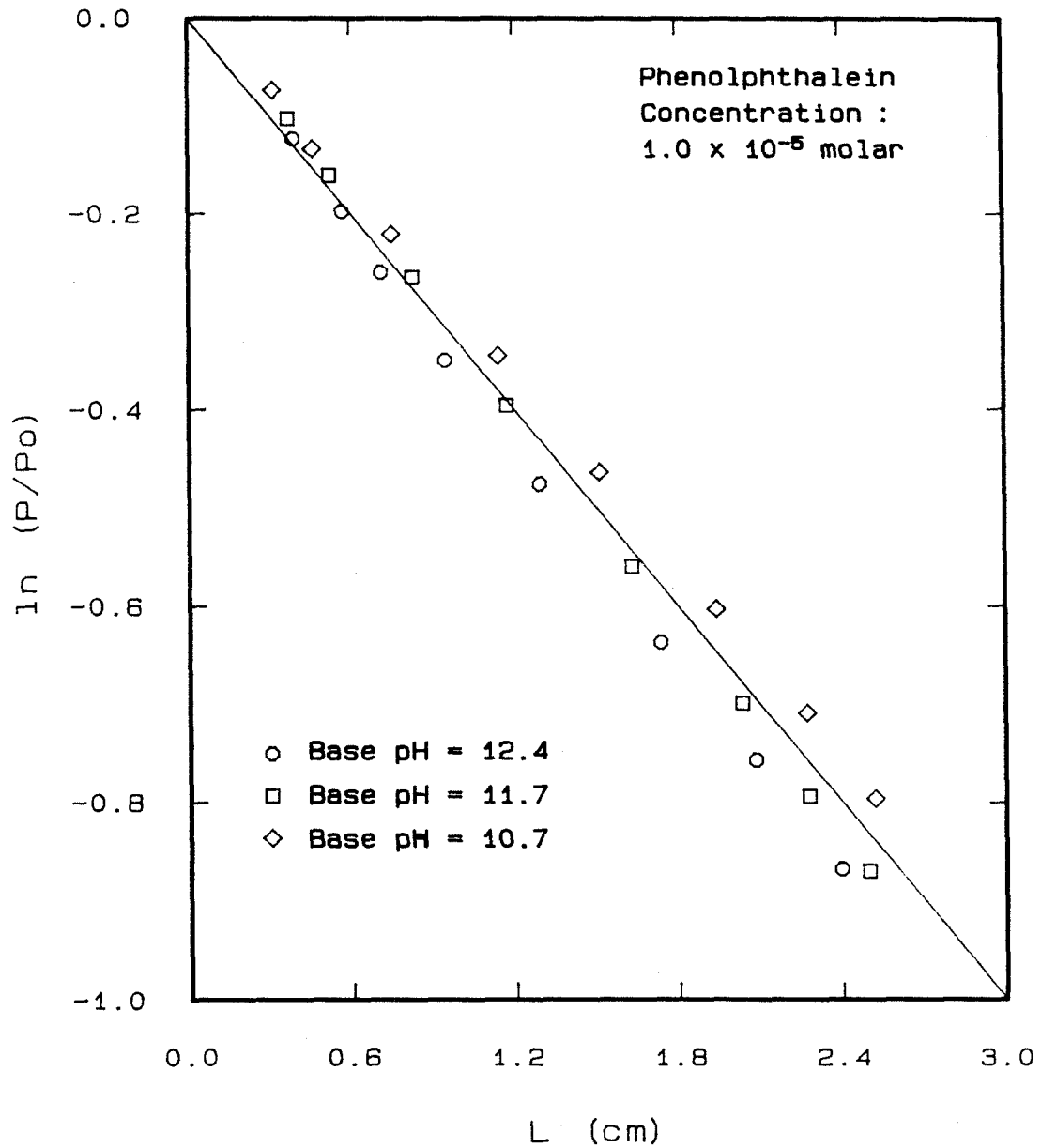
Figure A.2 : Effect of Base Concentration on the
Absorption Coefficient, α
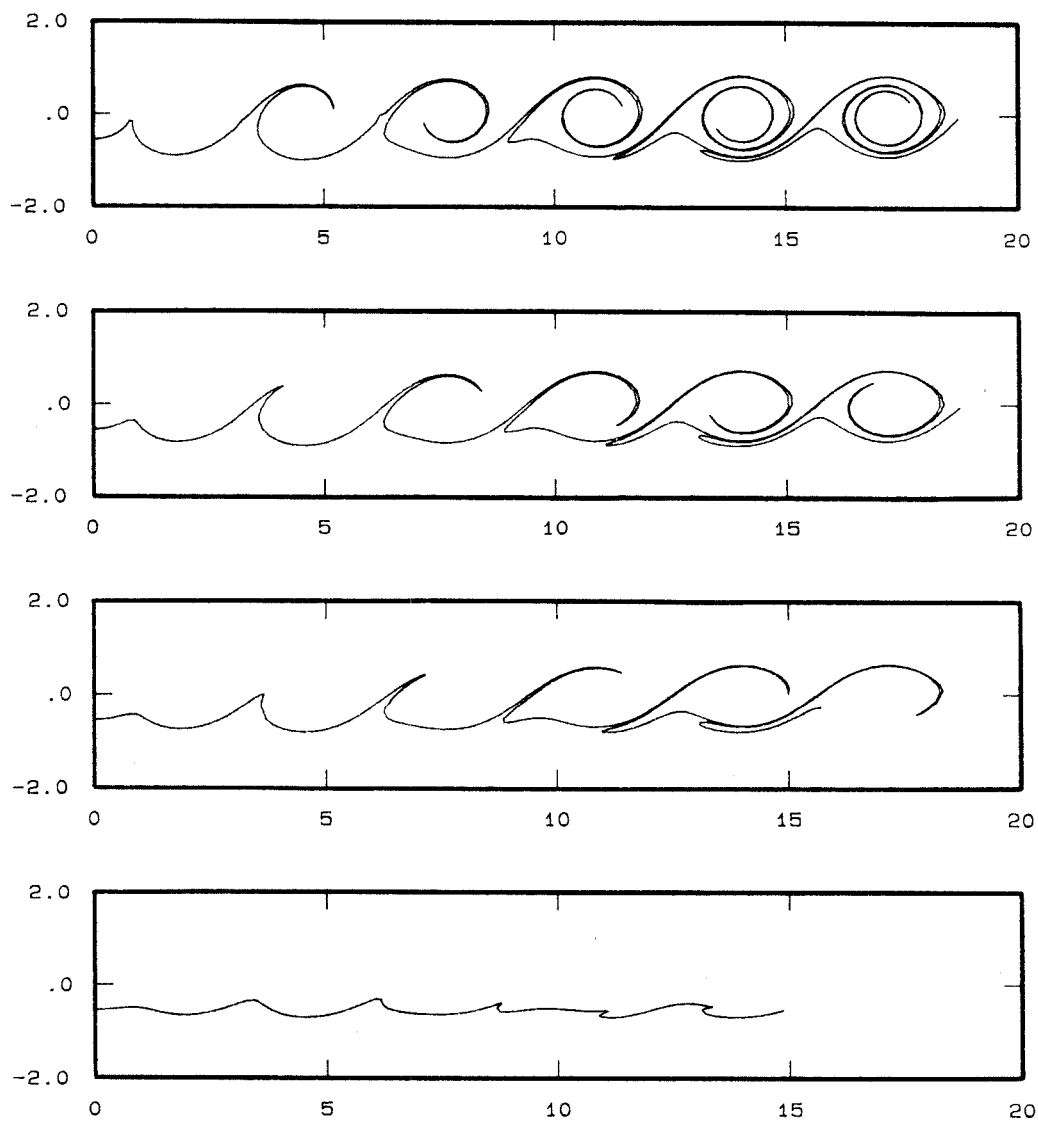
Figure B.1 : Effect of Vorticity Concentration on a Spatial Interface
U_c = 7.5 cm/sec , ΔU = 5 cm/sec , h = 0.5 cm
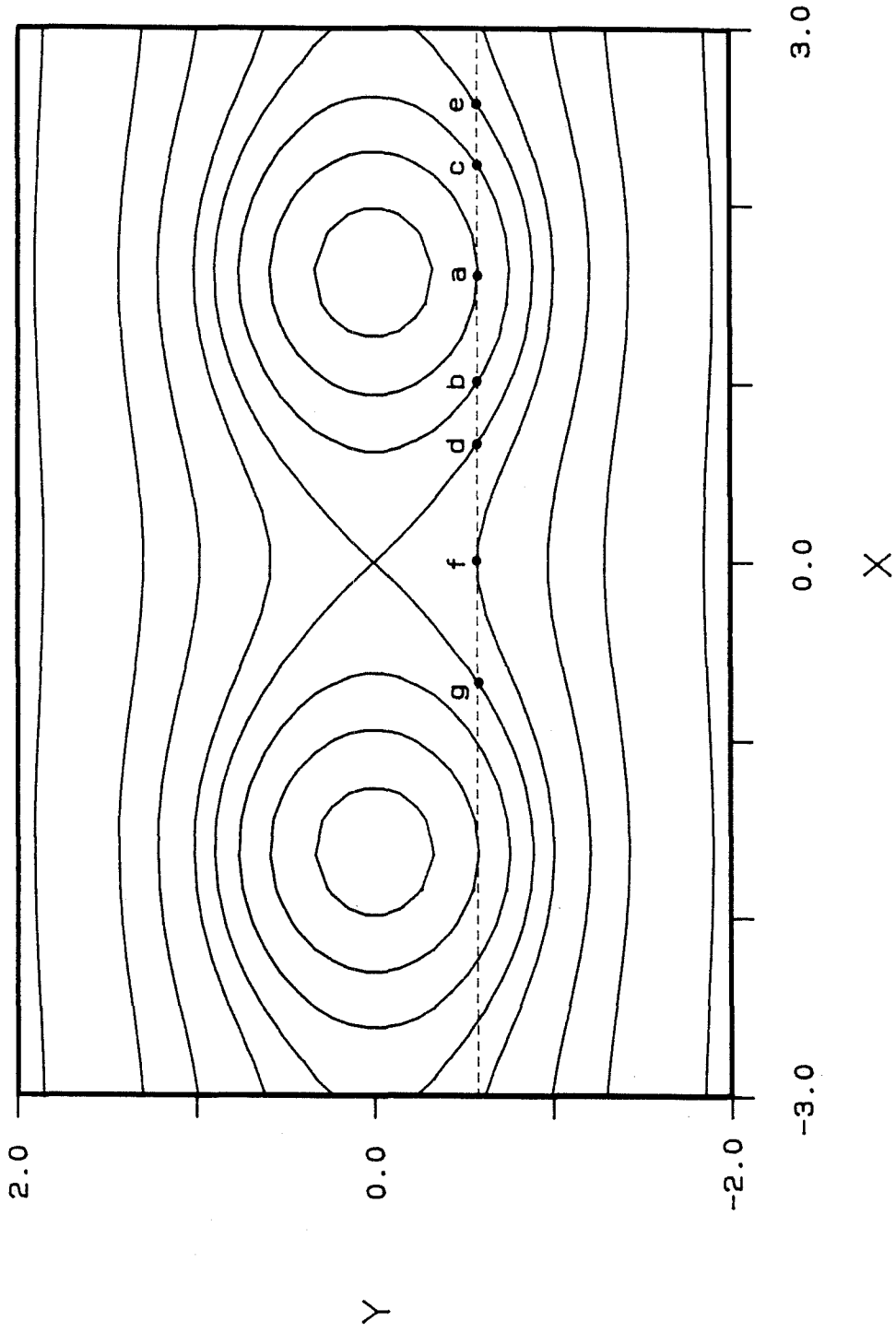(a) A = 1.0 (b) A = 0.7 (c) A = 0.5 (d) A = 0.25

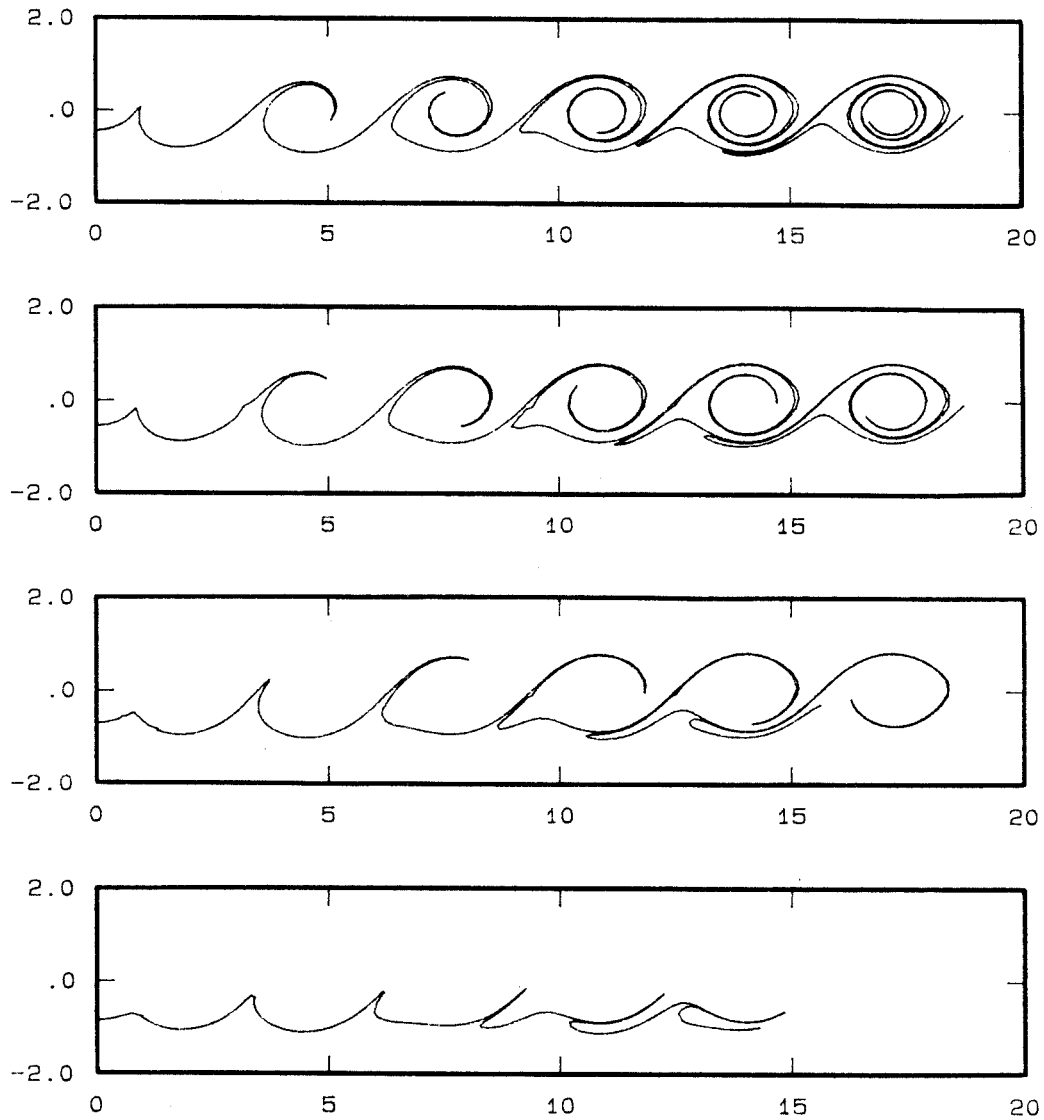Figure B.2: Streamline Pattern and Initial Interface for the Temporal Case

Figure B.3 : Effect of Point of Origin on a Spatial Interface , A = 0.8
U$_o$ = 7.5 cm/sec , ΔU = 5 cm/sec , h = 0.5 cm
(a) y$_o$ = -0.45 (b) y$_o$ = -0.55 (c) y$_o$ = -0.70 (d) y$_o$ = 0.85
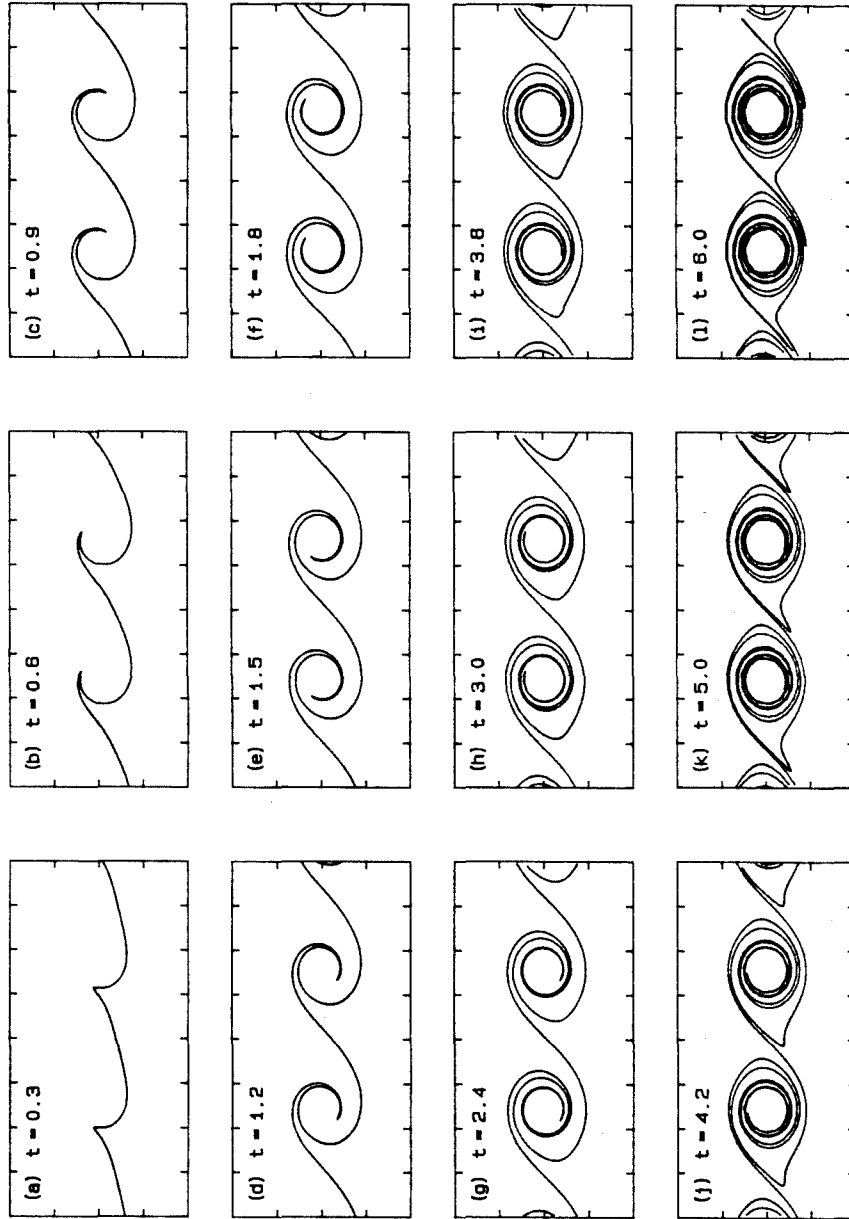
Figure B.4: Development of the Temporal Interface for a Row of Point Vortices
Dimensionless elapse time is indicated for each plot.
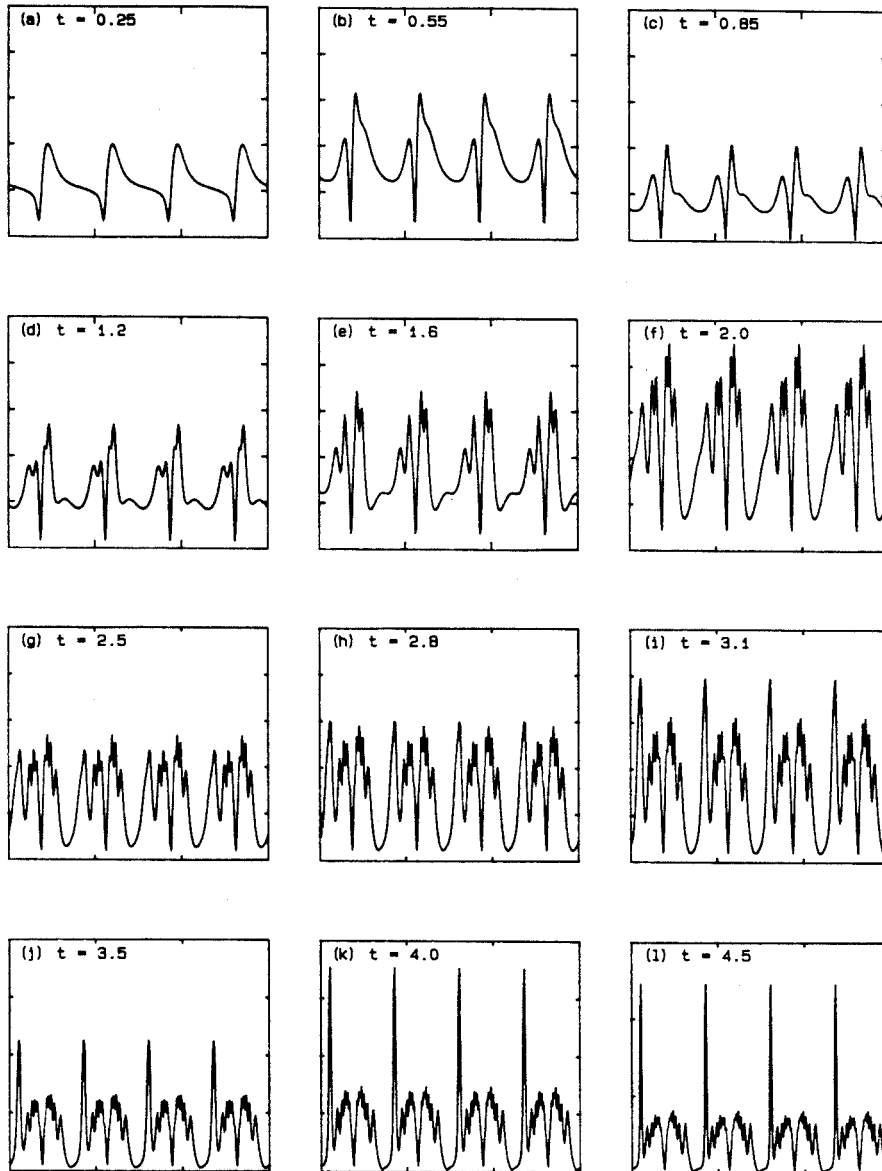$y_o = -0.4$, $\Delta t = 0.002$, $\xi_o = 0$

206

Figure B.5 : Development of Strain in the Temporal Interface Solution
shown in Figure B.4 . Abscissa for each plot is Point Label
Number (Scale is 0 to 300 for each plot). Ordinate for each
plot is Dimensionless Spacing between initially equidistant
points. Ordinate scales range from 0 to the following maxima
for each plot : (a) 0.2 (b) 0.2 (c) 0.5 (d) 0.5 (e) 0.5
(f) 0.5 (g) 1.0 (h) 1.0 (i) 1.0 (j) 2.0 (k) 2.0 (l) 3.0
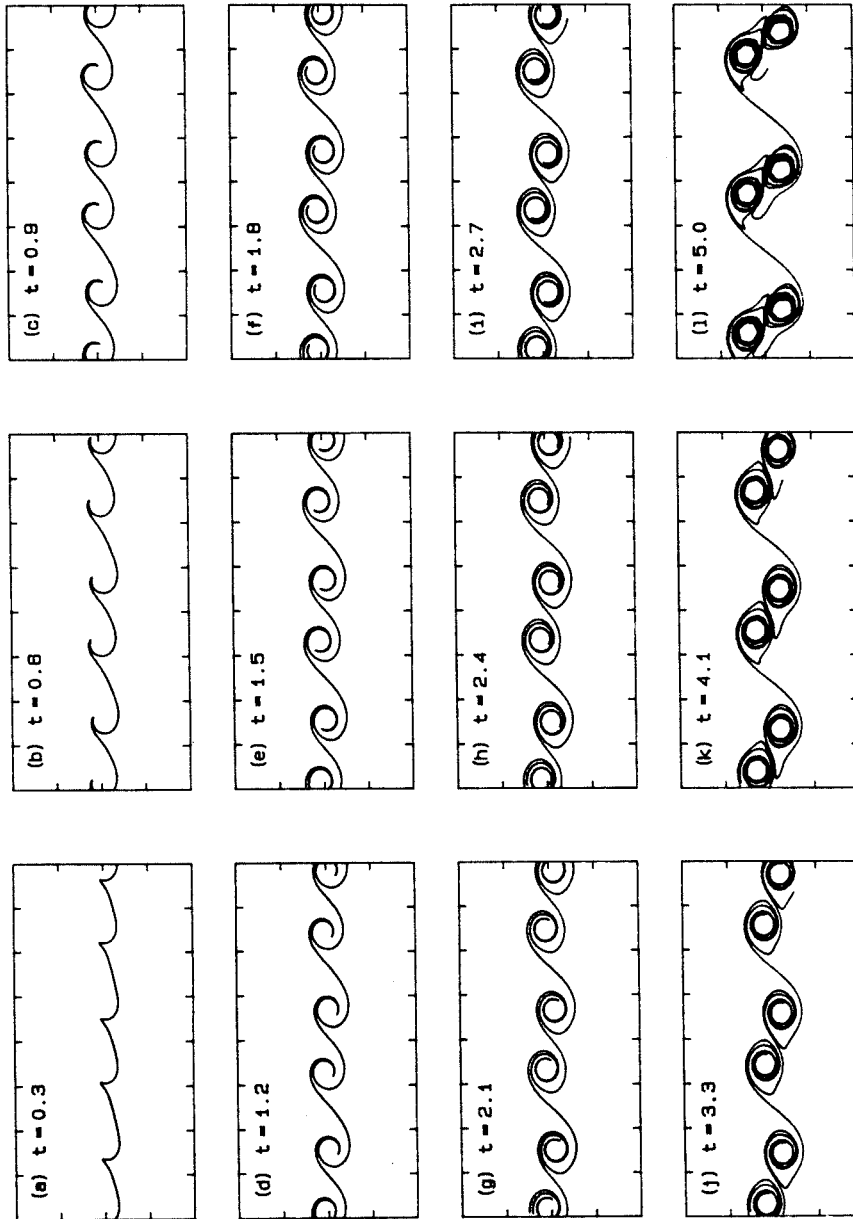Dimensionless elapse times are as indicated.

Figure B.6: Development of the Temporal Interface for a Pair of Orbiting
Rows of Point Vortices. Dimensionless elapse
time is indicated for each plot.
$y_0 = -0.4$, $\Delta t = 0.002$, $\xi_0 = 0.15$